Complex Structural and Magnetic Ordering of Layered Mixed-valent Iron Oxychalcogenide Compounds

Alexis N. Gillette



A thesis submitted in part fulfillment of the requirements for the degree of

Doctor of Philosophy at the University of Oxford

Worcester College

University of Oxford

June 2025

Declaration

The work described in this thesis was carried out in the Inorganic Chemistry Laboratory, South Parks Road, Oxford, from October 2022 to June 2025 under the supervision of Prof. Simon J. Clarke. Unless stated otherwise, all of the work described is my own and has not been submitted for any degree at this or any other university.

Alexis N Gillette

June 2025

Abstract

This thesis discusses the synthesis and characterization of several new layered mixed-valent iron oxychalgogenides.

Chapter 3 introduces the new phase $Sr_3Fe_2O_5Fe_2OS_2$ formed in the successful targeted intergrowth of the layers $[Ae_{n+1}M_nO_{3n-1}]^{2+}$ (*Ae* = Sr, *M* = Fe, *n* = 2) and $[M_2OCh_2]^{2-}$ (*M* = Fe, *Ch* = S). This phase crystallizes in the primitive, tetragonal *P*4/*mmm* space group with Fe^{3+} in FeO_5 square-pyramids in the cationic Fe1 layer while Fe^{2+} exists in distorted FeO_2S_4 octahedra in the anionic Fe2 layer. X-ray powder diffraction as well as electron diffraction and electron microscopy reveal some structural intricacies within select samples. Neutron powder diffraction reveals that the two Fe layers exhibit long-range magnetic order, but independently of each other and at different temperatures. Overall, each layer orders antiferromagnetically, with the Fe1 layer being ordered at room temperature and the Fe2 layer ordering at 115 K. Both layers also order similarly to phases that contain similar layer types, but the relationship between sequential Fe1 layers can be modelled with two different magnetic models which cannot be resolved with powder diffraction.

Chapters 4 and 5 discuss structural modifications to $Sr_3Fe_2O_5Fe_2OS_2$. Chapter 4 involves the fractional substitution of Ca for Sr on the *Ae* site which results in multiphase samples and cation order. Alternatively, chapter 5 discusses the topotactic reduction of this phase to remove the axial bridging oxygen that connects FeO_5 pyramids in the Fe1 layer to give $Sr_3Fe_2O_4Fe_2OS_2$. The reduction produces a multiphase sample with one fully-reduced phase and a partially-reduced phase. Magnetically, the products of both the *Ae* substitution and the topotactic reduction order very similarly to the parent phase presented in chapter 3.

Chapter 6 expands upon work on the similar phases $Ca_2Fe_{2.7-\delta}O_3S_{2-x}Se_x$ that was done by Bradley Sheath. This expansion resolves the space group of the superstructure that arises from the Fe-vacancy ordering of the all-sulfide phase as well as the characterization of the magnetic structure of the phases x = 0.5, 1, 1.5 as they evolve with temperature.

Acknowledgements

First and foremost, I would like to thank my supervisor Prof. Simon Clarke. Without his constant encouragement, support, and guidance, my DPhil experience would have been much less straightforward and certainly not as enjoyable. I am incredibly lucky to have had the opportunity to be a member of such a wonderful group, and cannot thank him enough for everything.

I would also like to thank my fellow group members for their contributions to making the Clarkies who we are. An immense thank you to co-captain of the Neutron Dream Team Dr. Rob Smyth for climbing to the top of Grenoble with me in the hellish heat, heading up our quiz team and always being down for "a billion beers." Thank you to Mila for being a constant source of support and friendship, whether it came to venting about science and stress or dropping everything to help with a wardrobe malfunction. You are an absolute inspiration and Ata is the luckiest kid to have a wonderful, driven mom like you!

Thank you also to Lemuel for your crystallography and JetPunk expertise, Katie for keeping the lab running and X-ray holders operational, Shay for inspiring us all to stay hydrated, and Kasamol for being a lovely presence in the office. Thank you as well to Annabel and Georgia for the lovely tea time chats and the inspiration to bring fiber arts into the office!

Even though they have since left us, I would also be remiss if I didn't extend a well-deserved thank you to former group members. Thank you Souvik for being a wonderful friend and your calming, assured mannerisms that complemented Rob so well as part of the BuLi boys, Nicola for contributing your expertise and some delicious baked goods to the group, Penny for our ranting sessions and whisky-addled adventures, and Brad for giving me a great kick-start to my project and normalizing late-morning (or afternoon) starts before I even arrived! Thank you also to our lovely masters students Alex, Callum, Ailsa, Louis, Ella, Lily, Jamie, Adam, Saumitra, and Henry for your contributions over the last few years.

Thank you to my wonderful collaborators and friend Sepideh Rahimi as well as Prof. Joke Hadermann for their incredible work on teasing out some of the intricacies of this project as well as for their hospitality in Antwerp when I wandered over to have a taste of electron microscopy.

I would also like to thank my friends and housemates who have kept me sane during the writing process. Corinne, Eugenia, and Allanah: may the Bunko Police never die!

Lastly, but certainly not least, I thank my loved ones whose belief in me never once wavered even when my belief in myself may have. My parents, Amanda and Matt, have been my biggest cheerleaders since the day I first drew breath and my fiancée, Rob, has been a constant source of support and comfort and I really would not have completed this DPhil without them.

Thank you all, from the bottom of my heart.

Table of Contents

1. Introduction

1.1. Solid-state chemistry 1
1.2. Mixed-anion solids 4
1.3. Oxychalcogenides 6
1.3.1. $[Ae_{n+1}M_nO_{3n-1}]^{2+}$ 7
1.3.2. $[M_2OCh_2]^{2-}$ layers 10
1.4. Magnetism 12
1.4.1. Diamagnetism 12
1.4.2. Paramagnetism 13
1.4.2.1. Curie paramagnetism 13
1.4.2.2. Curie-Weiss paramagnetism 13
1.4.2.3. Pauli paramagnetism 14
1.4.3. Ferromagnetism 15
1.4.4. Antiferromagnetism 16
1.4.5. Other complex magnetism 17
1.5. Magnetic exchange 18
1.5.1. Direct Exchange 18
1.5.2. Superexchange 19
1.6. Topotactic reduction 20
1.7. Aims of this thesis 21
References 23

2. Experimental Techniques

2.1. Synthetic techniques 26
2.1.1. Solid-state synthesis 26
2.1.2. Handling of air sensitive materials 28
2.1.3. Synthesis of *Ae*O precursors 29
2.2. Characterization techniques 30
2.2.1. Crystalline solids and symmetry 30
2.2.2. X-ray diffraction (XRD) 30
2.2.2.1. Single-Crystal X-ray Diffraction (SC-XRD) 33
2.2.2.2. Powder X-ray Diffraction (XRPD) 34
2.2.2.3. X-ray diffractometers 35
2.2.3. Neutron Powder Diffraction (NPD) 39
2.2.3.1. Institut Laue Langevin (ILL) 41

2.2.3.2. ISIS Neutron and Muon Facility....43
2.2.4. Refinement Methods....45
2.2.5. SQUID magnetometry....46
2.2.6. X-ray absorption near-edge spectroscopy (XANES)....47
2.2.7. Electron Diffraction....48
2.2.8. Electron Microscopy....49
2.2.9. Energy Dispersive X-rays (EDX)....49
2.2.10. Mössbauer spectroscopy....50
2.2.11. Bond valence sum (BVS) calculations....51
References....51

3. Synthesis and Characterization of $Sr_3Fe_2O_5Fe_2OS_2$

3.1. Synthesis....54
3.1.1. Ceramic synthesis....54
3.1.2. Flux synthesis....55
3.2. Structure Characterization....56
3.2.1. Idealized structure....56
3.2.2. Structural Variations....57
3.2.2.1. Variable temperature x-ray powder diffraction....62
3.2.2.2. High resolution powder neutron diffraction (HRPD)....64
3.2.2.3. Electron Diffraction....69
3.2.2.4. Transmission electron microscopy....72
3.3. Magnetic Characterization....77
3.3.1. Magnetometry....77
3.3.2. Room temperature NPD....79
3.3.3. Low variable temperature NPD....85
3.3.4. Low temperature NPD....88
3.3.5. High variable temperature NPD....89
3.4. Further Characterization....91
3.4.1. XANES measurements....91
3.4.2. Mössbauer Spectroscopy....91
3.5. Conclusions and Future Work....93
References....95

4. Synthesis and Characterization of $Sr_{3-x}Ca_xFe_2O_5Fe_2OS_2$

4.1. Synthesis....97
4.2. Structural characterization and trends....97

4.2.1. Room-temperature X-ray powder diffraction 97
4.2.2. SEM-EDX 102
4.2.3. Variable temperature X-ray powder diffraction 104
4.2.4. Room-temperature Neutron powder diffraction (D2B/HRPD) 106
4.2.5. Summary of structural trends 109
4.3. Magnetic characterization and trends 111
4.3.1. Magnetometry 111
4.3.2. Room temperature NPD 113
4.3.3. Low variable temperature NPD 114
4.3.4. Low temperature NPD 115
4.4. Conclusions 116
References 118

5. Topotactic reduction of $Sr_3Fe_2O_5Fe_2OS_2$

5.1. Introduction – Topotactic reduction of $Sr_3Fe_2O_5Cl_2$ 119
5.2. Synthesis 121
5.3. Structure Characterization 124
5.3.1. Room-temperature XRPD 124
5.3.2. Room-temperature neutron powder diffraction 128
5.3.3. Variable-temperature XRPD 134
5.4. Magnetic Characterization 137
5.4.1. Magnetometry 137
5.4.2. Room and Low temperature NPD 139
5.5. Further Characterization 145
5.5.1. XANES measurements 145
5.5.2. SEM-EDX 146
5.6. Conclusions 148
References 150

6. Further exploration into the structure and magnetism of $Ca_2Fe_{2.7-\delta}O_3S_{2-x}Se_x$

6.1. Nuclear structure of $Ca_2Fe_{2.7-\delta}O_3S_2$ 151
6.1.1. Introduction and previous work 151
6.1.2. Superstructure determination 153
6.1.3. Superstructure suppression 160
6.2. Magnetism of $Ca_2Fe_{2.7-\delta}O_3S_2$ in an applied-field 162
6.2.1. Introduction and motivation 162
6.2.2. Results and Discussion 163

6.3. Magnetism of $Ca_2Fe_{2.7-\delta}O_3S_{2-x}Se_x$ 165
6.3.1. Introduction and previous work 165
6.3.2. $Ca_2Fe_{2.7-\delta}O_3S_{1.5}Se_{0.5}$ (x = 0.5) 167
6.3.3. $Ca_2Fe_{2.7-\delta}O_3SSe$ (x = 1) 171
6.3.4. $Ca_2Fe_{2.7-\delta}O_3S_{0.5}Se_{1.5}$ (x = 1.5) 175
6.3.5. Summary of Trends 178
6.4. Conclusions 180
References 182

7. Conclusions 183
References 187

Appendices

Appendix A: Example refinements of data collected in banks not included in the text 188
Appendix B: Reference table of $Sr_3Fe_2O_5Fe_2OS_2$ samples 190
Appendix C: Refinement of sample ANG020, targeted composition $Sr_3Fe_{3.9}O_6S_2$. 190
Appendix D: Comparison of orthorhombic vs monoclinic space groups for $Sr_3Fe_2O_5Fe_2OS_2$ (ANG022b) 191
Appendix E: High VT-NPD data collected on HRPD for tetragonal $Sr_3Fe_2O_5Fe_2OS_2$ (ANG074) 192
Appendix F: VT-NPD data collected on D1B for $Sr_4Fe_2O_6Fe_2OS_2$ 193
References 194

Chapter 1: Introduction

Contents

1.1. Solid-state chemistry 1
1.2. Mixed-anion solids 4
1.3. Oxychalcogenides 6
1.3.1. $[Ae_{n+1}M_nO_{3n-1}]^{2+}$ 7
1.3.2. $[M_2OCh_2]^{2-}$ layers 10
1.4. Magnetism 12
1.4.1. Diamagnetism 12
1.4.2. Paramagnetism 13
1.4.2.1. Curie paramagnetism 13
1.4.2.2. Curie-Weiss paramagnetism 13
1.4.2.3. Pauli paramagnetism 14
1.4.3. Ferromagnetism 15
1.4.4. Antiferromagnetism 16
1.4.5. Other complex magnetism 17
1.5. Magnetic exchange 18
1.5.1. Direct Exchange 18
1.5.2. Superexchange 19
1.6. Topotactic reduction 20
1.7. Aims of this thesis 21
References 23

1.1. Solid-state chemistry

Solid-state chemistry is a sub-field of chemistry that is closely related to solid-state physics and materials chemistry which involves the synthesis, characterization, and application of materials in the solid state. In general, solid materials can be classified in two general categories: crystalline solids which exhibit long-range atomic order and amorphous solids which do not. Solid-state chemistry has played an essential part in the discovery and the understanding of many different

materials. Methods like X-ray diffraction techniques developed by Nobel laureates W.H. and W.L. Bragg [1] allow for the probing of the atomic structure of crystalline solids, and structure-property relationships can then be used to design and develop new materials that have applications in technological development. Advancements in energy storage, medical imaging, solar cells, memory storage, and more can all be attributed at least in part to this sub-field.

Li-ion batteries [2] are one of the most popular forms of energy storage, being used in mobile phones, laptops, and other rechargeable electronic devices. This technology operates on the reversible intercalation and deintercalation of lithium into and out of layered structures, storing electrical energy as chemical energy which can then be converted back into electrical energy for use in devices. $LiCoO_2$, characterized and proposed as a battery cathode material by Goodenough et al. in 1980 [3], became the first commercialized Li-ion battery cathode in the 1990's. Since then, there has been increasing demand for batteries with higher capacity, longer lifetimes, faster charging rates, higher safety, and higher sustainability. This has led to a vast amount of research into other cathode materials like Li_2MnO_2F [4] as well as research into the development of alternative Na- or K-ion [5] battery cathodes and even solid-state batteries with solid rather than liquid electrolytes [6].

In addition to energy storage, data storage is another sect of technological development that is contributed to in part by solid-state chemistry. Giant magnetoresistance achieved by alternating sheets of ferromagnetic and non-ferromagnetic materials [7] give large changes in resistance when subjected to a magnetic field versus not, and this is the chemical basis of data storage on a hard drive. As technology advances, the need for increased data storage in consistently smaller devices has led to the emerging field of spintronics which utilizes the spin of an electron as an additional degree of freedom (as opposed to just the charge) to increase the data storage density of devices [8]. Promising materials include the single-crystal thin films of the antiperovskite Mn_3GaN [9] and other 2D magnetic materials [10].

Superconductors are another type of material that has been at the forefront of solid-state chemistry research. Superconducting materials have zero resistivity and behave as perfect

diamagnets below their critical temperatures which means that at these low temperatures, large currents can be run through them with no loss to resistance. Because of this, a common application of superconductors involves running large currents through coils of superconducting wires to generate large magnetic fields. One common application for this is in MRI scanners. However, the critical temperatures of such materials are usually quite low and require expensive liquid helium to cool. Therefore, there has been much research into superconducting materials with critical temperatures above 77 K, the boiling point of the comparatively much cheaper liquid nitrogen. The breakthrough on liquid nitrogen superconductors came with the discovery of YBCO materials ($YBa_2Cu_3O_{7-\delta}$) in the 1980's [11] with critical temperatures up to approximately 90 K. As the critical temperature of a superconductor increases, the critical currents and critical fields (the currents and fields which will destroy the superconducting state) also tend to increase. Therefore, YBCO is currently used when very high fields are required like in very high-field NMR systems or in compact tokamaks used in fusion technology while other superconductors like NbTi are used in MRI instruments [12]. The cutting edge of research is constantly trying to make superconductors with higher and higher critical temperatures with the aim of achieving room-temperature superconductivity.

Semiconductors are also of particular interest within solid-state chemistry in light of their applications in renewable energy sources. These materials are a key component in solar cells and in photocatalytic water splitting. In solar cells, radiation of energy above the band gap of a semiconducting material will generate an electron-hole pair and therefore a potential difference at the junction between a p-type and n-type semiconductor. Ultimately, the charge separation from the electron-hole pair generates a current which converts the electromagnetic radiation from the sun into electrical energy. Si is commonly used due to its low cost and abundance, but higher cost, multijunction solar cells with materials like InGaP/(In)GaAs/Ge [13] can have greater efficiency. Photocatalytic water splitting [14] is another renewable energy source that produces H_2 and O_2 from water when an electron-hole pair is generated from the excitation of a semiconductor by radiation from the sun. The hole in the valence band then serves as an oxidation

catalyst, converting water into O_2 and H^+ cations, and the electron serves as a reduction catalyst reducing the H^+ ions into H_2. With these applications in mind, another sect of solid-state research is devoted to generating new and better semiconductors with appropriate band gaps and higher efficiencies for these types of applications.

1.2. Mixed-anion solids

Historically, oxides are one of the most extensively studied series of materials within solid state chemistry due to their natural abundance, stability, and ease of synthesis in our ambient, oxidizing atmosphere. Single-anion systems like halides and nitrides have also been widely studied in efforts to develop new materials and discover new and intriguing properties throughout the mid-20th and early 21st centuries. However, the exploration of single-anion species is reaching its compositional limits [15]. Consequently, the addition of another anion alongside oxygen to generate mixed-anion compounds like oxychalcogenides, oxypnictides [16], oxyhalides [17], and more has become prominent in the current era of solid-state chemistry.

There are several different characteristics of mixed-anion compounds which distinguish them from single-anion solids due to the differences between anions in charge, size, polarizability, chemical bonding preferences, and more. The first of these is local crystal field splitting due to different ligand fields when, for example, anion *X* is substituted for an oxygen in a generic MO_6 octahedron (see Figure 1.1). This can have a significant effect on electronic and magnetic structures of materials.

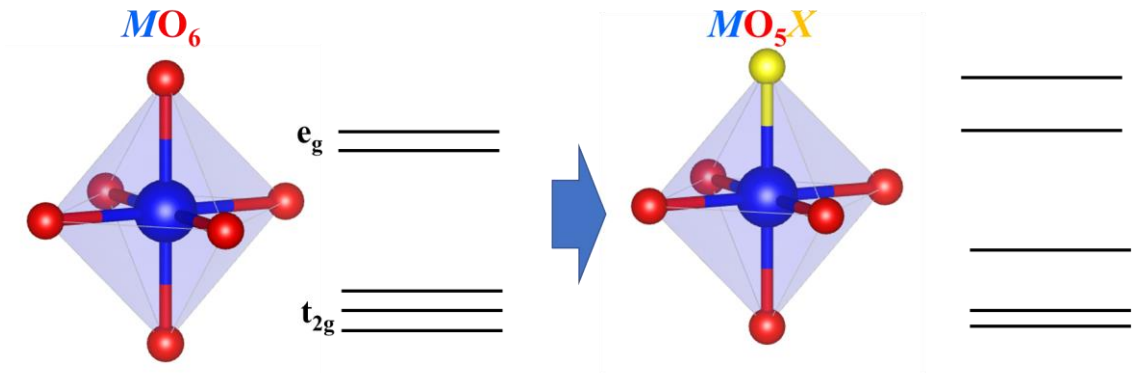


Figure 1.1. Crystal field splitting from the substitution of anion *X* for an oxygen in a generic MO_6 octahedron.

Additionally, the energy levels of orbitals typically increase with decreasing anion electronegativity. This means that the addition of different anions in mixed-anion species can tune band gaps of semiconductors (see Figure 1.2). This has been observed in many different mixed-anion compounds and has led to the development of several promising candidates for photocatalysis like the family $Ln_2Ti_2O_5S_2$ (especially *Ln* = Y) [18, 19].

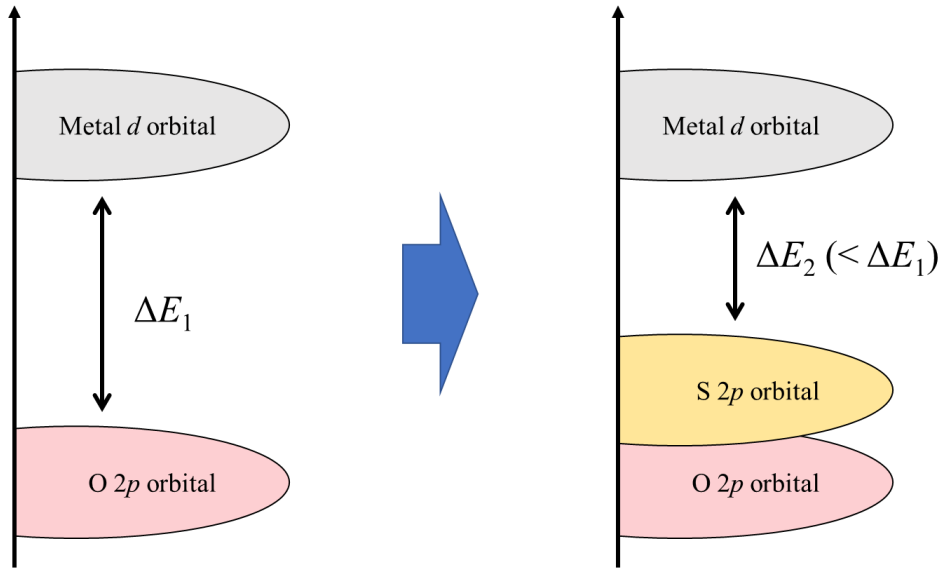


Figure 1.2. Illustration of the change in band gap from the addition of a less electronegative S anion into a metal oxide.

When the second anion (which is not oxygen) is of a similar size and has similar chemical requirements as oxygen, like in the cases of nitride or fluoride, the two anions can occupy similar

crystallographic sites which can result in either long-range disorder or ordered occupancies in similar sites. However, when the second anion is in the second row of the *p*-block or below, long-range anion ordering is often expected due to a difference in size alone though differences in polarizability (like between oxide and sulfide) would also contribute to this anion ordering. One of the common ways in which this anion ordering is realized is in the layering of mixed-anion compounds. Due to this layered nature of such species, one popular method that is used to conceptualize new target mixed-anion materials is known as the "building block" method, coined thus by Laurent Cario and colleagues [20, 21]. This method involves proposing new structures that are intergrowths of 2D "building block" layers that have been reported in literature (see Figure 1.3). This method also necessitates that the building blocks are selected based on complementary lattice parameters, charges, and chemical behaviour in order to obtain a stable compound.

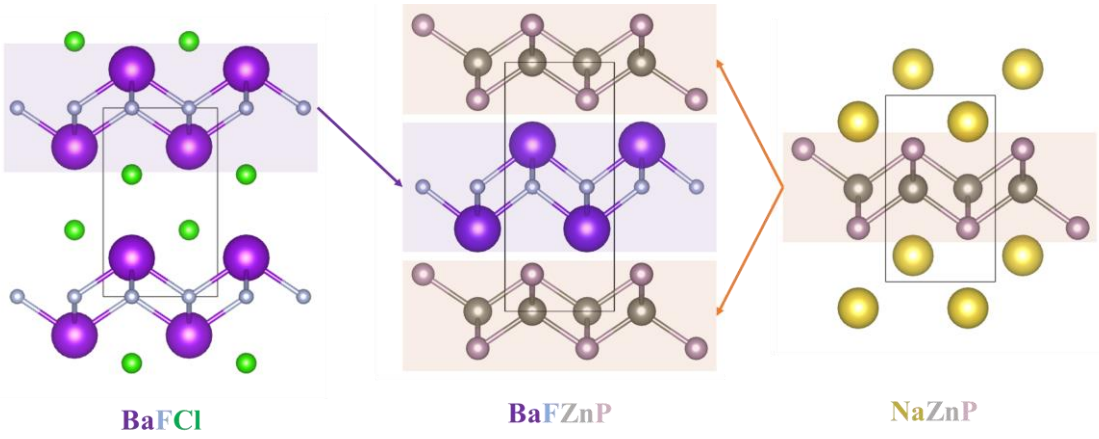


Figure 1.3. The intergrowth of layers $[Ba_2F_2]$ and $[Zn_2P_2]$ in compounds BaFCl and NaZnP respectively which form the intergrowth BaFZnP [19].

1.3. Oxychalcogenides

Oxychalcogenides are mixed-anion solids which contain oxide anions along with a chalcogenide anion: sulfide (S^{2-}), selenide (Se^{2-}) or telluride (Te^{2-}). Due to the size and polarizability differences between these anions and oxygen, they do typically adopt layered structures due to long-range anion order. However, the differences between the chalcogens themselves, like sulfur and selenium, are much less significant and due to this, they often can occupy the same crystallographic site and thus a solid-solution which has controllable ratios of the chalcogen and

can tune properties like band gaps and electrical properties [16, 22]. The layer types that are most relevant to this thesis are described here.

1.3.1. $[Ae_{n+1}M_nO_{3n-1}]^{2+}$

The cationic layer type that is most relevant to this thesis is the $[Ae_{n+1}M_nO_{3n+1}]^{2+}$ layer which forms a homologous series when these layers are separated by an antifluorite-type copper sulfide anionic layer. Members of this series with n = 1, 2, and 3 are shown in Figure 1.4 below.

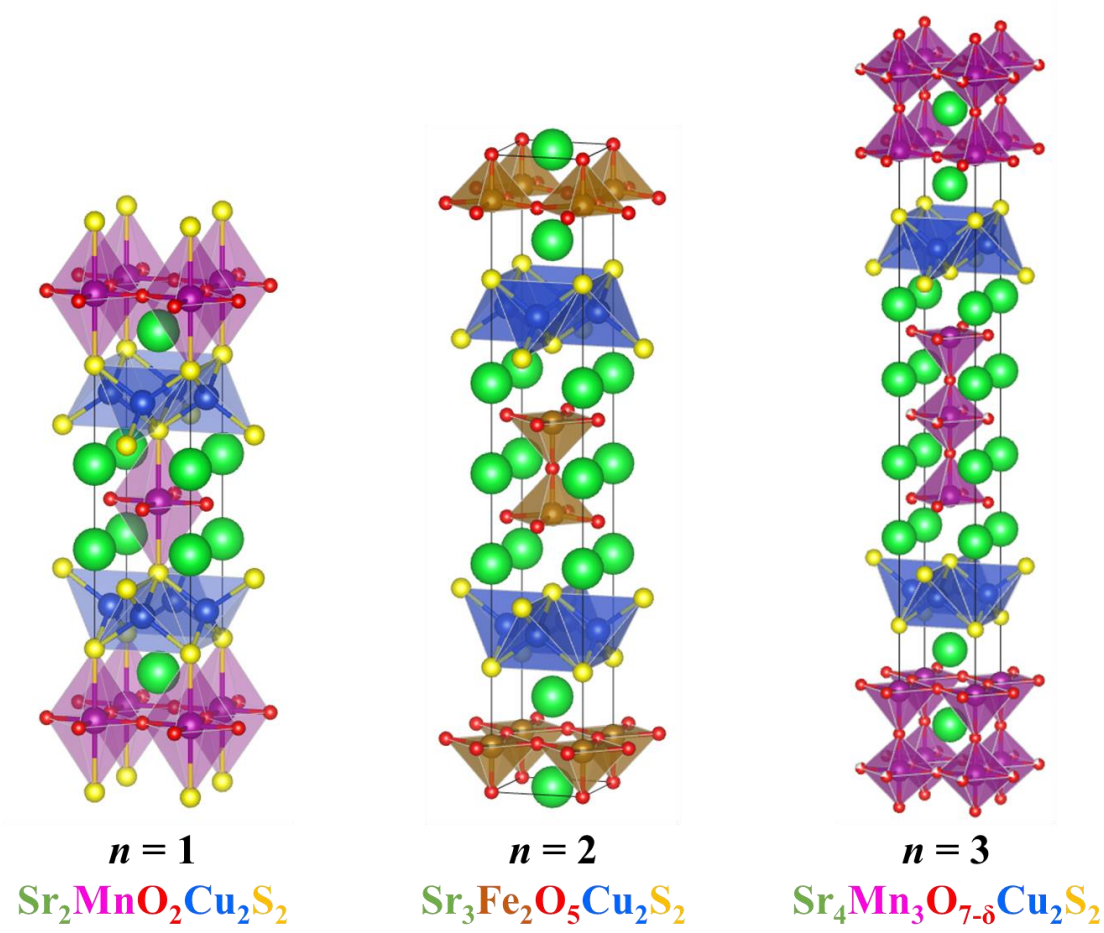


Figure 1.4. Members of the homologous series $Ae_{n+1}M_nO_{3n+1}Cu_2S_2$ (n = 1, 2, and 3) [23-25].

The n = 2 thickness of this layer is the most applicable to this thesis, and many different modifications have been carried out on phases containing this layer. The first of these is alkaline earth substitution, wherein a solid solution is formed with multiple alkaline earth cations. In these solid solutions, cation order arises in that the larger cation preferentially occupies the larger 12-coordinate *Ae*1 site and the smaller cation preferentially occupies the smaller, 8-coordinate *Ae*2

site (Figure 1.5.). This has been reported for $Sr_{3-x}Ca_xFe_2O_5Cu_2Ch_2$ [26], $Ba_{3-x}Sr_xFe_2O_5Cu_2Ch_2$, and $BaCa_2Fe_2O_5Cu_2S_2$ [27].

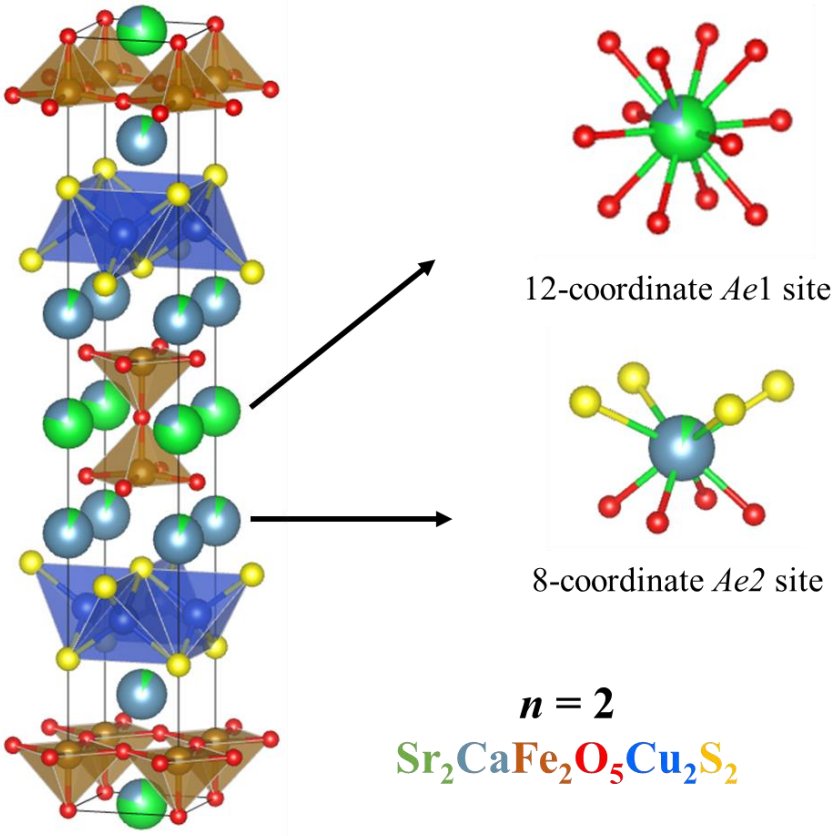


Figure 1.5. Cation order in $Sr_2CaFe_2O_5Cu_2S_2$.

In addition to this, an extra equivalent of *Ae*O can be inserted into the $[Ae_3M_2O_5]$ layer, which has the effect of separating the FeO_5 pyramids along *c* which then translate by ½ of a unit cell along *a* and *b* to generate the structure shown in Figure 1.6 for Sr_2FeO_3CuS [24].

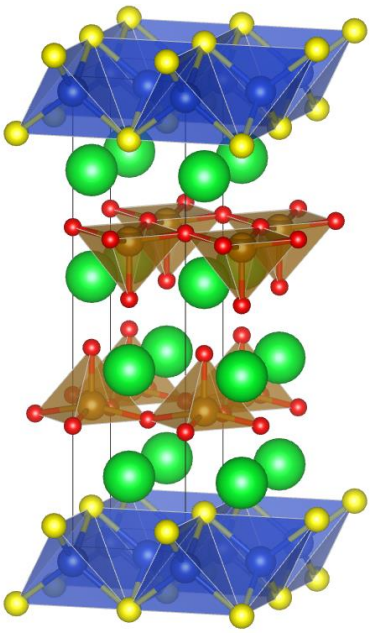


Figure 1.6. Structure of Sr_2FeO_3CuS showing the separation of FeO_5 pyramids from the $Sr_3Fe_2O_5Cu_2S_2$ shown in Figure 1.4.

The axial bridging oxygen can also be removed via topotactic reduction (section 1.6), as shown in the reduction of $Sr_3Fe_2O_5Cl_2$ to generate $Sr_3Fe_2O_4Cl_2$ [28]. This is discussed more at the beginning of chapter 5.

The metal ion in this layer is usually magnetic (Fe, Mn, Co), and this thesis in particular concerns layers where *M* = Fe. Indeed, the magnetic structure for many of these phases has been characterized and reported, and they all order antiferromagnetically along the ~180° Fe-O-Fe superexchanges as expected from the Goodenough-Kanamori rules (see section 1.5). It is found that the moments in compounds with mixed-*Ae* sites are tilted out of the basal plane whereas the moments for the all-Sr and all-Ba phases are oriented in the basal plane [26, 27]. The low temperature (T < 10 K) long-range-ordered magnetic moments for several phases are recorded below in Table 1.1.

Table 1.1. Saturated magnetic moments of iron in compounds that contain the $[Ae_{n+1}M_nO_{3n+1}]^{2+}$ layer type where $n = 2$ and M = Fe.

Compound	Fe moment (μ_B)
$Sr_3Fe_2O_5Cu_2Se_2$ [21]	3.6(2)
$CaSr_2Fe_2O_5Cu_2S_2$ [26]	3.068(20)
$Ca_2SrFe_2O_5Cu_2S_2$ [26]	2.930(16)
$CaSr_2Fe_2O_5Cu_2Se_2$ [26]	3.376(14)
$Ca_2SrFe_2O_5Cu_2Se_2$ [26]	3.433(15)
$Ba_3Fe_2O_5Cu_2Se_2$ [27]	4.22(5)
$BaSr_2Fe_2O_5Cu_2S_2$ [27]	3.38(5)
$BaSr_2Fe_2O_5Cu_2Se_2$ [27]	3.40(1)

All of the compounds discussed so far in this section have had the same $[Cu_2Ch_2]$ or other antifluorite-type anionic layer, but one exception to this is $Ca_2Fe_{2.7-\delta}O_3Ch_2$ which combines the $[Ae_{n+1}M_nO_{3n+1}]^{2+}$ ($n = 1$, Ae = Ca, M = Fe) with an $[M_2OCh_2]^{2-}$ (M = Fe) layer which is discussed further in section 1.3.2. Based on the building-block method, it therefore stands to reason that this $[M_2OCh_2]^{2-}$ also may be able to exist in an intergrowth with a $[Ae_{n+1}M_nO_{3n+1}]^{2+}$ layer with $n > 1$.

1.3.2. $[M_2OCh_2]^{2-}$ layers

The $[M_2OCh_2]^{2-}$ layer has been of interest in solid-state chemistry because it contains an MO_2 square lattice that is an antitype of the $[CuO_2]$ planes of cuprate superconductors [29]. Most commonly, these are separated by small layers like $[A_2]^{2+}$ or $[A_2X_2]^{2+}$ (e.g., $Na_2Fe_2OS_2$ [30] or $La_2O_2Fe_2OS_2$ [31]). Because the incorporation of these intervening layers results in an off-setting of the $[M_2OCh_2]^{2-}$ layers, they most often crystallize in the body-centred $I4/mmm$ space group with the one exception being the high-pressure $BaFe_2OCh_2$ (Ch = S, Se) [32, 33] which crystallizes in the tetragonal $P4/mmm$ space group. While these layers again exist with multiple combinations of elements (M = Mn, Fe, Co and Ch = S, Se), the phases that are most related to this thesis have M = Fe.

Given that Fe is a magnetic ion, it is unsurprising that the $[Fe_2OCh_2]^{2-}$ exhibits long-range magnetic order. In general, these layers as reported in literature all order around similar temperatures with similar ordered moments (see Table 1.2) and they order according to the 2-**k** magnetic structure first proposed by Fuwa *et al.* [34] and depicted in Figure 1.7. This magnetic

model is called a "2-**k**" model because it is described by two perpendicular propagation vectors, $\mathbf{k}_1$ = (½, 0, ½) and $\mathbf{k}_2$ = (0, ½, ½) and it is governed by the J_2 ~180° Fe-O-Fe superexchange and the J_3 ~90° Fe-S-Fe superexchange as opposed to the J_1 Fe-Fe direct exchange or 90° Fe-O-Fe superexchange (see section 1.5 for more about magnetic exchange). All of the moments order within the basal plane.

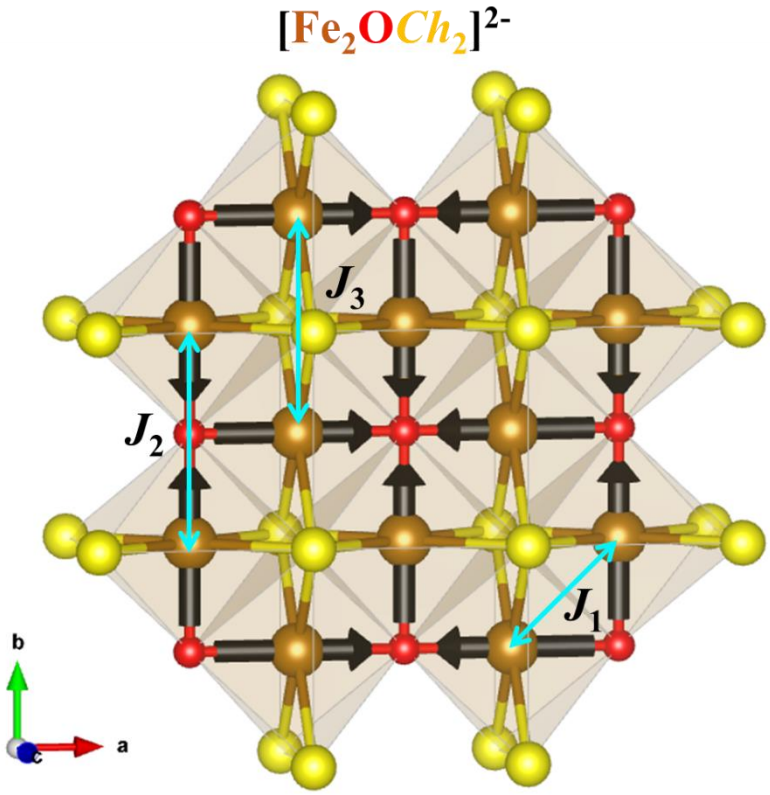


Figure 1.7. Illustration of the 2-**k** magnetic model that describes magnetic order in the $[Fe_2OCh_2]^{2-}$ layer with exchange interactions labelled.

Table 1.2. Reported ordering temperatures and magnetic moments for various compounds containing the $[Fe_2OCh_2]^{2-}$ layer which order according to the 2-**k** magnetic model depicted in Figure 1.7.

Compound	T_N (K)	Fe moment (μ_B)
$Sr_2F_2Fe_2OS_2$ [35]	106(2)	3.3(1)
$Pr_2O_2Fe_2OSe_2$	88.6 [36]	3.36(1) [37]
$Ce_2O_2Fe_2OSe_2$ [38]	92.3(2)	3.32(1)
$Nd_2O_2Fe_2OSe_2$	~ 90 [34]	3.18(1) [38]
$La_2O_2Fe_2OS_2$ [31]	105.48(3)	3.30(4)
$La_2O_2Fe_2OSe_2$	~ 90 [39]	3.50(5) [40]

One exception to this magnetic structure is the compound $Ca_2Fe_{2.7-\delta}O_3S_2$ which contains the layer $[Fe_{1.7-\delta}OS_2]$ which has ordered iron vacancies and crystallizes in the tetragonal *P*4/*mmm* space

group [41, 42]. Because this structure has ordered vacancies in the Fe_2O square lattice (and also because it has magnetic ions in the cationic $[Ca_2FeO_2]^{2+}$ layer), the $[Fe_{1.7-\delta}OS_2]$ layer orders differently with a canting both within and out of the basal plane (see chapter 6). However, this is still a 2-**k** magnetic structure that is generally antiferromagnetic, but since it is an uncompensated antiferromagnet as the vacant iron sites would all order in the same direction, there is a net ferromagnetic moment in the phase making it ferrimagnetic. The phases of the solid solution $Ca_2Fe_{2.7-\delta}O_3S_{2-x}Se_x$ introduce disorder on the *Ch* site which then disrupts the long-range Fe-vacancy ordering [41], and the magnetic behaviour of these phases is discussed in chapter 6.

1.4. Magnetism

Magnetism is an important property which contributes to the functionality and application of materials. Magnetic properties are determined both by the arrangement of the crystal lattice as well as the electronic structure, as the electronic structure and oxidation state of an element determines the number of unpaired electrons in a system and the local geometry determines how these spins interact with one another. This then in turn determines how a solid behaves in response to external magnetic fields. This section will introduce the common types of magnetism in solids.

1.4.1. Diamagnetism

In diamagnetic materials, there are no unpaired electrons. As a result of this, diamagnetic materials oppose applied magnetic fields according to Lenz's law as the paired electrons circulate around the nuclei and generate a small current which results in a magnetic moment to oppose applied fields. The susceptibility of diamagnets is always negative. Core diamagnetism is also generally weak (-10^{-6} – -10^{-4} emu mol^{-1}), but dominates over weak Pauli paramagnetism in cases of non-magnetic materials like copper or gold. Superconducting materials are much stronger, perfect diamagnets and display the Meissner effect [43].

1.4.2. Paramagnetism

Paramagnetism occurs in a material with unpaired electrons whose spins align parallel to an applied field which then leads to a positive magnetization. Depending on whether these electrons are localised or itinerant, there are further classifications of paramagnetism which include Curie, Curie-Weiss, or Pauli paramagnetism.

1.4.2.1.Curie paramagnetism

Curie paramagnetism describes that which is present in most materials with localised unpaired spins that do not interact. These materials obey the Curie Law (Equation 1.1) for which χ is the magnetic susceptibility, C is the Curie constant, and T is the temperature.

$$\chi = \frac{C}{T} \qquad \text{(Eqn. 1.1)}$$

The Curie constant can then be extracted from a plot of T vs $1/\chi$ and related to the effective magnetic moment μ_{eff} of the ions as described by Equation 1.2.

$$\mu_{eff} \approx 2.84\sqrt{C} \qquad \text{(Eqn. 1.2)}$$

The magnetic susceptibility from Curie paramagnets dominate the effects from core diamagnetism as it is usually on the order of 10^{-4} – 10^{-2} emu mol^{-1}.

1.4.2.2.Curie-Weiss paramagnetism

Curie-Weiss paramagnetism occurs when localized unpaired electron spins interact with each other thereby requiring an adjustment to the Curie law which gives the Curie-Weiss law below (Eqn. 1.3) where θ is the Weiss constant. The magnitude of the Weiss constant is dependent upon the strength of the interactions between magnetic moments and its sign reflects the type of interaction: a positive Weiss constant indicates parallel spins and a negative Weiss constant indicates antiparallel spins.

$$\chi = \frac{C}{T-\theta} \qquad \text{(Eqn. 1.3)}$$

1.4.2.3. Pauli paramagnetism

Pauli paramagnetism occurs in systems where the electrons are itinerant and no longer localized, like in metals. In these systems, when there is no applied field there are an equal number of spin up and spin down electrons in the conduction band. When an external magnetic field is applied, however, the degeneracy of spin states is lost and it becomes more energetically favourable for the spins to align with the field which means that the populations of spin up and spin down electrons is no longer equal (Figure 1.8). This generates a net positive magnetization of similar magnitude to core diamagnetism and independent of temperature, but proportional to the applied field. For a given offset like that shown in Figure 1.8, there is a narrower band with a higher density of states at the Fermi level which will give a larger spin polarisation and therefore a higher Pauli susceptibility. The Pauli susceptibility can therefore be used to estimate the density of states at E_F.

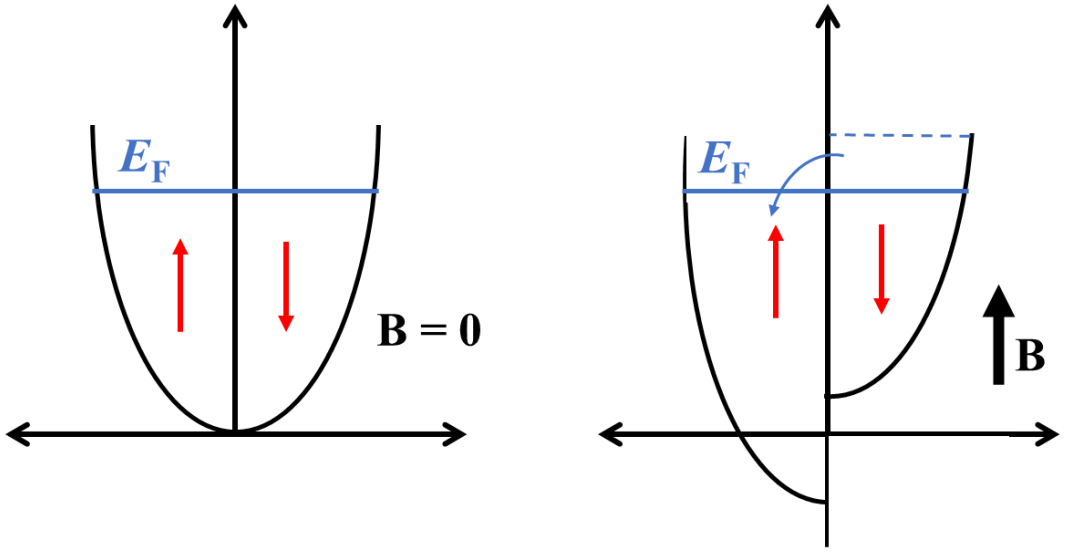


Figure 1.8. The change in density of states in an applied magnetic field.

Another kind of paramagnetism which is temperature-independent is known as Van Vleck paramagnetism. This occurs when low-lying excited states (which are not thermally populated) mix with the ground state resulting in a small paramagnetic contribution.

1.4.3. Ferromagnetism

Ferromagnetism occurs in solids which contain unpaired electrons which have strongly interacting spins. This can occur in itinerant spin-polarized materials like Fe or Ni or in more localized systems like NaXF$_3$ (X = V, Co) where the spins of electrons on individual atoms align [44]. The moments in these systems are locally grouped into domains below the Curie temperature (T_C) which are randomly oriented to give a net magnetic moment of zero for the sample when there is no external field applied. In the presence of an external field, the domains align to give a positive net magnetic moment on the order of 10^{-2} – 10^{0} emu mol^{-1}. However, above T_C, the thermal energy of the system is large enough that it disrupts the interactions and the material loses magnetic order and any domain structure. Given the large order of magnitude of a ferromagnetic signal, small ferromagnetic impurities can mask magnetization signals from paramagnetic, diamagnetic or weakly antiferromagnetic samples.

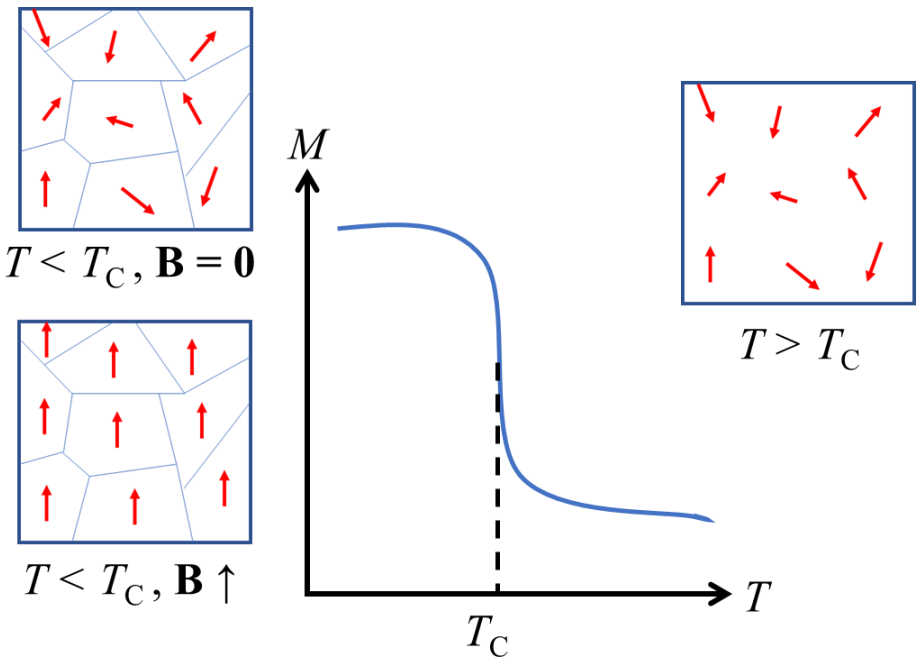


Figure 1.9. Magnetic susceptibility of a ferromagnet vs temperature alongside depictions of the alignment of a domain structure below T_C when cooled in an applied field versus when cooled in zero field.

Ferromagnets are often classified according to their coercivity and retentivity. Coercivity relates to the strength of the magnetic field which must be applied to overcome remnant magnetization after reaching saturation, and retentivity is the material's ability to retain order once the applied

field is removed. Materials with low versus high coercivity are soft versus hard ferromagnets, and materials with both high coercivity and high retentivity are known as permanent magnets. Both of these can be visualized in magnetization isotherms which are measured by magnetizing a sample, reversing the direction of the applied field, and then reversing the direction of the field again to create a hysteresis loop (Figure 1.10).

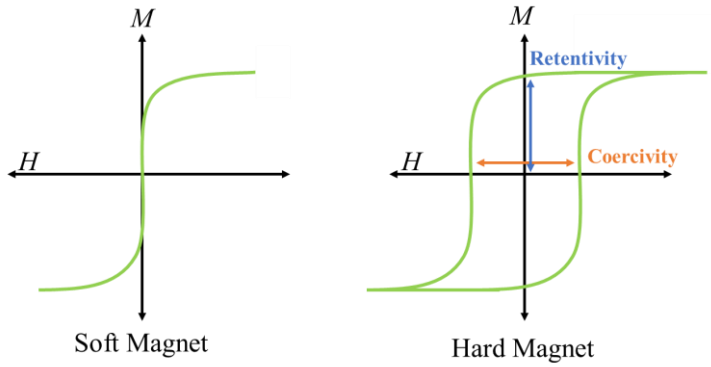


Figure 1.10. *M* v *H* isotherms for a soft (right) and a hard (left) magnet.

1.4.4. Antiferromagnetism

Antiferromagnetism arises from the long-range order of localized electrons' spins which align antiparallel below the Néel temperature (T_N) and lead to a net magnetization of zero. Above T_N, antiferromagnets behave according to the Curie-Weiss law, but as the thermal energy promoting randomness decreases below T_N, the antiferromagnetic coupling between neighbouring metallic centres dominates and there is a reduction in susceptibility as the spins are less able to align with the applied magnetic field. As discussed in section 1.3, many compounds that contain the $[Ae_{n+1}M_nO_{3n-1}]^{2+}$ or $[Fe_2OCh_2]^{2-}$ layers are antiferromagnets.

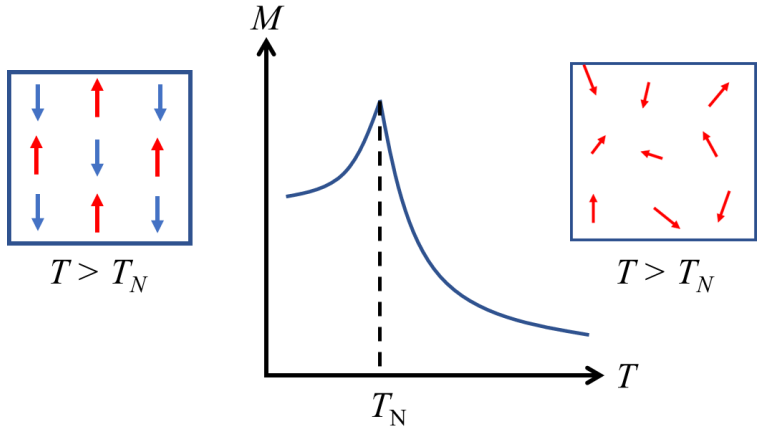


Figure 1.11. Magnetic susceptibility of an antiferromagnet vs temperature alongside depictions of the alignment spins above and below T_N.

1.4.5. Other complex magnetism

There are a few other kinds of magnetism in solids that are relatively more complex that those mentioned above. These are ferrimagnetism, metamagnetism, and frustrated magnetism.

Ferrimagnetism results from samples when spins are aligned antiparallel but have different magnitude of moments. Overall, this is antiferromagnetic order, but can result in net ferromagnetic behaviour. Spinel like $NiCo_2O_4$ [45] or uncompensated antiferromagnets like Fe_3O_4 [46] are examples of ferrimagnetic materials.

Metamagnetic materials undergo a magnetic phase transition from antiferromagnetic to ferromagnetic when strong magnetic fields are applied. For example, $Sr_2MnO_2Na_{1.6}Se_2$ [47] undergoes this transition. In low magnetic fields, this structure displays *A*-type antiferromagnetism where the Mn ions in individual layers order ferromagnetically but adjacent layers order antiferromagnetically making the structure overall antiferromagnetic. When an applied field reaches a strength of around 2 T, the layers instead align ferromagnetically making the overall structure ferromagnetic in fields above 2 T.

Frustrated magnetism occurs in spin-glass materials where there are strong interactions between spins within a lattice which cannot all be satisfied. One example of an instance where magnetic frustration occurs is with antiferromagnetism within a triangular lattice (Figure 1.12). At high temperatures, thermal energy overcomes these frustrations and the spins are randomly oriented, leading to paramagnetic behaviour. As the material is cooled, however, disordered clusters of spins begin to form and then ‘freeze’ in spin-glass materials below its ordering temperature (T_G). Evidence of “spin-glassiness” and frustrated magnetism include more pronounced deviations in the ZFC/FC curves, hysteresis loops that do not close at temperatures below T_G, and vertical displacement of hysteresis loops along the magnetization axis.

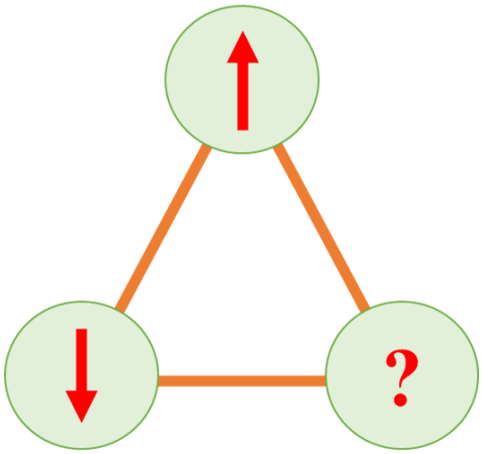


Figure 1.12. Spin frustration in a triangular lattice.

1.5. Magnetic exchange

Magnetic ions in a solid can interact through several different mechanisms. There are long-range interactions through space, but these have a spatial dependence of r^{-3} and are too weak to account for long-range observable magnetic order and are usually suppressed by thermal energy even at very low temperatures. However, interactions of unpaired electrons through overlapping frontier orbitals are much more significant.

1.5.1. Direct Exchange

Direct exchange occurs when the orbitals of neighbouring magnetic ions directly overlap and interact. This interaction has a spatial dependence on the order of r^{-12} meaning that the strength of this interaction rapidly decreases in space which thereby limits this interaction to nearest-neighbour magnetic ions. However, when magnetic ions are spatially distant to one another like in the case of more complex solids, this interaction is suppressed due to the significant spatial dependence. This exchange normally results in ferromagnetic (FM) coupling between metals with the same electron count (Figure 1.13).

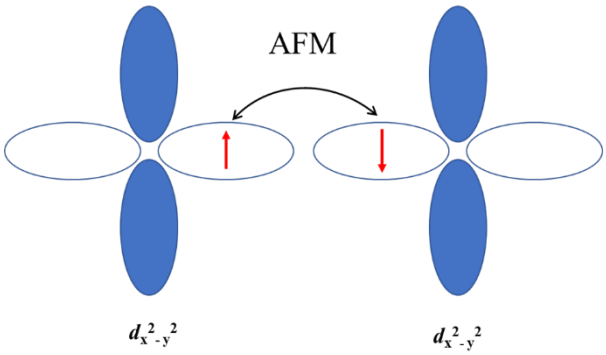


Figure 1.13. Direct exchange between two filled orbitals with FM coupling.

1.5.2. Superexchange

Two metallic ions that are too far apart to interact significantly through direct exchange can still interact and be coupled through a mediating non-magnetic ion. This is called a superexchange interaction. In this interaction, there is a donation of electron density from the anion to the metal through covalency which then necessitates that there is a preference in the spin state of the donated electron density according to the spin state of the unpaired electrons in the metal *d* orbitals. Hund's rules and the Pauli exclusion principle can then be used along with the geometry of an exchange and electron configurations of the involved anions to predict the coupling between two magnetic ions. This is the basis of the Goodenough-Kanamori rules [48-50]. The most common superexchanges are a 180° antiferromagnetic superexchange via a single anion orbital and a 90° ferromagnetic superexchange via two orthogonal anion orbitals as depicted in Figure 1.14 below.

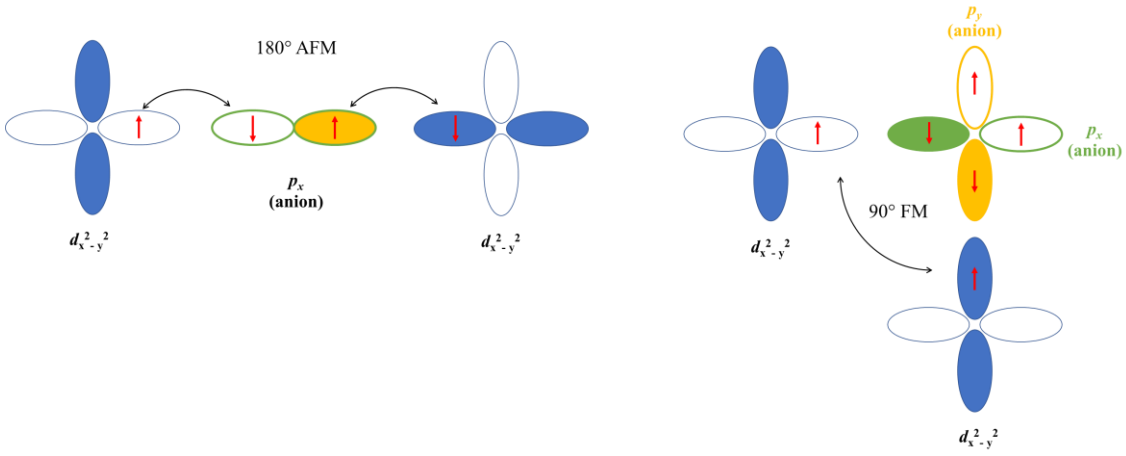


Figure 1.14. Depictions of an AFM 180° superexchange and a FM 90° superexchange.

1.6. Topotactic reduction

The driving force behind solid-state reactions is largely thermodynamic (see chapter 2.1), with the products being thermodynamically favored over the starting materials. However, due to the low mobility of ions in the solid state, this means that the activation energy for solid-state reactions is quite high, often requiring temperatures on the order of 1000°C to overcome the activation energy barrier. Given these extreme reaction conditions, these syntheses are under thermodynamic control and the most thermodynamically favored product will be produced. However, lower temperature soft-chemical techniques have been shown to provide access to a plethora of metastable, kinetic phases in the solid state. Techniques such as intercalation and deintercalation chemistry fall under this soft-chemical title, but the method most applicable to this thesis is topotactic reduction.

Topotactic reactions [51] are reactions for which the orientation of the crystalline product is determined by the starting material. Often, these involve the introduction or removal of an atom, either forming or breaking bonds. In this thesis, the topochemical reduction involves the deintercalation of an oxygen atom and the reduction of Fe^{3+} to Fe^{2+} while the symmetry of the parent and product phases remain the same. Further detail about this reaction can be found in Chapter 5.

1.7. Aims of this thesis

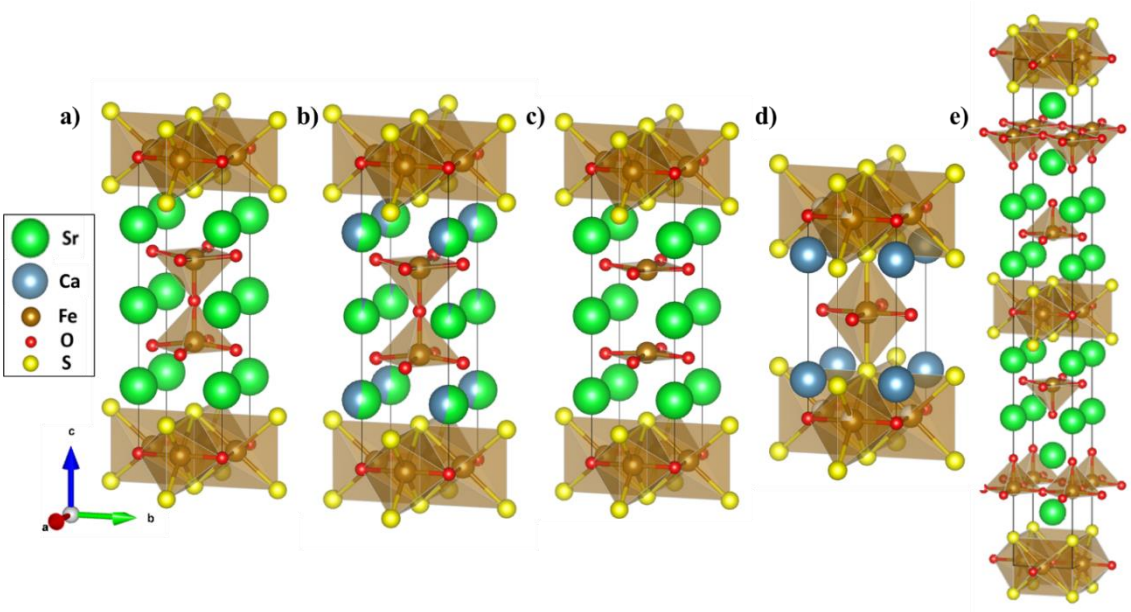


Figure 1.15. Compounds discussed in the course of this thesis.

The aim of this thesis was to synthesize new complex solids which are intergrowths of the $[Ae_{n+1}M_nO_{3n-1}]^{2+}$ and the $[M_2OCh_2]^{2-}$ layers introduced on section 1.3 using the building block approach of conceptualizing new target compounds and then to characterize their nuclear structure and magnetic behavior.

Chapter 3 introduces the product of this successful targeted synthesis combining the $[Ae_{n+1}M_nO_{3n-1}]^{2+}$ (n = 2, Ae = Sr, M = Fe) layer with the $[M_2OCh_2]^{2-}$ (M = Fe, Ch = S) layer to form $Sr_3Fe_2O_5Fe_2OS_2$ (Figure 1.15a). This compound is a layered, mixed-valent iron oxysulfide as it contains iron in the 3+ and 2+ oxidation states segregated by layer. It has been synthesized in high purity and its nuclear and magnetic structures have been characterized. Magnetically, this structure is antiferromagnetic with the individual layers ordering independently of each other. There are some outstanding queries concerning this compound in that X-ray powder diffraction data reveals some sample-dependent features that transmission electron microscopy has begun to give light to, and there are also two different magnetic models describing the $[Sr_3Fe_2O_5]^{2+}$ Fe1 layer that are cannot be fully resolved from neutron powder diffraction.

Chapter 4 describes the fractional substitution of Ca for Sr on the *Ae* site of $Sr_3Fe_2O_5Fe_2OS_2$ to form the solid solution $Sr_{3-x}Ca_xFe_2O_5Fe_2OS_2$ (Figure 1.15b). Ca can be incorporated in the structure up to $x = 1.7$, beyond which $Ca_2Fe_{2.7-\delta}O_3S_2$ is formed as a competing side phase and the phases below $x = 1$ do not seem to form readily (with one exception). The samples are also mostly two-phase, with a tetragonal phase and an orthorhombic phase that is just slightly distorted from a tetragonal symmetry both being formed in the synthesis. In both the tetragonal and orthorhombic phases cation order can be observed, with the smaller Ca cation preferentially occupying the smaller 8-coordinate site and the larger Sr cation occupying the larger 12-coordinate site. X-ray powder diffraction also suggests a slight difference in cation ordering between the two phases in that the 12-coordinate site in the orthorhombic phase is solely occupied by Sr and does not have any Ca-occupancy. The magnetic structures for the $x = 1$ and 1.5 phases are also characterized, and they behave much like the all-Sr phase though the magnetic moments on the iron sites at 5 K are slightly different.

In addition to alkaline earth metal substitution, chapter 5 describes another chemical variation to $Sr_3Fe_2O_5Fe_2OS_2$ by means of topotactic reduction to form $Sr_3Fe_2O_4Fe_2OS_2$ (Figure 1.15c). This reduction was carried out successfully, and the synthesis is described along with the nuclear and magnetic structure characterization.

Chapter 6 expands upon work carried out by Bradley Sheath concerning the solid solution $Ca_2Fe_{2.7-\delta}O_3S_{2-x}Se_x$ (Figure 1.15d). First, the space group of the superstructure due to Fe-vacancy ordering in the all-sulfide phase is resolved to be the non-centrosymmetric *Aea*2 rather than the centrosymmetric *Aeam* by single-crystal X-ray diffraction. A variable-field neutron powder diffraction experiment was also carried out on the all-sulfide compound, but no meaningful results were obtained due to the changes in the diffraction pattern being able to be attributed to preferred orientation, slight changes in the nuclear structure, or slight changes in the magnetic structure. Variable temperature neutron powder diffraction experiments were also carried out on the solid solution for phases $x = 0.5$, 1, and 1.5. This revealed that the phases generally ordered

in a similar manner to the $x = 0$ phase, but with increasing correlation between the layers due to the increasing average size of the anion on the chalcogen site and thus increased orbital overlap.

Chapter 7 summarizes the findings presented in the course of the thesis, suggesting further chemical variations to $Sr_3Fe_2O_5Fe_2OS_2$ which may lead to more new, related structures, like $Sr_4Fe_2O_6Fe_2OS_2$ (Figure 1.15e) which was synthesized and characterized by Annabel Lyon [52].

References

[1] Patterson, J.P.; George, R. *Phys. Med.* **2018**, *47*, 139-143.
[2] Deng, D. *Energy Sci. Eng.* **2015**, *3(5)*, 385-418.
[3] Mizushima, K.; Jones, P.C.; Wiseman, P.J., Goodenough, J.B. *Mater. Res. Bull.* **1980**, *15(6)*, 783-789.
[4] Deville, Q.; Wernert, R.; Dillay, V.; de Boisse, B.M.; Guignard, M.; Carlier, D. *Inorg. Chem.* **2024**, *63*, 5341-5350.
[5] Kubota, K.; Dahbi, M.; Hosaka, T.; Kumakura, S.; Komaba, S. *chem. Rec.* **2018**, *18*, 459-479.
[6] Li, C.; Wang, Z.; He, Z.; Li, Y.; Mao, J.; Dai, K.; Yan, C.; Zheng, J. *Sustain. Mater. Technol.* **2021**, *29*, e00297.
[7] Binasch, G.; Grünberg, P.; Saurenback, F.; Zinn, W. *Phys. Rev. B.* **1989**, *39*, 4828(R).
[8] Puebla, J.; Kim, J.; Kondou, K.; Otani, Y. *Commun. Mater.* **2020**, *1*, 24.
[9] Nan, T.; Quintela, C.X.; Irwin, J.; Gurung, G.; Shao, D.F.; Gibbons, J.; Campbell, N.; Song, K.; Choi, S.Y.; Guo, L.; Johnson, R.D.; Manuel, P.; Chopdekar, R.V.; Hallsteinsen, I.; Tybell, T.; Ryan, P.J.; Kim, J.W.; Choi, Y.; Radaelli, P.G.; Ralph, D.C.; Tsymbal, E.Y.; Rzchowski, M.S., Eom, C.B. *Nat. Commun.* **2020**, *11*, 4671.
[10] Mi, M.; Xiao, H.; Yu, L.; Zhang, Y.; Wang, Y.; Cao, Q.; Wang, Y. *Mater. Today Nano.* **2023**, *24*, 100408.
[11] Wu, M.K.; Ashburn, J.R.; Torng, C.J.; Hor, P.H.; Meng, R.L.; Gao, L.; Huang, Z.J.; Wang, Y.Q.; Chu, C.W. *Phys. Rev. Lett.* **1987**, *58(9)*, 908-910.
[12] Parizh, M.; Lvovsky, Y.; Sumption, M. *Supercond. Sci. Technol.* **2017**, *30*, 014007.
[13] Nishioka, K.; Takamoto, T.; Agui, T.; Kaneiwa, M.; Uraoka, Y.; Fuyuki, T. *Sol. Energy Mater.* **2006**, *90(1)*, 57-67.
[14] Nishioka, S.; Osterloh, F.E.; Wang, X.; Mallouk, T.E.; Maeda, K. *Nat. Rev. Methods Primers.* **2023**, *3*, 42.
[15] Kageyama, H.; Ogino, H.; Zhu, T.; Hasegawa, H. *Mixed-anion Compounds*, Royal Society of Chemistry, **2024**.
[16] Clarke, S. J.; Adamson, P.; Herkelrath, S. J. C.; Rutt, O. J.; Parker, D. R.; Pitcher, M. J.; Smura, C. F. *Inorg. Chem.* **2008**, *47(19)*, 8473-8486.
[17] Wei, X.; Akbar, M. U.; Raza, A.; Li, G. *Nanoscale Adv.* **2021**, *3*, 3353-3372.
[18] Boyer-Candalen, C.; Derouet, J.; Porcher, P.; Moëlo, Y.; Meerschaut, A. *J. Solid State Chem.* **2002**, *165(2)*, 228-237.
[19] Lin, L.; Li, Q.; Kanazawa, Y.; Kanie, K.; Nakabayashi, M.; Gu, C.; Lu, D.; Hisatomi, T.; Takata, T.; Domen, K. *J. Mater. Chem. A.* **2025**, *13*, 4940-4947.
[20] Cario, L.; Kabbour, H.; Meerschaut, A. *Chem. Mater.* **2005**, *17*, 234-236.
[21] Cario, L.; Lafond, A.; Morvan, T.; Kabbour, H.; André, G.; Palvadeau, P. *Solid State Sci.* **2005**, *7(8)*, 936-944.

[22] Tippireddy, S.; Prem Kumar, D.S.; Das, S.; Mallik, R.C. *ACS Appl. Energy Mater.* **2021**, *4(3)*, 2022-2040.
[23] Gál, Z.A.; Rutt, O.J.; Smura, C.F.; Overton, T.P.; Barrier, N.; Clarke, S.J.; Hadermann, J. *J. Am. Chem. Soc.* **2006**, *128(26)*, 8530-8540.
[24] Zhu, W.J.; Hor, P.H. *J. Solid State Chem.* **1997**, *134(1)*, 128-131.
[25] Zhu, W.J.; Hor, P.H. *J. Solid State Chem.* **2000**, *153(1)*, 26-29.
[26] Sheath, B.C.; Cassidy, S.J.; Clarke, S.J. *J. Solid State Chem.* **2021**, *293*, 121761.
[27] Smyth, R.D.; Wilson, J.A.D.; Manuel, P.; Clarke, S.J. *J. Solid State Chem.* **2022**, *307*, 122841.
[28] Dixon, E.; Hayward, M. *Inorg. Chem.* **2010**, *49*, 20, 9649-9654.
[29] Kelly, N.D. "Chemical and physical properties of layered oxychalcogenides containing an anti-cuprate square lattice" *In Preparation.* **2025**.
[30] Gamon, J.; Perez, A.J.; Jones, L.A.H.; Zanella, M.; Daniels, L.M.; Morris, R.E.; Tang, C.C.; Veal, T.D.; Hardwick, L.J.; Dyer, M.S.; Claridge, J.B.; Rosseinsky, M.J. *J. Mater. Chem. A.* **2020**, *8*, 20553-20569.
[31] Oogarah, R.K.; Suard, E.; McCabe, E.E. *J. Magn. Magn. Mater.*, **2018**, *446*, 101–107.
[32] Song, S.; Lin, Y.; Li, B.; Wu, S.; Zhu, Q.; Ren, Z.; Cao, G. *Phys. Rev. Mater.* **2022,** 6, 055002.
[33] Takeiri, F.; Matsumoto, Y.; Yamamoto, T.; Hayashi, N.; Li, Z.; Tohyama, T.; Tassel, C.; Ritter, C.; Narumi, Y.; Hagiwara, M.; Kageyama, H. *Phys. Rev. B.* **2016**, *94*, 184426.
[34] Fuwa, Y. Wakeshima, M. Hinatsu, Y. *J. Phys. Condens. Matter.* **2010**, *22*, 346003.
[35] Zhao, L.L.; Wu, S.; Wang, J.K.; Hodges, J.P.; Broholm, C.; Morosan, E. *Phys. Rev. B.* **2013**, *87*, 020406.
[36] Ni, N.; Jia, S.; Huang, Q.; Climent-Pascual, E.; Cava, R.J. *Phys. Rev. B.* **2011**, *83*, 224403.
[37] Oogarah, R.K.; Stockdale, C.P.J.; Stock, C.; Evans, J.S.O.; Wills, A.S.; Taylor, J.W.; McCabe, E.E. *Phys. Rev. B.* **2017**, *95*, 174441.
[38] McCabe, E.E.; Wills, A.S.; Manuel, P.; Chapon, L.; Evans, J.S.O. *Phys. Rev. B.* **2014**, *90*, 165111.
[39] Free, D.G.; Evans, J.S.O. *Phys. Rev. B.* **2010**, *81*, 214433.
[40] McCabe, E.E.; Stock, C.; Rodrigues, E.E.; Wills, A.S.; Taylor, J.W.; Evans, J.S.O. *Phys. Rev. B*, **2014**, *89*, 100402.
[41] Zhang, H.; Wu, X.; Li, D.; Jin, S.; Chen, X.; Zhang, T.; Lin, Z.; Shen, S.; Yuan, D.; Chen, X. *J. Phys.: Condens. Matter.* **2016**, *28*, 145701.
[42] Sheath, B.C. DPhil Thesis, *University of Oxford*, "Exploring the Synthesis and Characterization of Oxychalcogenide, Oxypnictide and Chalcogenide Materials," **2023**.
[43] Bardeen, J. *Phys. Rev.* **1955**, *97*, 1724.
[44] Chenine, D.; Aziz, Z.; Benstaali, W.; Bouadjemi, B.; Youb, O.; Lantri, T.; Abbar, B.; Bentata, S. *J. Supercond. Nov. Magn.* **2017**, *31*, 285-295.
[45] Marco, J.F.; Ramón Gancedo, J.; Gracia, M.; Gautier, J.L.; Ríos, E.I.; Palmer, H.M.; Greaves, C.; Berry, F.J. *J. Mater. Chem.* **2001**, *11*, 3087-3093.
[46] Chern, G.; Horng, L.; Shieh, W.K.; Wu, T.C. *Phys. Rev. B.* **2001**, *63*, 094421.
[47] Giri, S.; Dey, S.; Suard, E.; Clarke, S.J. *Chem. Mater.* **2024**, *36*, 5293-5858.
[48] Goodenough, J.B. *Phys. Rev.* **1955**, *100*, 564.
[49] Goodenough, J.B. *J. Phys. Chem. Solids.* **1958**, *6(2-3)*, 287-297.
[50] Kanamori, J. *J. Phys. Chem. Solids.* **1959**, *10(2-3)*, 87-98.
[51] Müller, U. "Symmetry Relationships between Crystal Structure: Applications of Crystallographic Group Theory in Crystal Chemistry" *Oxford University Press*. **2013**, p. 216.

[52] Lyon, A.L. MSc. Thesis, *University of Oxford*, “Structures and Magnetism of layered iron oxide chalcogenides,” **2024**.

Chapter 2: Experimental Techniques

Contents

2.1. Synthetic techniques 26
2.1.1. Solid-state synthesis 26
2.1.2. Handling of air sensitive materials 28
2.1.3. Synthesis of *Ae*O precursors 29
2.2. Characterization techniques 30
2.2.1. Crystalline solids and symmetry 30
2.2.2. X-ray diffraction (XRD) 30
2.2.2.1. Single-Crystal X-ray Diffraction (SC-XRD) 33
2.2.2.2. Powder X-ray Diffraction (XRPD) 34
2.2.2.3. X-ray diffractometers 35
2.2.3. Neutron Powder Diffraction (NPD) 39
2.2.3.1. Institut Laue Langevin (ILL) 41
2.2.3.2. ISIS Neutron and Muon Facility 43
2.2.4. Refinement Methods 45
2.2.5. SQUID magnetometry 46
2.2.6. X-ray absorption near-edge spectroscopy (XANES) 47
2.2.7. Electron Diffraction 48
2.2.8. Electron Microscopy 49
2.2.9. Energy Dispersive X-rays (EDX) 49
2.2.10. Mössbauer spectroscopy 50
2.2.11. Bond valence sum (BVS) calculations 51
References 51

2.1. Synthetic techniques

2.1.1. Solid-state synthesis

A typical ceramic solid-state synthesis method was used in the synthesis of many of the materials described in this thesis. In this synthesis method, stoichiometric ratios of the reagents were

weighed and ground together with an agate mortar and pestle until homogeneous all under an argon atmosphere in a glovebox. The powder was then transferred to a 13 mm diameter pellet press, contained within two argon-filled polyethylene bags for transfer outside of the glovebox, and then pressed under 3-5 tons of force. The pellets were then transferred back into the glovebox before being removed from the bags and the pellet die. The pellet was then placed inside an alumina crucible which was transferred into a silica tube on top of a silica spacer, both of which had been heated in a drying oven at a temperature of 180˚C for a minimum of 24 hours. A Young's tap was then secured to the open end of the silica tube to maintain the inert atmosphere as it was transferred out of the glovebox and then put under dynamic vacuum (10^{-2} mbar) for sealing with a blowtorch. The typical sealing setup is depicted below in Figure 2.1, and the bottom of the tube containing the reaction mixture was immersed in liquid nitrogen to prevent high temperatures from the tube sealing from evaporating the elemental sulfur out of the reaction mixture. After sealing, the reaction vessel was placed into a furnace and heated at a slow ramp rate (1°C min^{-1}) when using elemental sulfur to dwelling temperatures typically around 900˚C. After dwelling at high temperatures for periods of around 48 hours, the vessel was then cooled to room temperature within the furnace at the natural rate of the furnace.

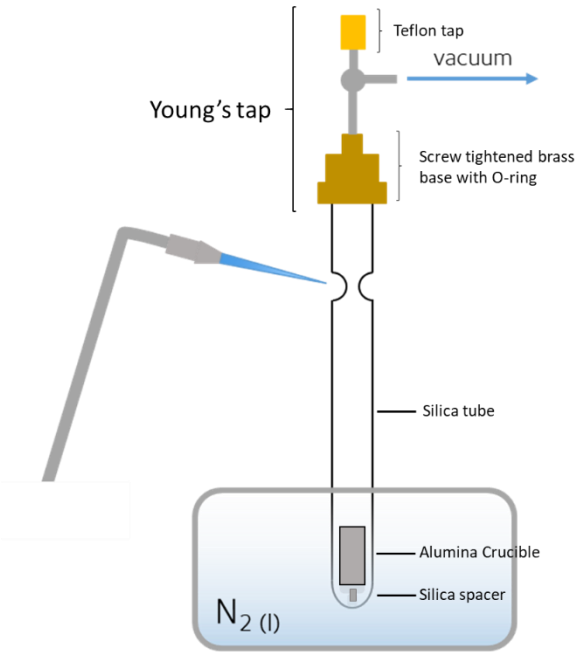


Figure 2.1. Diagram of the setup used in sealing samples in silica tubes under dynamic vacuum.

The diffusion of ions in solid-state reactions is very slow and has a high activation energy barrier, so long dwelling times at high temperatures are necessary in overcoming this. This also means that extensive grinding until homogeneity is reached as well as pressing into a pellet is important to decrease particle size and distribution, increase particle surface area, and increase contact between reagents. Chapters 3.1, 4.1, and 5.2 expand upon this by touching on the flux syntheses and low-temperature topotactic reductions as pertinent to the phases described in each respective chapter.

2.1.2. Handling of air sensitive materials

While some of the materials synthesized and studied in this thesis were not themselves sensitive to air or moisture, other synthesized materials and reagents like SrO, CaO, LiH and elemental metals are highly sensitive to the atmosphere. With this in mind, the air and moisture levels were kept low during the handling and storage of the starting materials and products as well as during synthesis by use of a Glovebox Technology argon-filled glovebox for which the oxygen level is continuously monitored by an oxygen sensor and is maintained to be below 2 ppm while working. Oxygen and water are removed from the circulating argon atmosphere by use of Cu catalysts and molecular sieves, and the glovebox is regenerated regularly to replenish the Cu catalysts by reducing any CuO back to Cu with a H_2/N_2 gaseous mixture. Other steps that are taken to maintain this atmosphere include leaving both the small and large antechambers under vacuum to prevent leaking or user error and pre-drying equipment in drying ovens prior to use within the glovebox to reduce the introduction of moisture to the system.

All reagents were stored in the glovebox as they are air-sensitive, and this inert atmosphere was maintained outside of the glovebox with argon-filled polyethylene bags when pressing pellets and the use of Young's taps on the end of silica tubes when transferring the tubes to the sealing line as noted above.

In the case of washing products under inert atmosphere (Chapter 5), the products with lithium-containing phases (LiH or Li_2O) were loaded into a dried Schlenk tube before removal from the glovebox. The reaction vessel was then attached to a nitrogen/vacuum Schlenk line and standard

Schlenk line techniques were used to ensure that an inert atmosphere was maintained during the transfer of liquids between Schlenk tubes. Solvated waste by-products were removed from the washed product using a cannula covered in filter paper before drying under dynamic vacuum, after which the vessel was kept under vacuum and transferred back into the glovebox.

2.1.3. Synthesis of *Ae*O precursors

SrO and CaO were synthesized as precursors for the Sr- and Ca-containing phases in this thesis and they were each made from the thermal decomposition of the appropriate carbonate as given in Equation 2.1. Other precursors were used as-received, so these were the only precursors that needed to be synthesized.

$$AeCO_3 \rightarrow AeO + CO_2 \uparrow \qquad \text{(Eqn 2.1)}$$

This reaction was carried out under dynamic vacuum to actively remove CO_2 from the reaction according to the scheme displayed in Figure 2.2. In this setup, the carbonate was placed in 2 alumina boats in a large silica tube which was fit with an end cap on one end and the other with a 3-way tap. The tube was then placed in a split-tube furnace and connected to a dynamic vacuum (10^{-2} mbar) with a fan placed under each end to prevent the O-ring from degrading due to high temperature exposure. The tube was then heated overnight for 18 hours at 840˚C followed by 4 hours at 1100˚C. After cooling naturally to room temperature, the reaction vessel was transferred under vacuum to the glove box. The purity of the product was then checked by in-house X-ray powder diffraction (XRPD).

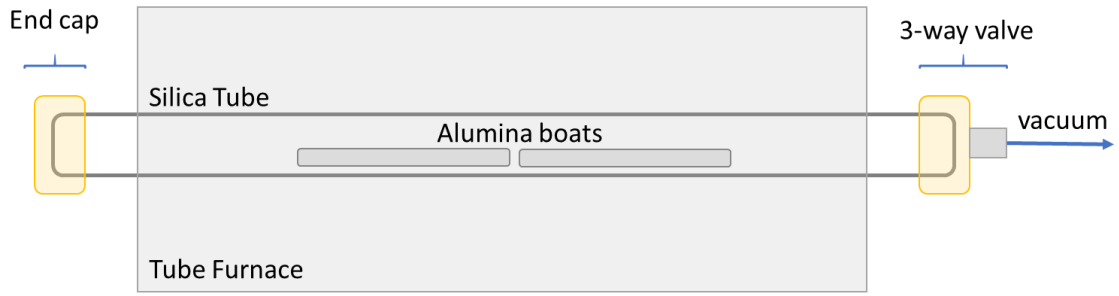


Figure 2.2. Diagram of the setup used in the thermal decomposition of $AeCO_3$.

2.2. Characterization techniques

2.2.1. Crystalline solids and symmetry

Crystalline solids are made up of translationally replicated imaginary parallelepipeds called unit cells which are described by the lengths of the sides (*a*, *b*, *c*) and the angles between sides (α, β, γ) which are also called lattice parameters. In a triclinic system, $a \neq b \neq c$ and $\alpha \neq \beta \neq \gamma$, and the allowed shapes of these parallelepipeds that can fill three-dimensional space give rise to the seven different crystal systems with triclinic being the lowest symmetry and cubic ($a = b = c$ and $\alpha = \beta = \gamma = 90°$) the highest. A lattice is defined by a periodic array of identical lattice points and a crystal structure is generated by decorating each lattice point with a group of atoms called the basis. There are 14 Bravais lattices in three-dimensions obtained by combining the crystal systems with intra-cell translational symmetry (or centring). Primitive lattices (given the symbol *P*) have a single lattice point within the unit cell and have only purely translational symmetry (i.e. no centring). Body centred lattices (given the symbol *I*) have an additional lattice point (often located at the centre of the unit cell), and the translation relates a lattice point at (x, y, z) to an identical lattice point at ($x + ½$, $y + ½$, $z + ½$). Lastly, face-centred lattices have additional lattice points on faces of the unit cell (given the symbol *F* if there is a lattice point on all faces, or the symbols *A*, *B*, or *C* if only one face has a lattice point and depending on which face the lattice point is located) [1]. Combining these 4 lattice types with the seven different crystal systems, according to symmetry constraints, gives rise to the 14 Bravais lattices, and combining these with combinations of symmetry elements gives rise to the 230 three-dimensional space groups [2].

Given the periodic arrays of atoms that make up crystalline solids, diffraction techniques are commonly employed to characterize the material by using incident radiation comparable to interatomic distances in crystalline solids (approximately 0.3 – 3 Å).

2.2.2. X-ray diffraction (XRD)

X-rays ($\lambda = 0.1 – 10$ Å) are one such type of incident radiation that is used for diffraction in order to probe the structure of crystalline solids. X-rays interact almost entirely with the electrons of

an atom, and the elastic, coherent scattering, that results from the scattering in which there is no loss of energy, is used in X-ray diffraction. Diffraction of X-rays from crystals was first discovered by Max von Laue in 1912 and he received the Nobel Prize in physics for his work in 1914 [3]. von Laue described diffraction from three-dimensional crystals by a combination of diffraction from three hypothetical one-dimensional crystals (Figure 2.3).

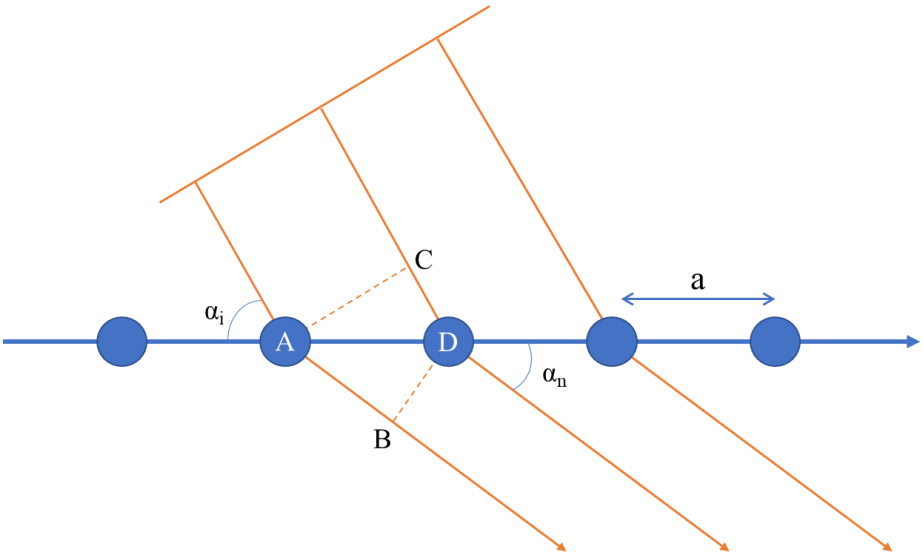


Figure 2.3. Laue scattering of a monochromatic plane wave from a one-dimensional crystal showing the derivation of the Laue equations.

In considering this single dimension, constructive interference occurs when the path difference between two photons is an integer multiple of the wavelengths of the incident plane wave. When considering this in three dimensions, this gives rise to the first Laue equation (Eqn. 2.2) for a single dimension below where α_i and α_n are the angles between the crystallographic axis and the incident and scattered radiation respectively and n_x is an integer number. Equations 2.3 and 2.4 make up the other two members of the Laue equations in the other two dimensions and when all three equations are simultaneously satisfied, constructive interference will occur.

$$(AB - CD) = a\,(\cos\alpha_n - \cos\alpha_i) = n_x\lambda \qquad \text{(Eqn. 2.2)}$$

$$b\,(\cos\beta_n - \cos\beta_i) = n_y\lambda \qquad \text{(Eqn. 2.3)}$$

$$c\,(\cos\gamma_n - \cos\gamma_i) = n_z\lambda \qquad \text{(Eqn. 2.4)}$$

However, these equations have a total of 12 variables, which, while they are mathematically rigorous, limits the practicality of their use. W.H. and W.L. Bragg proposed a different solution which considers diffraction as the reflection of radiation from planes of atoms (Figure 2.4). These

planes of atoms are known as Miller planes and are denoted by the Miller indices {*hkl*} where *h*, *k*, and *l* correspond to coordinates in reciprocal space and the planes intersect the unit cell at the cartesian coordinates $\frac{a}{h}$, $\frac{b}{k}$, and $\frac{c}{l}$. d_{hkl} is the shortest distance between the origin and the plane defined by the Miller indices *hkl*. Constructive interference then occurs when the path lengths of beams reflected from different planes differ by an integer number of wavelengths, and this relationship is given by Bragg's Law (Eqn. 2.5).

$$n\lambda = 2d_{hkl} \sin \theta \qquad \text{(Eqn. 2.5)}$$

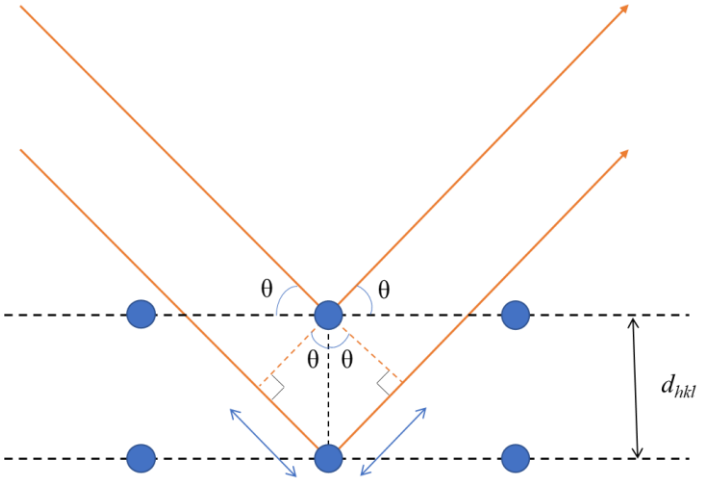


Figure 2.4. Scattering of monochromatic radiation from planes of atoms showing the derivation of Bragg's law. θ is the Bragg angle and the scattering angle is 2θ.

Systematic absences occur when diffraction from a set of Miller planes is not observed in the diffraction pattern. These arise from translational symmetry within a unit cell that creates destructive interference between identical scatterers (lattice centring, screw axes or glide planes), and they can be used to deduce the Bravais lattice type as well as a short-list of space groups that may represent the crystal.

The intensities of Bragg peaks (I_{hkl}) are proportional to the square of the structure factor F_{hkl} for which the real component is given in Equation 2.6 below [1].

$$F_{hkl} = \sum_{i=1}^{N} f_i(\theta)[cos2\pi(hx + ky + lz)] \times q \qquad \text{(Eqn. 2.6)}$$

For X-ray diffraction, the form factor ($f_i(\theta)$) is the summation of the contributions of all the electrons in an atom and scales with atomic number. This means that atoms with similar atomic numbers are difficult to differentiate, and heavier elements scatter X-rays more strongly, meaning

that they can dominate the diffraction pattern and make it more difficult to locate lighter elements. The angular dependence of this form factor arises from the fact that the electron cloud is not a point scatterer, so two photons that are scattered by different electrons from the same atom will have slightly different path lengths that will result in destructive interference that becomes more apparent at progressively higher angles. The angular term of the structure factor ($cos2\pi(hx + ky + lz)$ is the real component but there is also an imaginary component if the structure does not have a centre of inversion) contains information about the relative arrangement of the scattering atoms. However, since the intensities of Bragg peaks are related to the magnitude of the structure factor ($|F_{hkl}|^2$), the sign of F_{hkl} cannot, in principle, be determined from the intensities of Bragg peaks. This means that the phase (or the sign) of the structure is nontrivial. This is known as the phase problem in crystallography and can be solved by various methods like the Patterson method, direct methods, or charge-flipping [1]. The structure factor also depends on the Debye-Waller term (q) which corresponds to thermal displacement of electron density due to atomic vibrations. This also results in a decrease in Bragg intensity with increasing angle from destructive interference. One way to represent this is with isotropic thermal displacement, q_{iso} (Eqn. 2.7). In general, displacement parameters are anisotropic with the number of variables being determined by site symmetry, but whether or not these can be refined is dependent upon the quality of data.

$$q_{iso} = e^{\frac{-8\pi^2 U_{iso} sin^2(\theta)}{\lambda^2}} \qquad \text{(Eqn. 2.7)}$$

2.2.2.1. Single-Crystal X-ray Diffraction (SC-XRD)

In the case of single-crystal X-ray diffraction, a single crystal is mounted, placed in the path of a monochromatic beam, and then rotated as an area detector records the data. The result is a three-dimensional collection of peaks (which look like spots) in reciprocal space which makes up the diffraction pattern. CrysalisPRO software is used to index the observed reflections (assign the *hkl* values) and to determine the cell and the likely space group. SUPERFLIP software then does the structure solution to determine the structural model by solving the phase problem using charge-flipping and a subsequent refinement in Jana2020 is then used to optimise the structural

model. The collection and analysis of SC-XRD data in this thesis was carried out by Lemuel Crentsil.

2.2.2.2. Powder X-ray Diffraction (XRPD)

In powder diffraction experiments, the diffracted intensity of monochromatic radiation is measured as a function of 2θ which, from Bragg's Law, is directly related to the *d*-spacing (d_{hkl}) between Miller planes. In powder diffraction experiments, the individual crystallites of a polycrystalline sample are randomly arranged which results in diffracted cones of intensity (Debye-Scherrer cones) which result in the rings detected on a flat detector (instead of the spots from the single crystal experiment). This means that Miller planes with similar *d*-spacings can produce peaks that overlap in the diffraction patterns which can impede characterization since individual intensities are difficult to determine whereas in SC-XRD, reflections with the same *d*-spacing are individually measured. The typical intensity vs 2θ patterns can then be obtained by integrating intensity around the ring or by taking a cut through the ring where 2θ is the angle between the incident beam and the diffracted cone. Integrating the intensity of the rings leads to higher intensity which can illuminate small peaks, while taking a cut through the ring normally leads to higher resolution because it's possible to optimise the detector for resolution. However, since not all individual Bragg reflections are recorded with individual intensities like in SC-XRD due to the loss of a dimension and the overlap of peaks that results, *ab initio* structure determination and individual space groups cannot always be determined with XRPD alone.

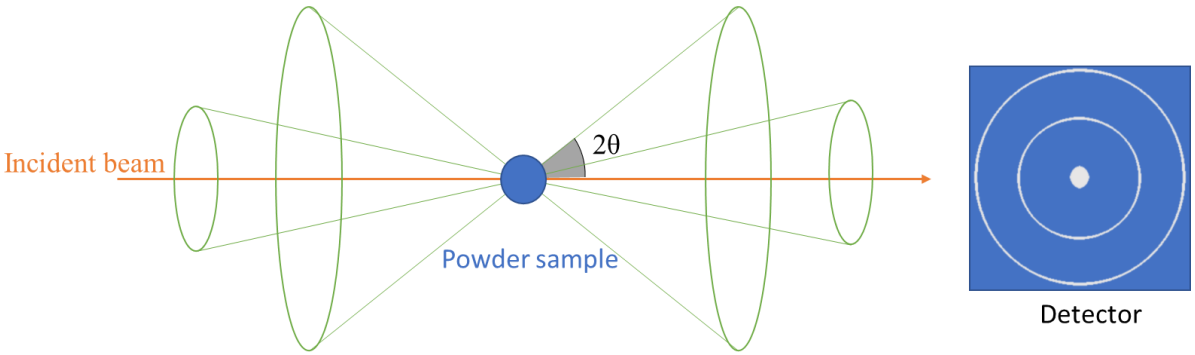


Figure 2.5. Debye-Scherrer cones from the diffraction of a polycrystalline sample.

2.2.2.3. X-ray diffractometers

X-ray diffraction instruments in laboratory settings produce X-rays by ionising electrons in targets of specific elements (often Cu) in order to cause another electron to drop from higher energy orbitals and emit photons of distinct energies. In the case of Cu, a heated tungsten filament produces electrons which are then accelerated through a voltage of 40 kV which then gives them enough energy to ionise the Cu 1*s* electron. This then causes electrons to drop from the 2*p* or 3*p* orbitals, resulting in the emission of K_α ($\lambda \sim 1.54$ Å) and K_β ($\lambda \sim 1.39$ Å) photons. The K_α radiation can then be selectively used by use of an energy filter or energy-discriminating detector. Due to the spin-orbit coupling of the excited state of Cu, the 2*p* state is made non-degenerate with the relaxation of the high-spin $^2P_{3/2}$ state producing $K_{\alpha 1}$ radiation ($\lambda \sim 1.54051$ Å) and that of the low-spin $^2P_{1/2}$ state producing $K_{\alpha 2}$ radiation ($\lambda \sim 1.54433$ Å). These two states are populated in a 2:1 ratio, and this means that the K_α radiation is therefore produced as a doublet. On some instruments the $K_{\alpha 1}$ is selected by means of a monochromator.

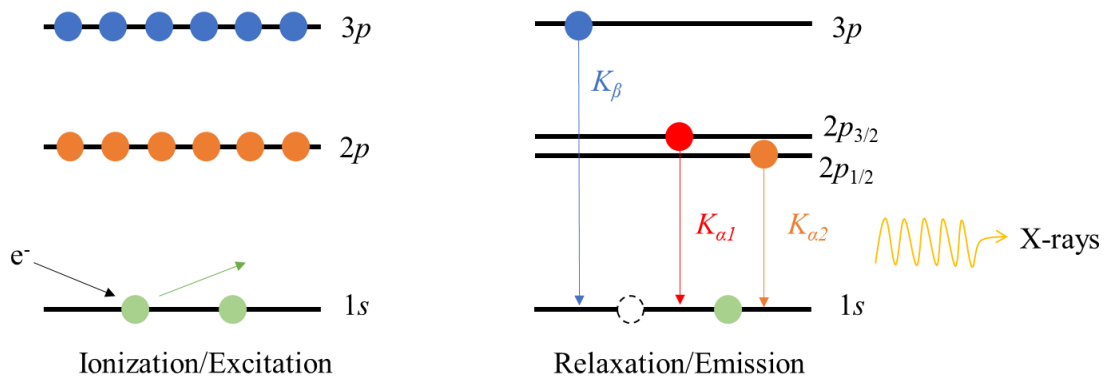


Figure 2.6. Production of X-ray radiation from the excitation and relaxation of a Cu-anode.

Synchrotrons produce X-rays by forcing electrons to change direction while travelling close to the speed of light. Because of this, the process of generating X-ray radiation is three-fold: generating electrons, accelerating electrons, and generating radiation. Electrons are produced by an electron gun which heats a high voltage cathode in a vacuum. These electrons are then directed into a linear accelerator and then fed into a booster ring where the beam is further accelerated using bending magnets. At this point, the electrons are travelling close to the speed of light and are directed into the storage ring. The radiation emitted as the electrons change momentum as

they pass through bending magnets or magnetic insertion devices (wigglers and undulators) spans a wide range of the electromagnetic spectrum and optics hutches are used on individual beamlines to monochromate and select the radiation appropriate for the experiments being conducted.

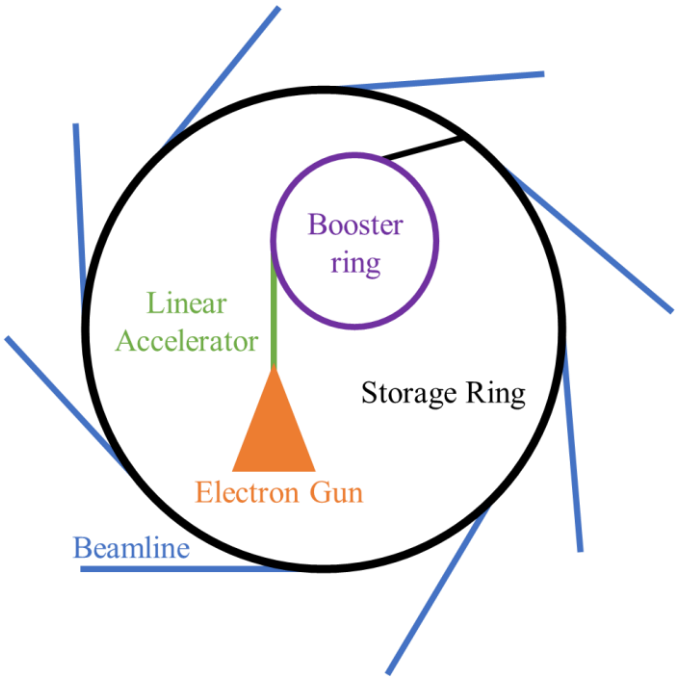


Figure 2.7. Schematic of a synchrotron radiation facility.

2.2.2.3.1. Bruker D8 ECO diffractometer

The Bruker D8 ECO diffractometer used for in-house powder diffractometry has a non-monochromated beam, meaning that both Cu $K_{\alpha 1}$ and $K_{\alpha 2}$ radiation are present in the incident beam. While this sacrifices some of the resolution of the powder diffraction patterns obtained, the higher intensity incident beam allows for rapid data collection with adequate signal-to-noise ratios achieved in scans of about 30 minutes in length. This diffractometer uses Bragg-Brentano geometry with a fixed sample position and a rotating incident beam and detector which is able to scan a 2θ range of 3° at the same time. The detector is also energy discriminating, meaning it removes the K_{β} radiation and suppresses unwanted signal from fluorescence which would add to the experiment noise.

2.2.2.3.2. Oxford Diffraction/Rigaku SuperNova A diffractometer

An Oxford Diffraction/Rigaku SuperNova A diffractometer was used for in-house single crystal X-ray diffraction. This instrument is equipped with switchable Cu and Mo sources, and the

monochromated Mo-K_α radiation (λ = 0.71073 Å) was used for the experiment conducted in this thesis (Chapter 6). The detector is a large area Atlas CCD which provides efficient and fast data collection. The instrument is also equipped with an Oxford Cryosystems Cryostream for variable temperature experiments (80 – 500 K), though only room-temperature data was collected and analysed in this thesis.

2.2.2.3.3. I11 Beamline, Diamond Light Source (PSD and VT and MAC)

The I11 beamline at the Diamond Light Source located on Harwell Campus in Oxfordshire, UK [4] is a high-resolution powder diffraction beamline. The beamline produces X-rays by use of an in-vacuum undulator with 90 Sm_2Co_{17} permanent magnets which produces X-rays with energies ranging between 5 – 30 keV. A single wavelength is selected using a cryogenically cooled double-crystal Si (111) monochromator, double-bounce harmonic rejection mirrors, and two sets of monochromatic slits. The wavelength used in the experiments in this these range around 0.823 Å, and the wavelength is determined with precision on the day of the experiment by refinement against the diffraction pattern of a silicon standard.

The I11 beamline has two different detectors: the position sensitive (PSD) detector and the multi-analyser crystal (MAC) detector. The PSD detector is a Mythen-2 Si μ-strip with 18 linear p-n junction strip detection modules mounted on the outer δ-circle of the diffractometer. This detector is used for quick scans and variable temperature experiments as it has the ability to measure a full diffraction pattern in a few seconds. Variable temperature experiments were run by use of a cryostream (90 - 100 K minimum) or a hot air blower (up to 900 K) that was used to heat or cool the sample at a constant rate of typically 6 or 12 K min^{-1} as patterns were continuously collected using the PSD detector. The fast temperature change rates lead to uncertainties on the temperature for any given measurement of approximately 1-2 K. These variable temperature experiments were conducted in order to investigate how the lattice parameters changed upon heating or cooling and identify if any phase transitions or decomposition occurred.

The MAC detector is made up of 5 MAC stages placed above the beam at 30° intervals with 9 Si(111) analyser crystals within each stage. This detector is typically used for scans requiring high resolutions with scans lasting up to around 30 minutes, though in this thesis it was used for quick scans to be used in conjunction with scans collected on the PSD detector to increase the precision of the refined lattice parameters of the solid solution discussed in chapter 4.

2.2.2.3.4. ID22 Beamline, European Synchrotron Research Facility

The ID22 beamline at the European Synchrotron Research Facility located on the EPN campus in Grenoble, France [5] is another high-resolution powder diffraction beamline (Figure 2.8a). The beamline produces X-rays by use of a 2.5 meter long in-vacuum undulator which produces X-rays with energies ranging between 6-75 keV ($\lambda \sim 2.1 - 0.165$ Å). A single wavelength is selected using a cryogenically cooled channel-cut Si (111) crystal with a 4 mm channel. For high-resolution powder diffraction studies, the beam is not focused before passing to the sample and the wavelength generally selected is 0.354 Å, calibrated with Si-standards for precision at the beginning of each experiment.

The diffractometer detector is comprised of a multi-analyser stage with 13 Si (111) crystals separated by ~ 2° and a Dectris Eiger2 X 2M-W CdTe pixel detector to analyse the X-rays transmitted by those crystals. The axial resolution of this detector allows for automatic corrections accounting for axial divergence, which results in narrower and more symmetric peaks.

There are multiple sample environments available for use in variable-temperature experiments, including an Oxford Cryosystems Cryostream 7+ nitrogen blower (80 – 500 K), a hot-air blower (up to 950°C) and a liquid helium flow cryostat (down to 4 K). The latter of these was used in this thesis for low-temperature X-ray diffraction experiments (Figure 2.8b).

a) b)

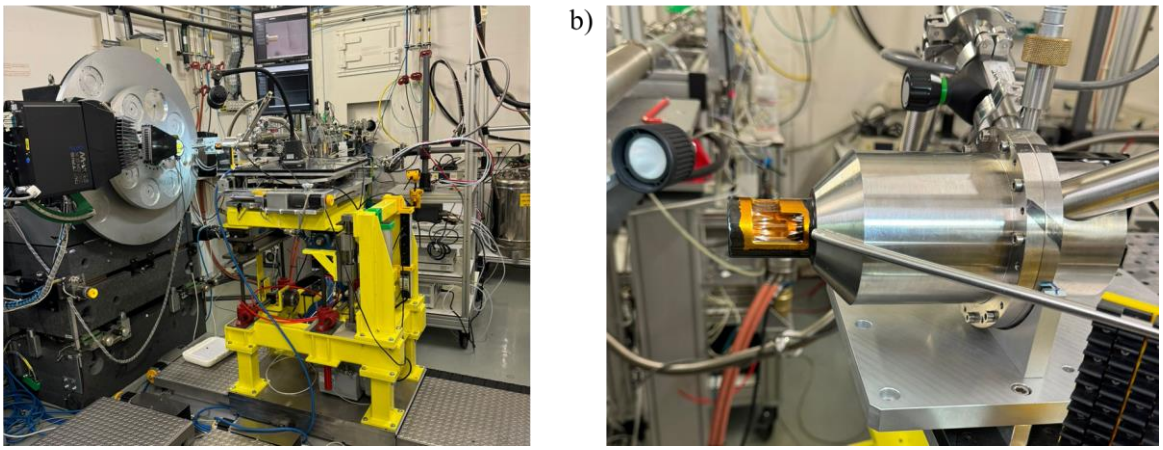


Figure 2.8. The a) experiment hutch of ID22 and b) sample window of the liquid helium flow cryostat.

2.2.3. Neutron Powder Diffraction (NPD)

Neutron diffraction is another diffraction technique that is often used to characterize the structure of crystalline solids. The de Broglie equation (Eqn 2.8) describes wave-particle duality, which is a quantum mechanical principle wherein all matter exhibits particle- or wave-like properties (depending on the experimental conditions) and the wavelength is inversely related to a particle's momentum. The wave-like property of neutrons is what is exploited in neutron diffraction experiments.

$$\lambda = \frac{h}{p} \qquad \text{(Eqn. 2.8)}$$

Since neutrons carry no electric charge, they do not interact with the electron cloud via the Coulomb interaction. Instead, neutrons interact with the nucleus of an atom via the strong nuclear force which means that the scattering lengths do not scale with atomic number like for X-rays, and there is also a difference in scattering lengths between different isotopes of the same element. This means that if sites are doped with a specific isotope (like a specific hydroxyl group being doped with ^{1}H vs the others being deuterated) then more information can be selectively obtained about the doped site. Additionally, the lack of scaling with atomic number means that neutrons can reveal information about sites with lighter elements in materials containing heavy elements that would otherwise dominate an X-ray diffraction pattern.

Table 2.1. The mean atomic X-ray scattering factors ($sin\,\theta\,/\,\lambda = 0.1$ Å^{-1}) [6] for free atoms and bound coherent neutron scattering cross-sections and scattering lengths [7] of the natural composition of elements discussed in this thesis.

Element	X-ray scattering factor	Coherent neutron scattering cross section (barns = 10^{-28} m^2)	Neutron scattering length, *b* (fm)
O	7.245	4.232	5.805
S	14.177	1.019	2.847
Ca	17.331	2.78	4.70
Fe	23.678	11.22	9.45
Sr	34.458	6.19	7.02

While neutrons do not interact via the Coulomb interaction, they do still experience the electromagnetic force due to its intrinsic magnetic dipole moment from the intrinsic spin ($S = ½$) of the particle. This means that neutrons diffract and yield magnetic Bragg peaks from long-range magnetically ordered crystal systems and a neutron diffraction patten is a superposition of structural and magnetic diffraction patterns. Ferromagnetic materials normally have magnetic structures that are commensurate with the nuclear structure, so the magnetic reflections of a ferromagnet will be at the same position as the nuclear reflections, increasing their intensity. Antiferromagnets, however, often cannot be described within the nuclear unit cell thus requiring a supercell expansion and yielding additional magnetic reflections that are not at the same location as the nuclear reflections.

The intensity of magnetic Bragg peaks also falls off very quickly with 2θ and are only visible at low angles. This is because, like X-rays, magnetic scattering of neutrons comes from interaction if the incident beam with the electron cloud. Even more than this though, it stems from interaction with only the outer valence electrons, meaning that the intensity falls off even quicker than seen in X-ray diffraction. However, this is not the case for neutrons diffracting from the nucleus. This is because the nucleus is much smaller than the electron cloud and is effectively a point scatterer. Therefore, there is less destructive interference stemming from neutrons interacting with "opposite sides" of the same nucleus and nuclear neutron Bragg diffraction is present to very high 2θ and the data can give more structural information than X-ray diffraction.

However, there are a few drawbacks to the use of neutron diffraction. The first of these is that there are fewer neutron sources than X-ray sources worldwide, meaning that beamtime is a limited resource. Neutron sources also usually give a lower flux than X-ray sources, meaning that larger samples and longer scan times are necessary to achieve meaningful results. The lower flux of neutron sources also means that X-ray sources give better resolution (because tighter collimation does not excessively compromise incident beam intensity). Therefore, X-ray diffraction is the standard method for structure solution, whereas neutron diffraction is used complimentarily when necessary and only after a material has been characterized using X-ray diffraction.

2.2.3.1. Institut Laue Langevin (ILL)

The Institut Laue Langevin located on the EPN campus in Grenoble, France is a reactor source neutron facility. In reactor sources, the neutron-induced nuclear fission is used to produce neutrons wherein heavy elements like ^{235}U absorb a neutron and then split into lighter nuclei, producing more neutrons (an average of 2.4 neutrons per fission event) and causing a chain reaction [7]. A moderator then slows the neutrons from kinetic energies of around 2 MeV to less than 1 eV as the neutrons collide with the moderator substance many times until reaching thermal equilibrium with the moderator so that the temperature of the moderator determines the mean kinetic energy of the neutrons. The ILL reactor normally has an output power of 58 MW and produces a flux of neutrons in the moderator region of 1.5×10^{15} cm^{-2} s^{-1} and different types of moderators (cold, thermal, and hot) then deliver neutrons to various beamlines for a plethora of different types of experiments [7].

2.2.3.1.1. D1B Beamline

The D1B beamline [8] at the ILL is an ideal instrument for use in characterizing the magnetic structures of materials due to the availability of a longer neutron wavelength, a high flux, and the variable temperature sample environment. D1B has two different monochromators (tabulated information in Table 2.2) mounted on a set of motors which allow the user to change between wavelengths fairly quickly.

Table 2.2. Monochromators on D1B at the ILL.

Monochromator	3-HOPG crystals	Ge single crystal
Neutron λ (Å)	2.52	1.28
Flux (neutrons cm^{-2} sec^{-1})	5.6×10^6	$\sim 10^5$

The neutrons are delivered to the instrument by a thermal curved guide H22 at a take-off angle of 44.22°, and 5 diaphragms collimate the beam between the monochromator and the sample. The neutrons are then detected by 1280 W/Re gold plated wires placed every 0.1° in a sealed gas chamber, covering 0.15 steradians and providing an 80% efficiency at a wavelength of 2.52 Å and a 60% efficiency at 1.28 Å.

The sample environment used for the purposes of this thesis was an Orange cryostat which allows for data collection at temperatures ranging from 2 K to 300 K. The high neutron flux on this instrument was essential in the variable-temperature neutron experiments described in chapters 3, 4, and 6, as individual scans only 2 minutes long each provided good counting statistics and allowed for the collection of data every 1-2 K on heating at a constant, slow rate. This in turn allowed for detailed information on the change in magnetic structure with temperature which would not have been possible with other beamlines which require longer counting times to obtain good statistics.

2.2.3.1.2. D2B Beamline

The D2B beamline [9, 10] at the ILL is another high-resolution powder diffractometer designed for crystallographic studies. The neutrons are delivered to the beamline with a high take-off angle of 135° and uses a vertical focusing Ge monochromator. The neutrons are then detected by 128 ^{3}He detectors spaced at intervals of 1.25°. Several different sample environments are available for use on D2B, and both the sample carousel at room-temperature as well as the cryostat (1.5 K to 300 K) were utilized in this thesis. The data presented in this thesis was collected at a wavelength of 1.594 Å (which is the optimum wavelength for the instrument) and scans at individual temperatures required 2-3 hours of counting time for good statistics. Normally the data collected from the central third of the detectors was used as this provides higher resolution, in

particular this section is exposed to less curvature of the Scherrer cones at low angles and hence less peak asymmetry, albeit at the sacrifice of some intensity.

2.2.3.1.3. XtremeD Beamline

XtremeD [11, 12] is a new beamline at the ILL designed for the study of materials under extreme conditions like high applied fields (currently up to 10 T), high pressures (currently up to 20 GPa), and high temperatures (currently 1.5 K up to 1200 K). In this thesis, we conducted the first user experiment on the beamline which was concerning variable applied-fields. XtremeD has two different monochromators: a variable focusing HOPG monochromator comprised of 81 crystals and a variable focusing Si(115) monochromator both of which allow for various wavelengths. The neutrons are detected by a curved Trench Multiwire Proportional Chamber ^{3}He detector. This is a new technology developed at the ILL [13] and covers an area 130° around the sample and allows for the collection of 2D diffraction patterns in a few seconds. The sample environment used in this thesis was the cryomagnet, which allows for environments ranging from 1.5 K to 300 K with applied fields up to 10 T.

2.2.3.2. ISIS Neutron and Muon Facility

The ISIS Neutron and Muon Facility is a spallation-based neutron source. Spallation sources bombard heavy element targets with pulsed high-energy protons (~1 GeV) – produced by synchrotrons, cyclotrons, or linear accelerators – which on collision drive the heavy element into an excited state which then decays into lighter nuclei and neutrons. For every collision, around 30 neutrons are produced of energies around 20-30 MeV and are slowed by moderators similar to those used by reactor sources. In the case of ISIS, the protons are generated by a 70 MeV H^- linear accelerator and after being stripped of their electrons are then stored in an 800 MeV proton synchrotron. In general, the pulse frequency of spallation neutron sources is between 10 – 60 Hz (50 Hz at ISIS) with pulse durations of around 100 μs after the moderator. The neutrons emerging from each pulse have a range of energies and therefore a range of speeds which then disperse in space and time along the beamline. The neutrons are therefore often measured according to their time of flight (TOF) which optimizes the use of the pulse structure and makes the amount of time

needed for an experiment roughly the same as high-flux reactor sources even though the time-averaged flux is often less [7].

2.2.3.2.1. General Materials (GEM) Beamline

The GEM beamline at ISIS [14, 15] was designed to be a good-resolution, high-flux powder diffractometer with wide angular range. The detector at GEM is an array of 7270 and 86 modules which cover a scattering angle of 1.1° to 169.3° with the *d*-spacing range and resolutions ($\Delta d/d$ %) of each bank shown in Table 2.3 below.

Table 2.3. Resolution and *d*-spacing range of each bank of the GEM diffractometer.

Bank	$\Delta d/d$ %	*d*-range (Å)
1	3.4	0.9 – 25.18
2	2.3	0.65 – 13.12
3	1.4	0.35 – 6.93
4	0.7	0.21 – 4.00
5	0.5	0.15 – 2.77
6	0.3	0.11 – 1.90

2.2.3.2.2. High Resolution Powder Diffraction (HRPD) Beamline

HRPD [16, 17] is a high-resolution diffraction beamline at ISIS. The beamline is situated ~ 96 m from Target Station 1 at ISIS, and the long flight path allows for very high resolution in the backscattering bank that is nearly *Q*-independent which makes HRPD one of the highest resolution neutron diffractometers in the world. This means that lattice parameters can be determined to high precision, subtle distortions are detectable like during phase transitions, and closely-spaced peaks at short *d*-spacings can be resolved. HRPD has three detector banks: bank 1 which is the backscattering bank, bank 2 which is the 90° bank, and bank 3 which is the low angle bank, and the resolution and *d*-range for each bank are described below in Table 2.4. The design of HRPD also aims to increase resolution by minimizing the uncertainty of the TOF by the long flight path and the use of high angle detectors since *d* is proportional to TOF × 2sinθ. As the reported $\Delta d/d$ shows (Table 2.4), the resolution of HRPD does achieve greater resolution and is one order of magnitude better for low *d*-ranges and similar for higher *d*-ranges compared to those of GEM, though there is a substantial amount of noise in bank 3 which can make it difficult to identify statistically significant small magnetic peaks.

Table 2.4. Resolution and *d*-spacing range of each bank of the HRPD diffractometer.

Bank	Fixed scattering angle	$\Delta d/d$ %	*d*-range (Å)
1	167.3 ± 8.8°	~ 6×10^{-2}	0.6 – 4.6
2	90.0 ± 9.6°	~ 0.2	0.9 – 6.6
3	29.9 ± 2.3°	~ 1	2.2 – 16.5

HRPD is currently shut-down (the last user experiment on HRPD before the shut-down is described in chapters 3 and 5) and is undergoing an upgrade to HRPD-X which aims to improve the resolution at high *d*-spacings, take advantage of new detector technology, and insert a nonmagnetic sample tank so that fields may be applied during experiments.

2.2.4. Refinement Methods

The Rietveld method [18], developed by H. M. Rietveld in the 1960's, is a popular method of refining a structural model against powder diffraction data. In this method, a good starting model is input and a theoretical pattern is produced and parameters are refined using a least-squares minimization (Eqn. 2.9).

$$S_y = \sum_{i=1}^{N} w_i \left(y_{obs,i} - y_{calc,i}(p)\right)^2 \qquad \text{(Eqn. 2.9)}$$

In this equation, the objective function, S_y, is the sum over all points in a diffraction pattern of all the weighted (w_i) differences in the observed ($y_{obs,\,i}$) and calculated ($y_{calc,\,i}$) intensities. The weighting here is proportional to 1/y, which ensures that weak reflections are still given sufficient weight. In the case of a single crystal refinement, a comparable least-squares refinement is carried out against individual integrated intensities, I_{hkl}, but in the case of powder refinements where there is peak overlap, the refinement is against the whole profile of individual intensity points which have contributions from multiple overlapping reflections. Therefore, in addition to the structural variables, additional parameters are refined to account for the background and peak profiles.

The quality of a refinement can then be quantified by different R-factors. The R-factor used most often in this thesis is the weighted profile R-factor, R_{wp}, as given by Equation 2.10.

$$R_{wp} = \sqrt{\frac{\sum_i w_i(y_i - y_{ci})^2}{\sum_i w_i y_i^2}} = \sqrt{\frac{S_y}{\sum_i w_i y_i^2}} \quad \text{(Eqn. 2.10)}$$

The statistically expected R-factor, R_{exp}, is given by Equation 2.11, and the goodness-of-fit parameter, χ, is given by the ratio of R_{wp} to R_{exp} (Eqn. 2.12).

$$R_{exp} = \sqrt{\frac{N_{obs} - N_{var}}{\sum_i w_i y_i^2}} \quad \text{(Eqn. 2.11)}$$

$$\chi = \frac{R_{wp}}{R_{exp}} = \sqrt{\frac{S_y}{N_{obs} - N_{var}}} \quad \text{(Eqn. 2.12)}$$

All of the powder diffraction pattern refinements carried out in this thesis were performed using the TOPAS Academic software, v6 [19]. Crystallographic information files (CIFs) for structures reported in literature were obtained from the Inorganic Crystal Structure Database (ICSD) [20]. When carrying out magnetic refinements, the ISODISTORT software [21] was used to generate magnetic CIFs which contained symmetry allowed magnetic 'modes' corresponding to different arrangements of long-range magnetic order for an input structure which could be activated and refined against NPD data.

2.2.5. SQUID magnetometry

Magnetic susceptibility measurements were carried out using a Quantum design MPMS magnetometer which uses a Superconducting QUantum Interference Device (SQUID) at its core to measure the magnetic moment of a sample [22, 23]. The SQUID is made up of a closed loop containing two Josephson junctions (for a DC SQUID) which are thin strips of insulating material that separate superconducting materials. When a small current is applied across this device, Cooper pairs tunnel through the junction and allow for conduction with zero resistance across the coil. However, when the applied current exceeds the critical current of the junctions, the resistivity becomes non-zero which then generates a voltage across the SQUID which is proportional to the magnitude of an external magnetic field.

During measurements, a sample is mounted on a long stick, lowered into the induction coils, and magnetized by a superconducting magnet. Once magnetized, the sample is translated vertically through the detector coil which produces a voltage according to Faraday's law and Lenz's law.

This detector coil is then coupled to a larger input coil which is in turn coupled to the SQUID which generates the output voltage proportional to the magnetic moment of the sample. This reveals a limitation to SQUID magnetometry, however, in that it measures the magnetization of the sample as a whole which means that small magnetic impurities can dominate the signal and obscure small changes in magnetization from a weakly magnetic sample.

SQUIDs are very sensitive detectors and can detect very small magnetic moments, which is very useful but also means that they must be shielded from fluctuating external fields so it is housed away from the sample environment and shielded by a superconducting shield. In addition to this, any magnetic signal from the sample environment must also be minimized and this is achieved by housing the sample in gelatin capsules secured within a plastic straw at low temperatures. At high temperatures, this is achieved by a small pellet of the sample being secured with an alumina-based cement directly onto the oven stick assembly and covered with Cu foil (Cu is almost non-magnetic) to reduce heat loss of the sample to the exchange gas.

The sample environment is kept under an inert He atmosphere which can be cooled to 1.8 K and the oven stick assembly can be heated up to 900 K. Additionally, the superconducting magnet can apply fields up to ± 7 T. Magnetization curves can therefore be obtained isothermally as a function of applied field (*MvH*) or in a static field (typically 100 Oe in this thesis) after being cooled in zero-field (ZFC) or in an applied field (FC)) as a function of temperature (*MvT*).

2.2.6. X-ray absorption near-edge spectroscopy (XANES)

X-ray absorption spectroscopy (XAS) involves techniques which probe the transition from the ground states of various metals to excited states. The investigation of transitions from core electronic states to excited electronic states is called X-ray absorption near-edge spectroscopy (XANES) while the investigation of excitations beyond the LUMO is referred to as extended X-ray absorption fine structure (EXAFS) [24]. This is done by directing an incident beam of X-rays at a sample at varying energies that are applicable to the element being probed, and the position of the absorption edge can reveal information on the valence states of the metal. In this thesis, XANES measurements were conducted on the B18 beamline at DLS [25, 26], which is a general

purpose XAS beamline covering a wide energy range (2-35 keV) equipped with Si(111) and Si(311) monochromators and various detectors that can be used for transmission and fluorescence XAS, XRD, and more measurements. The Fe K-edge (corresponding to excitation from the 1s orbital) was probed in particular in this thesis and standards of FeO and Fe_2O_3 were used for qualitative comparison, as the position of the absorption edge is influenced by the principle that higher oxidation states have a slightly more tightly bound 1s electron and it therefore requires more energy to excite electrons from the core to a higher orbital or ionise them. XANES measurements were carried out on B18 by Dr. Maria Alfredsson (University of Kent) through the Diamond Block Allocation SP37701.

2.2.7. Electron Diffraction

Electron diffraction is a complimentary technique to x-ray and neutron diffraction and can be extremely useful in the characterization of phases for which the growth of single crystals is non-trivial. Unlike neutrons and X-rays, electrons are charged particles and do interact with matter via Coulombic interactions and therefore are scattered by electric potential in a material. Like X-rays, the scattering amplitude increases with the atomic number and nuclear charge, *Z*, and the scattering factor f_e takes into account both this and the shielding from the electron cloud around the nucleus, f_x, as in Equation 2.13.

$$f_e(\theta) \propto Z - f_x \qquad \text{(Eqn. 2.13)}$$

One of the advantages of electron diffraction is that single crystal diffraction patterns can be obtained from extremely small amounts of materials, often crystallites on the nanometre scale are adequate, because electrons have larger scattering amplitudes and are easier to focus than X-rays. Additionally, because of the much shorter wavelengths used (typically 0.025 Å – for 200 kV electrons) the correlation length for electron diffraction is much shorter than that of X-rays so correlations that may be more diffuse in X-ray diffraction may appear much more distinct with electron diffraction. This means that shorter range structural features, such as stacking faults or short-range ordering of vacancies are more evident. 3D electron diffraction is a more specialized technique within electron diffraction that has increased in popularity since 2007 and maximizes

the completeness of data as all reflections within the tilt range of the TEM goniometer are measured [27]. This enables full structures to be determined from the intensity data, and is a developing state-of-the-art technique. 3D electron diffraction experiments were conducted using a ThermoFisher Tecnai G2 at a voltage of 200 kV, a tilt range of 84° (-42° to 42°), and an ASI Timepix3 direct electron detector. These experiments were carried out and analysed by Sepideh Rahimi and Professor Joke Hadermann at the Electron Microscopy for Materials Science (EMAT) institute at the University of Antwerp, Belgium.

2.2.8. Electron Microscopy

The two main types of electron microscopy are scanning electron microscopy (SEM) and transmission electron microscopy (TEM) [1]. In both of these instruments, electron beams are accelerated and focused through electric and magnetic fields, and the difference between the techniques lies in the detection methods. In the case of SEM, the backscattered electrons are detected, while in TEM, the electrons transmitted through a thin sample are detected and imaged on a suitable area detector. Both techniques can image materials down to the nanometre scale. In both cases, the electron microscope can be fitted with an EDS detector to analyse the X-rays produced by the excitation of various elements to perform elemental analysis.

SEM images were obtained on a JEOL JSM-5510LV scanning electron microscope with the assistance of Dr. Robert Smyth. TEM images were obtained via High-Angle Annular Dark Field Scanning Transmission Electron Microscopy (HAADF-STEM) collected on an aberration-corrected ThermoFisher Titan transmission electron microscope at a voltage of 300 kV. These were collected and analysed by Sepideh Rahimi and Professor Joke Hadermann at the Electron Microscopy for Materials Science (EMAT) institute at the University of Antwerp, Belgium.

2.2.9. Energy Dispersive X-rays (EDX)

Energy dispersive X-ray spectroscopy (EDS/EDX) [1] is a technique which uses either TEM or SEM to image crystals and qualitatively map the distribution of various elements over the individual crystallites as well as quantitatively obtain spectra at various points across the crystals to then give an average composition. EDX does this by measuring the energies of X-rays (that

are characteristic to each element) that are emitted when the electron beam ejects a core electron and an outer electron then relaxes to the lower energy core to fill that vacancy.

EDX data collection and analysis was done via TEM by Sepideh Rahimi at the Electron Microscopy for Materials Science (EMAT) institute at the University of Antwerp, Belgium in chapter 3. Other EDX studies were carried out with the assistance of Dr. Robert Smyth using an SEM instrument equipped with an Oxford Instruments EDS detector. The technique should be regarded as semi-quantitative to an extent which depends on sample preparation methods.

2.2.10. Mössbauer spectroscopy

Mössbauer spectroscopy [1, 28, 29] relies on the properties of the Mössbauer effect and concerns the recoil-free emission and absorption of gamma rays by nuclei. Normally, the conservation of momentum necessitates that when an atom absorbs radiation, it must recoil. However, in the case of an atom confined within an extended crystal lattice, the recoil energy is instead transferred to the rest of the lattice. The energy of the radiation absorbed can thus reveal information about differences between atoms in a crystal system.

During the collection of a Mössbauer spectrum, gamma radiation is directed at the sample and a detector measures the radiation transmitted through the sample as some will have been absorbed by nuclei. The energy at which radiation is absorbed by a nucleus is affected by the s-electron density because s-orbitals are the only orbitals for which the wavefunction has amplitude at the nucleus. Therefore, radiation is absorbed at different energies depending upon the chemical environment and oxidation state (chemical shift/isomer shift). In addition to this, splitting patterns in the energy absorbed depends on the distribution of charge around the nucleus (quadrupole splitting from non-spherical charge distribution) and magnetic order (hyperfine splitting from magnetic dipole interactions). Quadrupole splitting is indicated by doublets, whereas hyperfine splitting is indicated by sextets. In this thesis, only ^{57}Fe nuclei were investigated. Mössbauer spectra were collected and analysed by Magali Gimeno and Professor Michael Neidig at the University of Oxford.

2.2.11. Bond valence sum (BVS) calculations

BVS calculations estimate the oxidation states of ions in a compound based on bond distances to surrounding anions according to Equation 2.14.

$$\sum_{bonds} e^{\frac{R_0 - R}{b}} \qquad \text{(Eqn. 2.14)}$$

In this equation, R_0 is the bond valence parameter characteristic of the bond in question, determined from distances reported in the literature, R is the observed bond length, and b is a constant usually around 0.37 Å [30].

References

[1] Weller, M.T.; Young, N.A. *Characterization methods in Inorganic Chemistry*, Oxford University Press, **2017**.
[2] IUCr; Hahn, T. *International Tables for Crystallography Volume A: Space-group Symmetry, 2nd edition*, Wiley, **1986**.
[3] Eckert, M. *Ann. Phys*. **2012**. *524*, A83-A85.
[4] Thompson, S.P.; Parker, J.E.; Potter, J.; Hill, T.P.; Birt, A.; Cobb, T.M.; Yuan, F.; Tang, C.C. *Review of Scientific Instruments*, **2009**, *80*, 075107.
[5] Fitch, A.; Dejoie, C.; Covacci, E.; Confalonieri, G.; Grendal, O.; Claustre, L.; Guillou, P.; Kieffer, J.; de Nolf, W.; Petitdemange, S.; Muat, M.; Watier, Y. *J. Synchrotron Rad.* **2023**, *30*, 1003-1012.
[6] IUCr; Prince, E. *International Tables for Crystallography Volume C: Mathematical, Physical, and Chemical Tables, 3rd edition*, Wiley, **2004.**
[7] Boothroyd, A.T. "Principles of Neutron Scattering from Condensed Matter." *Oxford University Press*. **2020.**
[8] Puente Orench, I.; Clergeau, J.F.; Martínez, S.; Olmos, M.; Fabelo, O.; Campo, J. *J. Phys. Conf. Ser.* **2014**, *549*, 012003.
[9] Suard, E.; Hewat, A. *Neutron News*, **2001**, *12(4)*, 30-33.
[10] https://www.ill.eu/for-ill-users/instruments/instruments-list/d2b/characteristics
[11] Rodríguez-Velamazán, J.A.; Campo, J.; Rodríguez-Carvajal, J.; Moguera, P. *J. Phys. Conf. Ser.* **2011**, *325*, 012010.
[12] https://www.ill.eu/for-all-users/instruments/instruments-list/xtremed/characteristics
[13] Barkats, D.; Buffet, J.C.; Cuccaro, S.; Guerard, B.; Lafont, F.; Marchal, J.; Pentenero, J. Sartor, N. *EEE Nuclear Science Symposium and Medical Imaging Conference (NSS/MIC), Piscataway, NJ, USA*, **2021**, pp. 1-8.
[14] Williams, W.G.; Ibberson, R.M.; Day, P.; Enderby, J.E. *Phys. B.* **1997**, *241-243*, 234-236.
[15] https://www.isis.stfc.ac.uk/Pages/gem.aspx
[16] Fortes, A.D.; Gibbs, A.S. *J. Neutron Res.* **2020**, *22(2-3)*, 91-98.
[17] https://www.isis.stfc.ac.uk/pages/hrpd.aspx
[18] Rietveld, H.M. *Phys. Scr.* **2014**, *89(9)*¸098002.
[19] Coelho, A.A. *J. Appl. Crystallogr.* **2018**, *51*, 210-218.
[20] Zagorac, D.; Muller, H.; Ruehl, S.; Zagorac, J.; Rehme, S. *J. Appl. Crystallogr.* **2019**. *52*, 918-925.

[21] Campbell, B. J.; Stokes, H. T.; Tanner, D. E.; Hatch, D. M. *J. Appl. Crystallogr.* **2006**, *39*, 607-614.
[22] Kleiner, R.; Koelle, D.; Ludwig, F.; Clarke, J. *Proceedings of the IEEE*. **2004**, *92*, 1534.
[23] Fagaly, R.L. *Rev. Sci. Instrum.* **2006**, *77*, 101101.
[24] Yano, J.; Yachandra, V.K. *Photosynthesis Research.* **2009**, *102*, 241-254.
[25] Dent, A.J.; Cibin, G.; Ramos, S.; Smith, A.D.; Scott, S.M.; Varandas, L.; Pearson, M.R.; Krumpa, N.A.; Jones, C.P.; Robbins, P.E. *J. Phys. Conf. Ser.* **2009**, *190*, 012039.
[26] https://www.diamond.ac.uk/Instruments/Spectroscopy/B18/Specification.html
[27] Gemmi, M.; Mugnaioli, E.; Gorelik, T.E.; Kolb, U.; Palatinus, L.; Boullay, P.; Hovmöller S.; Abrahams, J.P. *ACS Cent. Sci.* **2019**, *5*, 1315-1329.
[28] Dronsfield, A.; Adetunji, J. *Educ. Chem.* **2002**, *39(4)*, 97-100.
[29] Fluck, E.; Kerler, W.; Neuwirth, W. *Angew. Chem.* **1963**, *2(6)*, 277-332.
[30] Brown, I.D.; Altermatt, D. *Acta Cryst.* **1985**, *41*, 244-247.

Chapter 3: Synthesis and Characterization of $Sr_3Fe_2O_5Fe_2OS_2$

Contents

3.1. Synthesis 54
3.1.1. Ceramic synthesis 54
3.1.2. Flux synthesis 55
3.2. Structure Characterization 56
3.2.1. Idealized structure 56
3.2.2. Structural Variations 57
3.2.2.1. Variable temperature x-ray powder diffraction 62
3.2.2.2. High resolution powder neutron diffraction (HRPD) 64
3.2.2.3. Electron Diffraction 69
3.2.2.4. Transmission electron microscopy 72
3.3. Magnetic Characterization 77
3.3.1. Magnetometry 77
3.3.2. Room temperature NPD 79
3.3.3. Low variable temperature NPD 85
3.3.4. Low temperature NPD 88
3.3.5. High variable temperature NPD 89
3.4. Further Characterization 91
3.4.1. XANES measurements 91
3.4.2. Mössbauer Spectroscopy 91
3.5. Conclusions and Future Work 93
References 95

This chapter will discuss the characterization of the as-yet unreported phase $Sr_3Fe_2O_5Fe_2OS_2$ (see Figure 3.1) which has been synthesized in high-purity polycrystalline samples. After a brief description of the synthesis, the idealized tetragonal structure is posited in section 3.2.1, followed by a further analysis of the structural intricacies and sample-dependences observed in section 3.2.2. $Sr_3Fe_2O_5Fe_2OS_2$ also exhibits long-range magnetic order at room temperature with a

further low-temperature order introduced around 115 K. The magnetic structure is characterized and discussed in section 3.3, followed by further characterization measurements that were carried out in section 3.4.

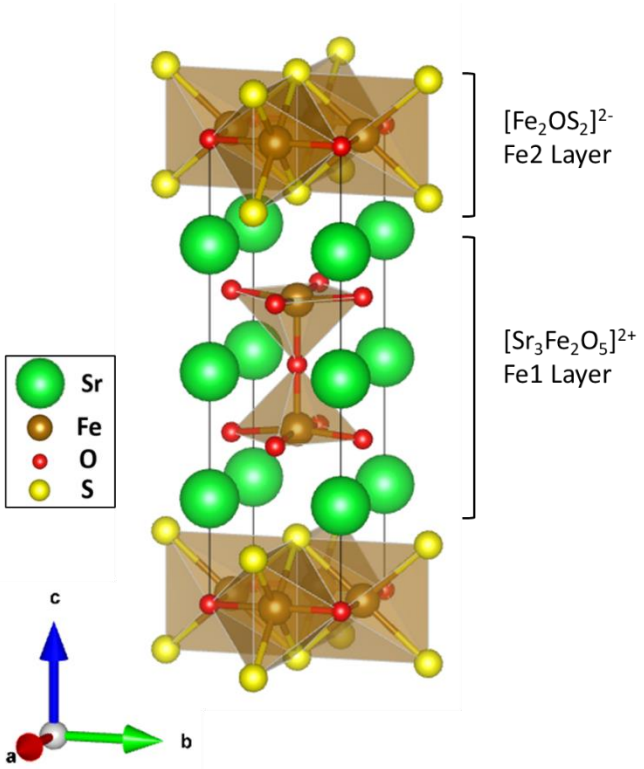


Figure 3.1. Unit cell of $Sr_3Fe_2O_5Fe_2OS_2$.

3.1. Synthesis

A reference table describing the synthesis method and product symmetry for all samples described in this chapter can be found in Appendix B.

3.1.1. Ceramic synthesis

The synthesis of $Sr_3Fe_2O_5Fe_2OS_2$ (=$Sr_3Fe_4O_6S_2$) can be achieved by use of a traditional high-temperature ceramic synthesis method. The reagents SrO (obtained from the decomposition of $SrCO_3$), Fe_2O_3 (Alfa Aesar, 99.998%), Fe (Alfa Aesar, 99+%), and S (Sigma Aldrich, 99.98%) were ground thoroughly in a 3:1:2:2 molar ratio in an agate mortar and pestle until reaching homogeneity under an argon atmosphere.

The pelletized reagent mixture, placed in an alumina crucible and sealed in an evacuated silica tube, was then heated at a slow, 1°C per minute, rate to 900°C to avoid the sublimation of the

volatile elemental sulfur in the reagent mixture so that the sulfur has time to react with the other elements instead of merely entering a gaseous phase. A dwell time of 24 hours proved insufficient as SrS often formed as an impurity, but increasing the dwell time to 48 hours proved to eliminate this impurity. Fe_3O_4 was another common impurity that appeared in every sample and persisted through higher synthesis temperatures (up to 1000°C, higher temperatures resulted in unsuccessful syntheses) and longer dwelling times (up to one month). Annealed samples also maintained the Fe_3O_4 impurity, and purposefully targeting an iron-deficient phase $Sr_3Fe_{3.9}O_6S_2$ resulted in a small SrS impurity in addition to the persistent Fe_3O_4 impurity indicating that iron vacancies within the phase are not the source of this impurity (see Appendix C).

3.1.2. Flux synthesis

An alternative synthesis to the ceramic synthesis above is a flux-assisted synthesis method which is typically used in an effort to facilitate ion mobility by the mechanism of the molten salt as well as potentially facilitating crystal growth. In this method, an alkali halide salt – in this case KI (Alfa Aesar, ultra-dry, 99.998%) – is ground with the reagent mixture in an agate mortar and pestle until reaching homogeneity under an argon atmosphere. This powder was then transferred directly into an alumina crucible without being pelletized, and then sealed in a quartz tube under dynamic vacuum and with the tip dipped in liquid nitrogen to prevent the sublimation of sulfur. The vessel was then heated to 600˚C at a rate of 1˚C per minute where it too dwelled for 48 hours before being cooled at slow rates (0.1-0.5˚C per minute) to room temperature. The flux was removed with deionized water under ambient atmosphere using a vacuum filtration system.

This method was initially attempted in an effort to use a slow cooling rate to form single crystals. Unfortunately, the product remained polycrystalline with no sign of any crystals large enough for single crystal measurements having formed.

3.2. Structure Characterization

3.2.1. Idealized structure

The structural model of $Sr_3Fe_4O_6S_2$ which was initially used in Rietveld refinements was generated by combining the appropriate slabs with appropriate bond distances from literature containing similar layer types (chapter 1.3) in the crystallographic visualization software VESTA. Indeed, the Rietveld refinement of X-ray powder diffraction patterns confirms that $Sr_3Fe_2O_5Fe_2OS_2$ crystallizes in the tetragonal *P*4/*mmm* space group (No. 123). The phase contains iron in two distinct coordination environments: a square pyramidal [FeO_5] connected by a bridging axial oxygen atom in the cationic Fe1 layer coordination and a distorted [FeO_2S_4] octahedral environment with O atoms arranged *trans* to one another in the anionic Fe2 layer (see Figure 3.1). By considering each individual layer and the charges assigned to the layers in literature (see chapter 1.3), charge balancing each layer leads to the assumed oxidation states of Fe^{3+} and Fe^{2+} in the Fe1 and Fe2 layers respectively, which is supported by the bond valence sums (Table 3.3), and is in line with the oxidation states found in related compounds (chapter 1.3).

Table 3.1. Refined structural model for $Sr_3Fe_2O_5Fe_2OS_2$ (ANG047b).

	Space Group = *P*4/*mmm* (No. 123)			
atom	site	*x*	*y*	*z*
Sr1	1*b*	0	0	½
Sr2	2*g*	0	0	0.22716(8)
Fe1	2*h*	½	½	0.36159(9)
Fe2	2*f*	½	0	0
O1	4*i*	½	0	0.3407(2)
O2	1*a*	0	0	0
O3	1*d*	½	½	½
S	2*h*	½	½	0.1273(1)

Table 3.2. Refined unit cell parameters of $Sr_3Fe_2O_5Fe_2OS_2$ (ANG047b).

a (Å)	3.96156(1)
c (Å)	13.51991(8)
V (Å^3)	212.181(2)
R_{wp} (%)	3.956

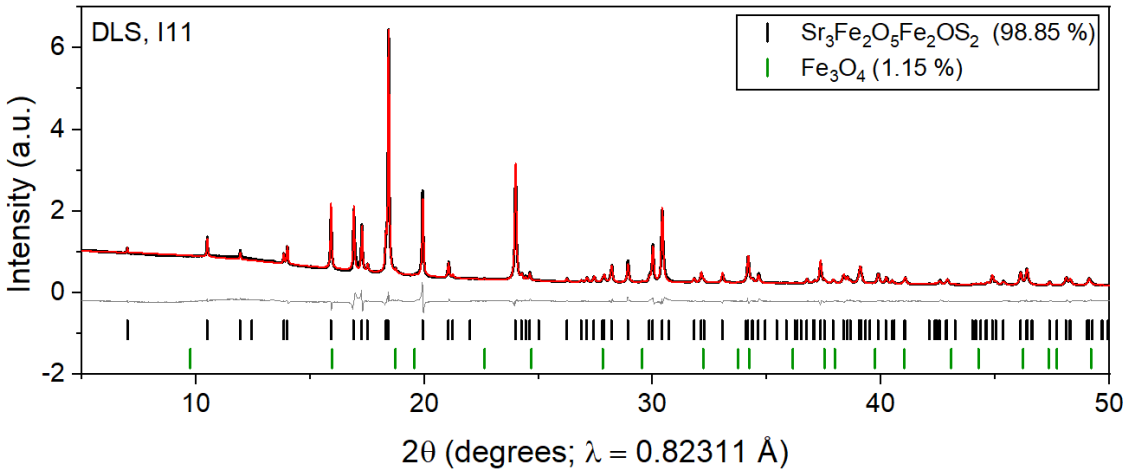


Figure 3.2. Rietveld refinement of the XRPD pattern of $Sr_3Fe_2O_5Fe_2OS_2$ (ANG047b) measured using the PSD detector on I11 at room temperature showing the observed (black), calculated (red) and difference (grey) curves.

Table 3.3. Bond valence sums calculations for the Fe1 and Fe2 sited of $Sr_3Fe_2O_5Fe_2OS_2$ (ANG047b).

Cation	Anion	Bond distance (Å)	BVS contribution	BVS $Sr_3Fe_2O_5Fe_2OS_2$
Fe1	O1	1.99244	4 × 0.5321	2.925
	O3	1.87345	1 × 0.7339	
	S1	3.17124	1 × 0.0631	
Fe2	O2	1.98266	2 × 0.4840	2.038
	S1	2.62677	4 × 0.3693	

3.2.2. Structural Variations

From sample to sample, there are structural variations that have been observed in the synchrotron X-ray diffraction patterns of $Sr_3Fe_4O_6S_2$. Some samples do not show any abnormalities in their XRPD patters as in Figure 3.2. However, there are some samples which do show abnormalities. One example of this is in a pair of diffuse peaks that appear between the (104) and (113) reflections. Another is the occasional splitting of the (200) and (020) peaks, indicating a slight orthorhombic distortion, but it is unclear from the X-ray powder diffraction patterns what compositional or structural variation causes these features to arise in some samples, but not others.

The diffuse peak anomalies have been observed in several different ceramic samples (see Figure 3.3). Note that the sharp peak within the first diffuse feature is a magnetite impurity peak. These diffuse features could possibly be partially accounted for by a Fe_2O_3 impurity due to the position of the peaks (Figure 3.4), but the refinement will not fit the peak shape of these diffuse features

very well and the amount of Fe_2O_3 that is needed in the refinement to account for the peaks is unrealistically large considering the composition used in synthesis (Figure 3.4). Additionally, the SEM of these phases (see section 3.4.3) does not support the presence of such a large iron oxide impurity. Closer inspection also unveils other regions in the Rietveld plot where the peaks and some features between peaks are not well fit (see Figure 3.4). There are a few different possibilities for what may explain these features. The first is that there is some sort of stacking faults or modulation in the structure of the main phase, whether in oxygen or iron vacancies, sulfur positions, or even a semi-periodic arrangement of stacking faults. While several different iron oxide phases that differ in occupancies and lattice parameters could account for the full intensity of the diffuse features, the integrated intensity is too high for the features to be solely from these given the refined composition of the main oxysulfide phase and the starting composition of the reaction. Further investigation is needed to resolve this.

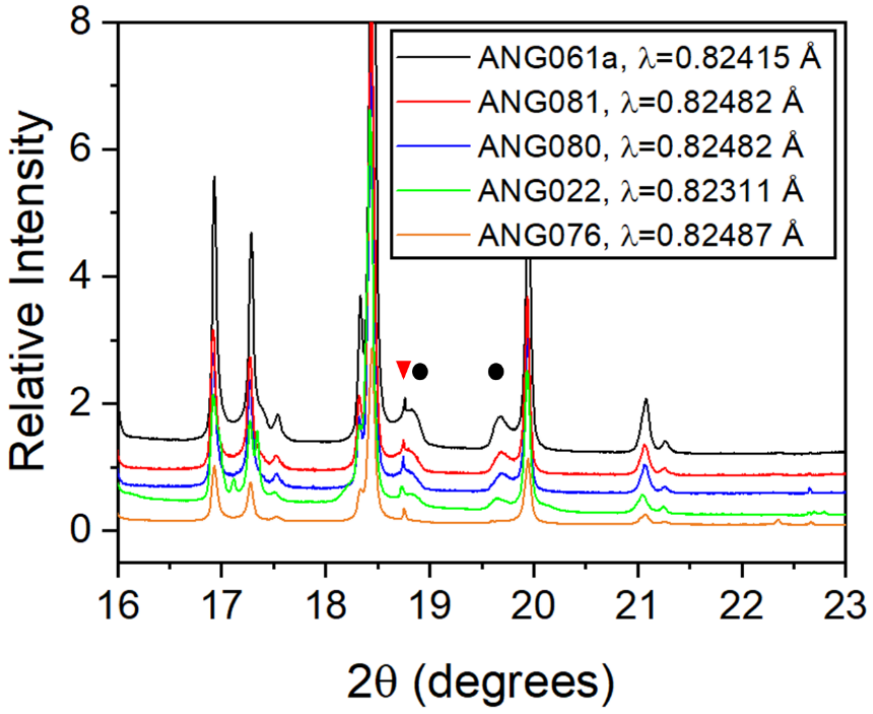


Figure 3.3. Several samples that exhibit the diffuse peaks (marked with black circles) between the (104) and (113) peaks and sample ANG047b with no diffuse peaks for reference. Data from multiple I11 sessions with slightly different silicon-calibrated wavelengths used.

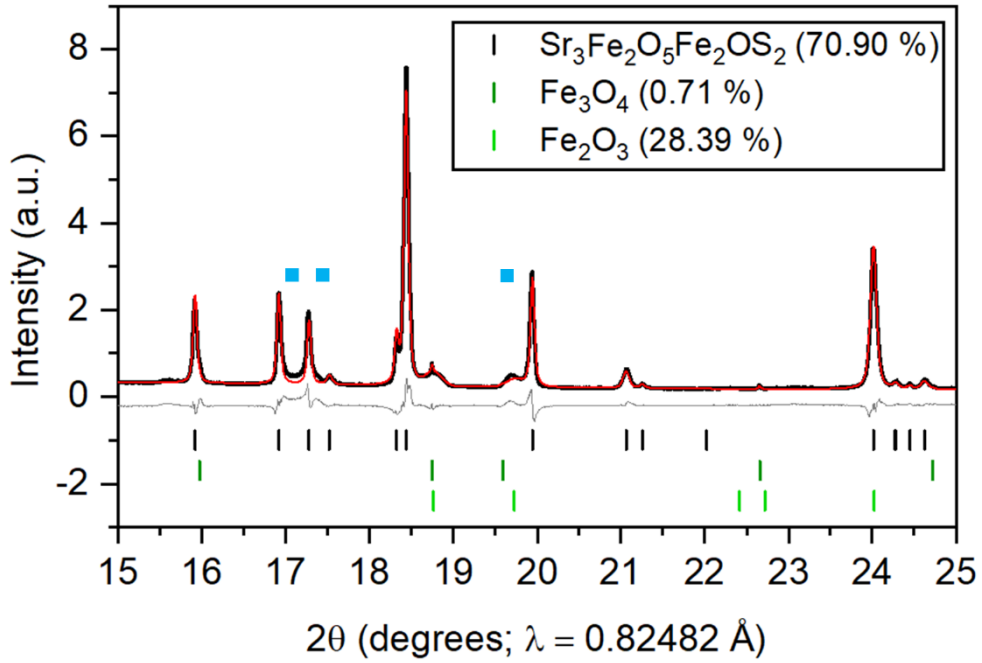


Figure 3.4. Zoomed in Rietveld refinement of sample ANG080 with the Fe_2O_3 phase included in the refinement. This pattern was collected on I11 on the PSD detector, and shows the observed (black), calculated (red) and difference (grey) curves. Blue squares indicate areas where the fit is not ideal. However, the refined composition of the main oxysulfide phase and the starting composition does not support the presence of such a large Fe_2O_3 impurity.

The splitting of the (200) and (020) peaks has been observed in both a normal ceramic sample (ANG012), as well as in a sample that was annealed at 900˚C for 2 months (ANG022b) (see Figure 3.5). In the case of ANG022b, the split peaks are of different intensities, and this could indicate multiple related phases within the sample: one that is tetragonal and one that is orthorhombic with the tetragonal phase accounting for the extra intensity on the (200) peak at the lower angle. However, the intensity difference can also be accounted for by using preferred orientation parameters with a single orthorhombic phase. The refined parameters are compared for this sample in Table 3.4. This sample is an anneal of the sample ANG022, which exhibited diffuse peaks, but these peaks also disappeared in the long anneal. These phases can also be fit to a monoclinic cell in the space group *P*2/*m*, but the beta angle is very nearly 90° within error and the lowering in symmetry does not greatly improve the refinement so an orthorhombic model was chosen for further analysis (see Appendix D for more detail). The orthorhombic samples also go through an orthorhombic-to-tetragonal structural transition, evidenced by the split (200) and (020) reflections coalescing into a single peak at 500 K in the VT-SXRPD data collected on

I11 at DLS (see Figure 3.6a). These samples will again undergo a tetragonal to orthorhombic transition on cooling back to room temperature (Figure 3.6b).

Table 3.4. Comparison of the refined parameters from I11 XRPD data of ANG022b using a single orthorhombic phase versus an orthorhombic and a tetragonal phase.

	Single phase	Two-phase	
R_{wp} (%)	4.682	4.305	
Space Group	*Pmmm*	*Pmmm*	*P4/mmm*
wt %	98.99	93.43	5.56
a (Å)	3.95571(2)	3.95585(3)	3.94352(5)
b (Å)	3.93948(3)	3.94019(4)	3.94352(5)
c (Å)	13.5644(1)	13.5616(1)	13.5723(3)
V (Å^3)	211.381(3)	211.383(4)	211.068(8)

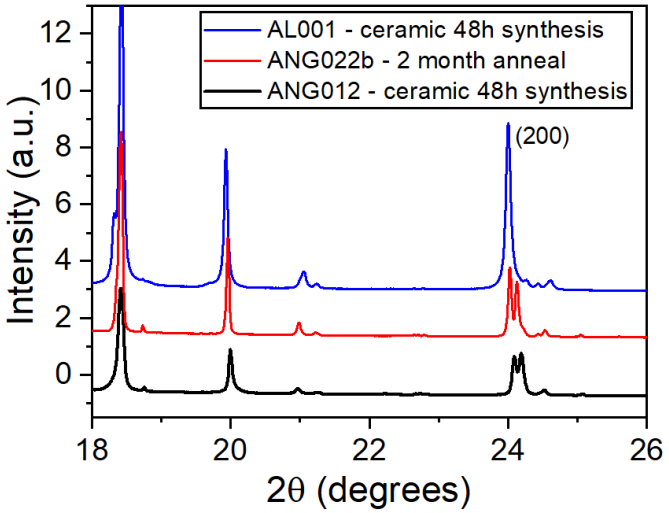


Figure 3.5. SXRPD patterns of ceramically synthesized orthorhombic distorted phases ANG012 (λ = 0.82497 Å) and ANG022b (λ = 0.82311 Å) with ceramically synthesized tetragonal AL001 (λ = 0.82311 Å) for reference measured on the PSD detector at I11 at room temperature. (AL001 synthesised by Annabel Lyon)

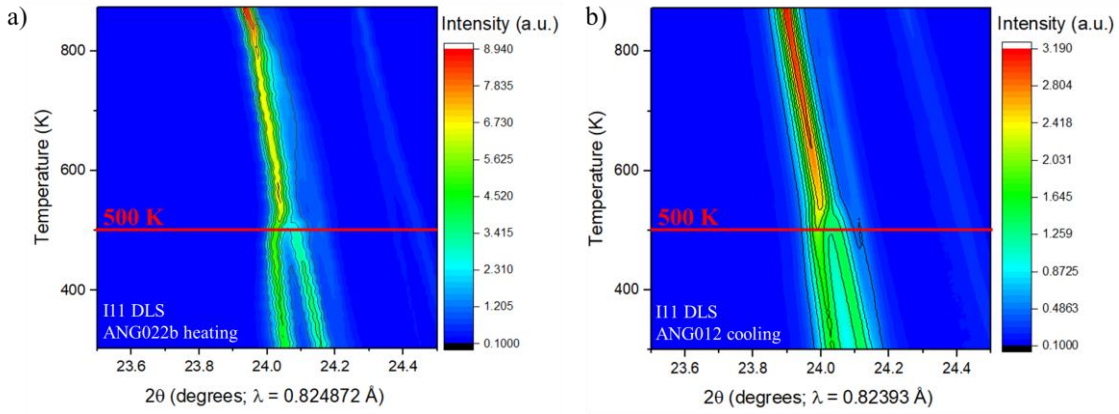


Figure 3.6. Zoomed-in contour plot showing the evolution of the split (200) and (020) peaks of sample ANG022b coalescing into a single peak on heating, indicating an orthorhombic to tetragonal transition at 500 K (left). Alongside is the contour plot of ANG012 on cooling showing the transition from tetragonal to orthorhombic indicated by the re-splitting of the (200) and (020) peaks at 500 K. There are slight differences between the heating and cooling but this can be attributed to the fact that the scans are from different samples.

In addition to the SXRPD data collected for this sample on I11, higher-resolution SXRPD data was also collected on ID22 at ESRF. The pattern collected at this beamline resolved more clearly the peaks that are split due to the orthorhombic distortion (see Figure 3.7), and with this in mind, the lattice parameters can be refined with more certainty than in the I11 data, wherein the split peaks are not as well resolved.

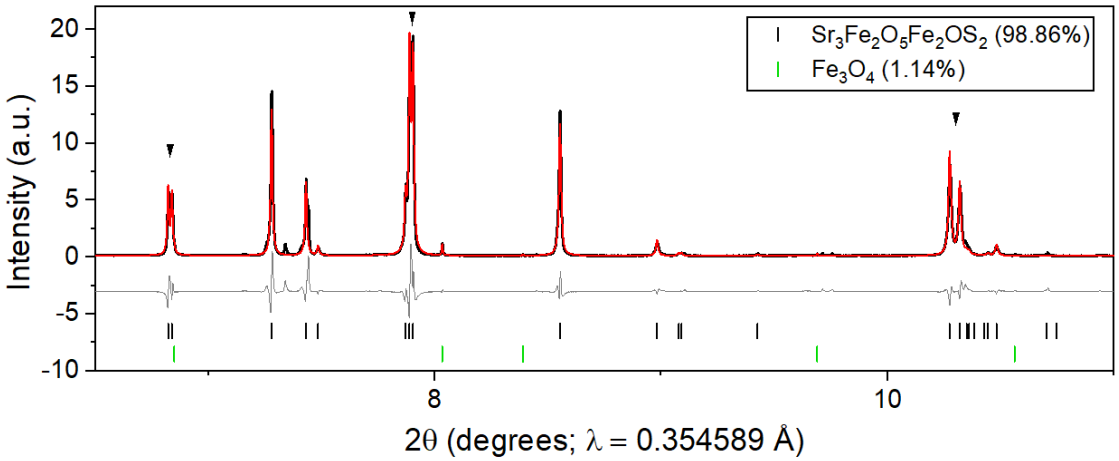


Figure 3.7. Rietveld refinement for ANG022b collected at room temperature on ID22 at the ESRF showing the observed (black), calculated (red) and difference (grey) curves. Black triangles indicate the split (103)/(013), (104)/(014), and (200)/(020) reflections from left to right.

Table 3.5. Refined lattice parameters and Fe2 occupancy for the orthorhombic ANG022 collected on I11 at the DLS and ID22 at the ESRF.

	I11	ID22
R_{wp} (%)	4.318	12.829
a (Å)	3.95575(1)	3.95977(1)
b (Å)	3.93941(1)	3.94286(1)
c (Å)	13.56446(8)	13.58674(4)
V (Å^3)	211.380(2)	212.128(1)
*occ*Fe2	0.978(3)	0.927(2)

In addition to the differences in the refined lattice parameters between the I11 and ID22 diffraction patterns, the occupancy on the Fe2 site in the Fe_2OS_2 layers is also refining to a lower value with the ID22 data set. Each orthorhombic pattern also freely refines an Fe2 occupancy below 1, though some, especially ANG012, are very nearly 1 within error. The Fe2 occupancy in the tetragonal phases also freely refines to 1 within error. Additionally, while it is plausible that slight compositional differences may be the source of the orthorhombic distortion in some samples, is no correlation between how orthorhombic a sample is and the refined occupancy of the Fe2 site (Figure 3.8, Table 3.6).

Table 3.6. Refined orthorhombic distortion and refined Fe2 occupancy of all orthorhombic samples at room temperature.

	ANG012	ANG022b		ANG072b		ANG047b
Beamline	I11	I11	ID22	I11	HRPD	I11
c (Å)	13.6082(2)	13.56601(9)	13.58943(4)	13.5722(3)	13.5478(6)	13.51991(8)
V (Å^3)	212.034(6)	211.463(2)	212.255(1)	212.015(8)	211.80(1)	212.181(2)
a/*b*	1.00404(2)	1.00415(1)	1.00429(0)	1.00209(3)	1.00329(5)	1
*occ*Fe2	0.992(5)	0.978(3)	0.927(2)	0.887(8)	0.865(12)	1

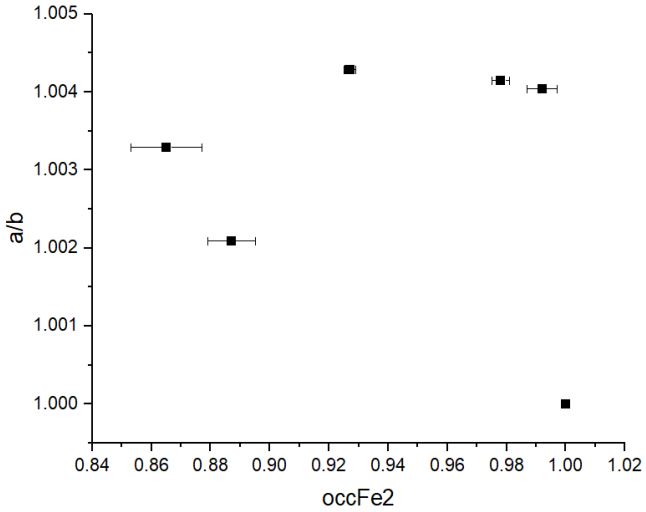


Figure 3.8. Plotted refined Fe2 occupancy against the *a* to *b* ratio.

The origins of these two anomalous features, the orthorhombic distortion and the diffuse peaks, have been a long-standing question since the discovery of this new phase at the start of this project, and were investigated by using a plethora of different methods. In the case of oxide perovskites, the tilting of MO_6 octahedra is often what gives rise to orthorhombic distortions [1,2], so investigating these samples with high-resolution neutron powder diffraction (section 3.2.2.2) (where O makes a relatively large contribution to the scattering) that would provide more insight into oxygen positions would hopefully help solve this anomaly. In addition to this, electron diffraction (section 3.2.2.3) was used in an effort to discover the space group of different samples and investigate if there is any structural modulation or diffuse scattering, and HAADF-STEM imaging (section 3.2.2.4) was used to probe the microstructure within different individual crystallites.

3.2.2.1. Variable temperature x-ray powder diffraction

Low-temperature SXRPD data was collected for the tetragonal sample ANG047b (see Fig 3.2) in small steps from 5 K to 130 K and at 300 K for reference on ID22 at ESRF. No structural

change was observed as the temperature decreased, aside from thermal contraction and the lattice parameters decrease in an approximately linear manner with temperature until around 100 K when the rate of thermal contraction slows, as is found for most solids (see Figure 3.9).

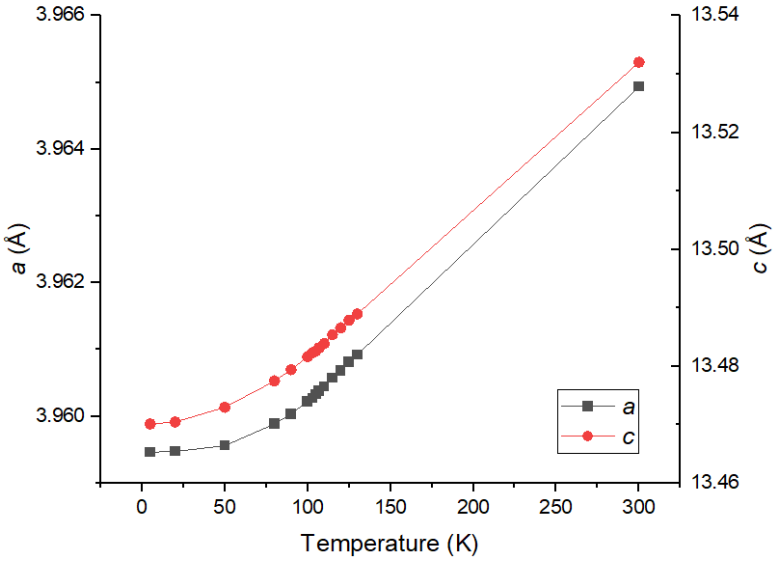


Figure 3.9. Change in lattice parameters for ANG047b as a function of temperature as refined from SXRPD collected on ID22 at ESRF.

In addition to this, variable temperature SXRPD data was collected for sample ANG044a from 90 K to 600 K. This sample also shows no change in symmetry with temperature and shows an approximately linear relationship between temperature and the refined lattice parameters until around 400 K when the peak shapes begin to change (see Figure 3.10). This change in peak shape is likely an artefact that is not indicative of a phase change since it persisted upon cooling again, and is likely due to decomposition from the capillary leaking and the compound reacting with air on heating or potentially a reaction with the silica of the capillary.

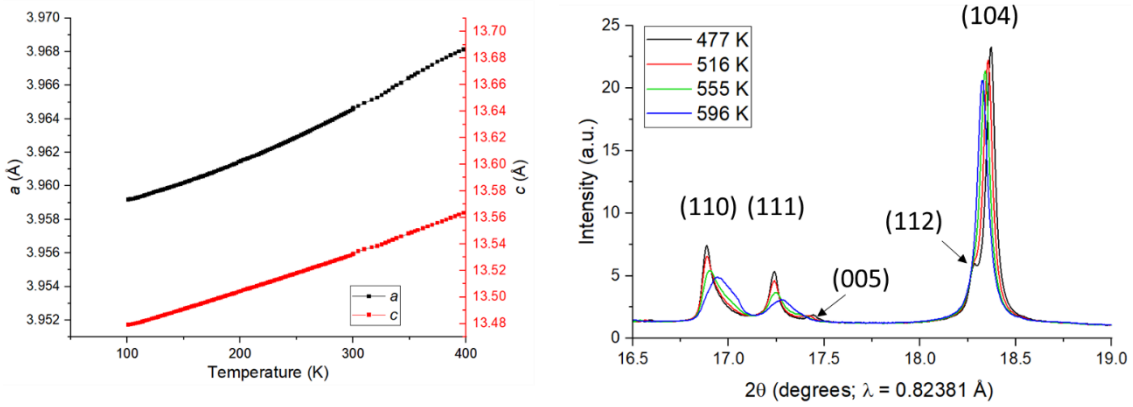


Figure 3.10. Change in lattice parameters for ANG044a as a function of temperature up to 400 K as refined from SXRPD collected on I11 at DLS alongside the patterns at various temperatures showing the change in peak shape.

3.2.2.2. High resolution powder neutron diffraction (HRPD)

The samples ANG074 (tetragonal, ceramic synthesis) and ANG072b (orthorhombic, ceramic synthesis and long anneal) were measured on HRPD at ISIS, a high-resolution neutron powder diffractometer. From SXRPD, ANG074 does not show an orthorhombic distortion nor does it have significant diffuse peaks between the (104) and (113) peaks (thus it is effectively a larger sample equivalent to ANG047b shown in Fig 3.2). ANG072b, on the other hand, has significant diffuse peaks between the (104) and (113) peaks and the peak shape of the (200) peak is not that of a clearly single peak, indicating that there may be a slight orthorhombic distortion in the phase. This feature can be especially seen in the difference curve at $2\theta = 24°$. It is important to note in Figure 3.11 that the Fe_3O_4 content is severely overestimated due to the Fe_3O_4 (311) reflection fitting both the sharp peak indicative of the magnetite presence in these samples as well as the diffuse feature that is located at the same angle while in reality, it should be fitting a small intensity sharp peak atop a large, broad peak.

While it may have been more ideal to measure a more significantly orthorhombic sample on the beamline to look into possible origins of the orthorhombic distortion that may arise due to oxygen pyramid tilting, only two samples had displayed a clear and significant orthorhombic distortion and neither was of a large enough size for powder neutron diffraction – this might be an area for future investigation when HRPD returns to service in late 2027. Large Ca-substituted phases with orthorhombic distortions had been obtained, however, so they were used as proxies in this investigation of the orthorhombic distortion. See chapter 4 for more on these phases.

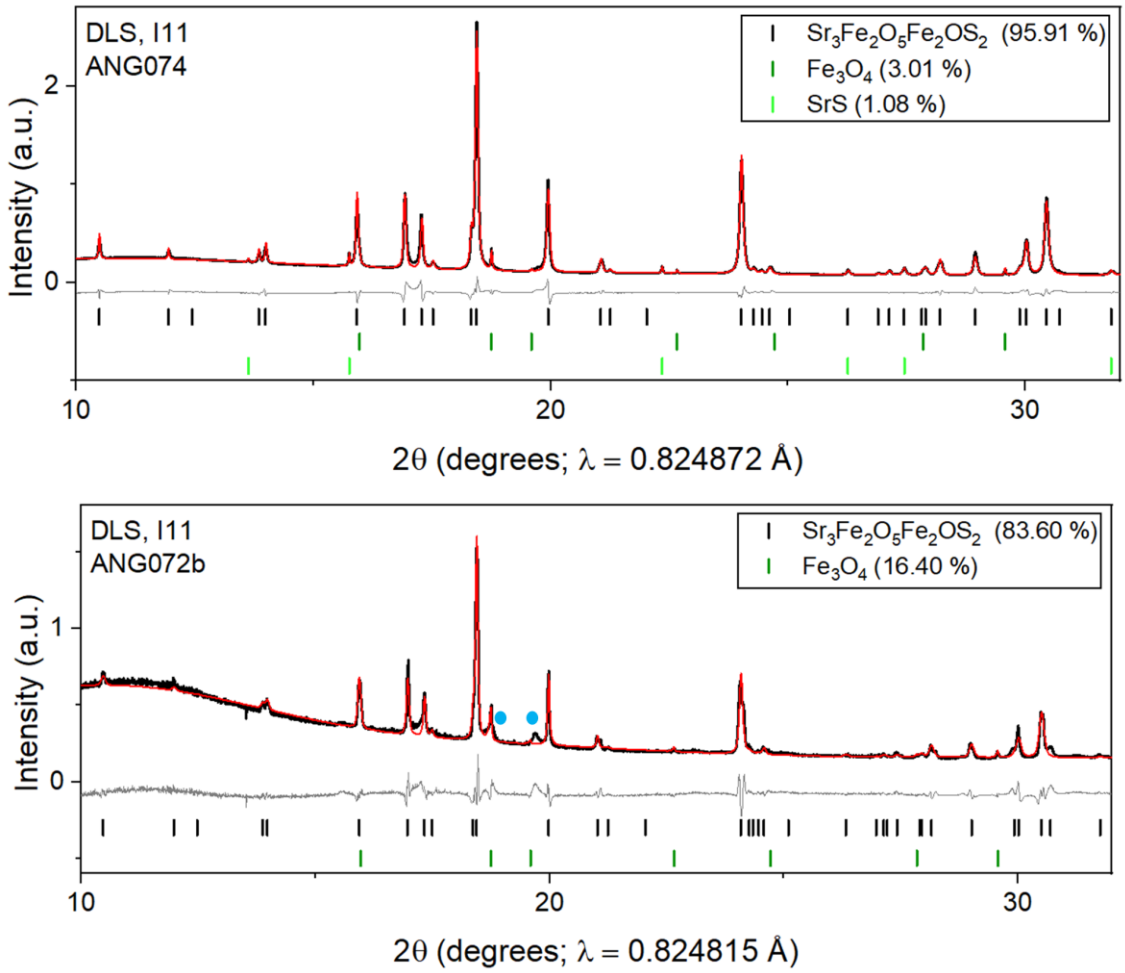


Figure 3.11. Rietveld Refinement plot of ANG074 (top, R_{wp} = 4.969%) and ANG072b (bottom, R_{wp} = 4.665%) SXRPD patterns measured on I11 at DLS showing the observed (black), calculated (red) and difference (grey) curves. Blue circles indicate diffuse peaks, with the first being over-compensated for by Fe_3O_4.

On HRPD, the diffraction pattern of ANG074 was as expected for a tetragonal sample with a magnetically ordered Fe1 lattice (see section 3.3.2 for more on the magnetic ordering). ANG072b, however, shows a clear orthorhombic distortion indicated by the clear splitting of the (200) and (020) peaks just below 2.0 Å in the bank 1 data (Figure 3.12).

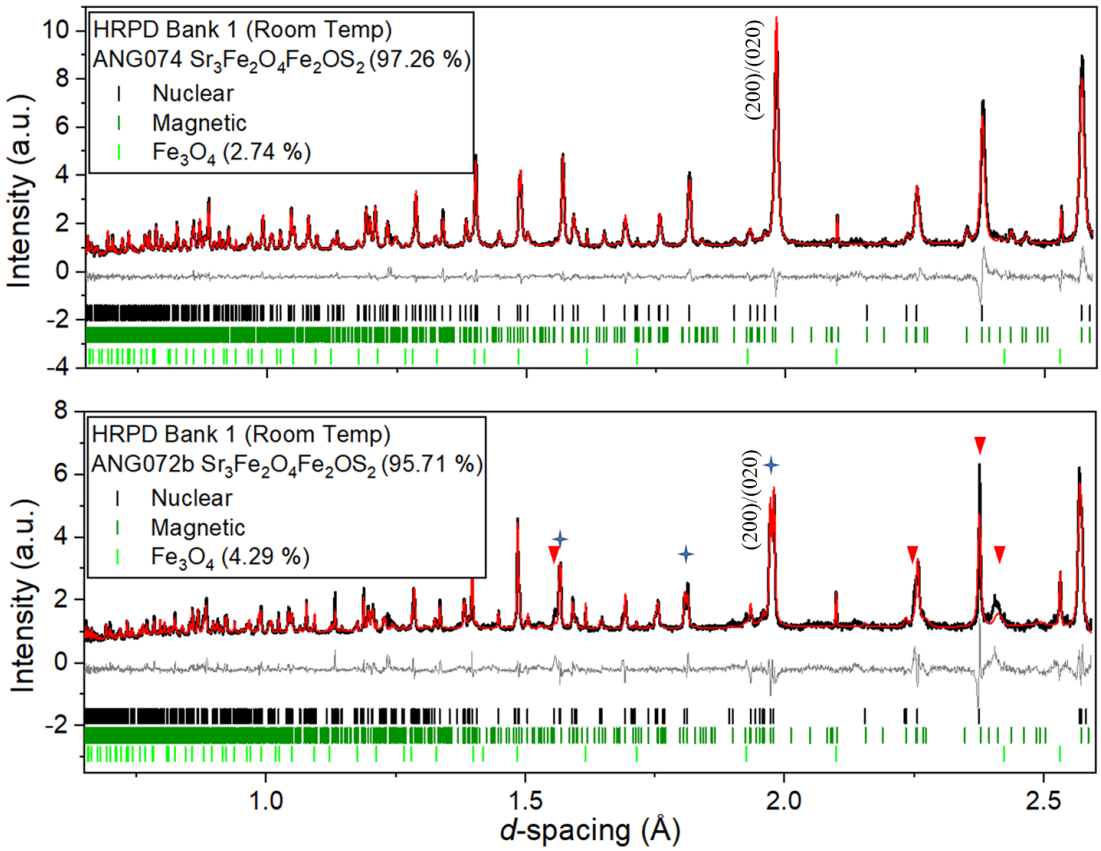


Figure 3.12. Rietveld refinement plot of ANG074 (top, R_{wp} = 4.969%) and ANG072b (bottom, R_{wp} = 4.665%) HRPD bank 1 patterns showing the observed (black), calculated (red) and difference (grey) curves. Blue stars indicate split peaks that are accounted for by the orthorhombic refinement and red triangles indicate discrepancies in the refinement.

While the refinement of ANG074 is very clean, there are several obvious discrepancies in the refinement of ANG072b. The first is the diffuse peak at d = 2.40 Å. In the refinement in Figure 3.12, this peak is fit partly by the magnetic structure, but there is obviously more intensity there that is unaccounted for. This is the same diffuse feature seen in the I11 XRPD pattern at 2θ = 18.75˚. There is also an intensity mismatch at d = 2.37 Å which corresponds to the (113) nuclear peak and there are several other small peaks at higher angles that are either not well represented or represented at all in the refinement which can be seen in the difference curve.

Distortion moment refinements have been carried out for the ANG072b room temperature data set using ISODISTORT in an effort to investigate whether or not inducing a twisting moment in the oxygen pyramids will improve the refinement and potentially be the source of the

orthorhombic distortion. Unfortunately, this did not improve the refinement so it is unlikely that FeO_5 pyramid rotation is the source of the orthorhombic distortion in ANG072b.

Variable temperature NPD patterns were collected on HRPD for both ANG072b and ANG074 from 150 K up to 873 K. No structural phase changes were observed for ANG074 for this temperature range, which is consistent with the variable temperature XRPD patterns collected on I11 at the DLS (see Appendix E for more). ANG072b, however, underwent a structural phase transition from an orthorhombic to a tetragonal symmetry between 498 K and 523 K which is consistent with the structural transition temperature observed in the XRPD patterns collected on I11 for ANG022b. The refinements for ANG074 (tetragonal at RT) and ANG072b (orthorhombic at RT) at 673 K (well above the orthorhombic to tetragonal transition) show very similar profiles (Figure 3.14) but have slightly different lattice parameters (Table 3.7). Additionally, the Fe2 occupancy of ANG072b (*occ*Fe2 = 0.86(1)) freely refined to be less than that of the tetragonal ANG074 (*occ*Fe2 = 1.000(5)) at T = 150 K when thermal displacement is less significant. This is also true at high temperatures after ANG072b had undergone the orthorhombic-to-tetragonal phase transition, but these parameters are highly correlated to the thermal displacement parameters and allowing the occupancies to refine does not significantly lower the R_{wp}. In fact, at high temperatures the Fe2 occupancy of ANG074 artificially refines to < 1 because of the correlation to the thermal displacement parameters. The other features that have slight discrepancies in the room-temperature data are also not resolved in the higher temperature data due to the higher background from the silica ampoule. This, along with the fact that the origin of the orthorhombic distortion has not been identified with the room-temperature high-resolution NPD, means that the high-temperature NPD has again shown the existence of an orthorhombic distortion that undergoes a transition to a tetragonal symmetry around 500 K, confirming what was shown in the SXRPD. The Fe2 occupancy also seems to be slightly different between the orthorhombic and tetragonal samples as SXRPD suggested. However, no further conclusions can be made at this time.

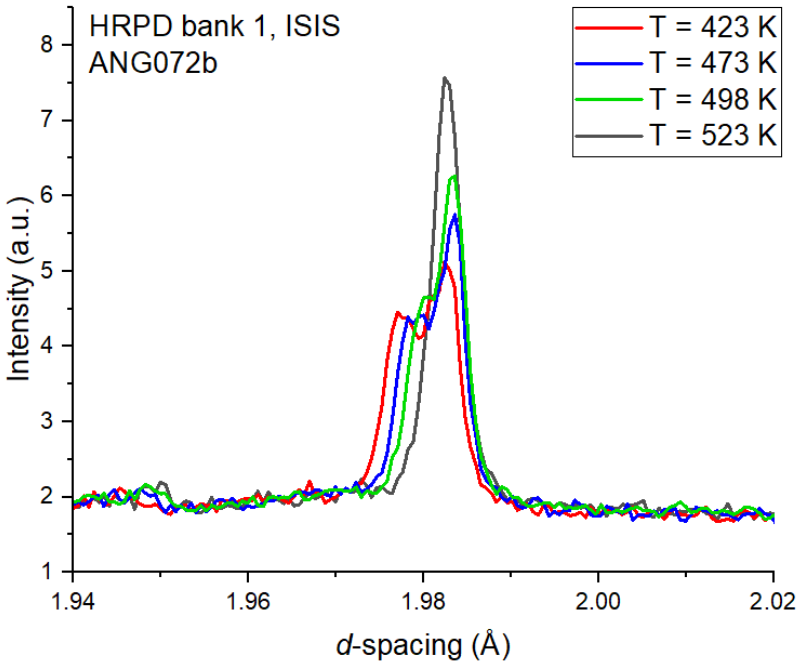


Figure 3.13. Neutron powder diffraction patterns of ANG072b collected on HRPD from T = 423 K to T = 523 K.

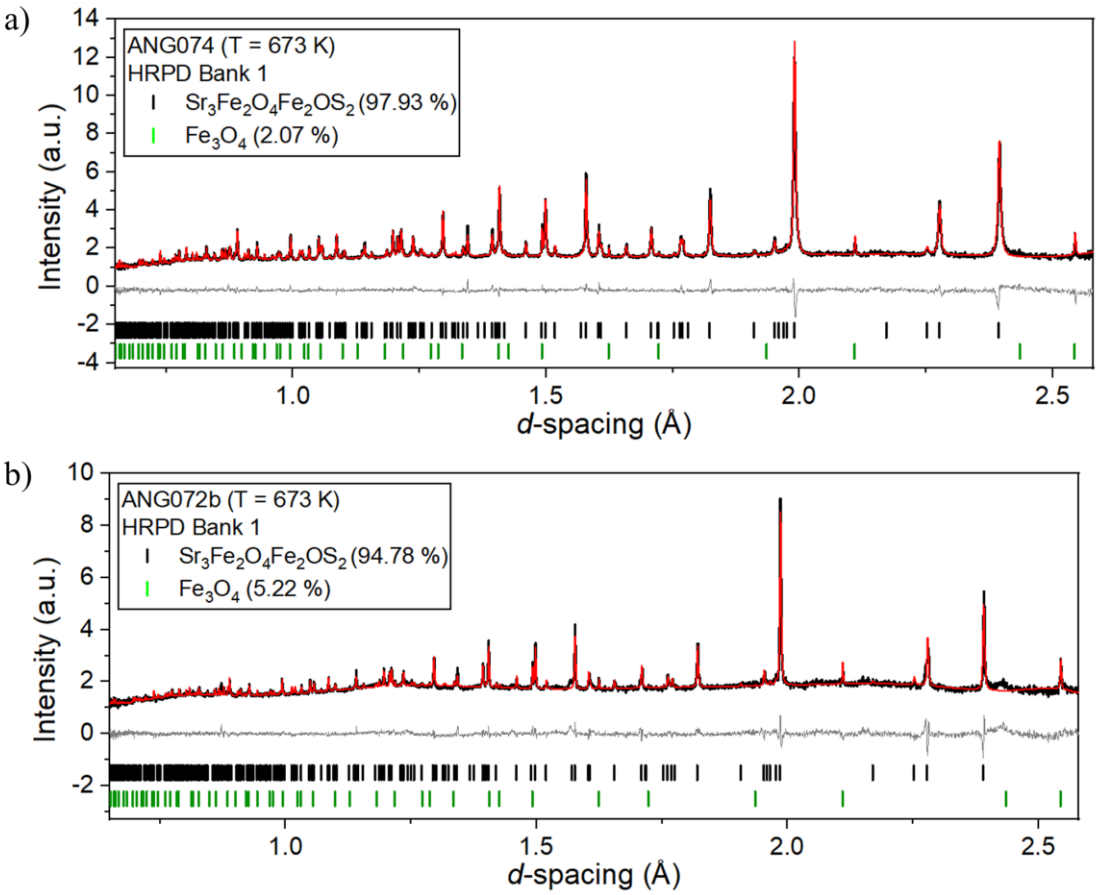


Figure 3.14. Refinements of HRPD Bank 1 NPD patterns at T = 673 K for ANG074 and ANG072b. This is after orthorhombic sample ANG072b has undergone the orthorhombic to tetragonal phase transition.

Table 3.7. Comparison of refined parameters for ANG074 and ANG072b at T = 673 K (after the orthorhombic to tetragonal phase transition for ANG072b).

	ANG074	ANG072b
Space group	*P*4/*mmm*	*P*4/*mmm*
R_{wp} (%)	4.138	4.703
a (Å)	3.98304(9)	3.9744(1)
c (Å)	13.6663(3)	13.6839(6)
V (Å^3)	216.81(1)	216.15(2)
*occ*Fe2[1]	0.933(6)	0.85(1)

[1]The occupancy of the Fe2 site was allowed to refine freely for both samples at high temperature and while this did result in occupancies < 1, the R_{wp} was not significantly lowered (~0.02 %) and the occupancy showed high correlation with the displacement parameters.

3.2.2.3. Electron Diffraction

3D electron diffraction patterns were collected and analysed by Sepideh Rahimi and Joke Hadermann at the University of Antwerp. Crystallites of several different samples were investigated with 3D ED in an effort to identify the space groups and look into any potential modulation. The tetragonal samples, ANG047b (see Fig 3.2) and ANG044a, did not show any modulation and best matched the Laue class 4/*mmm*. The orthorhombic samples ANG022b and ANG012 also best matched this Laue class, but the resolution of the 3D ED (0.36 Å) was insufficient to differentiate between tetragonal and orthorhombic symmetry given that the difference in the *a* and *b* lattice parameters is less than the resolution. However, there were some interesting features that were identified in some of the crystallites in these orthorhombic samples. In both ANG012 and ANG022b, there were modulations found in some of the crystallites (though not all of them). These modulations are evidenced by satellite reflections in the [h0l] plane (and [3kl] for some, see Figure 3.15d and e) as well as the [hk0.5] plane (Figure 3.16c and d). Modulation vectors for each crystal are displayed in Table 3.8.

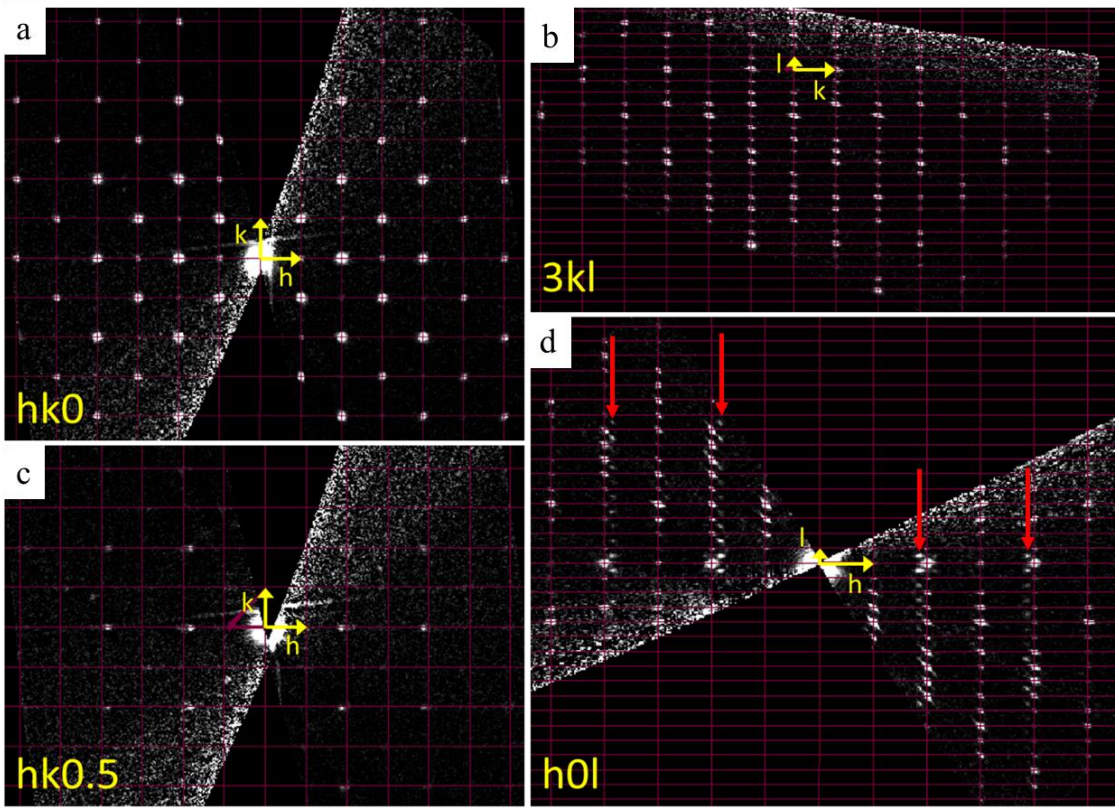


Figure 3.15. 3D ED patterns from the crystallite C81 of sample ANG022b. Note that [hk0.5] would not show any reflections if the material was not modulated. Satellite reflections in [h0l] are indicated by red arrows.

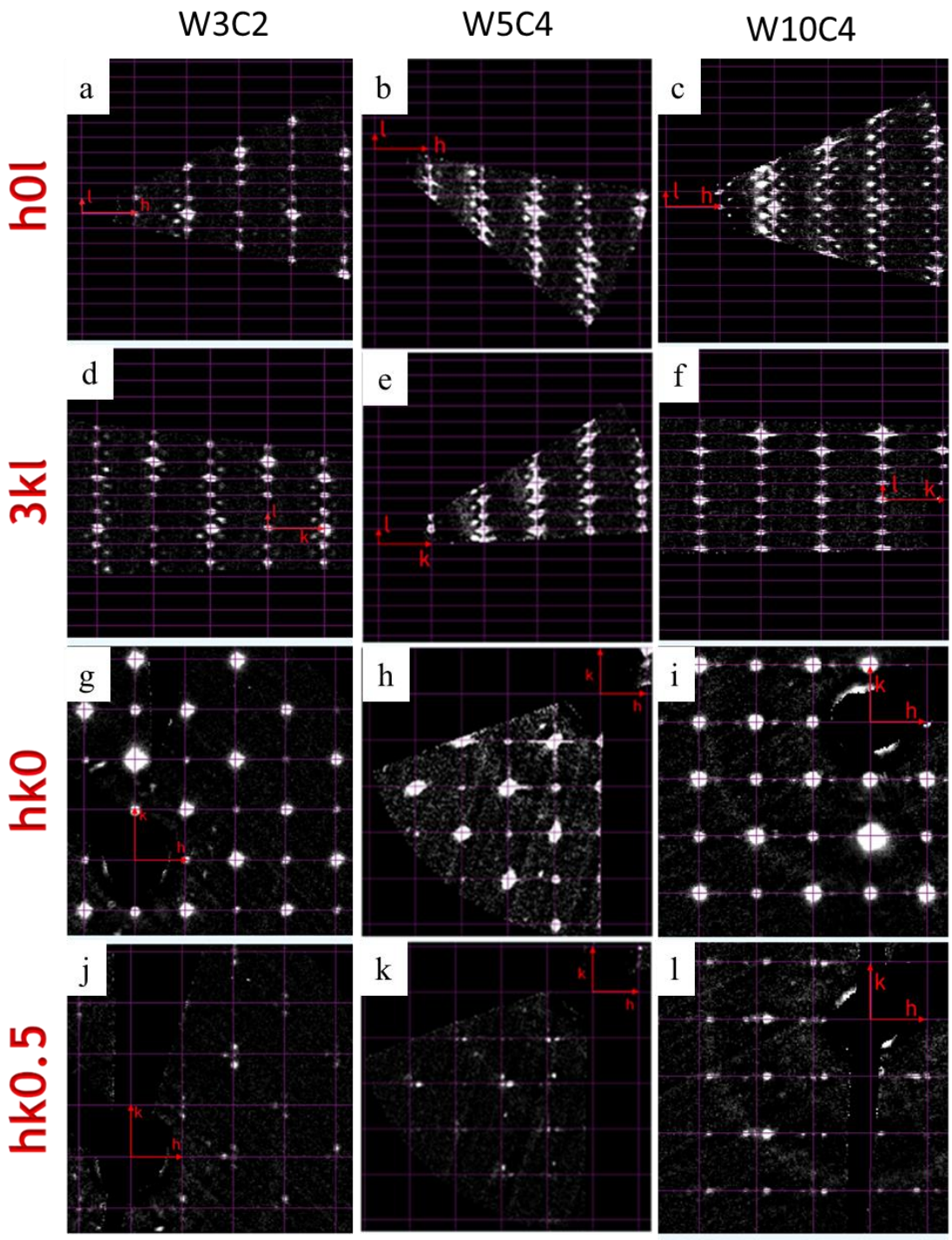


Figure 3.16. 3D ED patterns of crystallites W3C2, W5C4, and W10C4 of sample ANG012 (orthorhombic). Note that all have reflections in [hk0.5] which would not be present if there was no modulation. W3C2 and W5C4 show satellite reflections in both [h0l] and [3kl] which indicates possible twinning whereas W10C4 only has satellite reflections in [h0l] and not [3kl].

Table 3.8. Modulation vectors for crystallites in samples ANG012 and ANG022b. Starred crystallites show evidence of twinning.

ANG012 – W3C2*	ANG012 – W5C4*	ANG012 – W10C4	ANG022b – C81
$q = 0.2a^* + 0.5c^*$	$q = 0.2a^* + 0.5c^*$	$q = 0.18a^* + 0.5c^*$	$q = 0.15a^* + 0.5c^*$

While some crystallites in each sample show evidence of twinning and others do not, it is possible that the phases are indeed two-phase, with a tetragonal phase that is not modulated and a modulated orthorhombic phase. However, this cannot be confirmed given that the crystal systems cannot be determined due to the resolution being less than the proposed difference in lattice parameters.

3.2.2.4. Transmission electron microscopy

HAADF-STEM images were collected by Sepideh Rahimi and Joke Hadermann at the University of Antwerp. Aliquots of tetragonal flux-grown samples ANG044a and ANG047b were investigated via HAADF-STEM which revealed several structural anomalies at the atomic level within individual crystallites. The first of the anomalies can be attributed to 'antiphase boundaries' wherein two adjacent unit cells are offset by ½*c* where there is essentially a phase shift of π in the periodic arrangement of the blocks on either side of the boundary (Figure 3.17d). In different regions of a crystallite, these boundaries can be arranged in a regular way (Figure 3.17f) or with much more variation in the separation of the boundaries (as in 3.17d). These boundaries can also be observed with the crystal projected along the [001] direction, with dark lines parallel to (100) or (010) or even both directions corresponding to these types of boundaries (Figure 3.18). In addition to the antiphase boundaries, regions with an extended perovskite-type Fe1' layer are also observed which can both persist over long regions or form where the antiphase boundaries do not propagate over long distances (see Figure 3.17e and the circled 4 in Figure 3.17b). As Figure 3.17b shows, these anomalous regions exist along with a region ordered as expected and occur within the crystallite within only a few nanometres of each other.

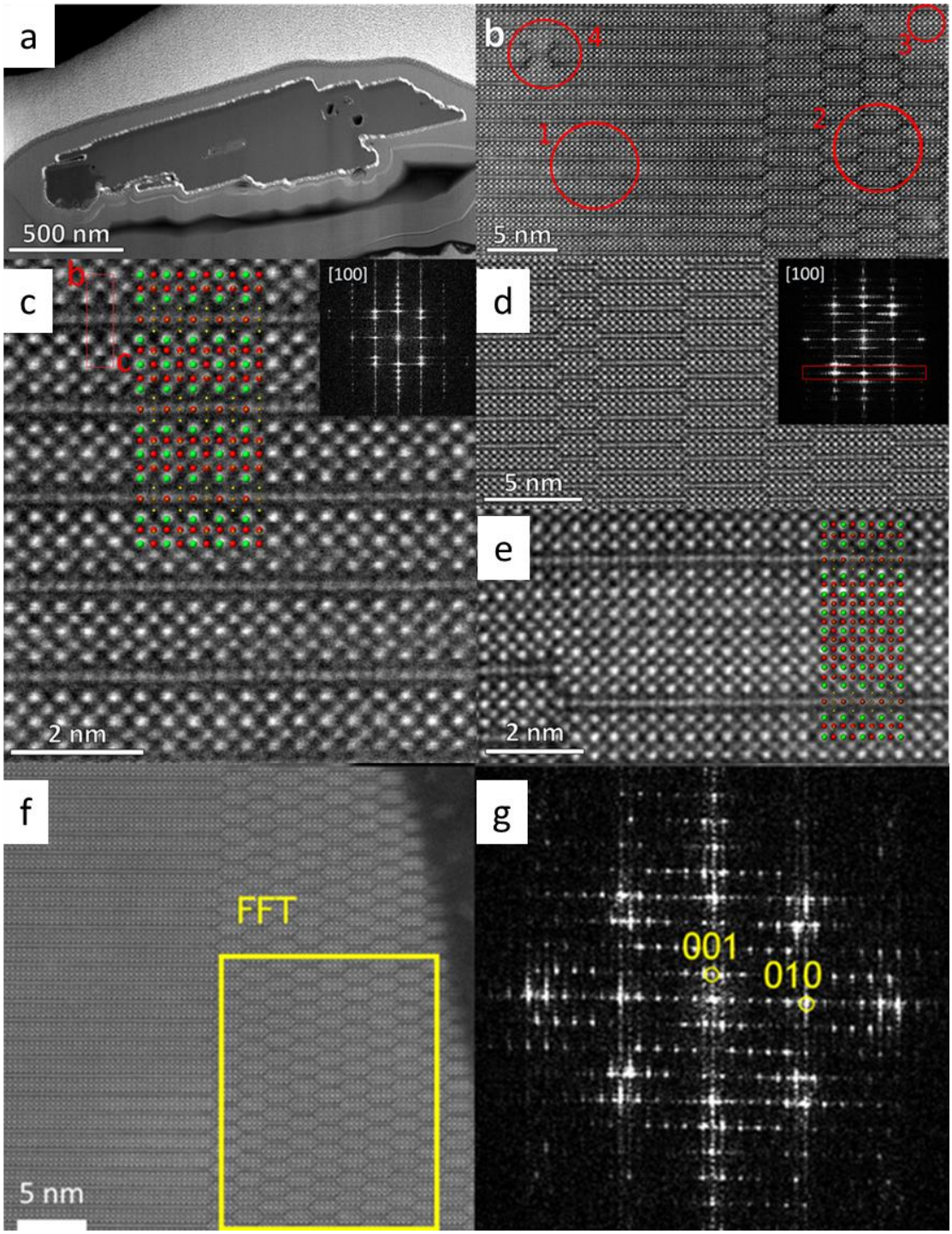


Figure 3.17. a) Low and b) high magnification of the cross-section of an ANG044a crystallite oriented along the [100] direction. c-e) are different areas in the crystallite indicated by the numbers 1-3 in (b) respectively. Preparation of the sample for these measurements, will be discussed in Sepideh Rahimi's thesis.

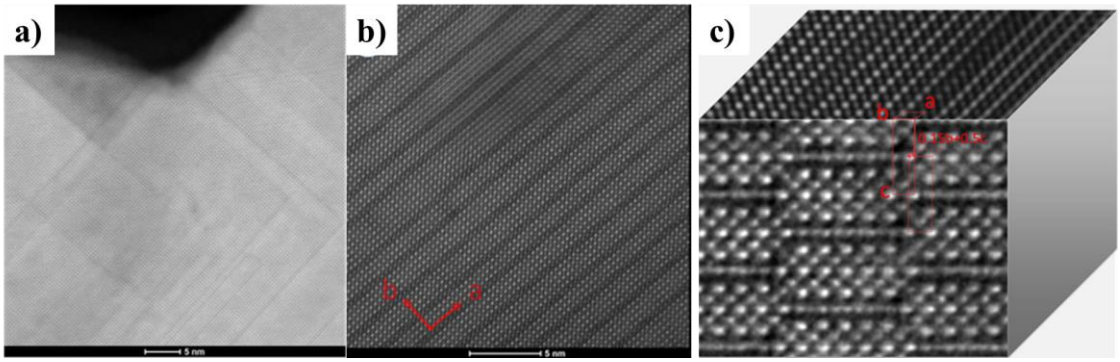


Figure 3.18. ANG044a crystallites oriented along the [001] direction showing a) dark lines parallel to (100) and (010), b) dark lines parallel to only parallel to (100), and c) a construction of how the antiphase boundaries correspond to the dark lines.

When one of the crystallites was examined with HAADF-STEM and EDX in conjunction with 3D ED, the overall suggested unit cell in Figure 3.19 was obtained in the refinement against the 3D ED data and gave good agreement with this electron diffraction data. This unit cell places a small amount of iron in the space that would be between Fe1 sites along the antiphase boundary, but when an iron site is placed there in the unit cell for the bulk refinements, the occupancy freely refines to zero. Other experiments such as EELS are underway in an effort to determine if this site is indeed occupied by iron, but the results are so far indeterminate.

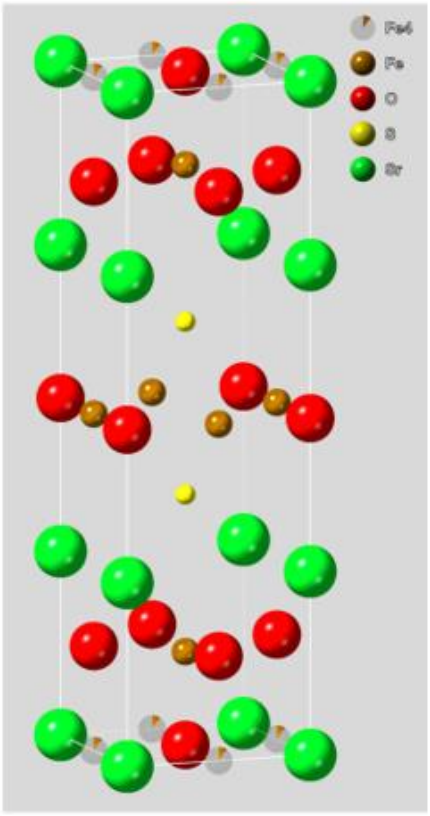


Figure 3.19. Refined unit cell of ANG044a crystallite C9.

The anomalies observed in individual crystallites open a large realm of possibility to explain sample-to-sample variations of $Sr_3Fe_2O_5Fe_2OS_2$. The extended perovskite blocks contain a lower molar ratio of iron to the other elements and free up some iron which could be part of the source for the iron in the magnetite impurity or the extra iron site that may exist at the antiphase boundaries. The curving of the layers that can be observed around some of these boundaries especially in more disordered regions (Figure 3.20) could be a source of an overall incommensurate modulation that gives rise to the diffuse peaks in the XRPD and NPD patterns. The antiphase boundaries often propagate in one of the basal directions but not the other and this could potentially be the source of an overall orthorhombic distortion as well. While no definitive conclusion can yet be made concerning the variations in $Sr_3Fe_2O_5Fe_2OS_2$ samples, it is clear that there are several different sources of variation not just from sample to sample but from crystallite to crystallite within the same sample.

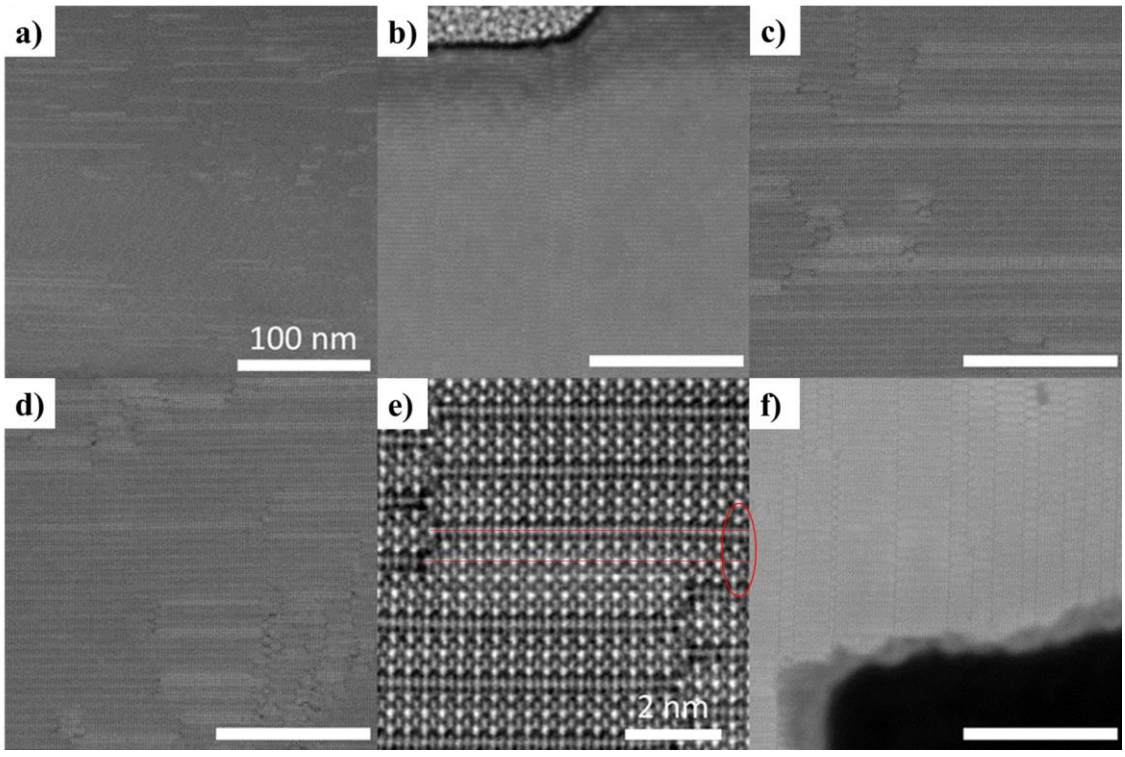


Figure 3.20. Several views of an ANG047b crystallite showing antiphase boundaries, extended perovskite layers (lighter areas in a,c,d and shown in e) and antiphase boundaries (b,f and shown in e). Curving of the Fe2 layer can be seen in (e) as well as deviation from the straight red lines is circled in red. All scale bars are 20 nm unless otherwise stated.

The above images were obtained from flux-grown tetragonal samples which did not show evidence of the diffuse peaks shown in Figure 3.3. HAADF-STEM images were also obtained

for a crystallite of sample ANG022b, which is a ceramically synthesized long annealed sample that showed an orthorhombic distortion in the XRPD pattern. This particular crystallite did not show any of the antiphase boundaries or extended perovskite-type layers that the flux-grown samples showed. However, there was evidence of vacancy order in the Fe2 layer that was observed (Figure 3.21b), but this order does not appear to be consistent across the sample (Figure 3.21c). The FFT of the region with the ordered vacancies does contain satellite peaks that resemble those seen in the electron diffraction (Figure 3.15d for example) and this suggests that that modulation may arise from vacancy order.

This sample was synthesized in the same way as the larger sample measured on HRPD, ANG072b (Figure 3.12), and this complex behaviour within individual crystallites could account for some of the discrepancies in the NPD refinement at room temperature.

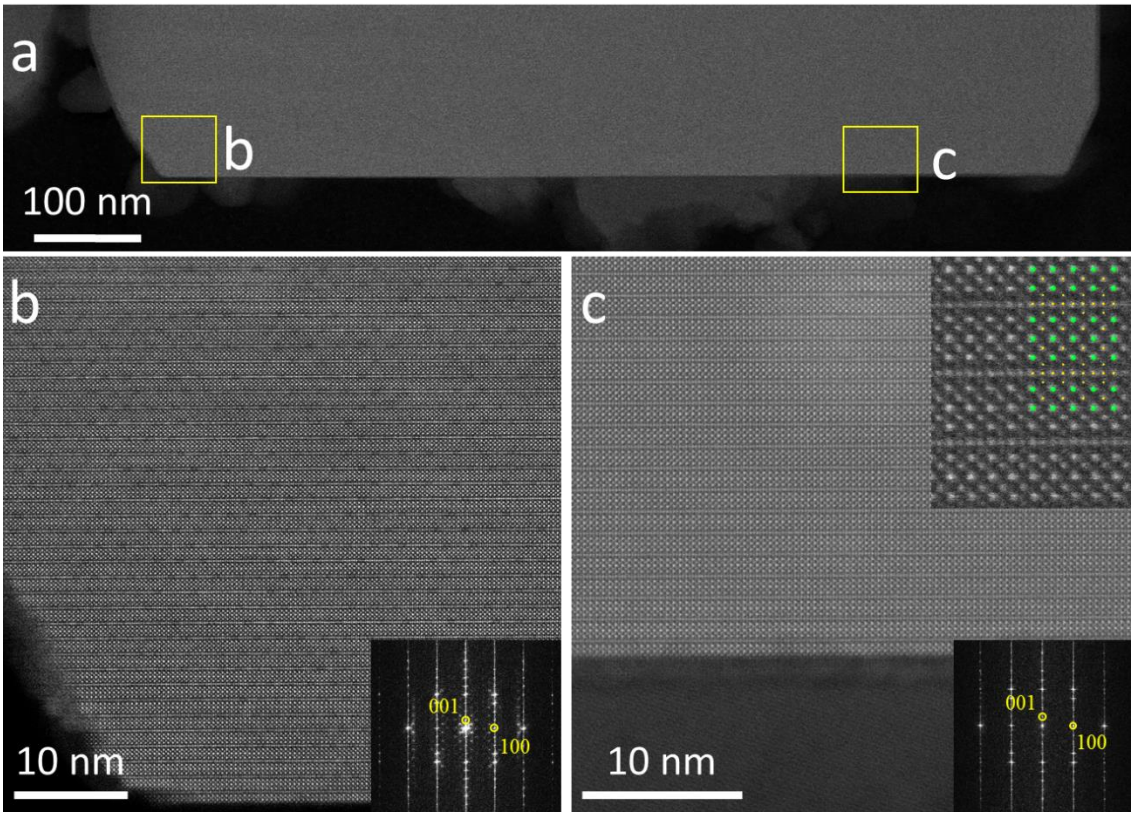


Figure 3.21. HR-STEM images of ANG022b showing a) an overview of the edge oriented to the [010] direction, b) the region with vacancy order, and c) a region without vacancy order.

It is not possible to distinguish between a tetragonal cell and an orthorhombic cell by using TEM in this case because the proposed differences in the *a* and *b* lattice parameters from the bulk

powder refinements are less than the resolution (0.8 Å). However, proposed future investigations by 4D-STEM tomography may resolve this since the [100] and [010] would show the same modulation in the case of a tetragonal cell. What is clear from this investigation is that while it remains unclear where the orthorhombic distortion originates since the orthorhombic distortion cannot be resolved with TEM, it is clear that there are modulations which would generate an orthorhombic cell when modulated along *a* and not *b*. A more in-depth investigation into the HAADF-STEM images and 3D ED as well as other cutting-edge microscopy experiments are to come in Sepideh Rahimi's PhD thesis (University of Antwerp).

3.3. Magnetic Characterization

3.3.1. Magnetometry

The first investigation into the magnetic behaviour of $Sr_3Fe_2O_5Fe_2OS_2$ was carried out using SQUID magnetometry at both low and high temperatures. One distinct transition can be observed in the ZFC and FC magnetization curves at low temperatures around 120 K. Unfortunately, this transition originates from the Fe_3O_4 impurity, with the 120 K transition occurring at the Verwey transition temperature. With this in mind, it seems as though the signal has been saturated by the magnetite impurity, and any magnetic ordering transition in the magnetization curves from the $Sr_3Fe_2O_5Fe_2OS_2$ phase cannot be detected. This is not unusual, however, as it is common for long-range magnetic ordering transitions to be unclear in layered materials. In addition to this, the *M vs H* isotherm at 5 K shows some displacement from the origin, indicating some glassy or frustrated behaviour at low temperatures.

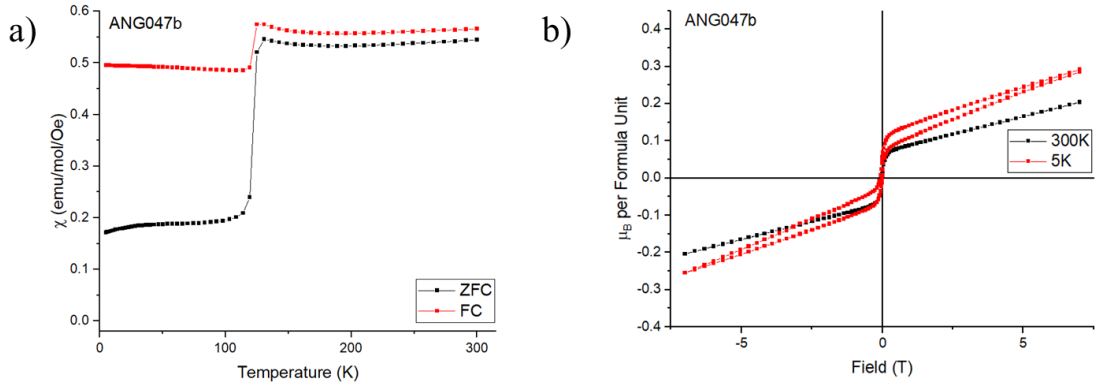


Figure 3.22. The a) magnetization curves alongside the b) *M vs H* isotherms at 300 K and 5 K of ANG047b.

In addition to the low-temperature magnetometry, high temperature magnetometry data was collected for sample ANG012 (Figure 3.23). There was a high-temperature transition observed for this sample at around 860 K, but this corresponds to the Curie temperature of Fe_3O_4 (T_C = 850 K) [3], meaning that no conclusions can be made from the high-temperature magnetization curves that pertain to $Sr_3Fe_2O_5Fe_2OS_2$.

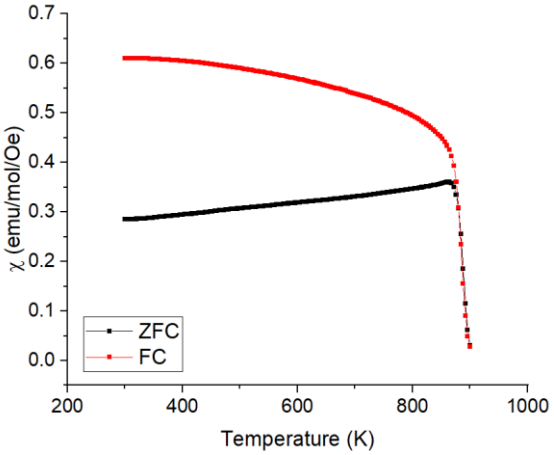


Figure 3.23. High temperature susceptibility curves for ANG012 from 300 to 900 K.

There is slight sample-to-sample variation in the magnetometry data, but the variation largely applies only to the magnitude of the transition changes due to different concentrations of magnetite in each sample and all samples show the same transition. ANG044a was the only sample that did not show bulk ferromagnetic behaviour when exposed to a 1 cm^3 Nd-Fe-B magnet and had no significant Fe_3O_4 (311) peak in the SXRPD data, but even then, the Verwey transition was still observed, though smaller, and the saturation of the isotherm curves was also much smaller and the deviation from the origin more obvious because of that.

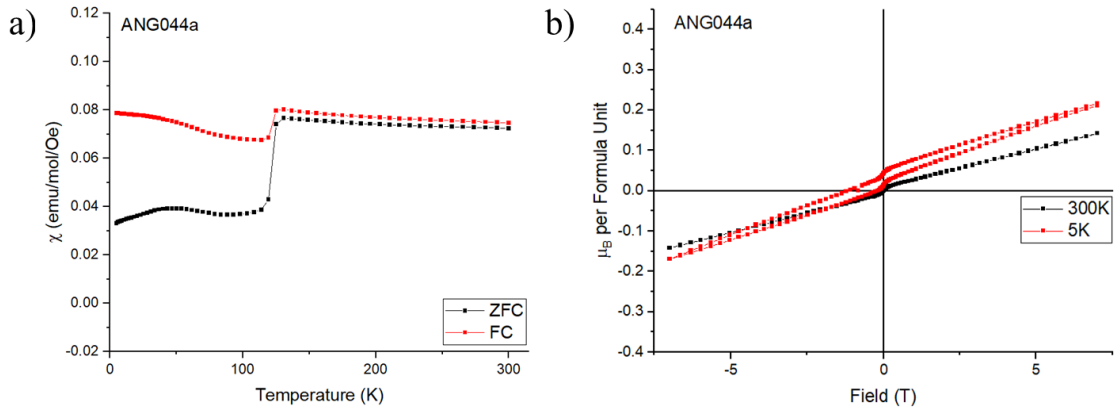


Figure 3.24. Magnetization curves (a) and *M vs H* isotherms (b) of ANG044a.

However, given the presence of the magnetite impurity in all samples and that the impurity saturates the SQUID signal at just 100 Oe when it is of a small enough concentration that it was not significantly detected in the SXRPD data, we cannot make any conclusions about the magnetism of $Sr_3Fe_2O_5Fe_2OS_2$ from the magnetometry. One of the disadvantages of magnetometry is that it measures how magnetic a bulk sample it and can be dominated by small amounts of highly magnetic impurities.

3.3.2. Room temperature NPD

Room-temperature neutron powder diffraction was collected for the tetragonal sample ANG022 on D1B at the ILL in the interest of investigating whether or not the phase $Sr_3Fe_2O_5Fe_2OS_2$ exhibits magnetic ordering, and indeed it does. At room-temperature, there are several extra peaks that arise and are not present in the X-ray powder diffraction patterns and they do not correspond to nuclear reflections of the cell. This indicates magnetic ordering that is not ferromagnetic. Since this is consistent with what is expected from literature, magnetic modes which result in antiferromagnetic order within an individual iron layer were refined first until the magnetic model was deduced. All of the magnetic peaks can be fit to a $\sqrt{2}a \times \sqrt{2}a \times 2c$ magnetic supercell, and only the Fe1 sites are ordered at room temperature. Within individual Fe1 layers, the Fe1 sites order antiferromagnetically within the basal plane along the Fe-O-Fe superexchanges in all directions with a moment of 3.58(4) μ_B. This is similar to related phases that contain the same layer (chapter 1.3.1). However, when it comes to the relationship between subsequent Fe1 layers, there are two different models that may describe the magnetism of the

phase which are indistinguishable in the powder diffraction data (see Figure 3.25c for refinement overlays). This is the first time this phenomenon has been observed, as primitive phases like $Pb_4Fe_3O_8X$ [4] and $YBa_2Fe_3O_8$ [5] contain a similar layer type (just extended to include an FeO_6 octahedron between the FeO_5 square pyramids) but subsequent layers are ordered strictly antiferromagnetically. The two different models describing the magnetism of $Sr_3Fe_2O_5Fe_2OS_2$ will be referred to as the two-structure model and the single-phase twisting model. As with the use of X-ray powder diffraction techniques for *ab-initio* nuclear structure determination, it is difficult to unambiguously confirm one of these magnetic structures over another. However, techniques like single-crystal neutron diffraction would resolve the ambiguity though the difficulty then lies in growing said crystals.

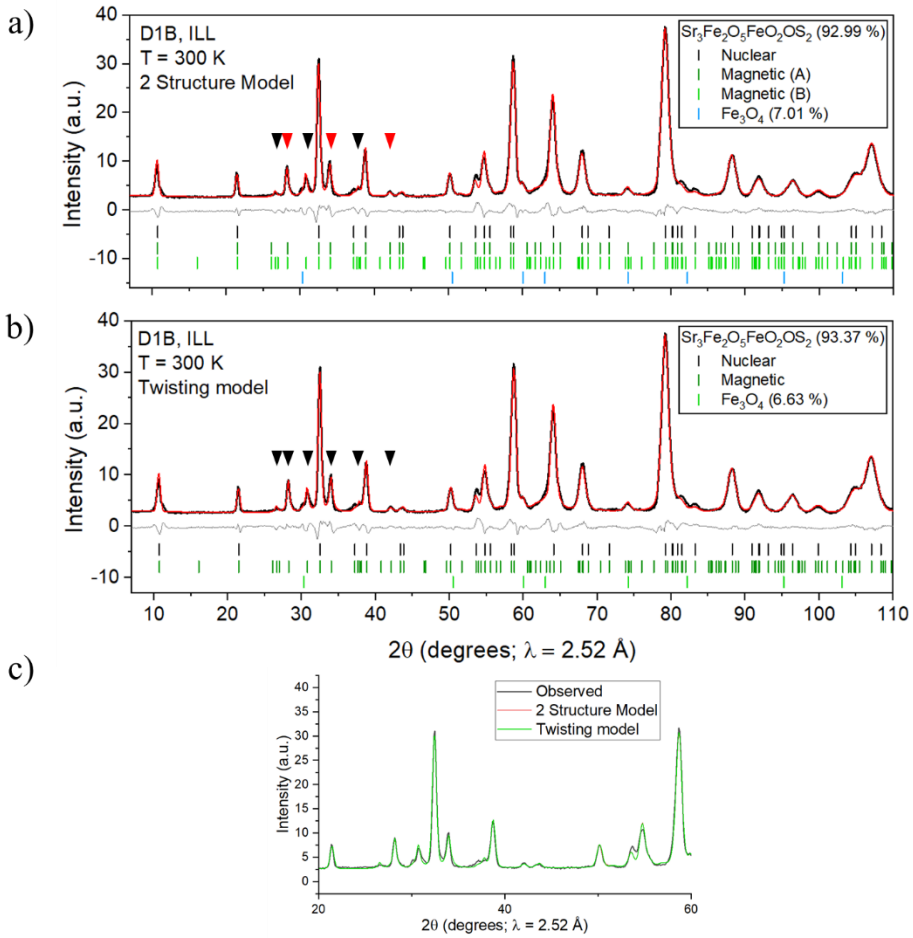


Figure 3.25. Rietveld refinements of a) the two-structure magnetic model and b) the single-phase twisting magnetic model of $Sr_3Fe_2O_5$ Fe_2OS_2 alongside c) an overlay of the two refinements showing no significant difference. Displayed are the observed (black), calculated (red), and difference (grey) curves. Black triangles indicate magnetic reflections in (b) whereas in (a), the black triangles pertain to the reflections from structure A and red triangles pertain to the those of structure B in Figure 3.26.

The first magnetic model that may describe the magnetic ordering in $Sr_3Fe_2o_5Fe_2OS_2$ exists on the assumption that two distinct but related magnetic phases exist simultaneously within the bulk sample and each of these structures corresponds to distinct magnetic reflections (see Figure 3.25a). Bulk samples containing two magnetic phases have been reported before in the case of $Sr_2CoO_2Cu_2Se_2$ [6] so it is a plausible model. The first of these structures is obtained by activating the mM5- E(a) mode with the propagation vector **k** = (½, ½, 0) on a magnetic supercell with a $\sqrt{2}a \times \sqrt{2}a \times c$ expansion and the second is obtained by activating the mA5- E(a) mode with the propagation vector **k** = (½,½,½) on a magnetic supercell with a $\sqrt{2}a \times \sqrt{2}a \times 2c$ expansion. Alternative methods of refinement could activate various combinations of the individual E(a) and E(b) modes of each magnetic mode, which leads to alternative structures wherein all of the magnetic moments are rotated about the *c*-axis. This is to be expected though, as in primitive tetragonal structures, spin direction can only be defined as to its angle from the unique axis [7].

The two magnetic structures obtained in this model are very similar. The difference between the structures stems from the relationship between subsequent Fe1 layers. In structure A (Figure 3.26), the subsequent layers stack directly atop one another, with the labelled Fe1a atom mapping onto the Fe1a' directly above it in the next layer. In structure B, subsequent layers are stacked with a ½ unit cell translation along either *a* or *b* (i.e., Fe1a maps onto Fe1b' which is ½ a unit cell translation from Fe1a'). Alternatively, the relationship between subsequent layers could instead be viewed as being related by a mirror plane to the Fe1 layer below it, with Fe1a and Fe1c mapping onto Fe1c' and Fe1a' respectively.

With the similarity of the models in mind and the hypothesis that they may exist simultaneously within a sample, the magnetic moments in each of these models were fixed to be equal and the ratio of the individual phases to which each magnetic model was linked were allowed to refine relative to each other. This is especially interesting to consider in light of the structural anomalies like the antiphase boundaries or extended perovskite-type layers revealed by the HAADF-STEM imaging, as it is not out of the realm of possibilities that due to these boundaries within individual crystallites, there are several disruptions in the ordering pattern between individual Fe1 layers

which might lead to the propagation of both structures so that they exist simultaneously not only within a bulk sample, but even individual crystallites.

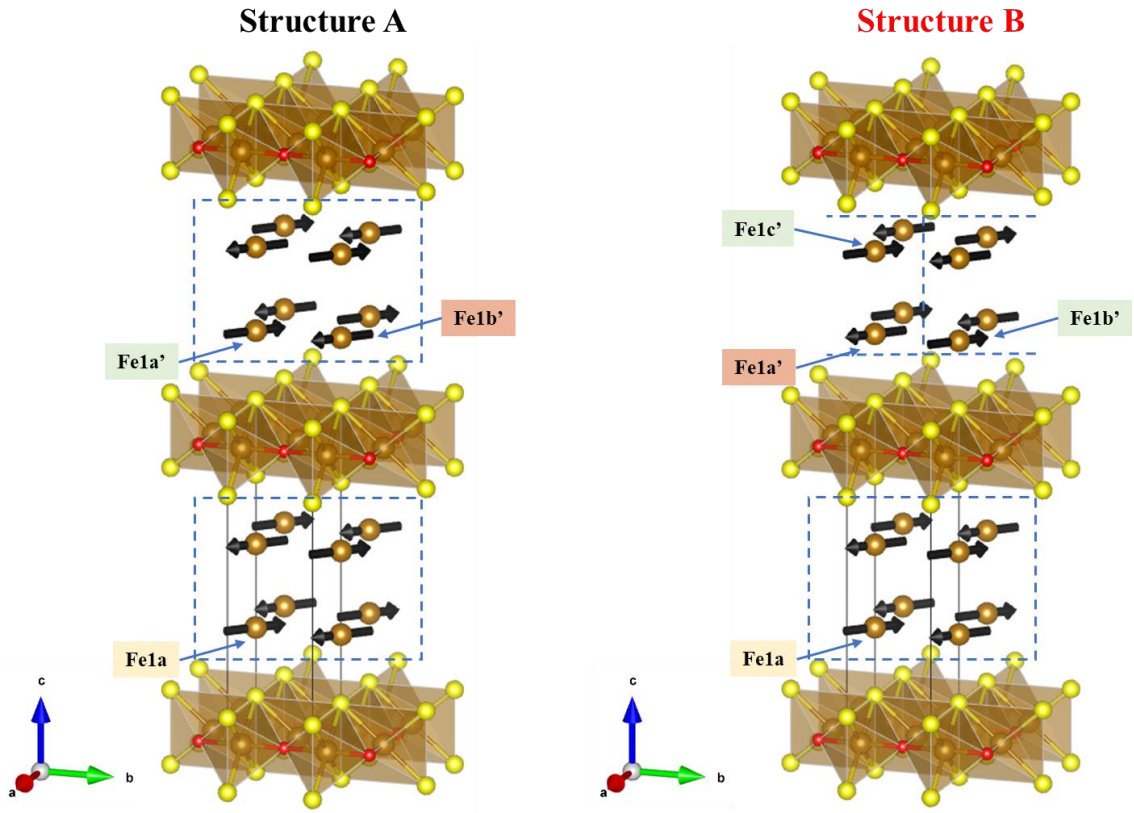


Figure 3.26. Two-structure magnetic model of $Sr_3Fe_2O_5Fe_2OS_2$ shown on a $2a \times 2b \times 2c$ nuclear cell.

Table 3.9. Magnetic reflections attributed to structure A vs structure B in the two-structure model and the single-phase twisting model

Structure A		Structure B		Twisting model			
(110)	d = 5.1653 Å	(110)	d = 5.4738 Å	(110)	d = 5.4738 Å	(210)	d = 5.1653 Å
(210)	d = 4.3072 Å	(310)	d = 4.7499 Å	(310)	d = 4.7499 Å	(410)	d = 4.3072 Å
(310)	d = 3.5078 Å	(510)	d = 3.8861 Å	(510)	d = 3.8861 Å	(610)	d = 3.5078 Å

A linear combination of the two magnetic structures above would result in alternating Fe1 double-layers, one with large magnetic moments and one with moments very close to zero. This would not be expected – one would expect all the moments localised on Fe1 ions to have the same magnitude. However, if the two structures are set to be orthogonal to each other, with the moments of structure A being along the nuclear *a* axis and those of structure B being along the nuclear *b* axis and then the moments allowed to individually refine instead of the ratio of the two structures, a linear combination would instead result in a single 'twisting' model with a 'twisting angle' of +/- 36.7(7)˚ from the *a* axis. This model can be achieved by refining the mM5- E(a)

equal to the mM5- E(b) and mA5- E(b) equal and opposite to the mA5- E(a) modes simultaneously in the same magnetic structure refinement and as Figure 3.25c shows, the resulting refinement is indistinguishable from the two-structure model described above. This refinement yields the structure displayed in Figure 3.27. Again, alternative methods of refinement with different combinations of the E(a) and E(b) modes yield identical refinements with different structures related by a rotation of all the moments about the *c*-axis. This again arises from the principle that in primitive tetragonal structures, spin direction can only be defined as to its angle from the unique axis [7]. This means that while the axis of the twisting angle is arbitrary, the angle itself is real in that it relates the moments in subsequent layers.

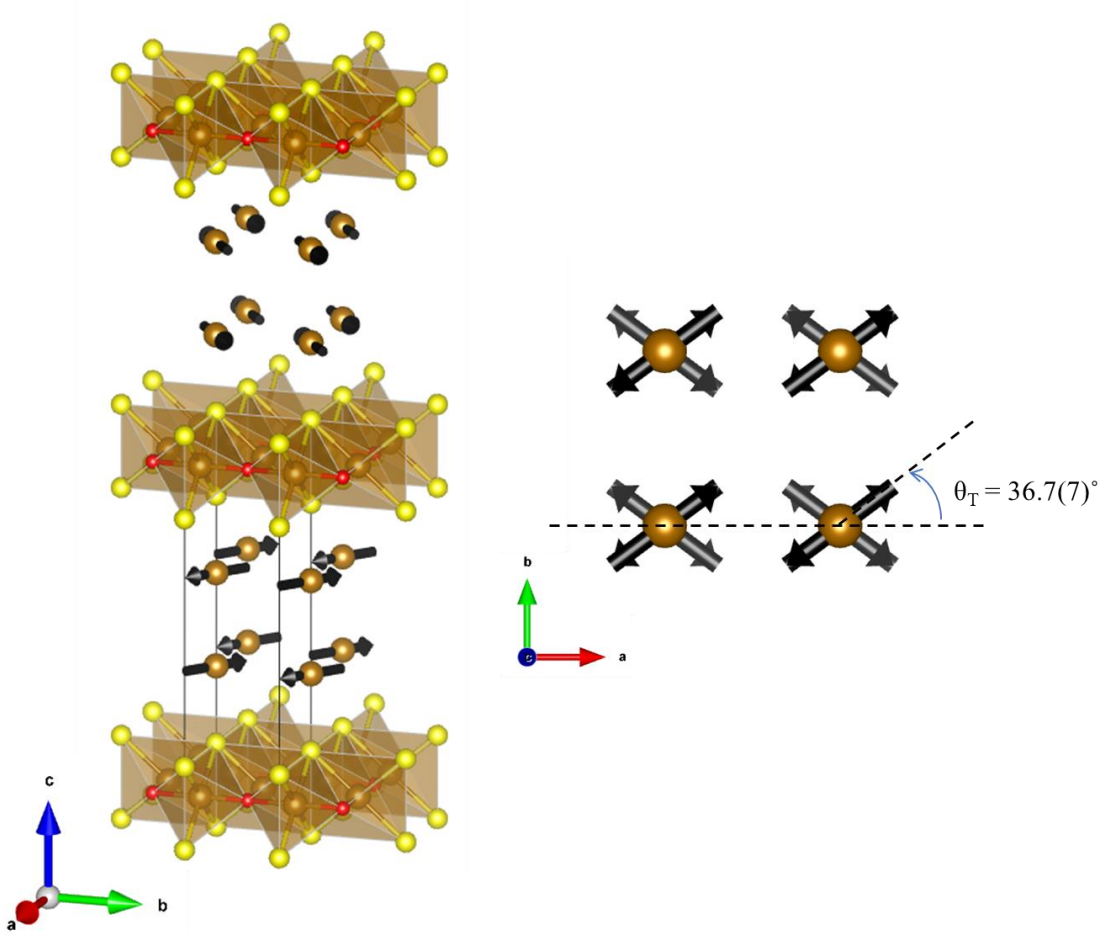


Figure 3.27. Single-phase twisting magnetic structure of $Sr_3Fe_2O_5Fe_2OS_2$ shown on a $2a \times 2b \times 2c$ nuclear cell.

Table 3.10. Comparison of the two-structure magnetic model and the single-phase twisting magnetic models of $Sr_3Fe_2O_5Fe_2OS_2$. The ratio parameter is obtained by taking the ratio of structure A to B in the two-structure model and by taking the ratio of the moments along *a* and *b* in the twisting model.

	Two-structure	Twisting
R_{wp} (%)	7.016	7.008
Moment (μ_B)	3.58(6)	3.58(4)

Given that the goodness of fit parameters and magnetic moments are so similar for the two magnetic models, the relationship between subsequent Fe1 layers that leads to the 2-structure model or the single-phase twisting model describing the magnetic structure of $Sr_3Fe_2O_5Fe_2OS_2$ cannot be resolved from just the room-temperature, unpolarized neutron powder diffraction patterns. However, the two-structure model does have the advantage of only requiring a single magnetic mode to be activated at the continuous, second-order magnetic ordering transition which is in line with the expectations of Landau theory.

Additionally, a further phenomenon was observed in the room-temperature neutron powder diffraction patterns collected for ANG072b, ANG074, and ANG075 on HRPD which is that there is sample-dependence in the magnetic model as it relates to the twisting angle/ratio of structures. As Figure 3.28 shows, sample ANG074 only exhibited the (210) and (410) reflections (as indexed by the twisting model) whereas ANG072b only exhibited the (310) and (510) reflections and ANG075b exhibited all four reflections like ANG022, the sample which has been discussed thus far in this section. This means that ANG074 ordered as solely structure A in the two-structure model, ANG072b ordered as solely structure B in the two-structure model, and ANG075b ordered as both (or the single-phase twisting model). Of course, given the poor S/N in bank 3 on HRPD, it is possible that the absent reflections for ANG074 and ANG072b are present but below the S/N. However, this phenomenon makes it clear that the ratio of structure A to structure B (or the twisting angle) is sample-dependent, and further measurements of these samples on a diffractometer that has better S/N at low angles would clarify if there is truly no intensity on the 'absent' peaks of ANG072b and ANG074 or if they are obscured by the high noise in HRPD bank 3.

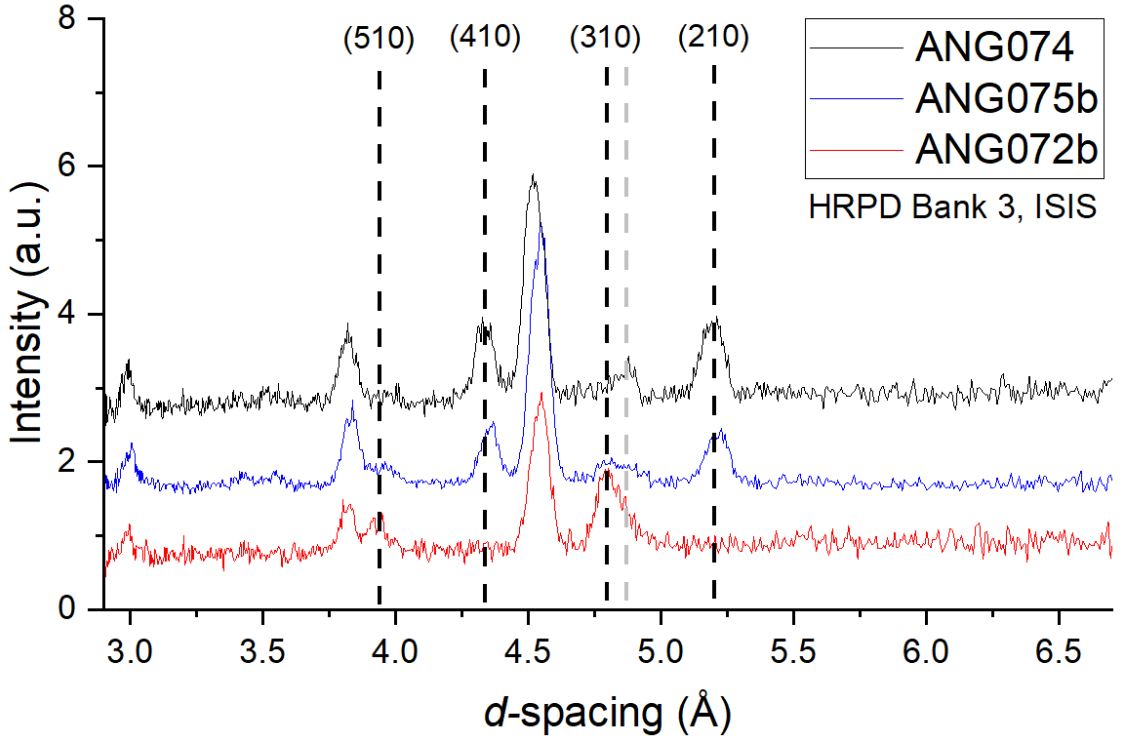


Figure 3.28. NPD patterns collected on HRPD bank 3 for ANG074, ANG072b, and ANG074 with reflections based on the single-phase twisting model labelled. The grey dashed line corresponds to the Fe_3O_4 (111) reflection.

3.3.3. Low variable temperature NPD

Variable temperature NPD data was collected on D1B at the ILL on sample ANG022 which contains both sets of magnetic peaks relating to the Fe1 layers in an effort to determine how the magnetic model of $Sr_3Fe_2O_5Fe_2OS_2$ changes upon cooling. Looking at the contour plot in Figure 3.29, two things are immediately evident. Firstly, there is an onset of new magnetic peaks around 115 K indicating a magnetic transition. This is around the same temperature as the Verwey transition that is seen in the magnetometry, but in this case, this is the onset of magnetic ordering in the Fe2 layer. Given that this is the temperature at which the Verwey transition happened for the magnetite impurity, this helps to explain why there were no other magnetic transitions observed in the magnetometry data (although, as noted above, magnetic ordering transitions in these low-dimensional materials are sometimes not very obvious by magnetometry). In addition to this, there is also a magnetic peak at $2\theta = 30.8^\circ$ (d = 4.77 Å) that grows as the temperature decreases and it saturates at 140 K (i.e. well above the ordering temperature for the Fe2 moments). This peak corresponds to structure B in the two-structure model discussed in section

3.3.2., which would imply that the magnetic moments in some layers are flipping to give more structure B-type ordering and less structure A-type ordering on cooling. Alternatively, in the case of the single-phase twisting model, this would correspond to a change in the twisting angle and the overall moment. This explanation makes more physical sense than Fe1 layers flipping magnetic moments to generate more of one type of ordering, so from here on in this thesis, the twisting model will be exclusively used in discussion of the magnetic ordering of the Fe1 layer. The twisting angle and consequently the Fe1 moment both slowly increase as the temperature decreases and after saturating at T = 140 K the twisting angle refines to be 42.0(7)˚ and the Fe1 magnetic moment refines to be 3.99(4) μ_B. However, it is also possible that some Fe1 moments that were not ordered at room temperature order upon cooling.

One important thing to note is that not only does the Fe1 moment saturate before the onset of the ordering of the Fe2 layer, but the ordering of the Fe1 layer does not change within error below 140 K which suggests that the two layers order completely independently of each other.

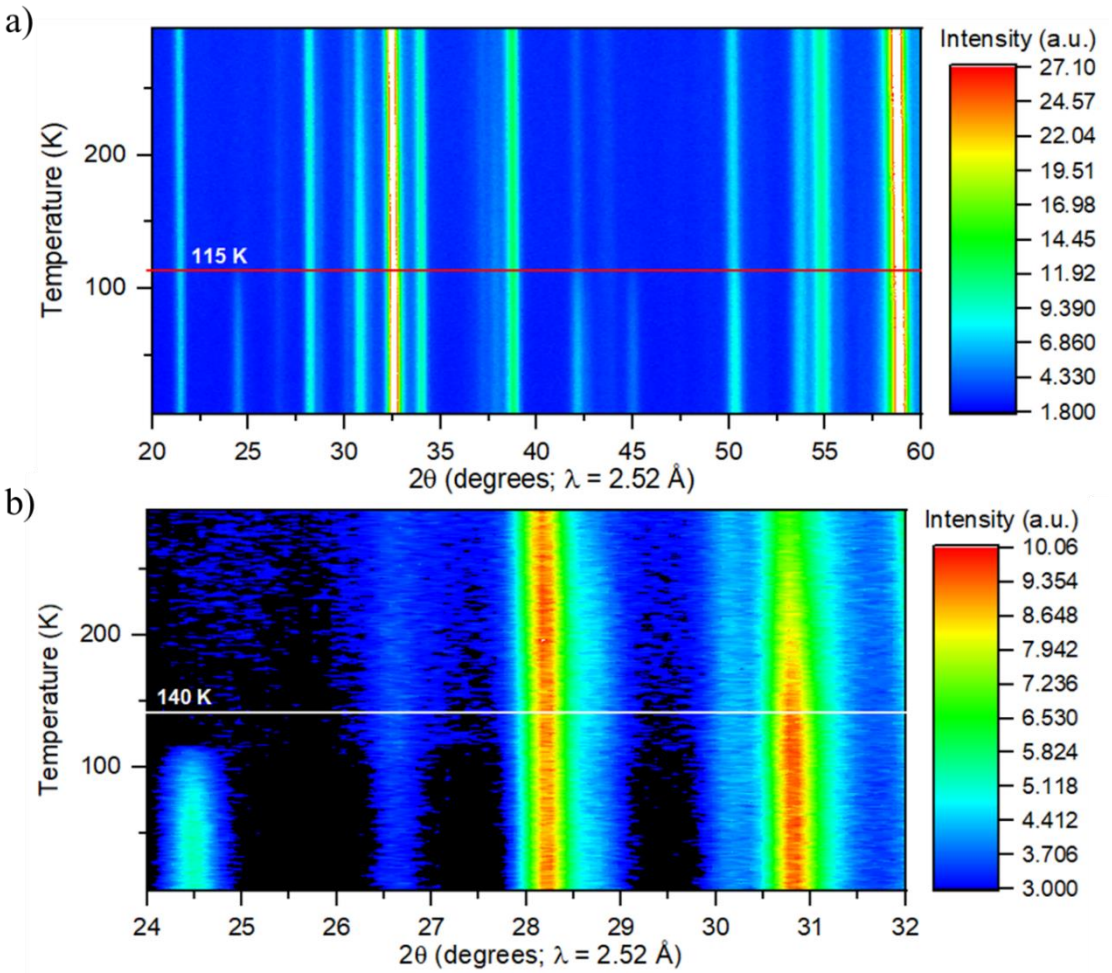


Figure 3.29. Contour plots showing a) the onset of magnetic peaks pertaining to the ordering of the Fe2 layer and b) the growth of the (310) magnetic peak at 30.8˚, saturating at T = 140 K.

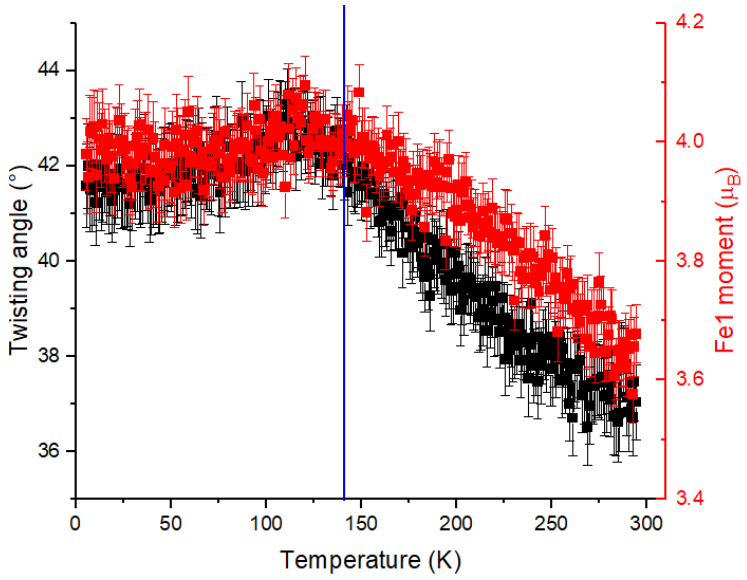


Figure 3.30. Twisting angle and Fe1 moment against temperature as obtained from a multi-refinement of the ANG022 NPD patterns collected on D1B at the ILL.

3.3.4. Low temperature NPD

As mentioned in section 3.3.3., upon cooling, there are additional magnetic reflections that appear starting at around 115 K which arise from the ordering of the Fe2 layer. These magnetic reflections can be indexed on a $2\sqrt{2}a \times 2\sqrt{2}a \times 2c$ supercell expansion by activating the mR2+ B2g(a,b) modes with the propagation vector **k** = (0, ½, ½) along with the same mM5- and mA5- modes that correspond to the Fe1 layer as discussed in section 3.3.2. The structure generated by activating these modes for the Fe2 sites is displayed in Figure 3.32, with several different exchange pathways labelled. This is the same ordering pattern as the 2**k** model described in the literature for this layer in other compounds (chapter 1.3.2), with the J_2 antiferromagnetic Fe-O-Fe 180° super exchange and the J_3 ~90° ferromagnetic Fe-S-Fe super exchange governing the ordering pattern rather than the J_1 Fe-Fe direct exchange by Goodenough-Kanamori rules, and DFT calculations in Kabbour *et.al.* on the same layer type support that his ordering scheme is the lowest in energy and therefore the most stable [8]. Between adjacent Fe2 layers, the moments are also antiferromagnetically aligned. At 5 K, both the Fe1 and Fe2 moments are saturated at 4.04(5) and 3.31(7) μ_B respectively, both of which are less than the 5 μ_B expected for high-spin d^5 Fe^{3+} ions and the 4 μ_B expected for high-spin d^6 Fe^{2+} ions most likely due to the covalency of the interaction with the ligands.

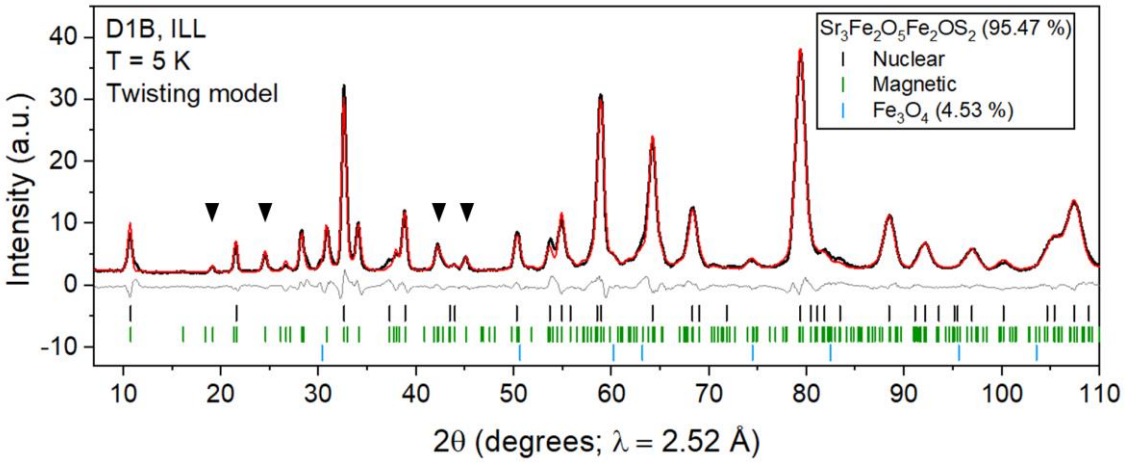


Figure 3.31. Rietveld refinement NPD data for $Sr_3Fe_2O_5Fe_2OS_2$ collected on D1B at the ILL at 5 K showing the observed (black), calculated (red), and difference (grey) curves. Black triangles indicate new magnetic reflections that appear below 115 K.

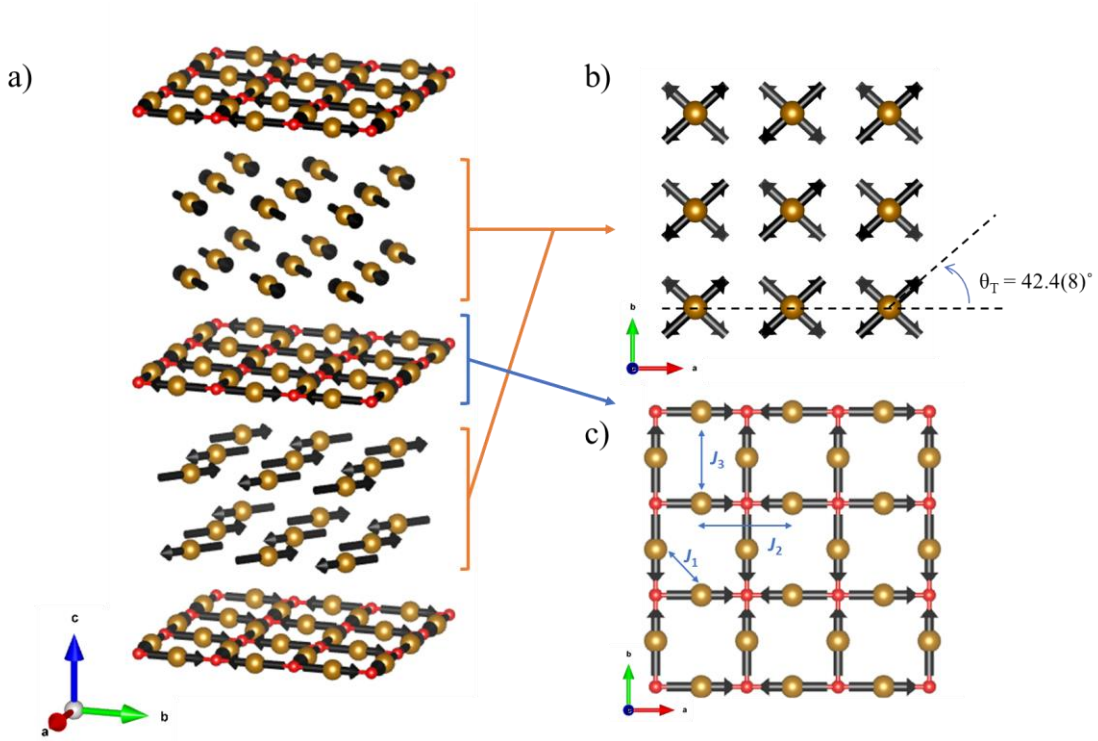


Figure 3.32. 5 K magnetic model of $Sr_3Fe_2O_5Fe_2OS_2$ shown on a) a nuclear $3a \times 3a \times 2c$ supercell alongside individual views of b) the Fe1 layer and c) the Fe2 layer with labelled exchange pathways.

Table 3.11. Comparison of Fe1 and Fe2 magnetic order at select temperatures. The twisting angle listed is the canting angle +/- from the *a*-axis when the mM5- and mA5- E(a) and E(b) moments are refined as discussed.

Temperature (K)	5	140	300
Fe1 moment (μ_B)	4.04(5)	3.99(4)	3.58(4)
Twisting angle (°)	42.4(8)	42.0(7)	36.7(7)
Fe2 moment (μ_B)	3.31(7)	0	0

3.3.5. High, variable temperature NPD

Since the Fe1 layer is magnetically ordered at room temperature and high-temperature magnetometry gave no indication of any high-temperature magnetic transition, it was of interest to investigate via NPD the temperature at which the Fe1 layer of $Sr_3Fe_2O_5Fe_2OS_2$ loses long-range magnetic order. This phase is reactive to both vanadium and air at high temperatures, so the samples were sealed in evacuated thin-walled silica ampoules prior to the experiment and these ampoules were then placed into 8 mm vanadium cans for the experiment on HRPD. As mentioned previously, HRPD is not optimized for magnetic structure determination due to the low signal-to-noise ratio in the low-angle bank 3. However, due to the additional structural investigation that was conducted with HRPD with regards to the orthorhombic distortion, a

simultaneous initial investigation into the magnetic structure at high temperatures was an efficient use of neutron beam time.

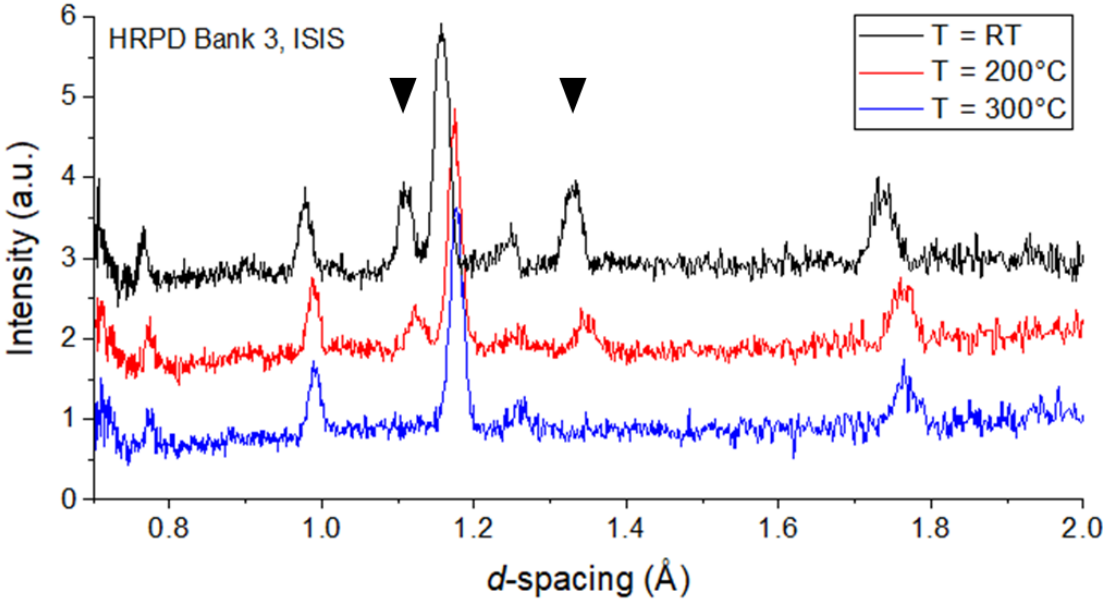


Figure 3.33. Comparison of NPD patterns of $Sr_3Fe_2O_5Fe_2OS_2$ (ANG074) collected at various high temperatures on HRPD bank 3 at ISIS Neutron and Muon Source. Black triangles indicate the (210) and (401) magnetic reflections from left to right.

As Figure 3.33 shows, the magnetic peaks shrink on heating from room temperature to 200°C and completely disappear by 300°C. Since this is the temperature range within which the orthorhombic samples undergo an orthorhombic to tetragonal transition, it is plausible that the onset of the orthorhombic magnetic structure may encourage a tetragonal to orthorhombic structural distortion in some of the orthorhombic samples. Unfortunately, the pattern in bank 3 for ANG072b was not as clean as ANG074, due to the fact that the (210) and (401) magnetic reflections were not observed at room temperature for 072b and only the (301) peak was which is not resolved from a nuclear Fe_3O_4 (111) reflection (Figure 3.28). Therefore, while the structural transition of 072b was clearly observed, the magnetic transition was more ambiguous. Ultimately, more data is needed in order to investigate this further with an instrument that is optimized for magnetic structure characterization as well as with more temperatures since a 100°C transition range is not precise enough to directly correlate the orthorhombic to tetragonal structural transition and the onset of long-range magnetic order in the Fe1 layer. However, given that the structural distortion may occur at the same temperature as the onset of magnetic order,

the activation of a second magnetic mode at the transitioning temperature would be allowed by Landau Theory.

3.4. Further Characterization

3.4.1. XANES measurements

XANES measurements were carried out on the B18 beamline at the DLS in an effort to further investigate the iron oxidation states in $Sr_3Fe_2O_5Fe_2OS_2$. The spectrum is shown below in Figure 3.34 alongside spectra for Fe_2O_3 (Fe^{3+}) and FeO (Fe^{2+}) standards.

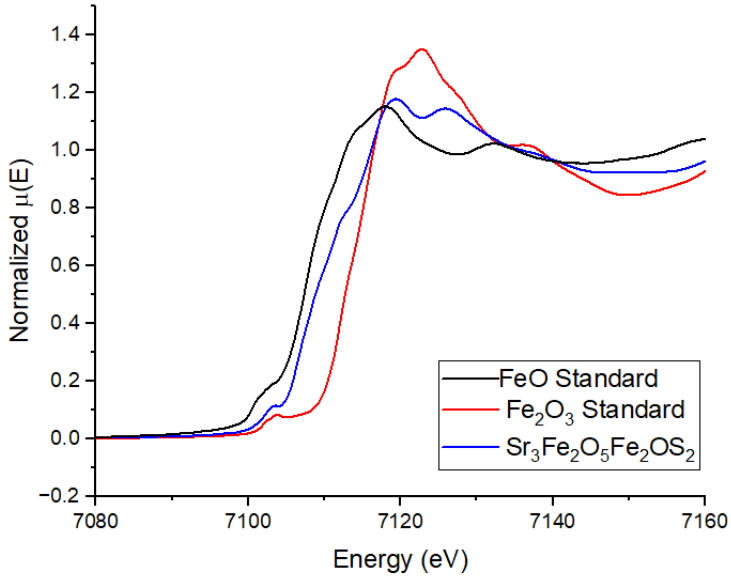


Figure 3.34. XANES K-edge for $Sr_3Fe_2O_5Fe_2OS_2$ and Fe^{2+}/Fe^{3+} standards.

The K-edge for the $Sr_3Fe_2O_5Fe_2OS_2$ lies between the Fe^{2+} and Fe^{3+} standards, which indicates an average oxidation state between the two. This data is consistent with the predicted oxidation states in the compound given the 1:1 ratio of Fe^{2+} and Fe^{3+} that would charge balance the layers in the compound (average oxidation state 2.5+).

3.4.2. Mössbauer Spectroscopy

Mössbauer spectroscopy data for $Sr_3Fe_2O_5Fe_2OS_2$ was collected and analysed by Magali Gimeno and Michael Neidig at the University of Oxford and the analysed spectra are shown in Figure 3.35. At room temperature, there is clearly one species exhibiting hyperfine splitting (green) which makes up about 53% of the signal and is indicative of magnetic ordering. This is assigned

to Fe1. The other species (red, purple, orange) only display quadrupole splitting which suggests that they are not magnetically ordered. The red doublet is therefore assigned to the Fe2 irons, which are not long-range ordered at room temperature. This supports the magnetic model obtained by neutron powder diffraction that has the Fe1 sites ordered at room temperature (50% of the Fe sites in the structure) while the Fe2 sites are not ordered. However, the origin of the other two doublets is more ambiguous as they could originate from Fe1 sites (that are not ordered) or Fe2 sites that have different local symmetry (possibly due to vacancies). Measurements on more samples may give insight into the origin of these two minority components.

Meanwhile, at T = 80 K, there is a much more complex spectrum. The fit in Figure 3.35b contains the same type of species in green showing hyperfine splitting (54%) as well as a second phase exhibiting hyperfine splitting in a very complex sextet in red (40%). The complex red sextet corresponds to the magnetic ordering of the Fe2 layer and the shape is very reminiscent of that observed below the magnetic ordering transition of the phase $Ba_2F_2Fe_2OSe_2$ that contains the same $[Fe_2OCh_2]$ layer [8]. This supports the claim that the Fe1 layer is the only layer ordered at room temperature, and the Fe2 layer then orders at lower temperatures.

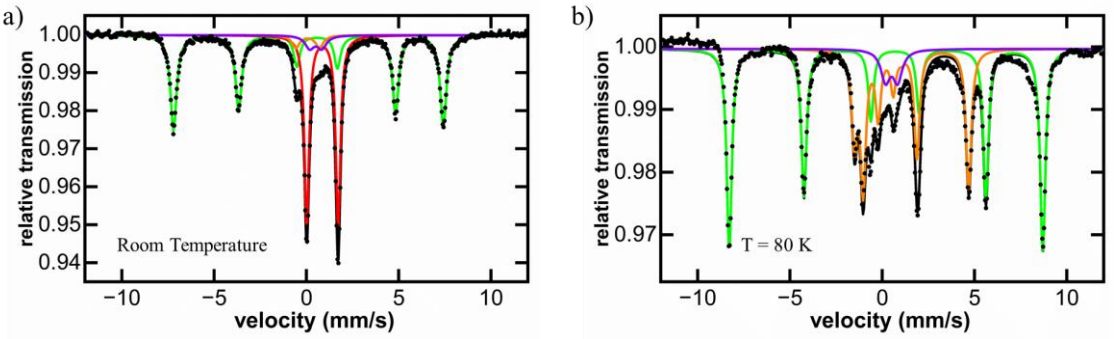


Figure 3.35. ^{57}Fe Mössbauer spectra for $Sr_3Fe_2O_5Fe_2OS_2$ (ANG022) collected at a) room temperature and b) 80 K.

Table 3.12. Fit parameters for the ^{57}Fe Mössbauer spectra of $Sr_3Fe_2O_5Fe_2OS_2$ at room temperature and 5 K. δ is the isomer shift and ΔE_Q is the electric quadrupole splitting.

Temperature (K)	Component	δ (mm/s)	ΔE_Q (mm/s)	Population (%)	Signal origin
300	Green sextet	0.34	1.21	53	Fe1
	Red doublet	0.87	1.70	38	Fe2
	Orange doublet	0.07	1.28	4	unknown
	Purple doublet	0.51	0.65	5	unknown
5	Green sextet	0.45	1.10	54	Fe1

	Red sextet	1.01	1.70	40	Fe2
	Purple doublet	0.51	0.65	6	unknown

3.5. Conclusions and Future Work

In conclusion, the new phase $Sr_3Fe_2O_5Fe_2OS_2$, designed using a building-block approach, has been successfully synthesized in high purity and its nuclear structure and magnetism have been characterized. Structurally, the phase crystallizes in the tetragonal *P*4/*mmm* space group, but there are intricacies evidenced by peak splitting and diffuse features that indicate sample-dependent structural distortions. At this time, the origin of the orthorhombic distortion is still under investigation, though ED studies reveal modulations in some of the orthorhombic samples' crystallites which could originate from iron vacancy order in the Fe2 layer seen in Figure 3.21b and this is supported by the fast Fourier transform (FFT) of that region. However, this vacancy order did not appear to persist across an entire crystallite nor was the modulation observed in every crystallite in the orthorhombic samples. In addition to this, the TEM studies also revealed structural intricacies in the form of antiphase boundaries and extended perovskite-type layers in flux-grown samples, though it is unclear why these originate. Further microscopy is being conducted on these samples by Sepideh Rahimi and Joke Hadermann at EMAT at the University of Antwerp, Belgium, and these studies will be published in Rahimi's PhD thesis.

In addition to this structural characterization, the magnetic structure of $Sr_3Fe_2O_5Fe_2OS_2$ was characterized mainly using neutron powder diffraction. The Fe1 and Fe2 layers of this structure order independently of one another, with the Fe1 layer ordering between 200-300°C and saturating at 140 K and the Fe2 layer ordering at 115 K. Overall, the Fe1 layer orders antiferromagnetically in the basal plane along the Fe-O-Fe superexchanges within each layer and the saturated moment at 140 K refines to be 3.99(4) μ_B. However, the relationship between subsequent Fe1 layers remains a bit ambiguous and can be described using a 2-phase model which assumes that there are two different magnetic models that exist simultaneously within the bulk, or a single-phase twisting model which is a linear combination of the two structures that comprise the 2-phase model. This is the first time, as far as we have been able to determine, that

this relationship has been observed, as most structures containing this layer type are body-centred and this relationship between Fe1 layers does not apply, or in the few primitive structures that contain a similar layer, this phenomenon is not observed. In addition to this, it seems that the magnetic model is somewhat sample-dependent, which can be described as a difference in the ratio of the two structures in the structural model or as a variation in twisting angle between samples. The Fe2 layer orders in the same way as many other structures that contain this same layer type and it governed by the antiferromagnetic Fe-O-Fe 180° superexchange and the ferromagnetic Fe-S-Fe ~90° superexchange. The magnetic moments of the Fe2 irons in this layer saturate to a magnitude of 3.31(7) μ_B at 5 K.

In addition to the further microscopy experiments that were mentioned above, there are several additional experiments that may yield further insights into the intricacies of this phase. Firstly, neutron powder diffraction data for the samples ANG072b, ANG074, and ANG075b collected on an instrument with better S/N and good resolution at low angles (longer d-spacings) would reveal more information about the sample dependence of the magnetic structure. Additionally, heat capacity and resistivity measurements would reveal information about the electronic behaviour of the phase. Sepideh Rahimi is also planning to conduct high-pressure experiments to investigate how this may affect the structural distortions and intricacies that are observed.

From the successful synthesis of this new structure type, there also stem many different paths to explore chemically and some of these are described in upcoming chapters. Chapter 4 deals with the substitution of Ca for Sr on the *Ae* site, Chapter 5 involves the topotactic reduction of the Fe1 layer to remove the axial bridging oxygen, and Appendix F mentions work done in collaboration with Annabel Lyon [9] concerning the addition of an extra equivalent of SrO in the Fe1 layer which induces a body centring to the unit cell (Figure 1.15e). Other substitutions may also be possible, on the *Ae*, *M*, or *Ch* sites. Additionally, the TEM experiments suggest another further target phases; i.e. relatives with extended perovskite-type layers.

References

[1] Glazer, A.M. *Acta Cryst*. **1972**, *28*, 3384.

[2] Woodward, P.M. *Acta Cryst*. **1997**, *53*, 32-43.

[3] Levy, D.; Giusterro, R.; Hoser, A. *Phys. Chem. Miner*. **2012**, *39*, 168-176.

[4] Knee, C.S.; Weller, M.T. *J. Mater. Chem*. **2001**, *11*, 2350-2357.

[5] Azad, A.K.; Zakaria, A.K.M.; Ahmed, F.U.; Paranjpe, S.K.; Das, A. *J. Magn. Magn. Mater*. **2000**, *214*, 251-257.

[6] Smura, C.F. *D. Phil Thesis, University of Oxford*. The Synthesis, Structures, and Properties of Multi-Anion Solids, **2008**.

[7] Shirane, G. *Acta Crystallogr*. **1959**, *12*, 282–285.

[8] Kabbour, H.; Janod, E.; Corraze, B.; Danot, M.; Lee, C.; Whangbo, M.H.; Cario, L. *J. Am. Chem. Soc.* **2008**, *130*, 8261-8270.

[9] Lyon, A.L. MSc. Thesis, *University of Oxford*, "Structures and Magnetism of layered iron oxide chalcogenides," **2024**.

Chapter 4: Synthesis and Characterization of $Sr_{3-x}Ca_xFe_2O_5Fe_2OS_2$

Contents

4.1. Synthesis 97
4.2. Structural characterization and trends 97
4.2.1. Room-temperature X-ray powder diffraction 97
4.2.2. SEM-EDX 102
4.2.3. Variable temperature X-ray powder diffraction 104
4.2.4. Room-temperature Neutron powder diffraction (D2B/HRPD) 106
4.2.5. Summary of structural trends 109
4.3. Magnetic characterization and trends 111
4.3.1. Magnetometry 111
4.3.2. Room temperature NPD 113
4.3.3. Low variable temperature NPD 114
4.3.4. Low temperature NPD 115
4.4. Conclusions 116
References 118

This chapter explores alkaline earth metal substitution of calcium for strontium in $Sr_3Fe_2O_5Fe_2OS_2$ to form the solid solution $Sr_{3-x}Ca_xFe_2O_5Fe_2OS_2$ ($0 < x < 1.7$). Like similar phases (chapter 1.3.1), the differently sized cations order between the differently sized *Ae* sites. There are also limits to the phases which readily form, with sample $x = 0.4$ being only value of x below 1 (with the exception of $x = 0$ as discussed in chapter 3) which readily formed, samples with $1 \leq x \leq 1.7$ forming multiphase products, and samples $x > 1.7$ forming the competing phase $Ca_2Fe_{2.7-\delta}O_3S_2$ (see chapter 6) as a side-product. The structural trends that are observed across the series as well as the aforementioned limits on Ca substitution will be discussed in section 4.2. These compounds also order magnetically similarly to the all-Sr phase, which will be discussed in section 4.3.

4.1. Synthesis

The synthesis of $Sr_{3-x}Ca_xFe_2O_5Fe_2OS_2$ can be achieved by the same traditional high-temperature ceramic synthesis method as the all-Sr compound as discussed in chapter 3.1. In this, the reagents SrO (obtained from the decomposition of $SrCO_3$), CaO (obtained from the decomposition of $CaCO_3$), Fe_2O_3 (Alfa Aesar, 99.998%), Fe (Alfa Aesar, 99+%), and S (Sigma Aldrich, 99.98%) were ground thoroughly in a (3-*x*):(*x*):1:2:2 molar ratio in an agate mortar and pestle until reaching homogeneity under an argon atmosphere. The pelletized reagent mixture, placed in an alumina crucible and sealed in an evacuated quartz tube, was then heated at a slow, 1°C per minute, rate to 900°C to avoid the sublimation of the volatile elemental sulfur in the reagent mixture so that the sulfur has time to react with the other elements instead of merely entering a gaseous phase which could also cause the tube to explode. The reaction then dwelled at high temperature for 48 hours before furnace cooling to room temperature.

The alternative method of a KI flux-assisted synthesis was attempted in an effort to grow single crystals, but the synthesis was unsuccessful and resulted in a product of various binary species. Since this was unsuccessful and the ceramic method produced samples in relatively high-purity, flux-assisted synthesis methods were abandoned.

4.2. Structural characterization and trends

4.2.1. Room-temperature X-ray powder diffraction

These phases were characterized by SXRPD collected on I11 at DLS using the PSD detector. In some cases, as the series was investigated in smaller steps, 10-minute scans using the MAC detector at I11 were used in conjunction with the PSD scans in an effort to more accurately determine the lattice parameters and their trends as a function of composition. In the cases where both the PSD and MAC data sets were available, Rietveld refinement was carried out on both data sets simultaneously with a single set of lattice parameters. The overall structural models (Tables 4.1 and 4.2) were derived from the model of $Sr_3Fe_2O_5Fe_2OS_2$, with the orthorhombic model (with *a* and *b* being slightly different as discussed with the structural variations of the all-

Sr phase in chapter 3) being used alone or in conjunction with the tetragonal model, when necessary, as determined by peak splitting in the diffraction patterns.

Table 4.1. Overall structural model for $Sr_{3-x}Ca_xFe_2O_5Fe_2OS_2$ for the phases with tetragonal *P*4/*mmm* symmetry.

	Space Group = *P*4/*mmm* (No. 123)				
atom	site	*x*	*y*	*z*	occupancy
Sr1	1*b*	0	0	½	1 – *occ*Ca1
Ca1	1*b*	0	0	½	*occ*Ca1
Sr2	2*g*	0	0	Sr2*z*	1 – *occ*Ca2
Ca2	2*g*	0	0	Ca2*z* = Sr2*z*	*occ*Ca2
Fe1	2*h*	½	½	Fe1*z*	1
Fe2	2*f*	½	0	0	1
O1	4*i*	½	0	O1*z*	1
O2	1*a*	0	0	0	1
O3	1*d*	½	½	½	1
S	2*h*	½	½	S1*z*	1

Table 4.2. Overall structural model for $Sr_{3-x}Ca_xFe_2O_5Fe_2OS_2$ for the phases with orthorhombic *Pmmm* symmetry.

	Space Group = *Pmmm* (No. 47)				
atom	site	*x*	*y*	*z*	occupancy
Sr1	1*c*	0	0	½	1 – *occ*Ca1
Ca1	1*c*	0	0	½	*occ*Ca1
Sr2	2*q*	0	0	Sr2*z*	1 – *occ*Ca2
Ca2	2*q*	0	0	Ca2*z* = Sr2*z*	*occ*Ca2
Fe1	2*t*	½	½	Fe1*z*	1
Fe2	1*e*	0	½	0	1
Fe2a	1*b*	½	0	0	1
O1	2*s*	½	0	O1*z*	1
O1a	2*r*	0	½	O1*z*	1
O2	1*a*	0	0	0	1
O3	1*h*	½	½	½	1
S	2*t*	½	½	S1*z*	1

Table 4.3. Refined structural parameters for $Sr_{3-x}Ca_xFe_2O_5Fe_2OS_2$ ($0 < x < 1.75$). Asterisks indicate samples for which only PSD data was available.

x	0*	0.4 [1]	1.0		1.2*	
Sample	ANG047b	ANG083	ANG037		ANG088	
R_{wp} (%)	3.956	7.270	7.132		8.202	
Space group	*P*4/*mmm*	*Pmmm*	*P*4/*mmm*	*Pmmm*	*P*4/*mmm*	*Pmmm*
wt %	98.85	93.20	48.47	51.53	18.52	81.48
a (Å)	3.96156(1)	3.93089(1)	3.94595(1)	3.92770(2)	3.93634(7)	3.92316(4)
b (Å)	3.96156(1)	3.94725(1)	3.94595(1)	3.94448(2)	3.93634(7)	3.93896(3)
a/*b*	1	0.99586(0)	1	0.99567(1)	1	0.99599(1)
c (Å)	13.51991(8)	13.50356(4)	13.36188(7)	13.3929(1)	13.3231(4)	13.3491(1)
V (Å^3)	212.181(2)	209.525(1)	208.051(2)	207.494(3)	206.44(1)	206.287(4)
*occ*Ca1	0	0.000(5)	0.000(9)	0.000(8)	0.00(5)	0.00(1)
*occ*Ca2	0	0.220(3)	0.454(6)	0.513(7)	0.62(3)	0.52(1)
Calc *x*	0	0.441(9)	0.94(1)	1.02(1)	1.25(9)	1.04(2)
Sr2*z*	0.22716(8)	0.22523(5)	0.2270(1)	0.2274(1)	0.2269(7)	0.2266(2)
Fe1*z*	0.36159(9)	0.36088(7)	0.3588(1)	0.3573(1)	0.3574(7)	0.3576(2)
O1*z*	0.3407(2)	0.3401(1)	0.3380(3)	0.3384(2)	0.335(1)	0.3383(4)
S1*z*	0.1273(1)	0.1274(1)	0.1308(2)	0.1252(1)	0.135(1)	0.1278(3)

x	1.4		1.5		1.6	
Sample	ANG089		ANG054		ANG090	
R_{wp} (%)	8.720		6.254		8.177	
Space Group	*P*4/*mmm*	*Pmmm*	*P*4/*mmm*	*Pmmm*	*P*4/*mmm*	*Pmmm*
wt %	39.24	60.76	54.48	45.52	43.94	56.06
a (Å)	3.93810(2)	3.91991(2)	3.93981(1)	3.91506 (2)	3.93677(1)	3.91521(2)
b (Å)	3.93810(2)	3.93599(2)	3.93981(1)	3.93645(3)	3.93677(1)	3.93281(2)
a/*b*	1	0.99592(1)	1	0.99457(1)	1	0.99553(1)
c (Å)	13.2714(1)	13.30604(7)	13.24715(9)	13.2890(1)	13.22574(9)	13.26359(7)
V (Å^3)	205.823(3)	205.296(2)	205.624(2)	204.804(3)	204.975(2)	204.230(2)
*occ*Ca1	0.07(1)	0.000(8)	0.106(7)	0.00(1)	0.18(1)	0.000(8)
*occ*Ca2	0.631(8)	0.634(6)	0.699(5)	0.770(8)	0.764(7)	0.707(6)
Calc *x*	1.34(2)	1.27(1)	1.50(1)	1.53(1)	1.71(1)	1.41(1)
Sr2*z*	0.2259(1)	0.2279(1)	0.2269(1)	0.2280(1)	0.2278(1)	0.2276(1)
Fe1*z*	0.3572(2)	0.3571(1)	0.3565(1)	0.3565(2)	0.3564(1)	0.3570(1)
O1*z*	0.3352(4)	0.3391(2)	0.3351(2)	0.3405(3)	0.3352(3)	0.3402(2)
S1*z*	0.1325(3)	0.1292(2)	0.1298(2)	0.1289(3)	0.1319(2)	0.1299(2)

x	1.75* [2]	
Sample	ANG064	
R_{wp} (%)	7.014	
Space Group	*P*4/*mmm*	*Pmmm*
wt %	51.33	39.05
a (Å)	3.93941(2)	3.91099(4)
b (Å)	3.93941(2)	3.93442(5)
a/*b*	1	0.99404(2)
c (Å)	13.2292(1)	13.2715(1)
V (Å^3)	205.304(3)	204.215(4)
*occ*Ca1	0.149(9)	0.00(1)
*occ*Ca2	0.786(6)	0.817(9)
Calc *x*	1.72(1)	1.63(2)
Sr2*z*	0.2284(1)	0.2294(2)
Fe1*z*	0.3559(1)	0.3550(2)
O1*z*	0.3355(3)	0.3397(4)
S1*z*	0.1340(2)	0.1270(3)

[1]ANG083 also contains Fe_3O_4 and SrS impurities.
[2]ANG064 also contains an impurity of $Ca_2Fe_{2.6}O_3S_2$ in 9.62 wt%.

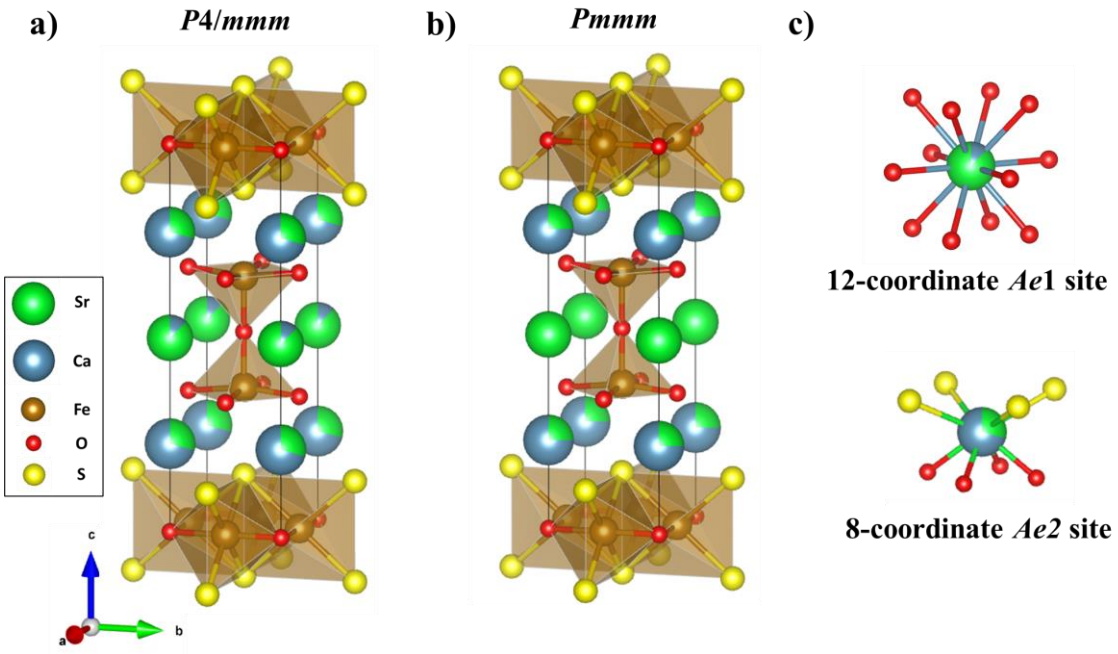


Figure 4.1. Refined unit cells for the a) tetragonal and b) orthorhombic phases in $Sr_{1.5}Ca_{1.5}Fe_2O_5Fe_2OS_2$ (ANG054) alongside c) the visualization to the individual *Ae*1 and *Ae*2 sites.

The first thing that is clear from the diffraction data is that for $x < 1$, only the $x = 0.4$ phase formed with high purity, with other members of the solid solution forming complex products with abnormal peak shapes and which cannot be properly indexed by the desired phase. In addition to this, the $x = 0.4$ phase is not tetragonal as one might expect, but is instead orthorhombic as indicated by the splitting of the (200) and (020) reflections in the SXRPD pattern (Figure 4.2).

When x reaches and surpasses 1, the samples are two-phase, containing a tetragonal phase crystallizing in the *P*4/*mmm* space group and an orthorhombic phase in the *Pmmm* space group for which the *a* and *b* lattice parameters are slightly different. This is indicated by the splitting of the (200) and (020) peaks as well as the large difference in intensity of the split peaks, and these peaks cannot be fit by a single orthorhombic or single tetragonal phase (Figure 4.2, 4.3). The volume of the orthorhombic phase is always smaller than that of the tetragonal phase, though both decrease across the series as more Ca is included in the phase. However, there is no trend that can be identified on whether the orthorhombic or tetragonal phase is more Ca-rich, and this is likely due to the inevitable parameter correlations in the refinements. There is also an upper boundary on how much Ca can be substituted for Sr on the *Ae* sites. In the $x = 1.75$ phase,

$Ca_2Fe_{2.6}O_3S_2$ is formed as a competing side-phase, and this remains true for any synthesis attempts to generate members of the solid solution with Ca-content above $x = 1.75$.

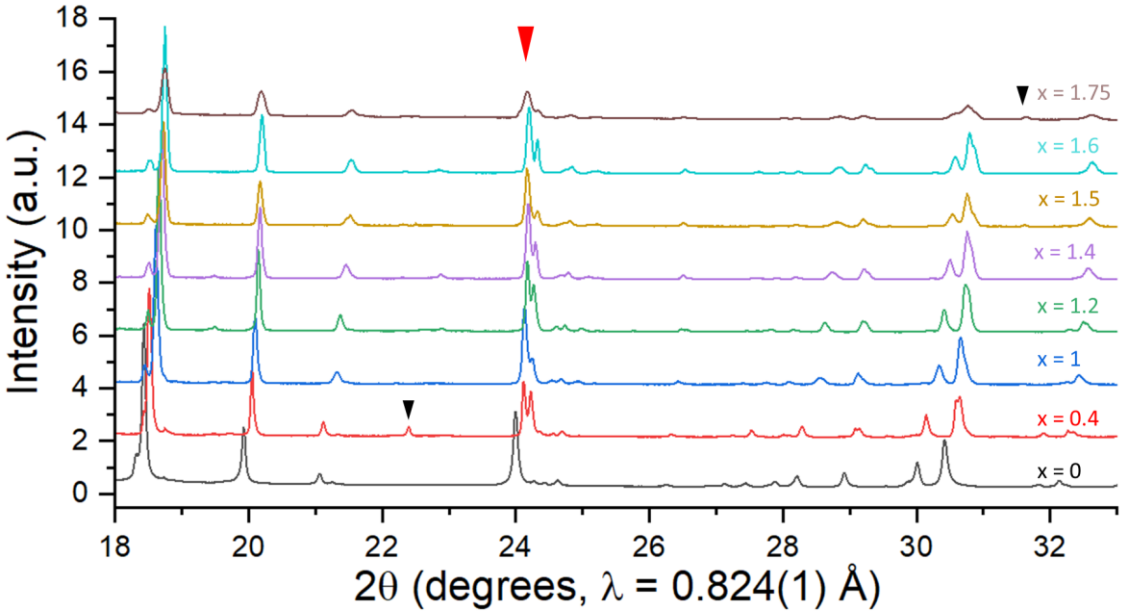


Figure 4.2. X-ray diffraction patterns for the solid solution $Sr_{3-x}Ca_xFe_2O_5Fe_2OS_2$ ($x < 1.75$) collected on the PSD detector on beamline I11 at DLS. The red triangle indicates the location of the (200)/(020) reflections for all patterns while the black triangles indicate reflections from impurities in individual patterns.

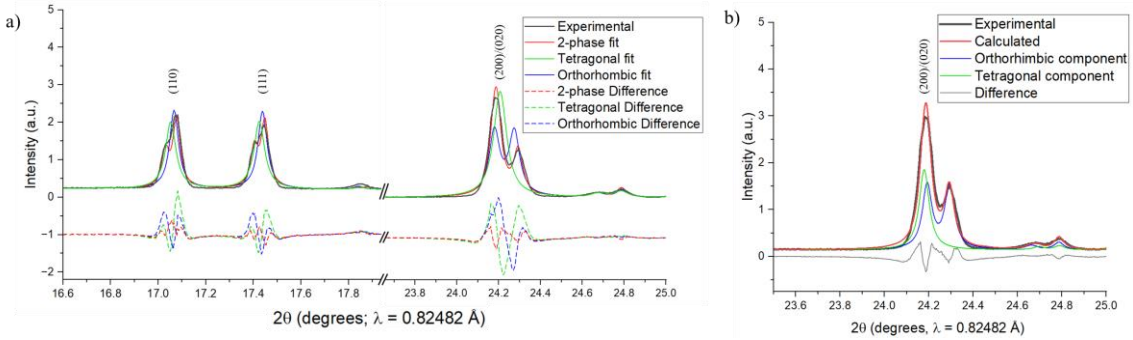


Figure 4.3. Comparison of a) how refinements with single tetragonal or orthorhombic phases and a multiphase refinement fit the (110), (111), and (200)/(020) peaks of the $x = 1.4$ phase (ANG089) alongside b) a breakdown of the individual phase components making up the 2-phase fit. Difference curves are also provided for the sake of comparison.

In addition to this, there is clear cation ordering between the two *Ae* sites, with the larger Sr cations preferentially occupying the larger 12-coordinate *Ae*1 site and the smaller Ca cations occupying the smaller 8-coordinate *Ae*2 sites (Figure 4.1c). This kind of cation ordering has been observed before in related phases $Ae_3Fe_2O_5Cu_2Ch_2$ (*Ae* = Ca, Sr, Ba and *Ch* = S, Se) (see Figure 1.5) [1,2]. The occupancies were initially calculated in the refinement by first allowing all of the occupancies to refine freely. In this free refinement, there was clearly cation ordering, but the

occupancies themselves did not make sense with the refined numbers indicating occupancies greater than 1 on individual sites. So, the occupancies were then fixed to the amount of Ca included in the precursors by assuming that all of the Ca cations occupied the 8-coordinate *Ae*2 site as a starting point for the refinement. However, given that there are two phases present and they may not have the same composition, there is an intrinsic limit to how much the refinement can be constrained. With this in mind, the occupancies obtained from the refinement with constrained compositions were used as the starting occupancies in the input file for a refinement for which the only restriction on the occupancies was that the total occupancy on each site was restricted to 1. One thing that is particularly interesting is that in the multiphase refinements, there is a difference in the cation ordering within the two phases. The orthorhombic phase never refines with any Ca on the larger *Ae*1 site, whereas once *x* reached 1.4, there is from then on always some Ca on the *Ae*1 site in the tetragonal phase. No preferred orientation parameters were enabled in these refinements as they were not very significant and are also strongly correlated to the phase fraction.

4.2.2. SEM-EDX

SEM-EDX was carried out on the $x = 1$ and $x = 1.5$ members of the solid solution series $Sr_{3-x}Ca_xFe_2O_5Fe_2OS_2$ in an effort to confirm the ratio of Sr to Ca and that the Sr and Ca cations were evenly dispersed throughout the product. Particles of the two different phases, tetragonal and orthorhombic, will not be distinguishable from their appearance. Therefore, the quantification of the relative Sr and Ca percentages obtained from the SEM is likely unable to distinguish the two phases as the refinements above suggest that the Sr:Ca ratios are fairly similar in the two different phases.

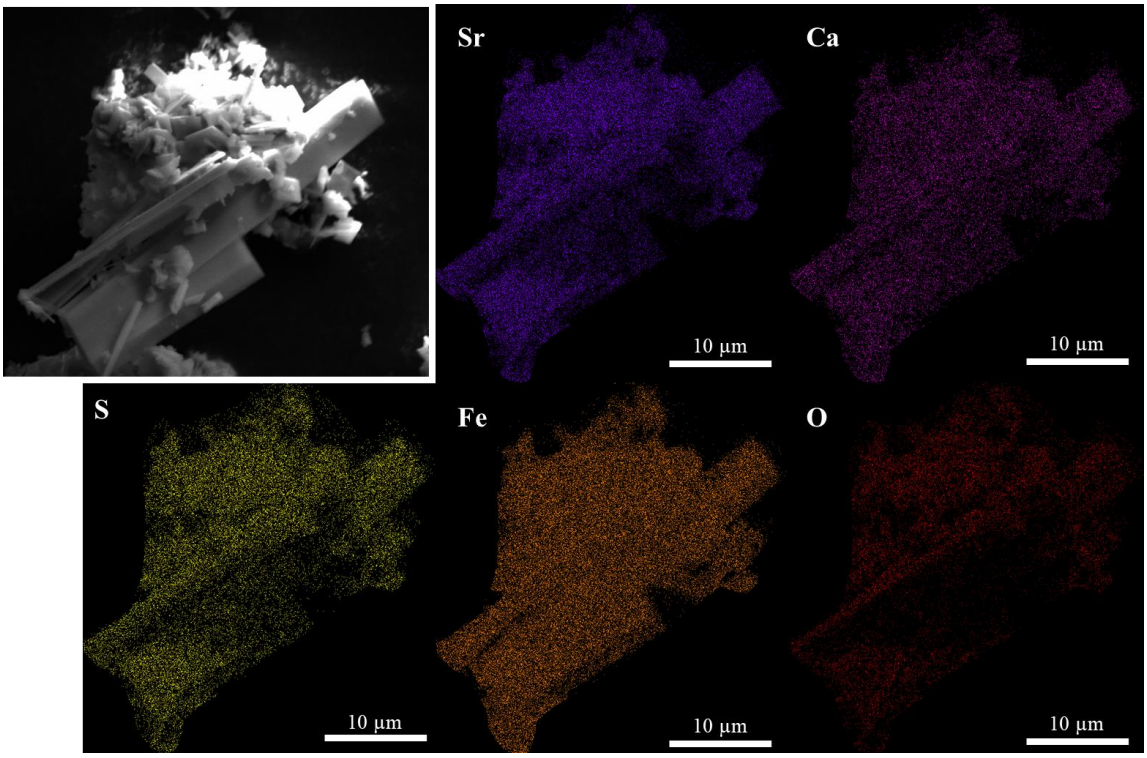


Figure 4.4. SEM imaging and EDX mapping of a particle of $Sr_2CaFe_2O_5Fe_2OS_2$ (ANG049a).

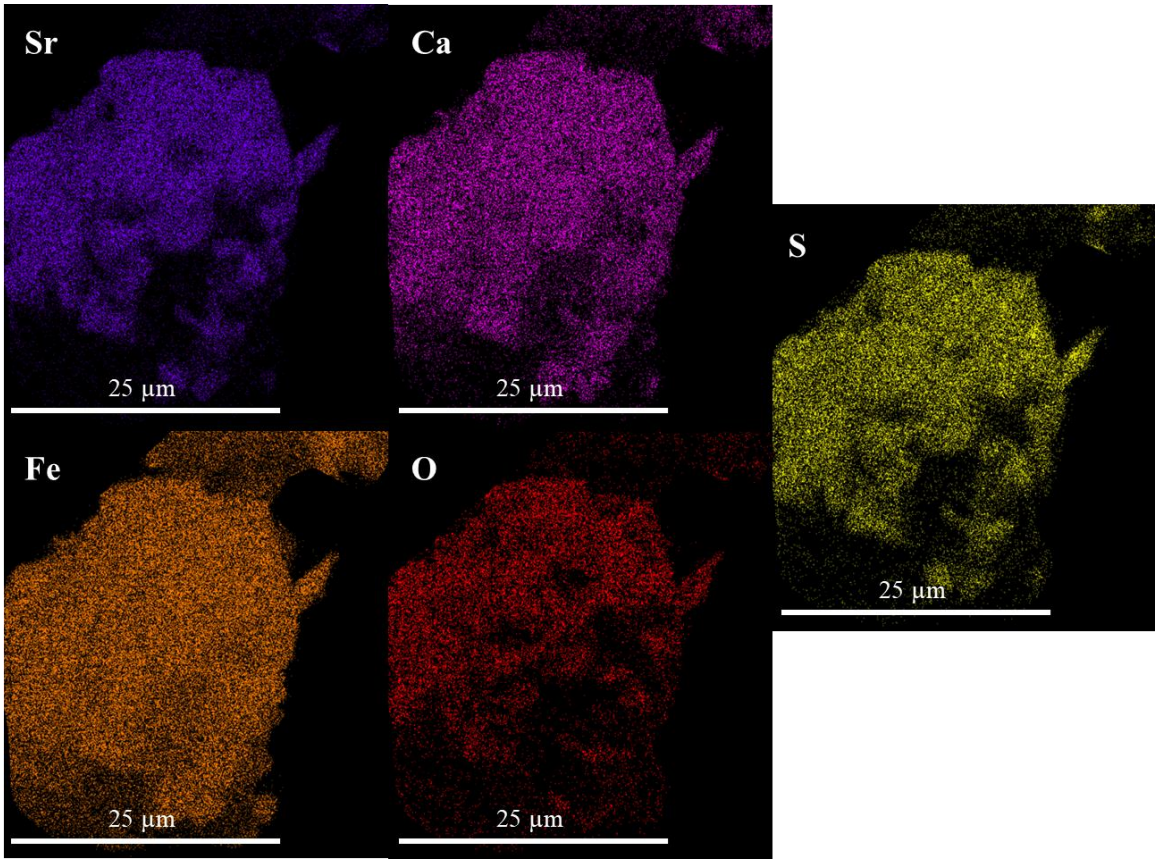


Figure 4.5. EDX mapping of a particle of $Sr_{1.5}Ca_{1.5}Fe_2O_5Fe_2OS_2$ (ANG048).

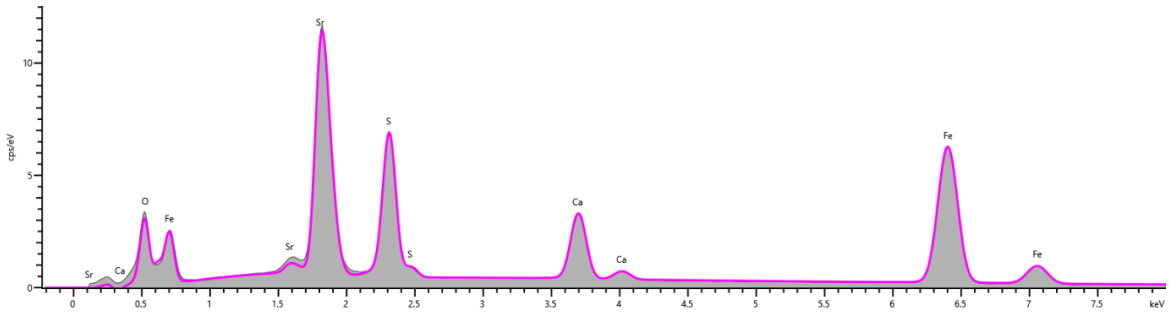


Figure 4.6. Sample SEM-EDX elemental analysis spectrum for $Sr_2CaFe_2O_5Fe_2OS_2$ (ANG049a).

Table 4.4. Average SEM-EDX elemental analysis for $Sr_2CaFe_2O_5Fe_2OS_2$ (ANG049a) and $Sr_{1.5}Ca_{1.5}Fe_2O_5Fe_2OS_2$ (ANG048). Due to its low atomic mass, O content is estimated.

x	Sr (at. ratio)	Ca (at. ratio)	Fe (at. ratio)	O (at. ratio)	S (at. ratio)
1	1.9(3)	0.9(3)	3.9(9)	6(1)	2.0(6)
1.5	1.5(1)	1.4(2)	3.7(7)	7(1)	2.0(1)

The SEM-EDX mapping shows that in both the $x = 1$ and $x = 1.5$, Sr and Ca seem to be evenly dispersed throughout the particles, with no regions that are particularly rich in one or the other. In addition to this, the average SEM-EDX analysis shows that both samples have the Ca-content anticipated by the starting materials within error. There are regions in Figure 4.5 that seem to be Sr-deficient, but this is due to the morphology of the particle and the contrast in the brightness of the colors used to represent each element.

4.2.3. Variable temperature X-ray powder diffraction

Variable-temperature synchrotron X-ray powder diffraction data was collected on beamline I11 at DLS from 100-1100 K as well as on ID22 at ESRF for temperatures down to 5 K for the $x = 1$ and $x = 1.5$ members of the solid solution $Sr_{3-x}Ca_xFe_2O_5Fe_2OS_2$ (samples ANG037 and ANG048 respectively). At T = 440 K and 530 K for the $x = 1$ and 1.5 phases respectively, the orthorhombic phase in each sample undergoes an orthorhombic to tetragonal phase transition on heating and the sample becomes single-phase. This is indicated by the merging of the (200) and (020) reflections as shown in Figure 4.7, and could potentially be due to cation mobility, though this is more applicable in the $x = 1$ phase since the $x = 1.5$ phase of sample ANG048 (different from ANG054 reported in table 4.3) has so little of the tetragonal phase at room temperature.

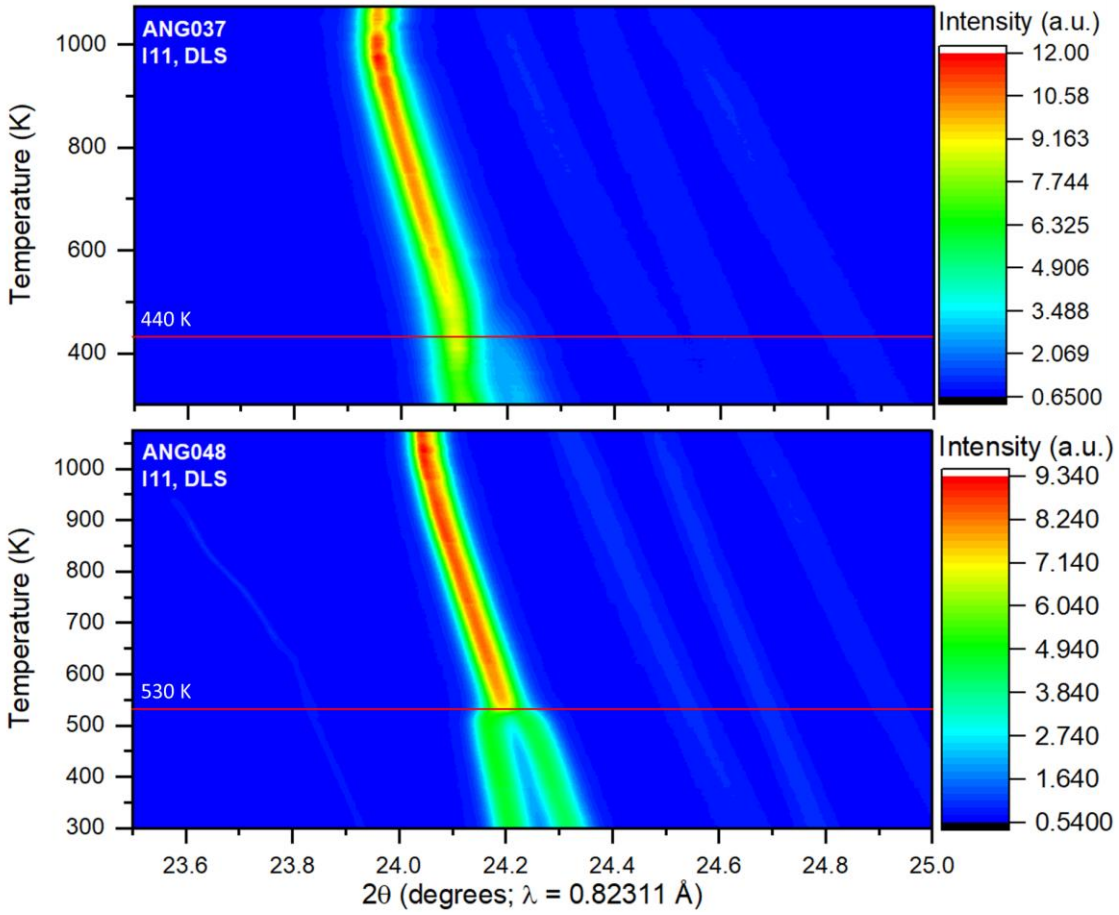


Figure 4.7. Contour plots showing the phase change of $Sr_{3-x}Ca_xFe_2O_5Fe_2OS_2$, x = 1 (top) and 1.5 (bottom) as indicated by the merging of the (200) and (020) reflections.

In addition to this, the lattice parameters for the tetragonal and orthorhombic phases have been calculated via individual refinements for various temperatures using the ID22 and I11 data sets for the x = 1 and x = 1.5 phases for temperatures up to the phase transition. Only an orthorhombic phase for the x = 1.5 phase was tracked, as the refinements for this particular sample fit well with only an orthorhombic phase and any tetragonal phase refined to exist in < 2 % by weight. In both cases, there is no evident phase transition or change in the unit cell volumes beyond thermal expansion until the aforementioned orthorhombic to tetragonal phase transition (Figure 4.8). There is some discontinuity in the lattice parameter trends when switching from one beamline or one environment to another since the lattice parameters are highly sensitive to the set-up of the experiments, but the overlap in temperatures shows that there is still a semblance of continuity and the addition of a small constant would make the trends all line up. Additionally, the I11 data shows that the curve in the ESRF cell volumes for the orthorhombic phase of ANG037 is an

artifact. The volume trend also shows the more gradual nature of the phase change for the $x = 1$ sample in how the volume of the orthorhombic phase gradually merges into the tetragonal linear trend, corresponding to the gradual merging of the (200) and (020) reflections in Figure 4.7.

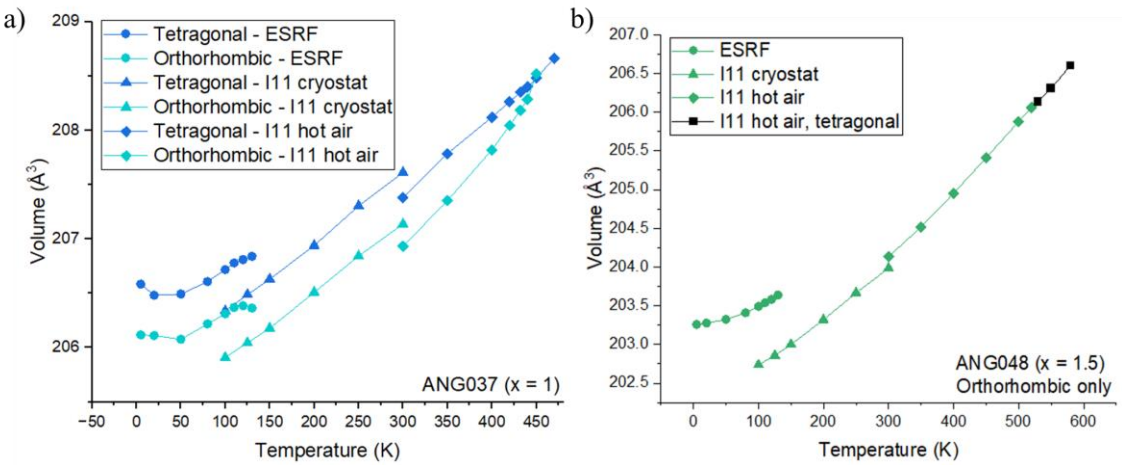


Figure 4.8. Refined unit cell volumes for a) ANG037 ($x = 1$) and b) ANG048 ($x = 1.5$) for temperatures from 5 K through the phase transition temperatures of 440 K and 530 K respectively. Errors are smaller than the data points.

4.2.4. Room-temperature Neutron powder diffraction (D2B/HRPD)

Neutron powder diffraction experiments were carried out for select members of the solid solution on beamlines D2B at the ILL and HRPD at ISIS Neutron and Muon Source in an effort to further investigate the structural intricacies that arise from the two-phase model of $Sr_2CaFe_2O_5Fe_2OS_2$ (ANG037). Both D2B and HRPD have high resolution at shorter *d*-spacings which, in addition to the neutron's sensitivity to lighter elements, makes them ideal instruments for this type of investigation. Unfortunately, D2B's resolution was not high enough to resolve the split (200) and (020) peaks of the orthorhombic phase (Figure 4.9a) and the refinement therefore yields imprecise lattice parameters and occupancies as well as inaccurate phase proportions in the sample. In fact, the D2B pattern can also be fit well with a single orthorhombic or a single tetragonal phase due to the lack of peak resolution and since there is less correlation, this increases the precision and accuracy of the occupancies and lattice parameters. The diffraction pattern collected in Bank 1 of HRPD, however, has the two peaks clearly resolved (Figure 4.9b), and the refined lattice parameters reasonably agree with those refined from the SXRPD pattern and the difference is presumably from the use of different instruments (Table 4.5). Contrastingly,

the Ca-occupancies do not agree between the I11 and HRPD refinements, as the HRPD refinements assign more Ca to the tetragonal phase and much less to the orthorhombic phase. Overall, this sample does follow the trend of the orthorhombic phase having no Ca-occupancy on the *Ae*1 site.

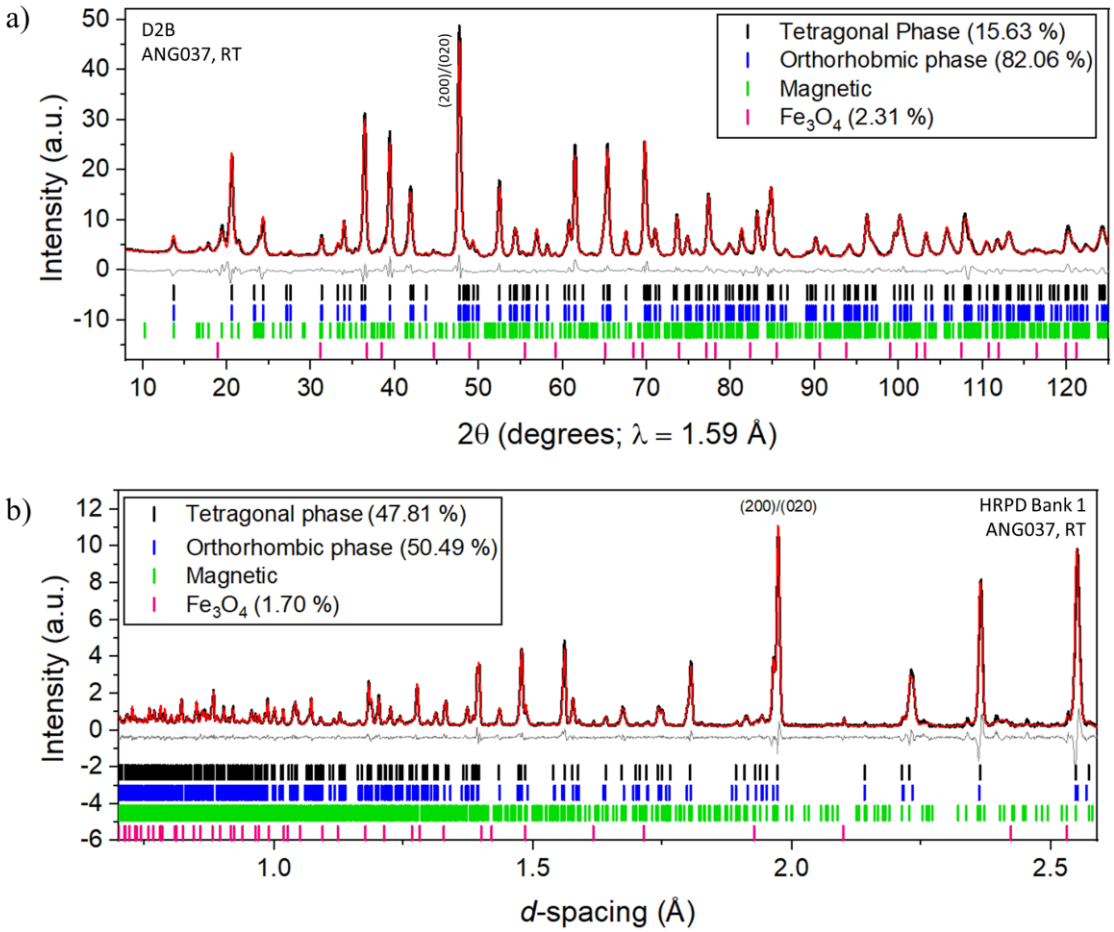


Figure 4.9. Rietveld refinements of room-temperature neutron diffraction patterns of $Sr_2CaFe_2O_5Fe_2OS_2$ (ANG037) collected on a) D2B and b) HRPD bank 1 showing the observed (black), calculated (red) and difference (grey) curves with the (200)/(020) reflections labelled.

Table 4.5. Comparison of refined structural parameters of $Sr_2CaFe_2O_5Fe_2OS_2$ (ANG037) from diffraction patterns collected on I11, D2B, and HRPD.

Beamline	I11		D2B	HRPD	
R_{wp} (%)	7.132		6.163	5.706	
Space Group	*P*4/*mmm*	*Pmmm*	*P*4/*mmm*	*P*4/*mmm*	*Pmmm*
wt %	48.47	51.53	98.76	47.80	50.50
a (Å)	3.94595(1)	3.92770(2)	3.93140(5)	3.95130(7)	3.9323(1)
b (Å)	3.94595(1)	3.94448(2)	3.93140(5)	3.95130(7)	3.9505(1)
a/*b*	1	0.99567(1)	1	1	0.99538(4)
c (Å)	13.36188(7)	13.3929(1)	13.3435(3)	13.3840(3)	13.4225(3)
V (Å^3)	208.051(2)	207.494(3)	206.236(8)	208.962(9)	208.51(1)
*occ*Ca1	0.000(9)	0.000(8)	0.01(2)	0.27(4)	0.00(5)
*occ*Ca2	0.454(6)	0.513(7)	0.31(2)	0.44(3)	0.34(4)
Calc x	0.94(1)	1.02(1)	0.63(4)	1.15(8)	0.69(9)
Sr2*z*	0.2270(1)	0.2274(1)	0.2285(1)	0.2267(2)	0.2308(3)
Fe1*z*	0.3588(1)	0.3573(1)	0.3593(1)	0.3596(1)	0.3581(2)
O1*z*	0.3380(3)	0.3384(2)	0.3408(1)	0.3392(2)	0.3418(2)
S1*z*	0.1308(2)	0.1252(1)	0.1307(3)	0.1229(5)	0.1348(5)

High-resolution neutron diffraction data was also collected for $Sr_{1.5}Ca_{1.5}Fe_2O_5Fe_2OS_2$ (ANG054, so different from the only orthorhombic x = 1.5 sample ANG048 described in section 4.2.3) on HRPD, and like for the x = 1 phase, the (200) and (020) peaks are resolved in the bank 1 pattern (Figure 4.10) and the refined parameters are in fair agreement with those obtained in the refinement of the SXRPD pattern (Table 4.6). The largest discrepancies come again from the *Ae* site occupancies, with the orthorhombic having more Ca on the *Ae*1 site than the tetragonal phase which is definitely different from the SXRPD refinements. In this case, the SXRPD refined values are deemed more reliable given that X-rays are most sensitive to the heavier elements like Ca and Sr in comparison to the lighter O and S (see Table 2.1 for reference). In fact, manually changing the refined occupancies on the *Ae* site did not noticeably change the refinement, only changing the R_{wp} by less than 0.01%. Overall, however, the high-resolution diffraction pattern doesn't reveal any other intricacies that may explain why the sample is multiphase or why the orthorhombic phase is distorted from a tetragonal symmetry and further work is needed, perhaps by way of TEM.

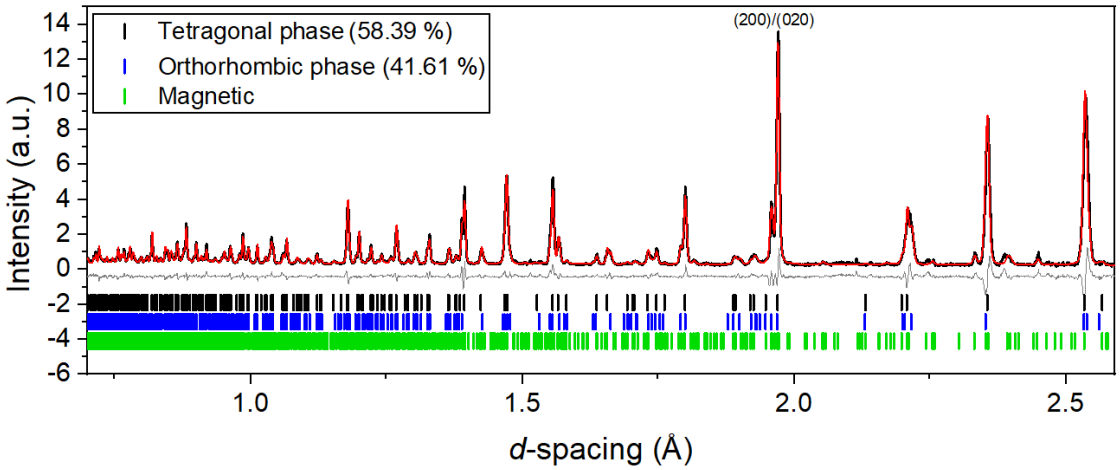


Figure 4.10. Rietveld refinement of room-temperature neutron diffraction pattern of $Sr_{1.5}Ca_{1.5}Fe_2O_5Fe_2OS_2$ (ANG054) collected on a HRPD bank 1 showing the observed (black), calculated (red) and difference (grey) curves with the (200)/(020) reflection labelled.

Table 4.6. Comparison of refined structural parameters of $Sr_{1.5}Ca_{1.5}Fe_2O_5Fe_2OS_2$ (ANG054) from diffraction patterns collected on I11, D2B, and HRPD.

Beamline	I11		HRPD	
R_{wp} (%)	6.254		6.940	
Space Group	*P4/mmm*	*Pmmm*	*P4/mmm*	*Pmmm*
wt %	54.48	45.52	58.39	41.61
a (Å)	3.93981(1)	3.91506 (2)	3.94491(7)	3.9207(1)
b (Å)	3.93981(1)	3.93645(3)	3.94491(7)	3.9433(1)
a/*b*	1	0.99457(1)	1	0.99427(5)
c (Å)	13.24715(9)	13.2890(1)	13.2649(3)	13.3145(4)
V (Å^3)	205.624(2)	204.804(3)	206.435(9)	205.85(1)
*occ*Ca1	0.106(7)	0.00(1)	0.18(3)	0.21(5)
*occ*Ca2	0.699(5)	0.770(8)	0.61(2)	0.54(3)
Calc x	1.50(1)	1.53(1)	1.41(6)	1.31(9)
Sr2*z*	0.2269(1)	0.2280(1)	0.2281(2)	0.2308(4)
Fe1*z*	0.3565(1)	0.3565(2)	0.3579(1)	0.3572(2)
O1*z*	0.3351(2)	0.3405(3)	0.3380(1)	0.3404(2)
S1*z*	0.1298(2)	0.1289(3)	0.1247(5)	0.1342(8)

4.2.5. Summary of structural trends

One thing that is evident across the solid solution $Sr_{3-x}Ca_xFe_2O_5Fe_2OS_2$ is that there are limits to the amount of Ca that can be included in the phase, as low values of *x* did not readily form clean products (with the exception of a sample with $x = 0.4$ that was characterised as a single-phase orthorhombic sample), values of *x* ranging from 1 to 1.7 normally formed multiphase products with a tetragonal and orthorhombic phase (although see below), and phases with *x* greater than 1.7 could not be formed due to a competing side product of $Ca_2Fe_{2.6}O_3S_2$ (Figure 6.1). This allows for the creating of a phase diagram found below in Figure 4.11, though it is rudimentary at best especially given that there is some sample variation in regards to the multiphase samples, as

shown by the x = 1.5 sample that is multiphase (ANG054: Table 4.3, Figure 4.10) and the x = 1.5 sample that is single-phase with only an orthorhombic phase (ANG048: Figure 4.7). Further work is definitely needed in order to fully map out the phase diagram, and the use of microscopy may be helpful in revealing as yet unexplained intricacies.

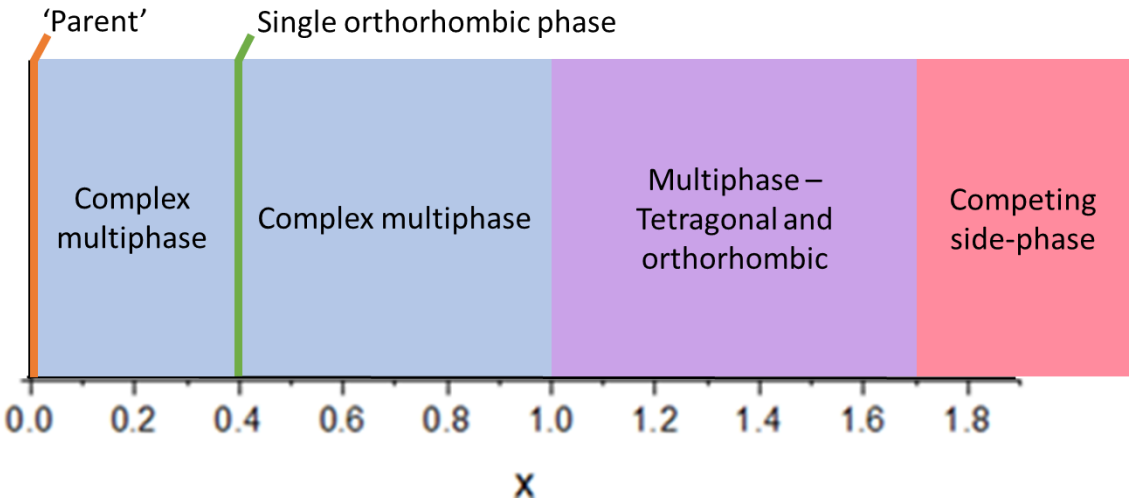


Figure 4.11. Rudimentary phase diagram of the solid solution $Sr_{3-x}Ca_xFe_2O_5Fe_2OS_2$ at room temperature.

Overall, there are not many other clear trends across the solid solution $Sr_{3-x}Ca_xFe_2O_5Fe_2OS_2$. There is clear cation ordering within the phases as Ca preferentially occupies the smaller *Ae*2 site and Sr preferentially occupies the larger *Ae*1 site, with the orthorhombic phase containing no Ca on the *Ae*1 site and the tetragonal phase containing more disorder on the *Ae*1 site. However, the site occupancies listed in Table 4.3 do not reveal clearly the reason for the formation of the different symmetry phases in the same sample, nor why the phase fractions vary for different samples made in similar ways with similar compositions. The only other clear trend is in the cell parameters themselves, as the cell parameters and volumes all decrease as expected as more of the smaller Ca cation is incorporated into the structure (Figure 4.12).

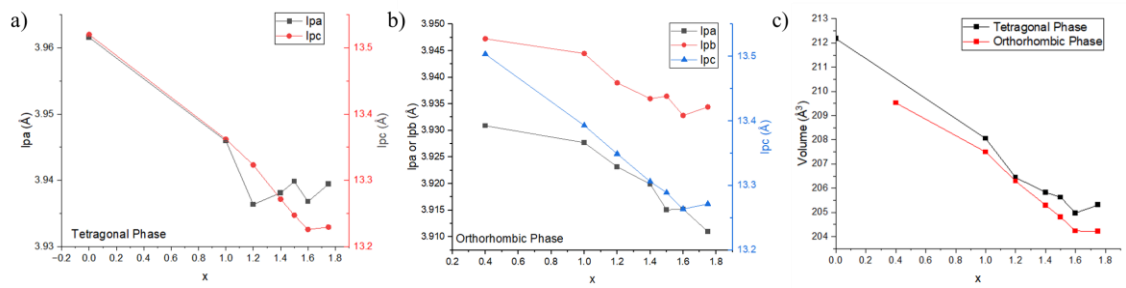


Figure 4.12. Lattice parameter trends for a) the tetragonal phase and b) the orthorhombic phase of the series $Sr_{3-x}Ca_xFe_2O_5Fe_2OS_2$ ($x < 1.75$) alongside c) the volume trends for both phases. All error bars are smaller than the data points.

4.3. Magnetic characterization and trends

4.3.1. Magnetometry

As for the $x = 0$ phase, the first investigation into the magnetic behaviour of $Sr_{3-x}Ca_xFe_2O_5Fe_2OS_2$ was carried out using SQUID magnetometry at high and low temperatures. The ZFC and FC susceptibility curves (Figure 4.13) show wide variation between samples, and there is no clear trend across the solid solution. The $x = 1$ and 1.5 phases show a low temperature transition around 25 K in the ZFC curves, but the $x = 1.75$ phase shows two transitions at slightly higher temperatures. The FC curve of the $x = 1.75$ phase is also abnormal. Some of these transitions may be from Ca-doped magnetite, as doping has been shown with several elements to reduce the Verwey transition temperature [4]. More data, such as low variable temperature neutron powder diffraction, is needed in order to determine if the transitions observed in these phases are characteristic of the phase itself or an artefact of a magnetic impurity. This is not abnormal, as since magnetometry is used to effectively measure how magnetic a sample is, small amounts of magnetic impurities can often complicate the data and increase the difficulty of interpretation.

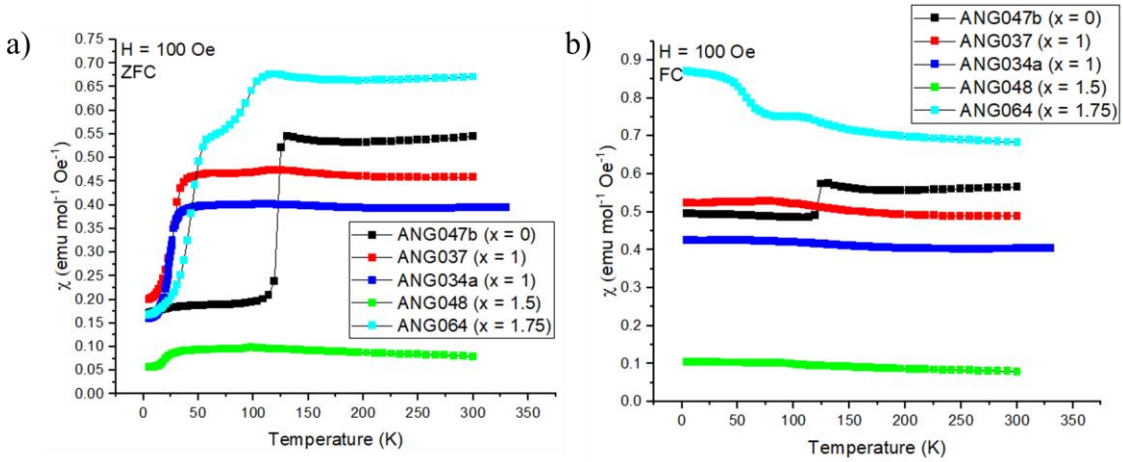


Figure 4.13. The a) zero-field cooled and b) field cooled susceptibility curves of several members of the $Sr_{3-x}Ca_xFe_2O_5Fe_2OS_2$ solid solution.

As for the susceptibility curves, the magnetization isotherms (Figure 4.14) likewise show no obvious trend across the solid solution. At 5 K, the x = 1.75 phase displays a strange shape that is somewhat reminiscent of the $Ca_2Fe_{2.6}O_3S_2$ impurity [2], but the shape persists to higher fields. One other feature that can be identified is that all of the 5 K isotherms are asymmetric about the origin, which indicates a spin-glassiness like the x = 0 phase, though there is no way to identify where this behaviour originates from without further investigation with other techniques.

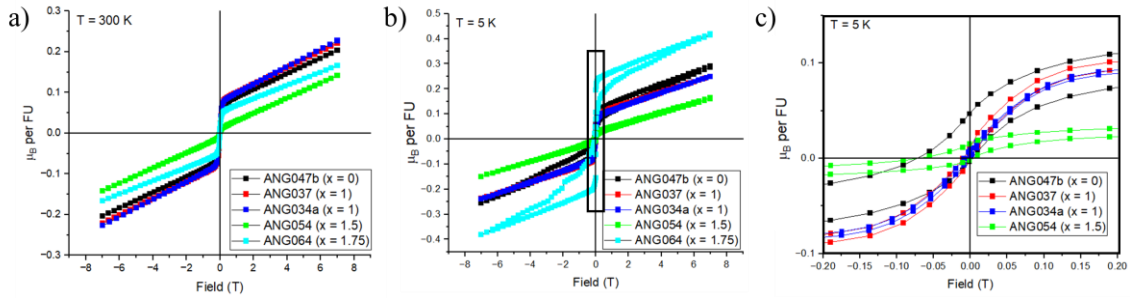


Figure 4.14. The *M vs H* isotherms of several members of the $Sr_{3-x}Ca_xFe_2O_5Fe_2OS_2$ solid solution at a) 300 K and b-c) 5 K.

The magnetometry measurement that was perhaps most revealing were the high temperature susceptibility curves measured from 300 to 800 K (Figure 4.15). This is because as x goes beyond 1.7, there is an evident transition around 320 K which is characteristic of the $Ca_2Fe_{2.6}O_3S_2$ [2]. This supports the evidence presented by XRD that beyond x = 1.7, there is a competing side phase of $Ca_2Fe_{2.6}O_3S_2$ that is formed in the synthesis. The other high-temperature transition is

also likely from magnetite or a magnetite-like phase containing a dopant that would lower the Curie temperature.

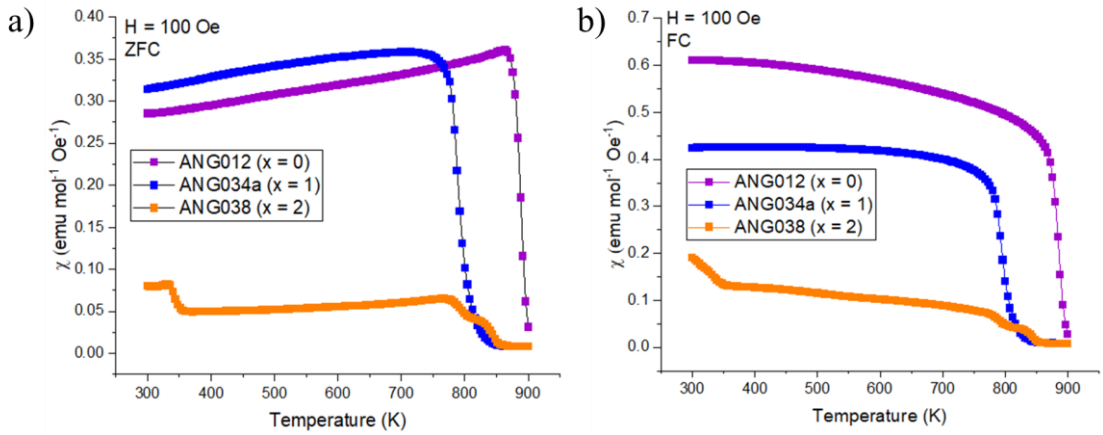


Figure 4.15. The high temperature a) ZFC and b) FC susceptibility curves of several members of the $Sr_{3-x}Ca_xFe_2O_5Fe_2OS_2$ solid solution from 300 to 900 K.

4.3.2. Room temperature NPD

Neutron powder diffraction was collected on D1B for $Sr_2CaFe_2O_5Fe_2OS_2$ (ANG037) and $Sr_{1.5}Ca_{1.5}Fe_2O_5Fe_2OS_2$ (ANG054) in order to investigate the magnetic structures and compare them with the parent $x = 0$ phase. The resolution of nuclear peaks on D1B does not allow for the differentiation between the orthorhombic and the tetragonal phases. Due to this, a single tetragonal nuclear phase was used in these refinements and the magnetic cell is fit to this tetragonal phase. Both phases have magnetic reflections at room temperature, and these magnetic peaks can be indexed on a $\sqrt{2}a \times \sqrt{2}a \times 2c$ supercell expansion. Both the $x = 1$ and $x = 1.5$ phases order in the same manner as the $x = 0$ phase, and the magnetism can be modelled using either the two-structure model or the single-phase twisting model as described in chapter 3.3.2. Using the twisting model, the magnetic moments for the $x = 1$ and 1.5 phases refine to be very similar to that of the $x = 0$ phase, and while the twisting angles vary more than the moments themselves, this is to be expected based on the sample dependence to the twisting angles that was shown for the $x = 0$ phase in Figure 3.33. The two-structure model and the single-phase twisting model are both depicted in Figures 3.26 and 3.27 respectively. The refined moments and angles for the $x =$ 0, 1, and 1.5 phases are listed in Table 4.7.

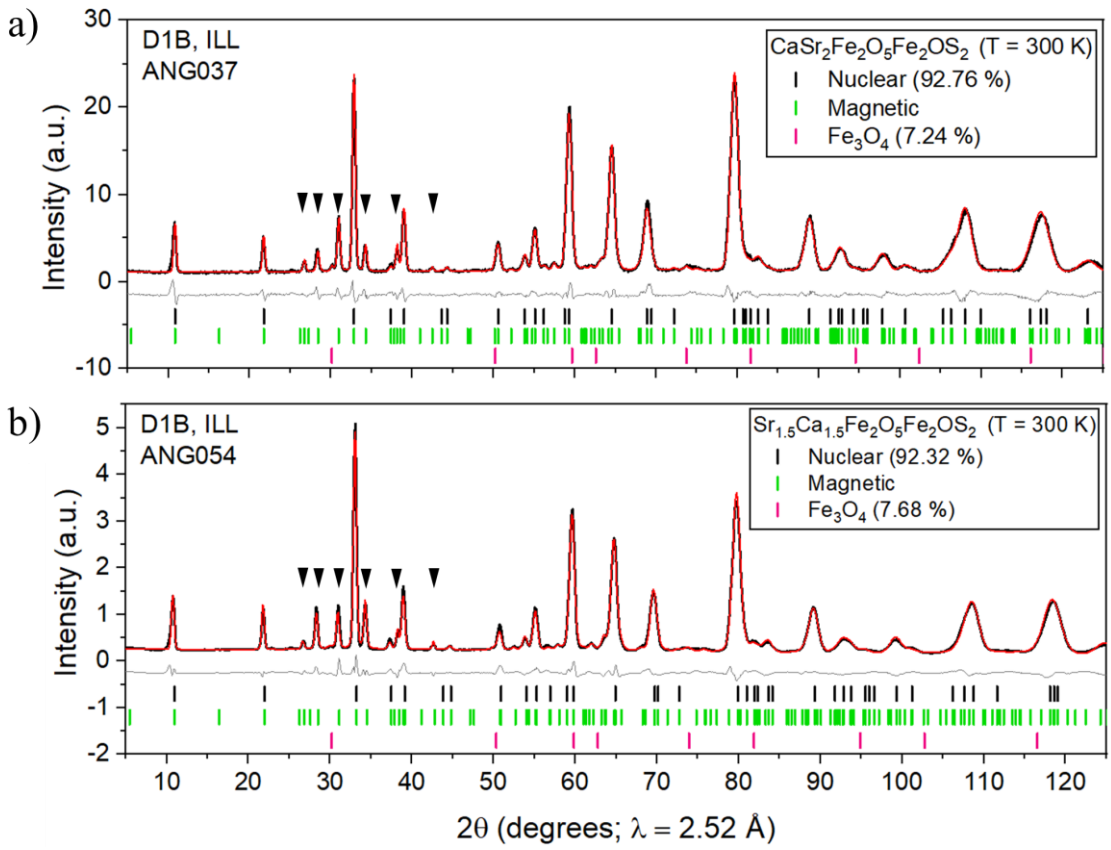


Figure 4.16. Refinement of room-temperature neutron diffraction patterns of the a) $x = 1$ and b) $x = 1.5$ phases showing the observed (black), calculated (red), and difference (grey) curves. Black triangles indicate the magnetic reflections.

Table 4.7. Comparison of the room temperature magnetic models of the $x = 0$, 1, and 1.5 phases.

x	0	1	1.5
Fe1 moment (μ_B)	3.58(4)	3.37(4)	3.48(4)
Twisting angle (°)	36.7(7)	17.6(7)	24.0(6)

4.3.3. Low variable temperature NPD

In addition to room-temperature, neutron diffraction patterns were collected at varying low temperatures on D1B for $Sr_2CaFe_2O_5Fe_2OS_2$ (ANG037) and $Sr_{1.5}Ca_{1.5}Fe_2O_5Fe_2OS_2$ (ANG054) in an effort to determine how the magnetic models change upon cooling. In both cases, there are new magnetic reflections that onset at 110 K and 115 K for the $x = 1$ and 1.5 phases respectively. This is reminiscent of the onset of magnetic order in the Fe2 layer of the $x = 0$ phase (chapter 3.3.3). Both phases also display growth of magnetic peaks on cooling like seen in the parent which saturates around 140-145 K and corresponds to the reorientation of the Fe1 moments in the basal plane (Figure 4.17) which has also been observed in the $x = 0$ phase. The $x = 1$ phase

also has one magnetic peak which diminishes on cooling around 28.4° (Figure 4.17a) and this also corresponds to the reorientation of the Fe1 moments within the basal plane and a change in the twisting angle.

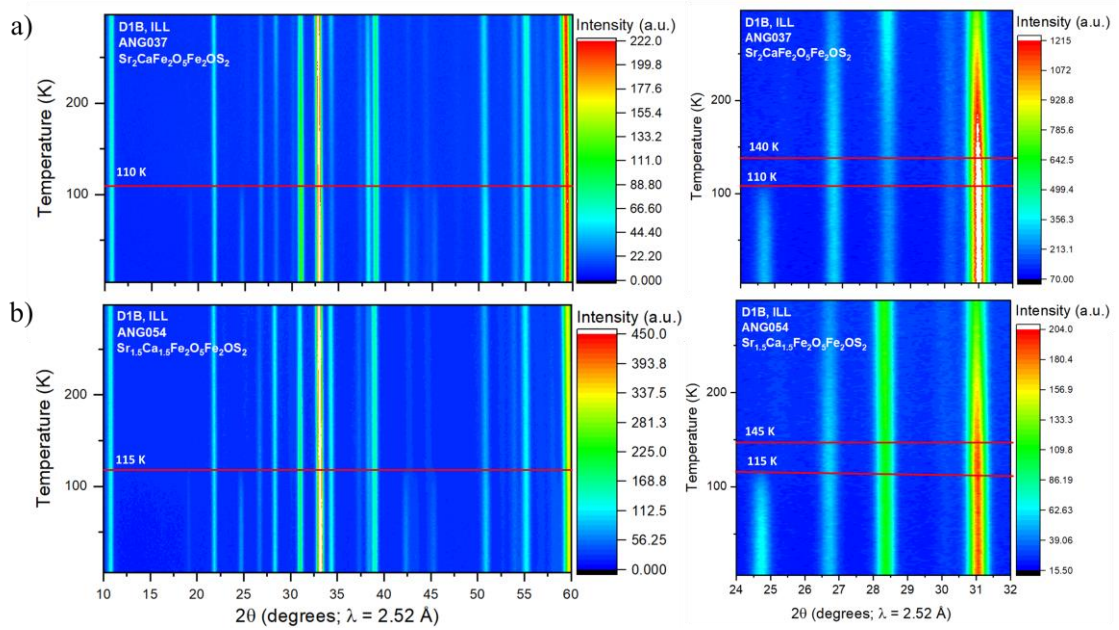


Figure 4.17. Contour plots of D1B diffraction patterns from the a) $x = 1$ and b) 1.5 phases alongside zoomed-in views that show the growth of the (310) magnetic peak around 26.5° for the $x = 1.5$ phase as well as the onset of magnetic reflections that correspond to the onset of long-range magnetic order in the Fe2 layer of each phase (right).

4.3.4. Low temperature NPD

As mentioned above in section 4.3.3., upon cooling there are additional magnetic reflections that appear around T = 110 K and 115 K for the $x = 1$ and 1.5 phases respectively, and these reflections correspond to the onset of long-range magnetic order in the Fe2 layer. These reflections can be indexed on a $2\sqrt{2}a \times 2\sqrt{2}a \times 2c$ supercell expansion like the $x = 0$ phase, as the Fe2 layer adopts the same magnetic structure as the $x = 0$ phase and many other phases that contain the same layer type [5-7]. The low temperature magnetic structure is depicted in Figure 3.32. All of the phases in the solid solution order in the same manner at low temperature in addition to room temperature and with relatively similar moments, with the smallest ordered moment being in the $x = 1$ phase, though further measurements are needed to determine if this from sample dependence or if this is a trend that can be observed across the solid solution from $x = 1$ to 1.7.

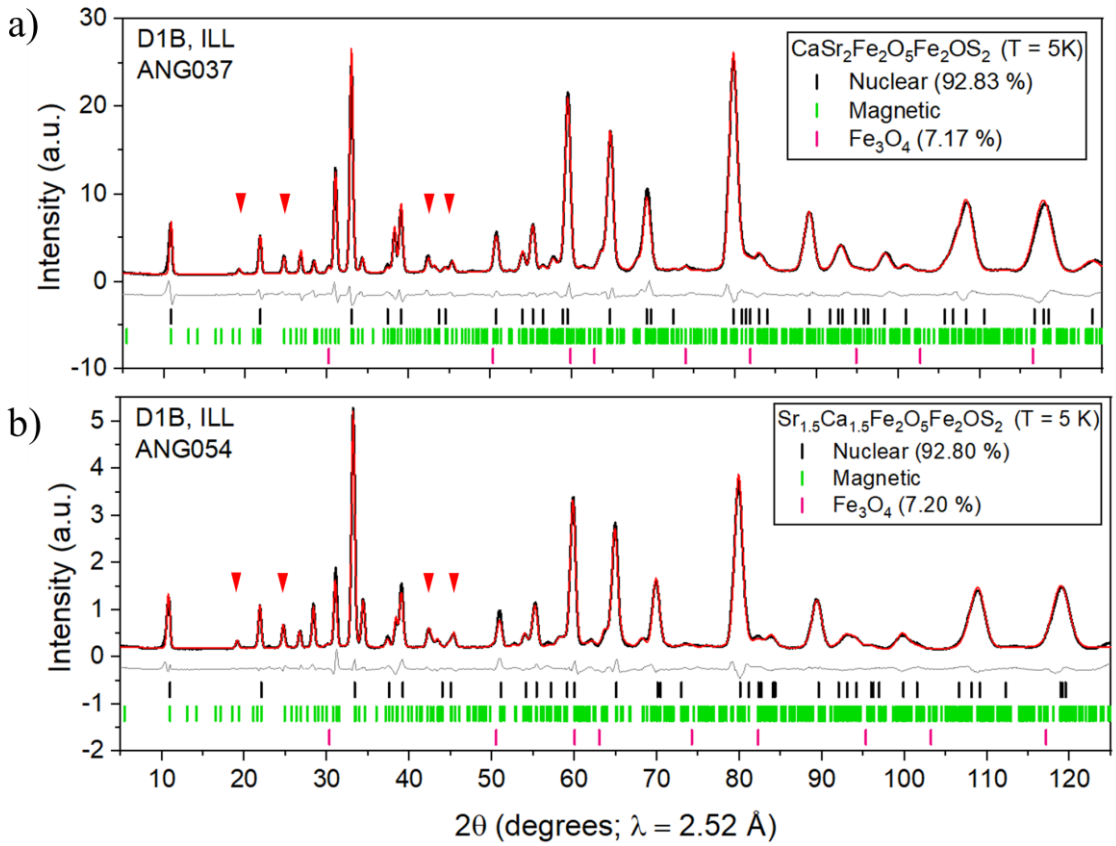


Figure 4.18. Refinement of 5 K neutron diffraction patterns of the a) $x = 1$ and b) $x = 1.5$ phases showing the observed (black), calculated (red), and difference (grey) curves. Red triangles indicate the new magnetic reflections present below 115 K but not at room temperature.

Table 4.8. Comparison of the low temperature magnetic models of the $x = 0$, 1, and 1.5 phases.

x	0	1	1.5
Fe1 moment (μ_B)	4.04(5)	3.72(4)	3.92(4)
Twisting angle (°)	42.4(8)	22.4(5)	40.3(5)
Fe2 moment (μ_B)	3.31(7)	2.50(5)	3.02(5)

4.4. Conclusions

As shown in Figure 4.12, there are some clear structural trends in the change of lattice parameters across the solid solution $Sr_{3-x}Ca_xFe_2O_5Fe_2OS_2$ in that they all decrease as more Ca is substituted for Sr. Nearly all of the samples are two-phase, with a tetragonal and an orthorhombic phase present in all samples with x between 1 and 1.7 with only one exception ($x = 1.5$ ANG048, section 4.2.3). However, the refined parameters show no clear indication as to the differences in these phases in terms of total Ca-content across the series, though it does seem that the orthorhombic

phase has consistently more Ca on the Ca1 site than the tetrahedral phase. There is also an upper limit to the amount of Ca that can be incorporated into the compound, as members with $x > 1.7$ formed a competing side-phase of $Ca_2Fe_{2.7-\delta}O_3S_2$. Further work is necessary in order to identify more clear trends involving this solid solution. For example, long-term annealing may equilibrate the orthorhombic and tetragonal phases into a single phase. However, given that VT-SXRPD shows that the phases are tetragonal at high temperatures and therefore during synthesis, it is more likely that there is something driving the orthorhombic distortion upon cooling which could be investigated by cooling rate experiments. High pressure studies would also be useful to investigate if the upper Ca-limit can be pushed further and more Ca can be added into the structure without the formation of the side phase. Both of these methods may also be able to synthesize more phases with $x < 1$ in high purity.

Magnetically, these materials also adopt the same magnetic structure as the $x = 0$ compound. Since only two samples were used in neutron powder diffraction experiments, no trends across the solid solution can be identified without further experiments. Additionally, the peaks in the data collected on D1B and D2B were not resolved enough to be able to distinguish between the orthorhombic and tetragonal phases, so identifying any potential differences in the magnetic structures of the orthorhombic and tetragonal phases would require experiments on instruments with better resolution. Instruments from spallation sources like WISH or HRPD-X (to be running in 2028) at ISIS Neutron and Muon Source would be ideal for this kind of experiment, as both are high-resolution neutron diffraction beamlines that cover low *d*-spacings [8,9]. HRPD in particular has been shown already to resolve the (200) and (020) reflections of the orthorhombic and tetrahedral phases (section 4.2.4), and after the upgrade to HRPD-X, the coverage at low 2θ is set to be improved so that the data showing the magnetic peaks (which currently are observed in bank 3 but with low S/N) will hopefully be available with a higher signal/noise ratio as well as with the high resolution.

References

[1] Sheath, B.C.; Cassidy, S.J.; Clarke, S.J. *J. Solid State Chem.* **2021**, *293*, 121761.
[2] Smyth, R.D.; Wilson, J.A.D.; Manuel, P.; Clarke, S.J. *J. Solid State Chem*. **2022**, *307*, 122841.
[3] Sheath, B.C. DPhil Thesis, University of Oxford, Exploring the Synthesis and Characterization of Oxychalcogenide, Oxypnictide and Chalcogenide Materials, 2023.
[4] Walz, F.; Kronmüller, H. *Phys. Rev. B.* **1998**, *58*, 14163.
[5] Oogarah, R.K.; Suard, E.; McCabe, E.E. *J. of Magn. Magn. Mater*. **2018**, *446*, 101–107.
[6] Zhao, L.L.; Wu, Se.; Wang, J.K.; Hodges, J.P.; Broholm, C.; Morosan, E. *Phys. Rev. B*, **2013**, *87*, 165111.
[7] McCabe, E.E.; Stock, C.; Rodrigues, E.E.; Wills, A.S.; Taylor, J.W.; Evans, J.S.O. *Phys. Rev. B*, **2014**, *89*, 100402.
[8] Chapon, L.C.; Manuel, P.; Radaelli, P.G.; Benson, C.; Perrott, L.; Ansell, S.; Rhodes, N.J.; Raspino, D.; Duxbury, D.; Spill, E.; Norris, J. *Neutron News*, **2011**, *22*, 22-25.
[9] Fortes, A.D.; Gibbs, A.S. *J. Neutron Res.* **2020.** *22*, 91-98.

Chapter 5: Topotactic reduction of $Sr_3Fe_2O_5Fe_2OS_2$

Contents

5.1. Introduction – Topotactic reduction of $Sr_3Fe_2O_5Cl_2$ 119
5.2. Synthesis 121
5.3. Structure Characterization 124
5.3.1. Room-temperature XRPD 124
5.3.2. Room-temperature neutron powder diffraction 128
5.3.3. Variable-temperature XRPD 134
5.4. Magnetic Characterization 137
5.4.1. Magnetometry 137
5.4.2. Room and Low temperature NPD 139
5.5. Further Characterization 145
5.5.1. XANES measurements 145
5.5.2. SEM-EDX 146
5.6. Conclusions 148
References 150

5.1. Introduction – Topotactic reduction of $Sr_3Fe_2O_5Cl_2$

The body-centred compound $Sr_3Fe_2O_5Cl_2$ was first reported in 1984 by Leib and Muller [1]. The phase is synthesized from binaries in air by use of a $SrCl_2$ flux, and it crystallizes in the *I*4/*mmm* space group [1,2]. In 2004, Knee *et al.* performed a neutron diffraction study and determined the structure to be an orthorhombic G-type antiferromagnet with a magnetic supercell of dimensions $\sqrt{2}a \times \sqrt{2}b \times c$ with moments of 3.74(4) μ_B per Fe centre directed within the *ab* plane and canted 39˚ from the *a* magnetic lattice vector at room temperature.

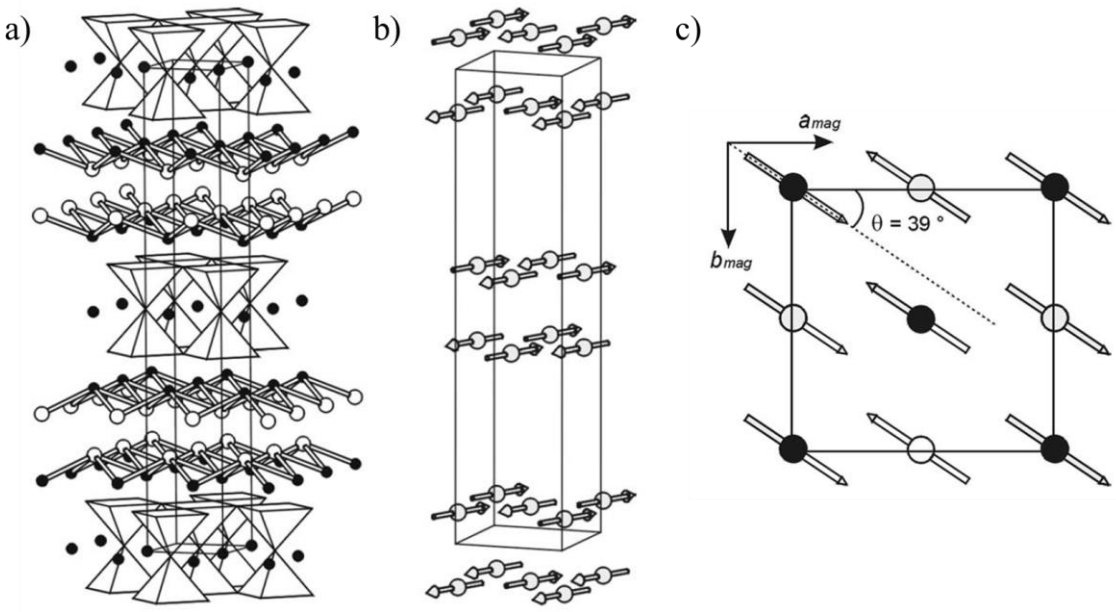


Figure 5.1. The nuclear (a) and magnetic (b) structure of $Sr_3Fe_2O_5Cl_2$ and the canting of the magnetic moments [3].

In 2010, Dixon and Hayward performed a topotactic reduction on this phase by use of LiH as a reducing agent to produce $Sr_3Fe_2O_4Cl_2$ [4]. Neutron diffraction was used to characterize the structure and magnetism of the new compound. In the room temperature nuclear structure, there was a comparative reduction in the *c* lattice parameter from 23.7969(2) Å to 22.653(1) Å and an expansion of the *a* lattice parameter from 3.94685(2) Å to 4.008(1) Å from the parent resulting in an overall reduction of the unit cell volume from 370.700(4) $Å^3$ to 364.01(1) $Å^3$ [3,4]. In addition to this, the occupancy of the axial bridging oxygen freely refined to zero with NPD which confirmed the stoichiometry of the product to be $Sr_3Fe_2O_4Cl_2$ with deintercalation of oxygen from the centre of the oxide slab. Magnetically, the phase was also found to order as a G-type antiferromagnet around 378 K with a moment of 2.81(9) μ_B per Fe centre at 5 K. This magnetic structure, unlike its parent, was reported to order with moments pointing along *c*.

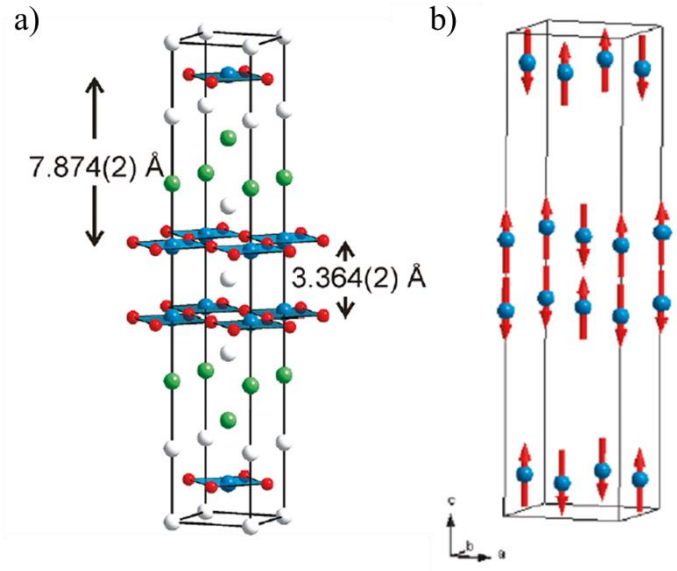


Figure 5.2. Nuclear (a) and magnetic (b) models of $Sr_3Fe_2O_4Cl_2$ [4].

The $[Sr_3Fe_2O_5]^{2+}$ layer in $Sr_3Fe_2O_5Cl_2$ that undergoes reduction in this topotactic reaction is the same layer type as in $Sr_3Fe_2O_5Fe_2OS_2$. This layer also exists in the phase $Sr_3Fe_2O_5Cu_2S_2$ [5], but the LiH would more likely reduce the Cu^+ cations in this phase, rather than the oxide slab. The motivation for the work in this chapter was to use LiH to reduce $Sr_3Fe_2O_5Fe_2OS_2$ to $Sr_3Fe_2O_4Fe_2OS_2$ and investigate the nuclear and magnetic structure of the product.

5.2. Synthesis

$Sr_3Fe_2O_4Fe_2OS_2$ was synthesized via the topotactic reduction of $Sr_3Fe_2O_5Fe_2OS_2$ using LiH as a reducing agent. In this reaction, the parent compound was initially ground in a 1:4 molar ratio with LiH (Thermo Scientific 99.4%) in an argon-filled glovebox, the powder transferred into a silica or Pyrex tube, sealed under dynamic vacuum while dipped in liquid nitrogen, and then placed in a furnace where it was heated at 2°C per minute to 300°C where it dwelled for 48 hours before being cooled back to room temperature at the natural rate of the furnace. This reaction produces H_2 gas in addition to Li_2O, so the amount of LiH must be controlled in order to prevent an explosion of the sealed vessel. Because of this, the vessel had to be periodically opened to alleviate any accumulated pressure and prevent a possible explosion. Therefore, multiple heating cycles were carried out with small excesses of LiH. Additionally, after each cycle the powders are re-ground with additional LiH (approximately 1-2 molar equivalences after each cycle to

maintain an excess) and then placed in a new vessel which is then evacuated, sealed, and heated once more. When the reaction seemed to have reached a point (as judged by XRPD) where most of the product is fully reduced, the reaction was deemed concluded to ensure that there was no danger in over-reducing and/or decomposing the sample.

When initially attempting the synthesis of this compound, various synthesis temperatures were investigated, starting at 250˚C, and the addition of more LiH at various stages in the synthesis was deemed necessary for the reaction to reach what was deemed to be completion. It was determined that the best synthesis method which generated the fewest impurities was several cycles of heating at a rate of 2˚C per minute to 300˚C and dwelling for 48 hours.

Table 5.1. Synthesis information for each aliquot in the reduction cycles for each sample referenced in the course of this chapter. Starred samples were used in neutron powder diffraction experiments.

Sample	Predecessor	Mol equiv LiH added	Dwell temp (°C)	Dwell time
ANG066b	ANG065a	4	250	48h
ANG066c	ANG066b	0	300	24h
ANG066d	ANG066c	0	315	24h
ANG066e1	ANG066d	0	350	36h
ANG066e2	ANG066d	1	315	36h
ANG066f1	ANG066e1	1	370	48h
ANG066f2	ANG066e2	0	370	48h
ANG066g1	ANG066f1	wash and filter		
ANG066g2	ANG066f2	wash and filter		
ANG086a	ANG080	4	300	48h
ANG086b	ANG086a	2	300	48h
ANG086c	ANG086b	0	300	48h
ANG086d	ANG086c	1	300	48h
ANG086e	ANG086d	1	300	48h
ANG086f*	ANG086e	wash and filter		
ANG087a	ANG081	4	300	48h
ANG087b	ANG087a	2	300	48h
ANG087c	ANG087b	0	300	48h
ANG087d*	ANG087c	wash and filter. Oxidized at some point after HRPD experiment		
ANG087e	ANG087d	2	300	48h
ANG087f	ANG087e	1	300	48h
ANG087g*	ANG087f	wash and filter		

In-house X-ray powder diffraction was initially used to verify that the reaction had progressed, and changes in the peak shapes and locations clearly indicated that the reaction had indeed

progressed, especially when considering the position of the main (104) peak located around 35° in the parent material shifting to around 36° in the fully reduced material.

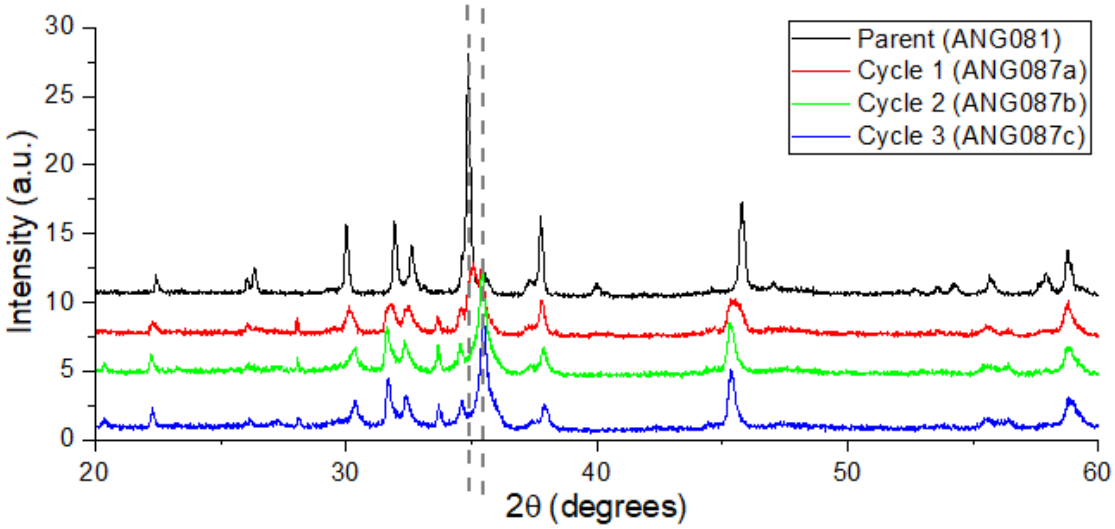


Figure 5.3. In-house (λ = 1.5460 Å) X-ray powder diffraction patterns of sample ANG087 collected after sequential cycles in the reduction process.

The product in this synthesis is air-sensitive, and within 30 minutes of removing the lid on the X-ray sample holder, there is a slight shift in peak positions that can be observed in the in-house powder diffractometry that only becomes more evident over time as the air-exposed sample oxidises back towards the stoichiometry of the parent material.

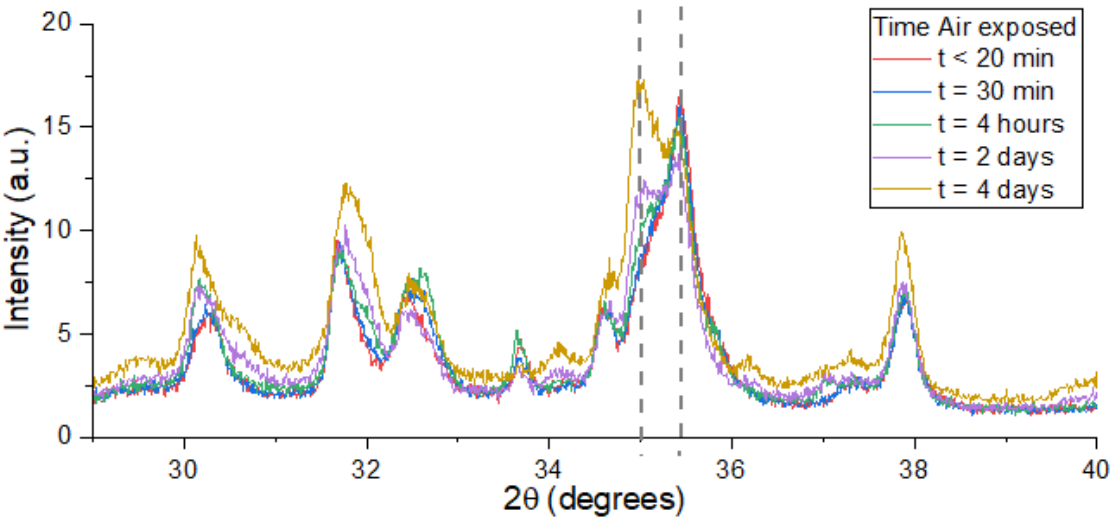


Figure 5.4. X-ray powder diffraction patterns of $Sr_3Fe_4O_{5-\delta}Fe_2OS_2$ (ANG066d) collected in-house (λ = 1.5460 Å) after different periods of time exposed overlaid.

The product from the heating cycles does contain Li_2O and excess LiH (as seen in the X-ray diffraction patterns), but these can be removed by washing the powder with anhydrous methanol

(Alfa Aesar 99.9%) under a N_2 atmosphere on a Schlenk line and filtering off the liquid. Annealing at both 900°C and 500°C was attempted on small portions of product in an attempt to increase crystallinity, but the samples instead decomposed into $Sr_4Fe_4O_7S_2$ (Figure 1.15e) and binaries in the case of the 900°C anneal and the parent and binaries in the case of the 500°C anneal.

Due to the decrease in crystallinity and broadening of diffraction peaks that is often observed in topotactic reactions, in-house X-ray diffraction was insufficient to fully visualize how the reaction changed from one heating cycle to the next. With this in mind, aliquots were saved from each cycle in order to obtain synchrotron X-ray diffraction patterns at higher resolutions and with higher intensity better suited for detecting small changes in lattice parameters and resolving multi-phase samples.

5.3. Structure Characterization

5.3.1. Room-temperature XRPD

As the reaction progresses from cycle to cycle, the diffraction peaks show a clear change in lattice parameters as the sample changes from the parent phase to an intermediate mixture of partially reduced phases and the fully reduced $Sr_3Fe_4O_5S_2$ phase. The peak corresponding to the fully reduced phase grows as cycles progress until its intensity reaches a plateau and the reaction doesn't seem to proceed any farther.

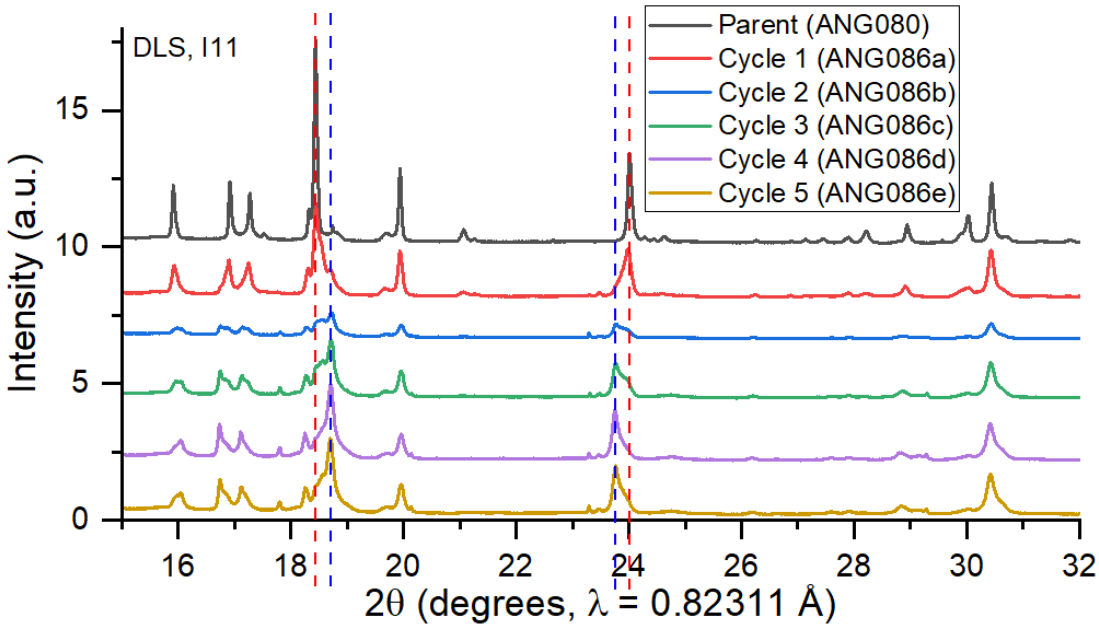


Figure 5.5. Synchrotron X-ray powder diffraction patterns of aliquots taken after successive cycles in the reduction of $Sr_3Fe_4O_6S_2$ to $Sr_3Fe_4O_5S_2$ (ANG086). Dashed lines reference the main peak positions of the parent (red) and fully reduced (blue) phase. The greater resolution obtained in the synchrotron diffraction patterns shows that the reaction has indeed plateaued after 4 cycles.

However, despite the reaction having plateaued after the fifth cycle in the case of ANG086 and no longer showing any significant changes in the X-ray diffraction pattern, the peak shapes (for example see the reflection at $2\theta = 24^{\circ}$ in Figure 5.5 which is the (200) reflection) suggests that there is still more than one phase present and multiple phases are indeed needed in the Rietveld refinements in order to fit the peak shapes. More LiH was added to the reaction between cycles 4 and 5, but there was no significant change in the diffraction patterns and increasing the synthesis temperature in an effort to push the reaction past this plateau results in the beginnings of decomposition.

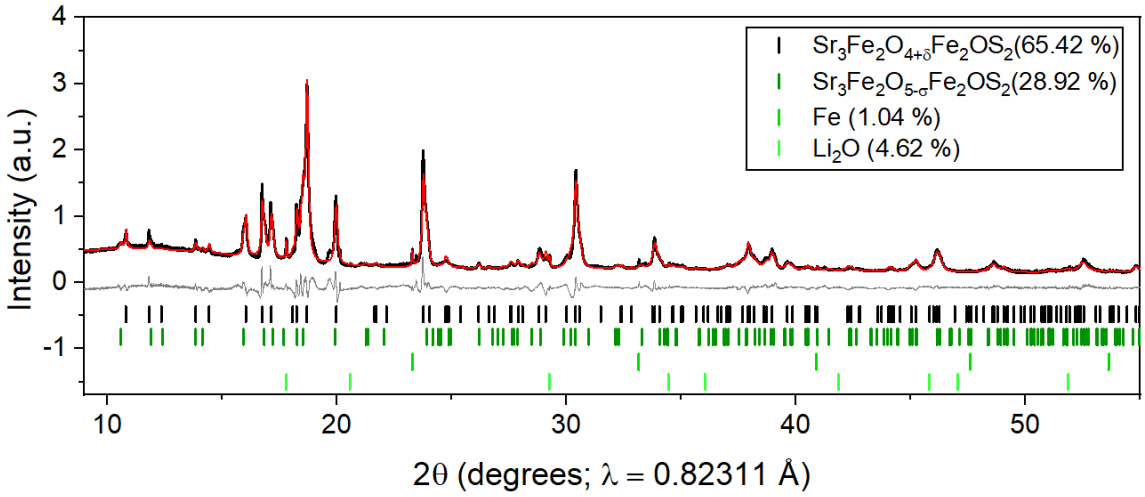


Figure 5.6. Rietveld refinement of the XRPD pattern of washed $Sr_3Fe_2O_4Fe_2OS_2$ (ANG086e) measured on the PSD detector on I11 at room temperature showing the observed (black), calculated (red) and difference (grey) curves.

Table 5.2. General **s**tructural model for $Sr_3Fe_2O_{4-\delta}Fe_2S_2$. Fully characterized model given in Table 5.4

Space Group = *P*4/*mmm* (No. 123)					
atom	site	*x*	*y*	*z*	occupancy
Sr1	1*b*	0	0	½	1
Sr2	2*g*	0	0	*z*Sr2	1
Fe1	2*h*	½	½	*z*Fe1	1
Fe2	2*f*	½	0	0	1
O1	4*i*	½	0	*z*O1	1
O2	1*a*	0	0	0	1
O3	1*d*	½	½	½	*occ*O3
S	2*h*	½	½	*z*S	1

Table 5.3. Structural parameters refined from SXRPD pattens collected on I11 at DLS for aliquots taken in the reduction of $Sr_3Fe_4O_6S_2$ to $Sr_3Fe_4O_5S_2$ (ANG086). For the sake of simplicity, a maximum of three phases are refined for each data set. All refined structures are in the *P*4/*mmm* space group.

	ANG080	ANG086a			ANG086b		
		Phase A	Phase B	Phase C	Phase A	Phase B	Phase C
R_{wp} (%)	8.808		7.945			4.603	
wt %	96.20	41.04	41.25	17.47	15.28	31.24	52.10
a (Å)	3.96493(2)	3.96814(5)	3.9799(1)	3.9945(2)	3.9689(1)	3.9865(1)	4.0032(9)
c (Å)	13.5382(1)	13.5299(3)	13.3839(8)	13.135(1)	13.502(1)	13.323(1)	13.106(5)
V (Å^3)	212.831(3)	213.045(8)	212.00(2)	209.59(3)	212.69(2)	211.75(2)	210.03(1)
*z*Sr2	0.22652(8)	0.2260(1)	0.2321(3)	0.2464(5)	0.2281(5)	0.2349(4)	0.2403(2)
*z*Fe1	0.3624(3)	0.3639(2)	0.3671(5)	0.3618(6)	0.3609(9)	0.3691(6)	0.3613(3)
*z*O1	0.3422(3)	0.3409(6)	0.338(1)	0.3618(6)	0.343(1)	0.347(1)	0.3613(3)
*z*S	0.1268(2)	0.1278(4)	0.134(1)	0.120(1)	0.118(1)	0.1479(9)	0.1206(6)
*occ*O3	1	1	0.42(5)	0.27(8)	1	0.27(5)	0.23(3)

	ANG086c			ANG086d		ANG086e	
	Phase A	Phase B	Phase C	Phase B	Phase C	Phase B	Phase C
R_{wp} (%)		6.573		7.571		7.310	
wt %	13.48	30.52	55.59	21.66	72.63	28.92	65.42
a (Å)	3.9694(1)	3.9869(1)	4.00381(8)	3.9768(2)	3.99907(7)	3.9742(2)	3.99732(7)
c (Å)	13.5145(9)	13.329(1)	13.1104(4)	13.365(1)	13.0955(4)	13.379(1)	13.1037(4)
V (Å^3)	212.94(2)	211.87(2)	210.16(1)	211.37(4)	209.43(1)	211.32(2)	209.38(1)
*z*Sr2	0.2268(4)	0.2326(4)	0.2386(2)	0.2325(4)	0.2375(1)	0.2302(3)	0.2371(1)
*z*Fe1	0.3603(7)	0.3691(6)	0.3633(2)	0.3651(7)	0.3634(2)	0.3650(5)	0.3628(2)
*z*O1	0.345(2)	0.351(1)	0.363392)	0.338(2)	0.3634(2)	0.338(1)	0.3628(2)
*z*S	0.1190(9)	0.136(1)	0.1227(4)	0.126(1)	0.1257(4)	0.126(1)	0.1256(4)
*occ*O3	1	0.38(6)	0.287(3)	0.29(9)	0.30(3)	0.51(6)	0.35(3)

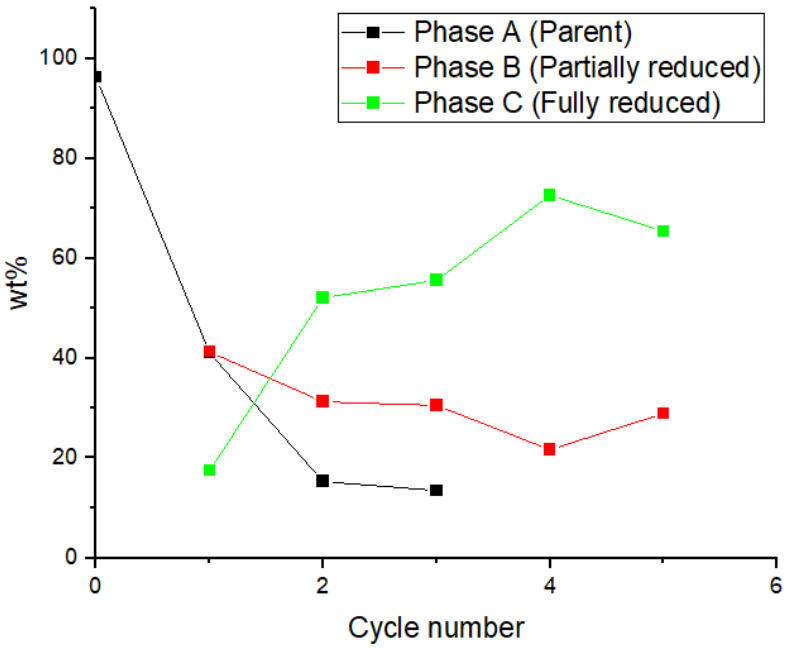


Figure 5.7. Evolution of phases A, B, and C throughout the reduction of sample ANG086.

In the refinements above, all of the relevant lattice parameters and site occupancies of the three phases were allowed to freely refine after copying the refinement from the previous member in the reduction. Alternatively to this, the lattice parameters and structures of phase A and C can be fixed according to the refinements of ANG080 and ANG086e respectively since the peak positions of the parent and the fully reduced phase do not seem to change across cycles. In this treatment, by only allowing the structure of phase B, the peak shapes of phases A and C, and the relative amount of each phase present in each sample to refine, we find a very similar trend with A gradually disappearing over the cycles until cycle 4, B remaining relatively steady with the O3 occupancy decreasing, and C gradually increasing in fraction over the course of subsequent cycles. A comparison of the refinements with parameters of phases A and C fixed versus freely

refining can be found in Figure 5.8 and shows that there is no significant difference in the two methods.

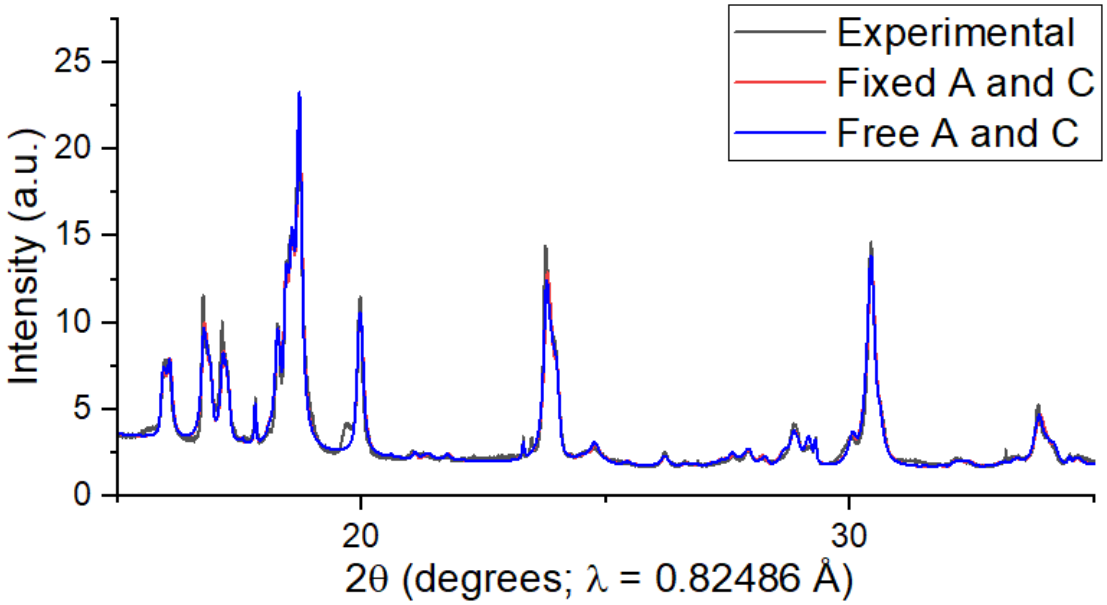


Figure 5.8. A comparison of the refinements of ANG086c when the parameters of phases A and C are fixed versus freely refined.

As the reaction progresses, it is evident from the refinements that the amount of the parent structure definitely decreases and that there is certainly more than one phase present. However, the details of these phases, especially as it pertains to the oxygen occupancy on the *O*3 site, is difficult to resolve from the powder X-ray diffraction data. The refined oxygen occupancies are imprecisely determined from the SXRPD patterns due to the lack of sensitivity of this technique to light elements. Therefore, neutron powder diffraction was used in an attempt to fully characterize the product of the reduction of $Sr_3Fe_2O_5Fe_2OS_2$.

5.3.2. Room-temperature neutron powder diffraction

Given that X-ray scattering cross section varies with atomic number, X-rays are more sensitive to heavier elements, and that oxygen is the lightest element in the phase $Sr_3Fe_2O_{5-\delta}Fe_2OS_2$ and it is also the element that is changing its contribution to the scattering the most, neutrons are more appropriate to quantify the occupancy of oxygen on the O3 site as well as that of the other oxygen sites, which could plausibly also be changing in the reactions. With this in mind, preliminary

room-temperature high-resolution neutron powder diffraction data was collected on HRPD to investigate in more depth the oxygen positions and occupancies.

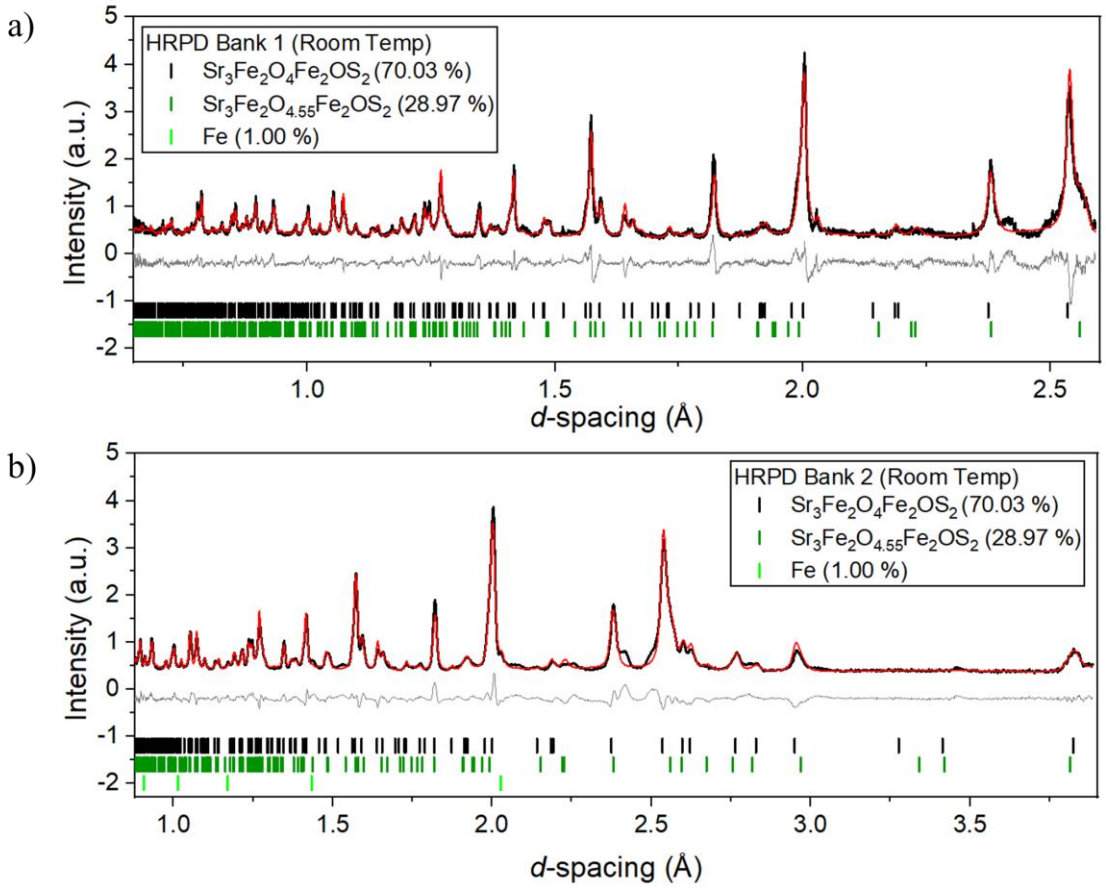


Figure 5.9. Rietveld refinement of the NPD patterns of $Sr_3Fe_2O_4Fe_2OS_2$ (ANG087d) measured on HRPD bank 1 (a) and 2 (b) at room temperature showing the observed (black), calculated (red) and difference (grey) curves.

There are several things that can be taken from this diffraction pattern. The first is that there are no extra peaks apparent so it appears as if the reduced phase may no longer be magnetically ordered at room temperature. There is a side peak that is not fit by the refinement around 2.35 Å, but this is also seen in the X-ray diffraction patterns (Figure 5.8) and belongs to a side phase that cannot be identified or is a diffuse feature that has yet been unindexed. However, using these data, the presence of a magnetic phase cannot be entirely eliminated due to the larger signal-to-noise ratio in bank 3 of HRPD which covers the longer *d*-spacings where magnetic peaks would be expected to arise (HRPD is not the optimal instrument for probing magnetic ordering). Secondly, there is no peak splitting which would have indicated a lowering of symmetry so we can conclude that there was no perovskite-like twisting in the oxygen planes/pyramids, especially

given that HRPD is optimized for this type of investigation due to its high resolution. In addition to this, the peak shapes show evidence of multiple phases, as clearly evidenced by the (104) and (200) peaks in Figure 5.10. These phases are a fully reduced phase (phase C) and a partially reduced phase (phase B) that has not fully reacted as the X-ray diffraction indicated.

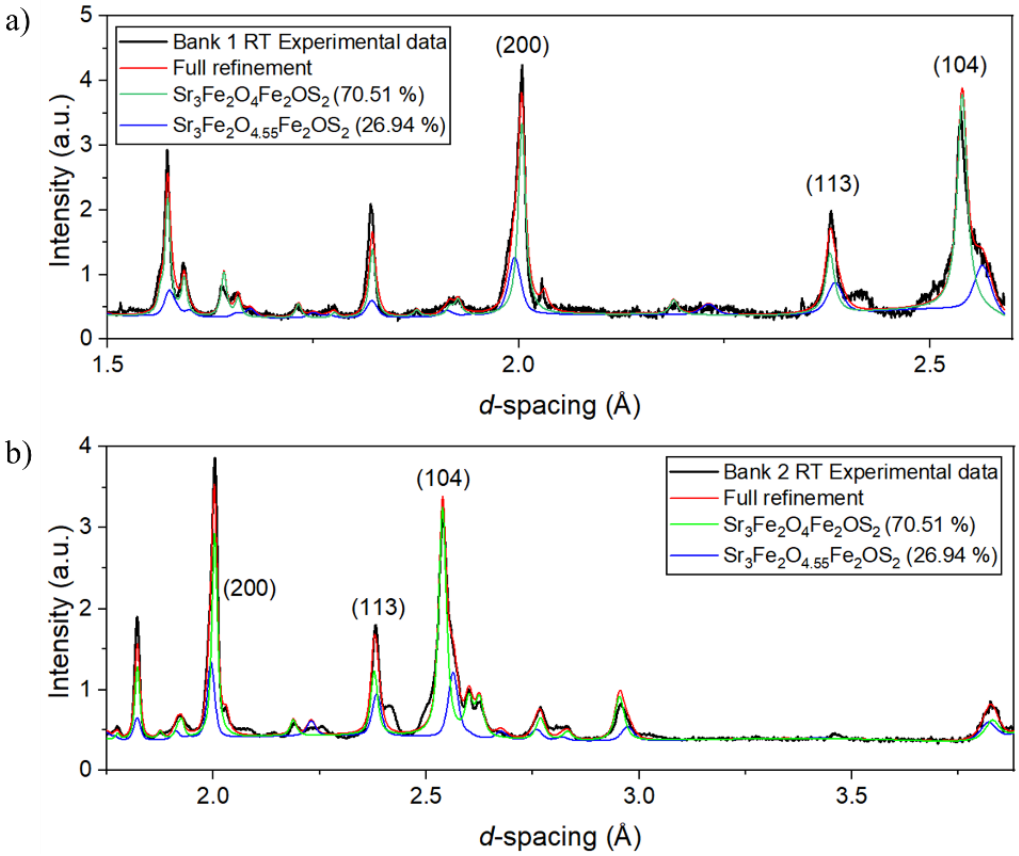


Figure 5.10. Components of the refinement of $Sr_3Fe_2O_4Fe_2OS_2$ (ANG087d) on HRPD bank 1 (a) and bank 2 (b).

Table 5.4. Refined structural parameters for the two phases present in ANG087d from HRPD compared to the I11 refined parameters. Phase C is the fully reduced $Sr_3Fe_2O_4Fe_2OS_2$ and Phase B is the partially reduced $Sr_3Fe_2O_{5-\delta}Fe_2OS_2$ as in section 5.3.1. These refinements used isometric displacement parameters.

	HRPD		I11	
P4/mmm	Phase C	Phase B	Phase C	Phase B
wt %	70.03	28.97	60.84	38.13
a (Å)	4.0049(1)	3.9874(3)	4.0011(1)	3.9801(2)
c (Å)	13.1232(5)	13.380(2)	13.1203(5)	13.378(1)
V (Å^3)	210.49(1)	212.73(5)	210.04(1)	211.93(3)
*z*Sr2	0.2345(3)	0.2248(8)	0.2385(2)	0.2305(3)
*z*Fe1	0.3655(2)	0.3660(6)	0.3642(2)	0.8663(5)
*z*O1	0.3652(3)	0.3511(5)	0.3642(8)	0.338(1)
*z*S	0.1125(9)	0.110(2)	0.1261(5)	0.130(1)
*occ*O3	0.00(1)	0.62(4)	0.07(3)	0.31(6)

Further powder diffraction measurements were performed on the GEM diffractometer at ISIS. This has a lower resolution in *d*-spacing than HRPD (as discussed in Chapter 2), but produces more informative data at longer *d*-spacings enabling magnetic scattering to be analysed. The room-temperature neutron diffraction pattern collected on GEM confirms what the HRPD refinements suggest: that two distinct phases are needed to fully fit the pattern (evident in the (104) peak). The refined parameters for ANG086d are listed in Table 5.4 alongside the refined parameters of ANG087d from SXRPD on I11 for comparison. In both diffraction patterns, there are clearly two phases present which are the fully (C) and partially reduced (B) phases. The refined parameters are also very similar, though the oxygen positions and occupancies are more accurately determined via HRPD given that neutrons have a larger scattering cross section compared to the heavier elements than X-rays do. One small difference in the two refinements from the same sample in these separate measurements on I11 and HRPD though is the ratio of phase B to phase C, but this can be accounted for by the fact that the peaks for the two phases are more well-resolved in the HRPD patterns given its high-resolution. This means that overall, the HRPD refinement likely gives a more accurate reflection of the composition of the sample.

Aside from the differences in the individual samples, the main difference between the HRPD and GEM data sets is that there are clear magnetic peaks at long d-spacings evident in the room temperature GEM pattern, and these are discussed more in-depth in section 5.4.2.

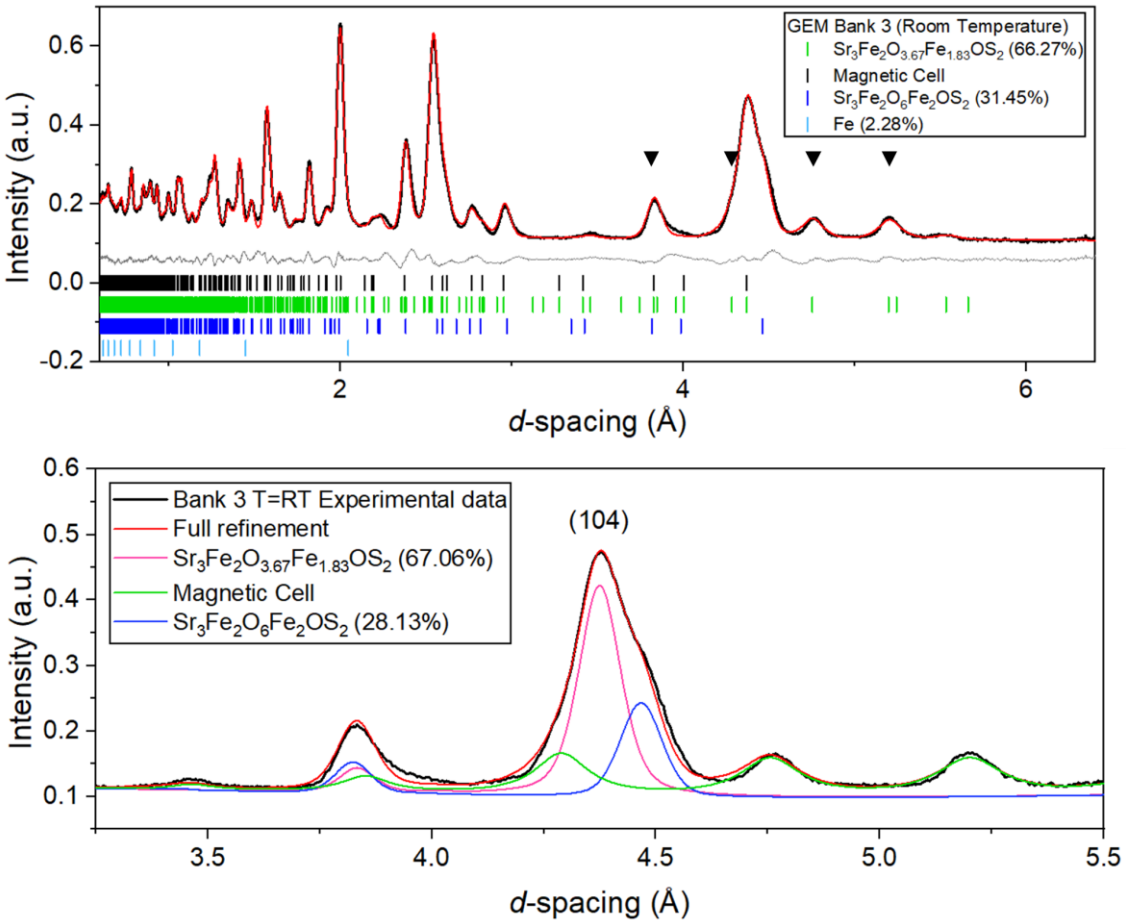


Figure 5.11. Rietveld refinement of the NPD pattern of $Sr_3Fe_2O_4Fe_2OS_2$ (ANG086f) measured on GEM bank 3 at room temperature showing the observed (black), calculated (red) and difference (grey) curves above a breakdown of the refinement of the (104) peak. Magnetic reflections indicated with black triangles.

Table 5.5. Refined structural parameters for the two phases present in ANG086f from GEM and ANG087d from HRPD data.

*P*4/*mmm*	$Sr_3Fe_2O_{4-\sigma}Fe_2OS_2$		$Sr_3Fe_2O_{5-\delta}Fe_2OS_2$	
	ANG086f GEM	ANG087d HRPD	ANG086f GEM	ANG087d HRPD
wt %	66.07	70.03	30.83	28.97
a (Å)	4.00218(7)	4.0049(1)	3.9843(1)	3.9874(3)
c (Å)	13.1075(4)	13.1232(5)	13.382(1)	13.380(2)
V (Å^3)	209.94(1)	210.49(1)	212.45(2)	212.73(5)
*z*Sr1	0.2373(2)	0.2345(3)	0.2279(4)	0.2248(8)
*z*Fe1	0.3657(2)	0.3655(2)	0.3657(2)	0.3660(6)
*z*O1	0.3635(2)	0.3652(3)	0.3471(2)	0.3511(5)
*z*S	0.1199(8)	0.1125(9)	0.133(1)	0.110(2)
*occ*Fe2	0.911(3)	0.975(7)	1	1
*occ*O1	0.926(4)[1]	0.906(8)[1]	1	1
*occ*O3	0.00(1)	0.00(1)	0.80(2)	0.62(4)

[1]Note that errors obtained from the refinements are usually an underestimate of the true uncertainties.

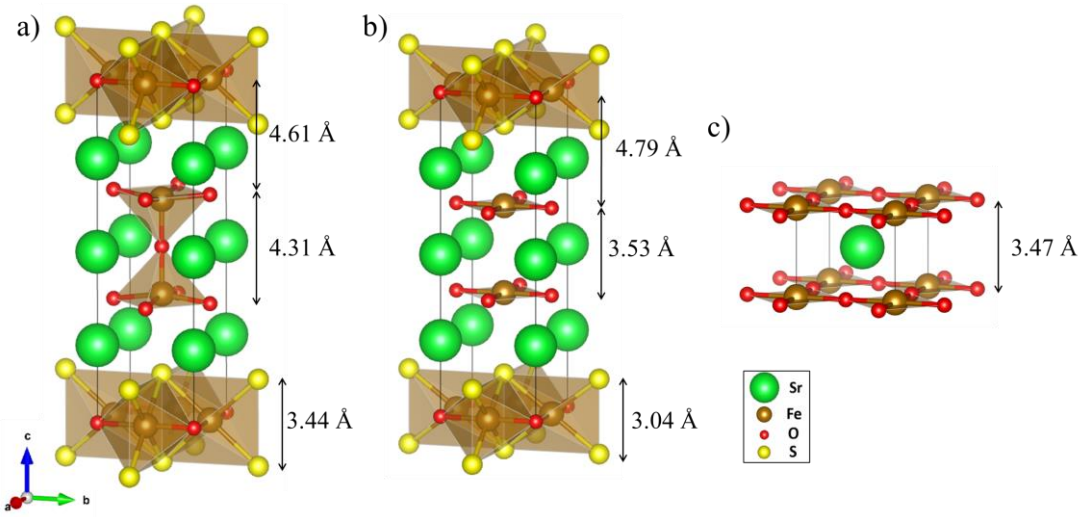


Figure 5.12. Comparison of the refined room-temperature nuclear structures of (a) $Sr_3Fe_2O_5Fe_2OS_2$, (b) $Sr_3Fe_2O_4Fe_2OS_2$ and (c) $SrFeO_2$ [6].

Table 5.6. Comparison of bond valence sums calculated for the Fe1 and Fe2 sites of $Sr_3Fe_2O_4Fe_2OS_2$ and $Sr_3Fe_2O_5Fe_2OS_2$ at room temperature.

Cation	Anion	BVS contribution	BVS $Sr_3Fe_2O_4Fe_2OS_2$	BVS $Sr_3Fe_2O_5Fe_2OS_2$
Fe1	O1	4 × 0.5178	2.128	2.876
	S1	1 × 0.0417		
Fe2	O2	2 × 0.4840	2.446	2.134
	S1	4 × 0.3693		

Some other interesting changes to note from the parent to the reduced compound are that the *a* lattice parameter expands slightly while the *c* lattice parameter contracts as is expected both from removing an oxygen and from comparison with similar phases [4]. Investigating the distances between atoms within layers, the largest decrease in the *c* lattice parameter comes from the removal of the oxygen on the O3 site, as the distance between *O*1 sites decreases by around 0.8 Å to 3.53 Å, which is very similar to the distances between nearest-neighbour oxygens in the *c* direction in the phase $SrFeO_2$ [6]. The thickness of the Fe2 layer, as judged by the distance between sulfide planes, has also decreased by 0.4 Å, which could be potentially due to the removal of some Fe or O from the layer due to over-reduction or decomposition. Indeed, there is some indication that there may be a deficiency of a few percent on the Fe2 and O2 sites, but given strong parameter correlations it is hard to be certain. In addition to this, the bond valence sums (Table 5.5) clearly indicate a much lower Fe1 oxidation state which supports the conclusion

that the reduction of the Fe1 iron occurs from Fe^{3+} to Fe^{2+} by oxygen deintercalation from the O3 site.

5.3.3. Variable-temperature XRPD

Variable temperature X-ray powder diffraction data was collected for the washed sample ANG087d using the PSD detector on I11. The planned temperature range for this experiment was from 25°C to 600°C, but due to instrument programming crashes, the complete temperature range was not collected in a continuous first pass. Instead, data was collected continuously from 25°C to 200°C, during which no decomposition or structural transitions were observed. The data collection stopped due to a program crash while the sample continued heating to 370°C before the crash was noticed and the heating program stopped. At this point, the sample was cooled back to room-temperature and another PSD scan revealed that by 370°C, the sample had undergone some decomposition into some partially reduced phase, some parent and a bit of SrS (Figure 5.13).

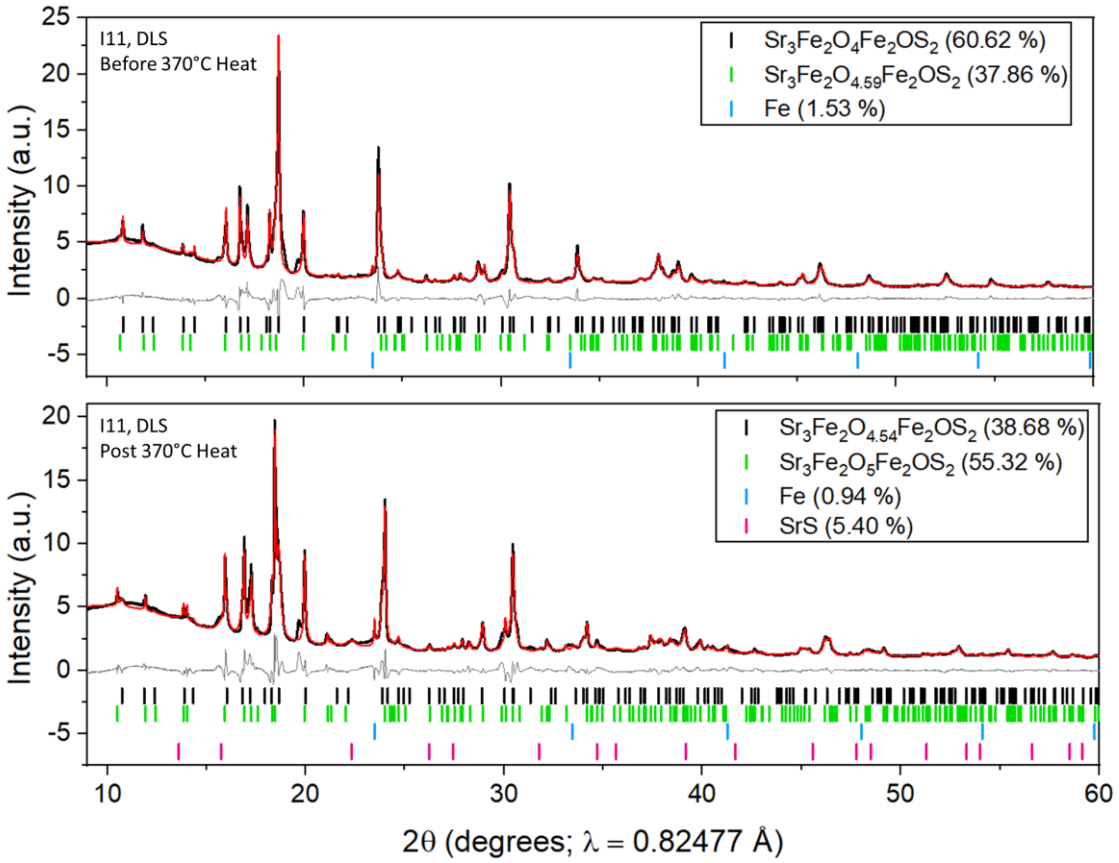


Figure 5.13. Rietveld refinement of room-temperature X-ray diffraction pattern of ANG087d collected on the PSD detector at I11 (DLS) before (top) and after (bottom) being heated to 370°C showing the observed (black), calculated (red) and difference (grey) curves.

The same now-partially-decomposed sample was then heated again from 25°C to 600°C which revealed that above 370°C, the sample undergoes further decomposition, producing elemental iron and SrS in addition to more of the parent phase with no significant amount of the reduced phase remaining (Figures 5.14 and 5.15).

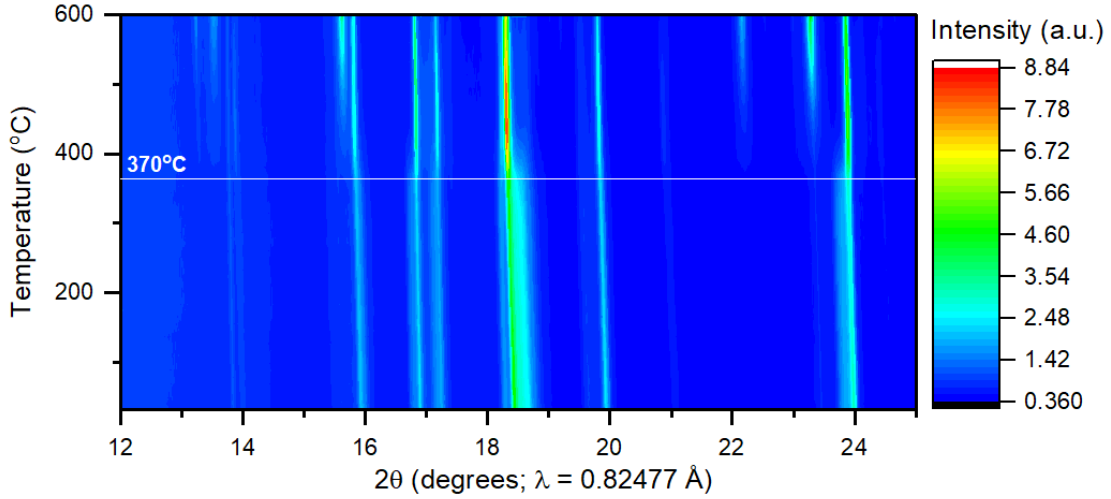


Figure 5.14. Variable temperature X-ray powder diffraction patterns of ANG087d collected from 25°C to 200°C on the PSD detector at I11 (DLS) after the initial heat to 370°C showing further impurity peaks that arise at temperatures above 370°C.

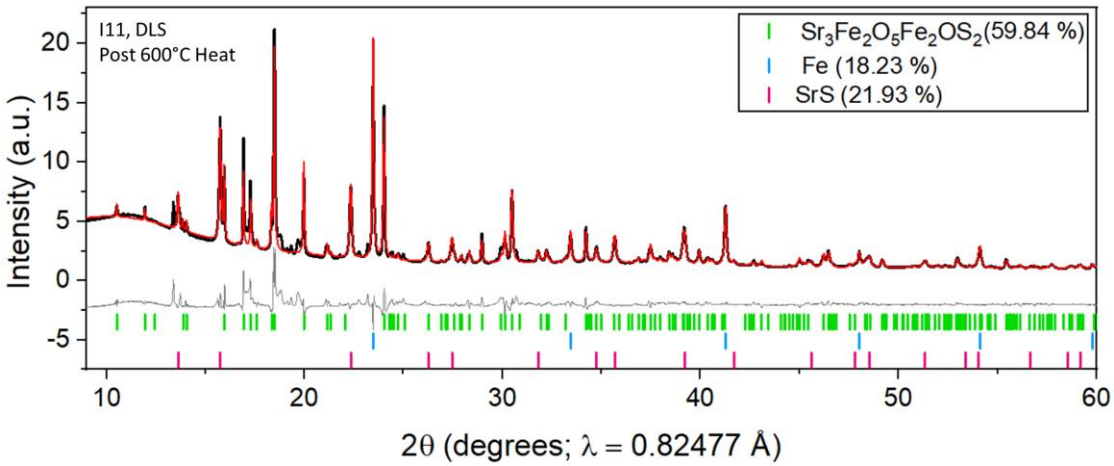


Figure 5.15. Rietveld refinement of room-temperature X-ray diffraction pattern of ANG087d collected on the PSD detector at I11 (DLS) after being heated to 600°C showing the observed (black), calculated (red) and difference (grey) curves. Black triangles indicate reflections from SrS and red triangles indicate reflections from elemental Fe.

From this, it is evident that the reduced $Sr_3Fe_2O_4Fe_2OS_2$ loses thermal stability between 200°C and 370°C and will begin to produce the more O-rich parent, non-reduced $Sr_3Fe_2O_5Fe_2OS_2$ – SrS forms to compensate and is visible in the powder pattern. When it is then heated to higher temperatures, the sample undergoes further decomposition into the parent material and more SrS and elemental Fe with no more of the reduced phase remaining.

5.4. Magnetic Characterization

5.4.1. Magnetometry

Magnetometry data collected for aliquots of samples that were taken after each cycle of the reduction of ANG066 (an exploratory sample prepared before the samples ANG086 and ANG087 discussed above, see Table 5.1) shows that there is a strong ferromagnetic signal that increases as the reduction progresses in both the *M* v *H* curves and the susceptibility curves (Figure 5.16). The likely cause of this ferromagnetic signal is the evolution of an elemental Fe impurity that can be observed in the X-ray diffraction patterns. The impurity likely first arises from the reduction of the magnetite impurity in the parent material, as we first see the disappearance of the Verwey transition after one cycle and this has the effect of revealing the Fe2 layer's antiferromagnetic transition in the parent material. After this first cycle, however, the ferromagnetic signal keeps growing which is likely from some of the decomposition that occurs in this sample as the cycles continue. Since the saturation magnetization of elemental Fe is 218 emu/g at room temperature [6], the theoretical weight percent of elemental Fe in a sample that would exhibit the FM signal in the magnetometry data can be calculated using Eqn. 5.1 where M_S is the saturation magnetization of the hysteresis curve in emu and m_S is the mass of the sample measured.

$$\text{wt \% Fe} = \frac{M_S}{m_S} \times 218 \text{ emu/g} \times 100 \% \qquad \text{(Eqn 5.1)}$$

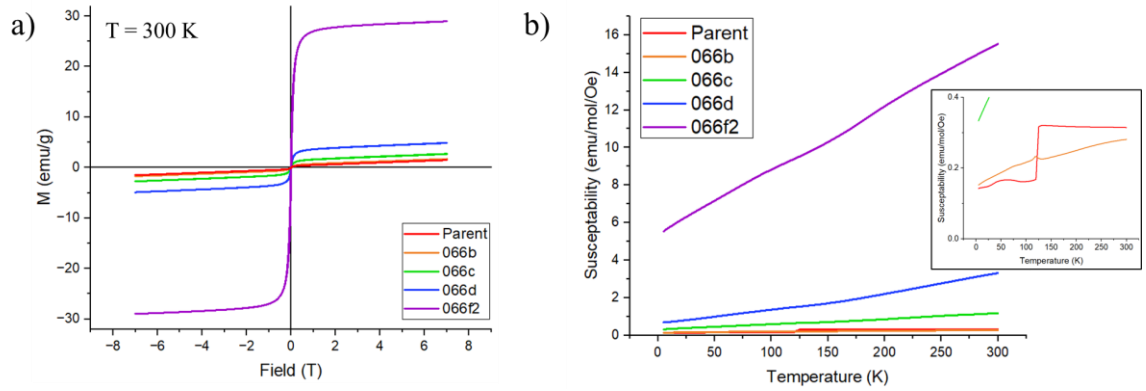


Figure 5.16. 300 K MvH magnetization curves (a) and zero-field cooled susceptibility curves (b) for aliquots of ANG066 as the reduction progresses.

Table 5.7. Refined and calculated wt% of Fe in ANG066b-f obtained from in-house XRPD Rietveld refinements and the saturation of *M* v *H* magnetization curves respectively.

	Refined Fe wt %	Calculated Fe wt %
ANG066b	0	0.523
ANG066c	0.35	0.644
ANG066d	0.88	1.54
ANG066f2	7.71	12.24

ANG066 was a sample that exhibited more decomposition than the samples ANG086 and ANG087 discussed above, as it was an exploratory sample in which the synthesis temperatures exceeded the 300˚C that was later determined to be optimal. When considering sample ANG086e, the Fe impurity is much smaller at 1.04 wt% by SXRPD. Calculating the wt% of Fe required to give the ferromagnetic signal based on the saturation of the 300 K *M* v *H* isotherm, this sample would contain around 1.74 wt% Fe. The calculated amount of Fe in each sample is consistently more than that which is refined in the XRPD data, but this could be because some of the Fe is not crystalline, such as in very small particles, which are therefore not fully accounted for in the XRPD patterns and the refinements.

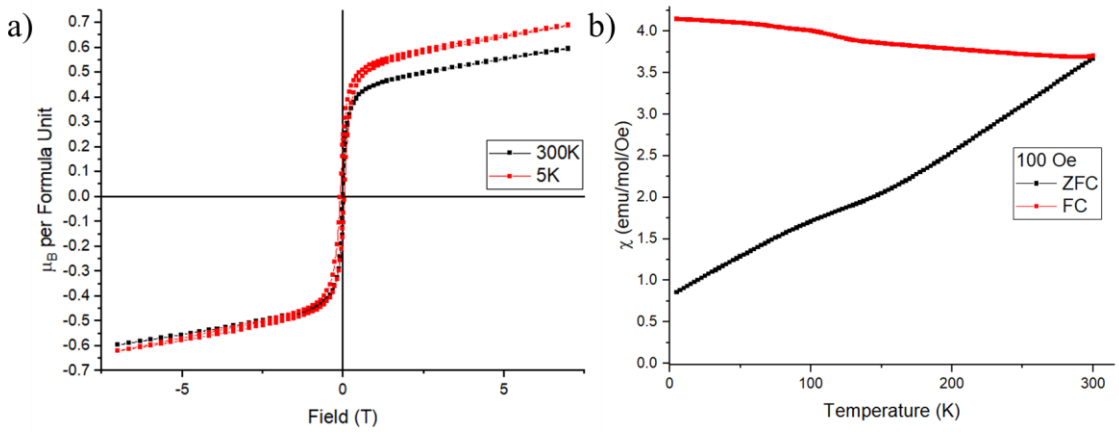


Figure 5.17. a) *M* v *H* isotherms and b) susceptibility curves for ANG087e.

With this evidence in mind, it is apparent that the signal in the magnetometry is dominated by the Fe impurity, as the divergence of the ZFC and FC curves is standard behaviour for a ferromagnet below its Curie temperature. In addition to this, it also seems as if the Fe_3O_4 impurity in the parent reduces first in the reaction, but based on the domination of the signal by the ferromagnetic Fe impurity, no other conclusions about the magnetism of the reduced phase can be made based only on the magnetization data.

5.4.2. Room and Low temperature NPD

Low temperature NPD data was collected on GEM in an investigation which sought to establish whether or not the reduced phase $Sr_3Fe_2O_4Fe_2OS_2$ orders magnetically at room temperature and lower temperatures. GEM was used because the small signal to noise ratio at large *d*-spacings at HRPD made it impossible to determine for certain whether or not there were any small magnetic peaks in that region. As mentioned in section 5.3.2, there are statistically significant magnetic peaks that are present in the GEM room-temperature diffraction pattern for $Sr_3Fe_2O_4Fe_2OS_2$.

Since the reduced samples are multi-phase, the first concern that had to be settled is which phase is the magnetic phase. Thankfully, since the two phases have different lattice parameters, it became quickly evident that the magnetic peaks in the room-temperature neutron diffraction data arise due to the magnetic ordering of the fully-reduced phase. When a magnetic model is assigned to fit the partially-reduced phase, the magnetic reflections appear at *d*-spacings inconsistent with the magnetic peaks. With that being said, there is some extra intensity on the magnetic peaks (especially to the right of the peak around 3.8 Å) that could be due to some weak ordering in the partially reduced phase (see Figure 5.19). The attempted addition of a second magnetic phase into the refinement consistently crashed the program, indicating that the calculation was too computationally expensive to carry out. Additionally, it makes sense that magnetic order in the partially reduced phase would be suppressed due to disorder on the partially-occupied *O*3 site in the Fe1 layer.

The magnetic structure of $Sr_3Fe_2O_4Fe_2OS_2$ at room temperature (Figure 5.18) is similar to that of the parent structure in that the magnetic reflections can be indexed on a $\sqrt{2}a \times \sqrt{2}b \times 2c$ magnetic supercell by activating the mM5- (E(a)) and mA5- (E(b)) modes with k-vectors (½, ½, 0) and (½, ½, ½) respectively. This again means that only the Fe1 layer is ordered antiferromagnetically along the Fe-O-Fe superexchange pathways and there is a twisting between layers of 35.6(6)˚ and a moment of 4.06(4) μ_B.

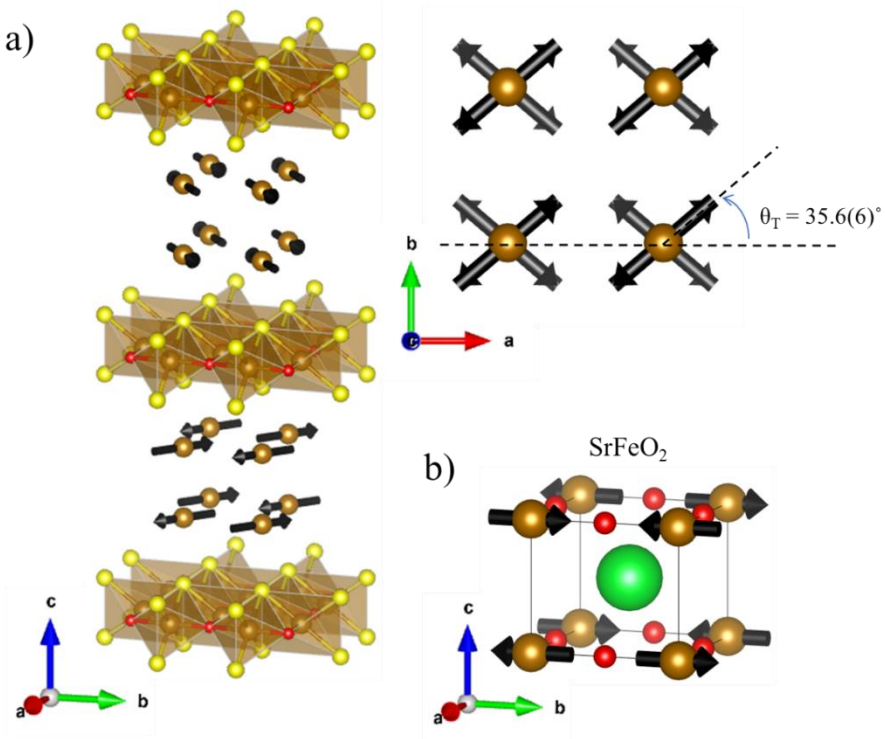


Figure 5.18. Refined room temperature magnetic model of a) $Sr_3Fe_2O_4Fe_2OS_2$ alongside b) the magnetic structure of $SrFeO_2$ [6].

Alternative methods of refinement could activate various combinations of the individual E(a) and E(b) modes of each magnetic mode, and this leads to alternative structures wherein all of the magnetic moments are rotated about the *c*-axis. This is to be expected though, as in primitive tetragonal structures, spin direction can only be defined as to its angle from the unique axis [8]. This means that the axis of the twisting angle is arbitrary, though the angle itself is real in that it relates the moments in subsequent layers. In addition to this, the alternative two-model structure discussed in chapter 3.3.2 can be adopted, like in the parent, but the twisting model will be the primary model used in this discussion going forward.

At 100 K, there has been an emergence of additional magnetic reflections that indicate that both the Fe1 and Fe2 layers are ordered at this temperature. At this temperature, the refined Fe1 moment has maintained its magnitude, refining to 4.10(8) μ_B per Fe centre, and the canting angle has also stayed the same, refining to 34(1)˚. This trend is different from the parent material, because this means that the Fe1 moment was saturated at room temperature whereas the magnetic moment of the parent changed intensity and twisting angle on cooling and saturated around 140 K with a similar moment of 4.07(5) μ_B. However, the twisting angle of the parent increased closer to 45˚ from 36.7(7)˚ to 42.4(8)˚ unlike the reduced structure. In terms of the Fe2 layer, the reduced phase orders in an antiferromagnetic model similar to that in the parent material, with the mR2+ B2g(a) and (b) modes with **k**-vectors of (0, ½, ½) fixed to be equivalent resulting in antiferromagnetic coupling along the Fe-O-Fe superexchange pathways. The magnetic moment on the Fe2 ions at 100 K is 2.44(9) μ_B which is slightly smaller than the low temperature model of the parent material but is similar enough that it is unlikely there were any significant changes to the Fe2 layer in the reduction.

The 5 K magnetic model is unchanged from the 100 K model with the only difference arising from some evolution of the magnetic moments to 4.23(4) μ_B and 3.40(6) μ_B in the Fe1 and Fe2 layers respectively. In this analysis it is also clear that the phase that is ordering at this temperature is that of the fully reduced phase rather than the partially reduced phase, as like at room temperature, the magnetic peak positions are only correctly positioned when the magnetic model is fit to the fully reduced phase due to the difference in lattice parameters. Additionally, since the entire intensity of the additional magnetic peaks are fit with the single magnetic phase pertaining to the fully reduced phase, the Fe2 layer in the partially-reduced phase also seems not to be contributing to the Bragg intensity arising from long-range magnetic order; it is presumably affected by the Fe1 sublattice disorder.

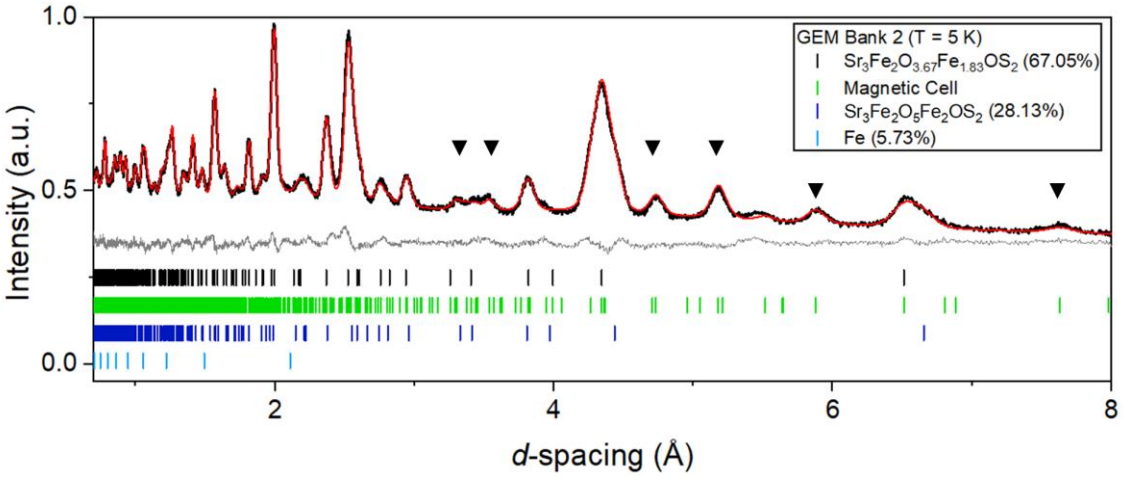


Figure 5.19. Rietveld refinement of the NPD patterns of $Sr_3Fe_2O_4Fe_2OS_2$ (ANG086f) measured on GEM bank 2 at T = 5 K showing the observed (black), calculated (red) and difference (grey) curves. Black triangles denote magnetic reflections.

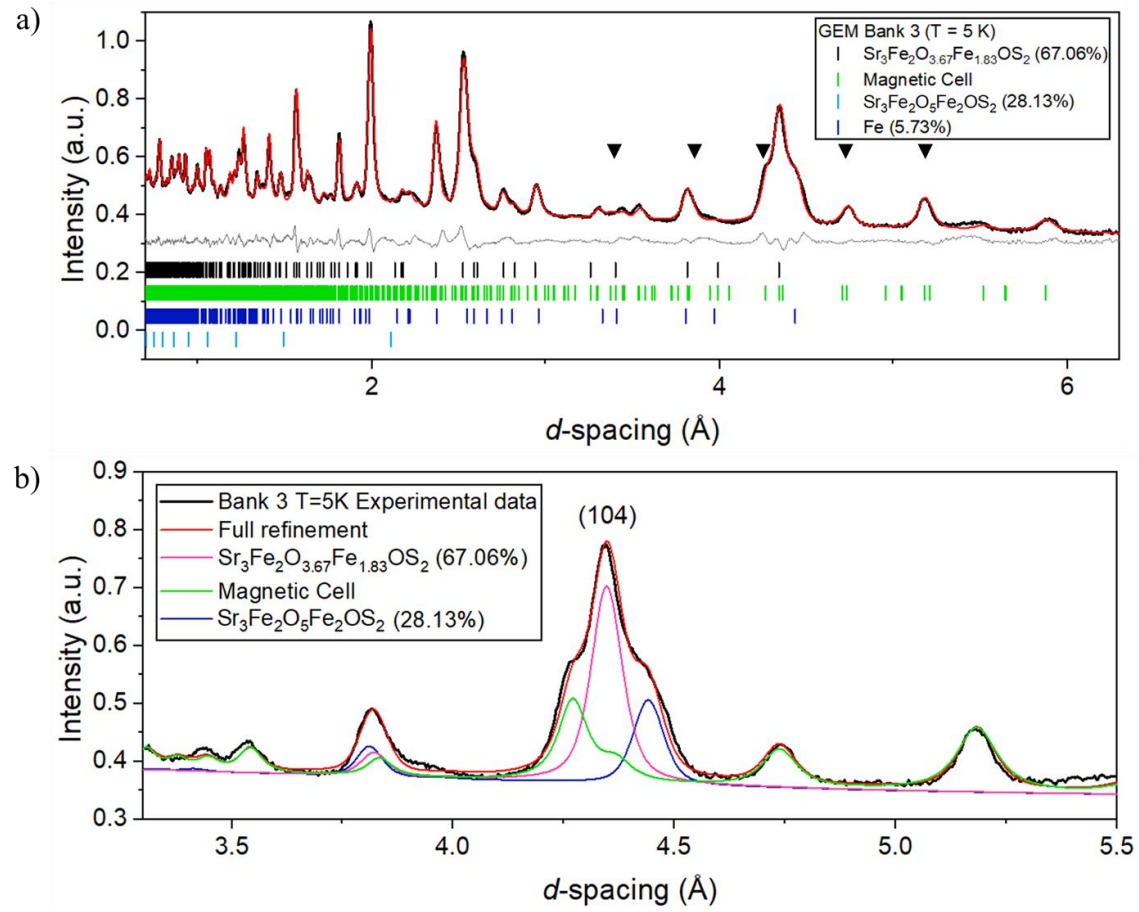


Figure 5.20. Rietveld refinement of the NPD patterns of $Sr_3Fe_2O_4Fe_2OS_2$ (ANG086f) measured on GEM bank 3 at T = 5 K showing the observed (black), calculated (red) and difference (grey) curves (a) and a breakdown of the individual refined structures showing the presence of all three phases (b). Black triangles denote magnetic reflections.

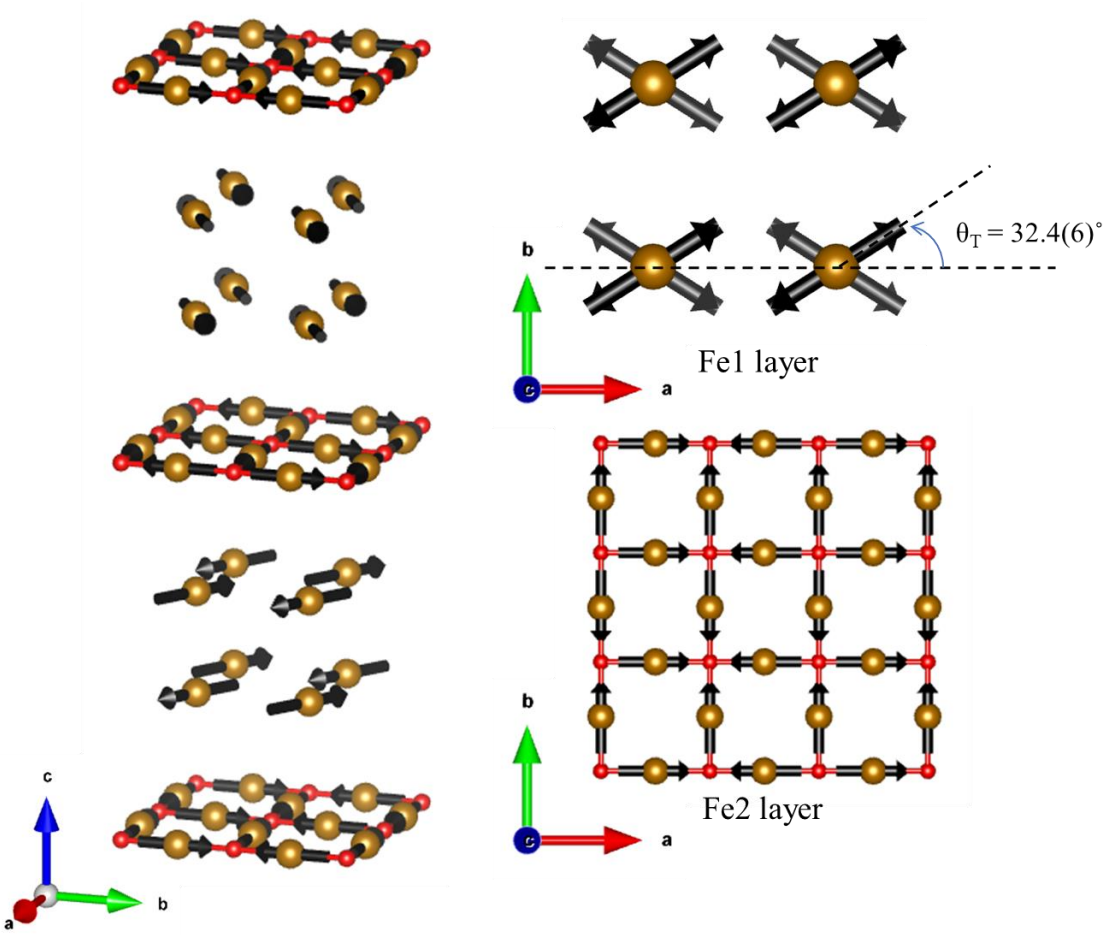


Figure 5.21. Refined 5 K magnetic model of $Sr_3Fe_2O_4Fe_2OS_2$.

Further investigation into the temperature at which the Fe2 layer orders magnetically reveals that the additional magnetic reflections decrease in intensity from 30 K to 90 K and disappear upon warming between 100 K and 107 K (Figure 5.22). This is just slightly lower than the 115 K transition temperature of the oxidized parent phase suggesting that the layer is not significantly altered electronically. In addition to this, individual refinements show that the Fe2 moment decreases in magnitude upon warming as expected from the lower intensity of the magnetic reflections (Figure 5.23b). The Fe1 moment, however, does not change significantly and the twisting angle slightly increases upon warming (Figure 5.23) which is different from the parent phase. In the parent phase, the twisting angle increases upon cooling as the moment saturates around 140 K. In this reduced phase, the change of the refined twisting angle for this reduced phase may be an artefact and instead arise from the decrease in the resolution between the magnetic and nuclear peaks at higher temperatures as there is no significant change in the intensities of any of the other magnetic peaks corresponding to the ordering of the Fe1 sublattice.

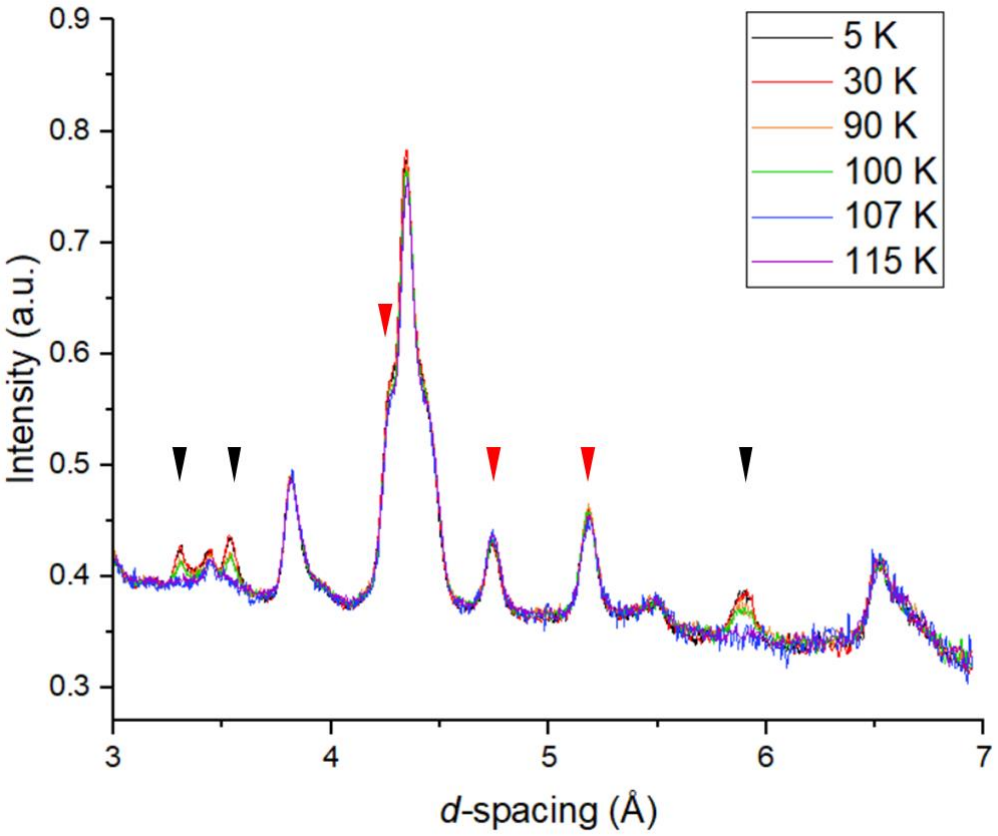


Figure 5.22. Neutron diffraction patterns of ANG086f collected on GEM at different temperatures with black triangles indicating reflections that correspond to the magnetic ordering of the Fe2 sublattice and red triangles indicating those of the Fe1 sublattice.

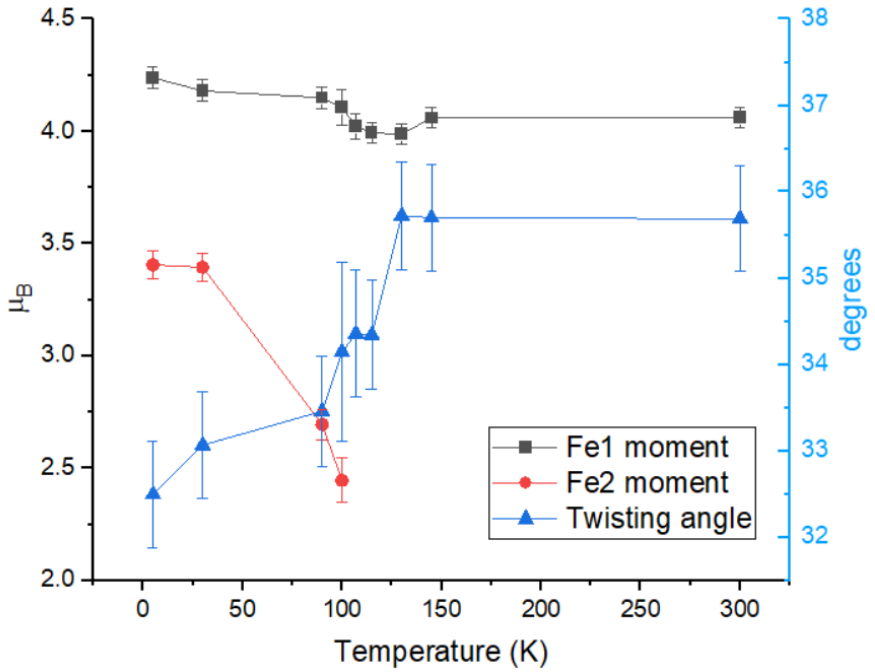


Figure 5.23. The refined moments and twisting angles of the magnetic model of $Sr_3Fe_2O_4Fe_2OS_2$ as a function of temperature.

5.5. Further Characterization

5.5.1. XANES measurements

XANES measurements were carried out on the B18 beamline at the DLS in an effort to further investigate the iron oxidation states in the samples as the reduction of $Sr_3Fe_2O_5Fe_2OS_2$ progresses. The samples ANG086a-f were chosen as these were part of the most straightforward reduction, with the 066 series being exploratory and the 087 series having been inadvertently oxidized (see Table 5.1). The spectra are shown below in Figure 5.24 along with spectra for Fe_2O_3 (Fe^{3+}) and FeO (Fe^{2+}) standards.

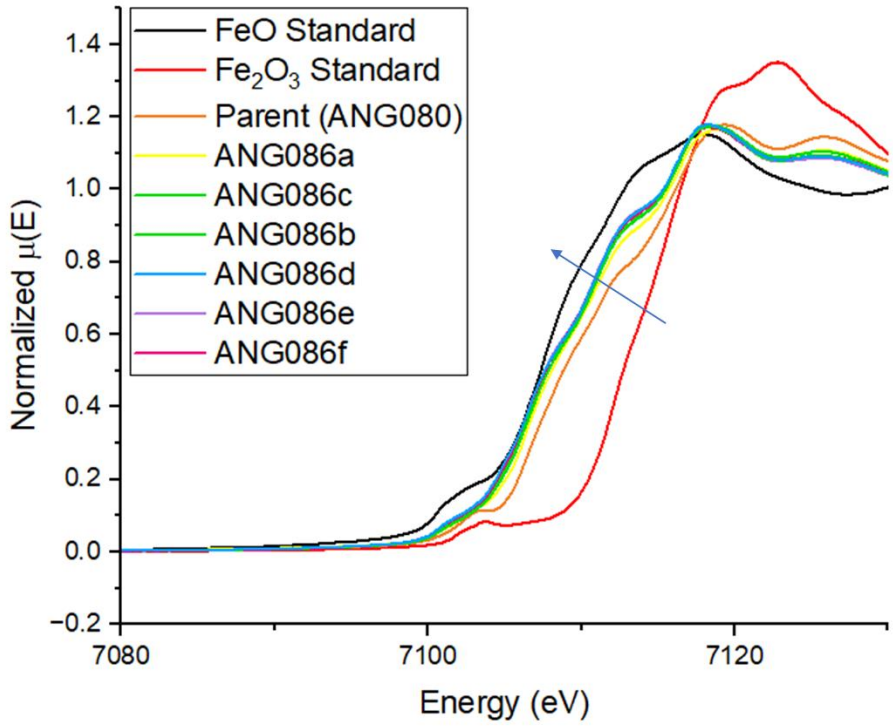


Figure 5.24. XANES K-edge for $Sr_3Fe_2O_{5-x}Fe_2OS_2$ as the reduction progresses (ANG080, ANG086a-f) and Fe^{2+}/Fe^{3+} standards. The blue arrow indicates the direction of the K-edge movement as the reduction progresses.

As the reduction progresses, the change in Fe oxidation state is evident from the shift in the Fe K-edge away from the Fe_2O_3 standard and the parent compound toward the FeO standard. While the precise edge position depends on the exact Fe-coordination environment, this movement indicates that the average Fe oxidation state becomes closer to 2+, supporting the claim that the Fe^{3+} in the parent phases is indeed being reduced to Fe^{2+} as the reaction progresses.

5.5.2. SEM-EDX

During the washing of ANG066f2, the powder exhibited ferromagnetic behaviour around the magnetic stir bar, clinging to the poles of the magnet and aligning along magnetic field lines like iron shavings in an elementary school science project.

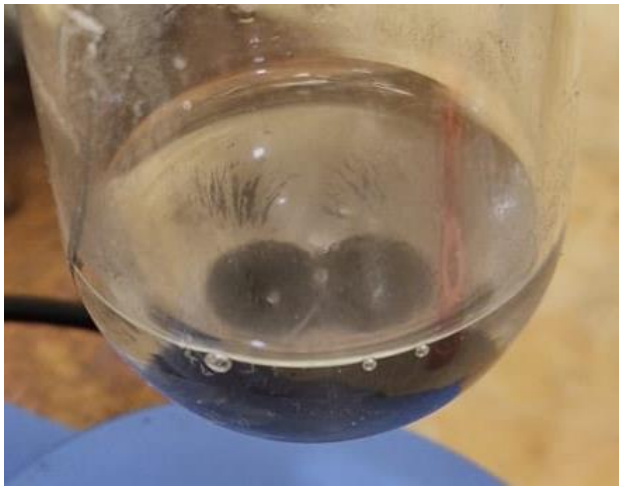


Figure 5.25. Photo of the washed ANG066f2 aligning according to the magnetic field lines of the magnetic stir bar.

This bulk ferromagnetic behaviour is consistent with the presence of an Fe impurity as suggested by both X-ray powder diffraction and SQUID magnetometry. It also suggests that individual crystallites contain regions of Fe and SEM-EDX was used to confirm this hypothesis. Indeed, as regions identified in Figures 5.26 and 5.27 (circled in red) show, individual crystallites do have Fe-rich regions with nearly no Sr or S. SEM-EDX therefore supports a conclusion that there are Fe-rich areas in individual particles which explains the bulk ferromagnetic behaviour seen in Figure 5.25 and the SQUID magnetometry.

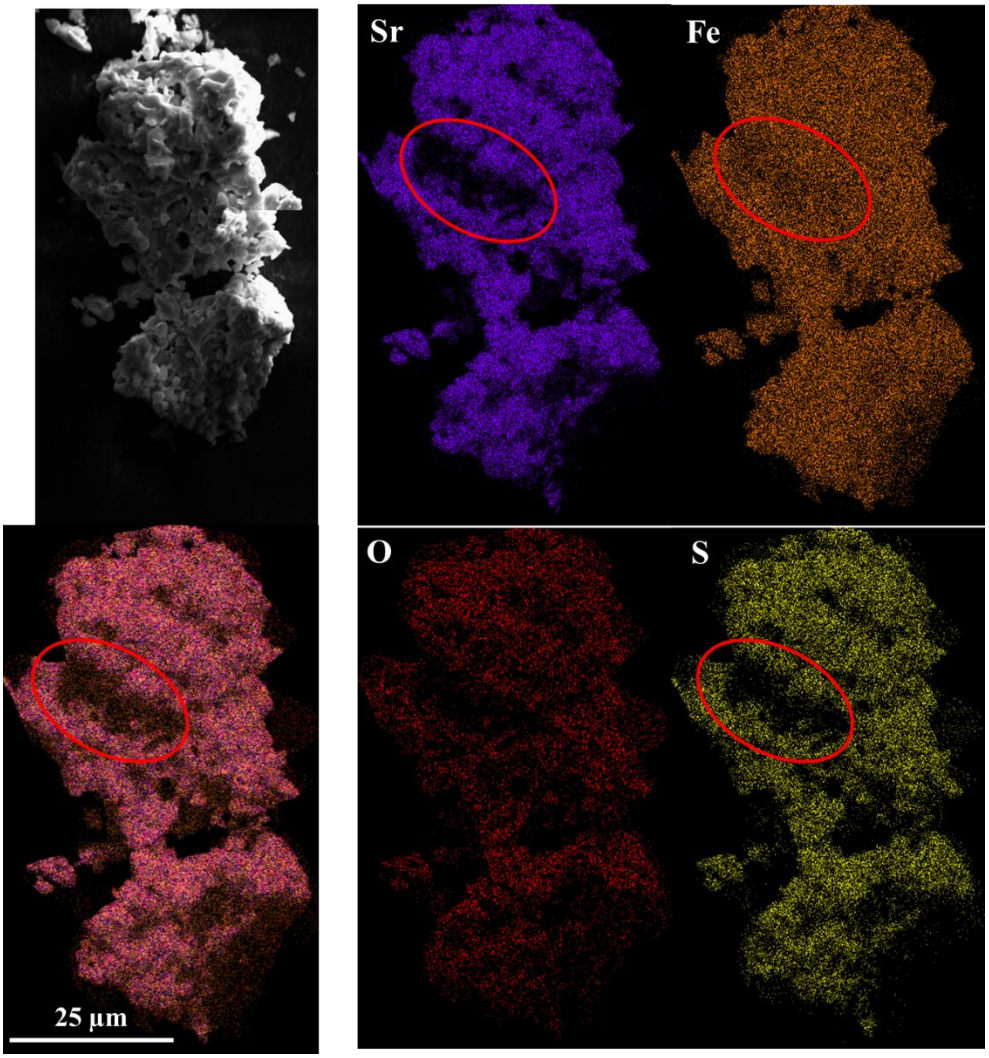


Figure 5.26. SEM imaging and EDX mapping of a single particle of $Sr_3Fe_2O_4Fe_2OS_2$ (ANG066g2) with Fe-rich regions circled in red.

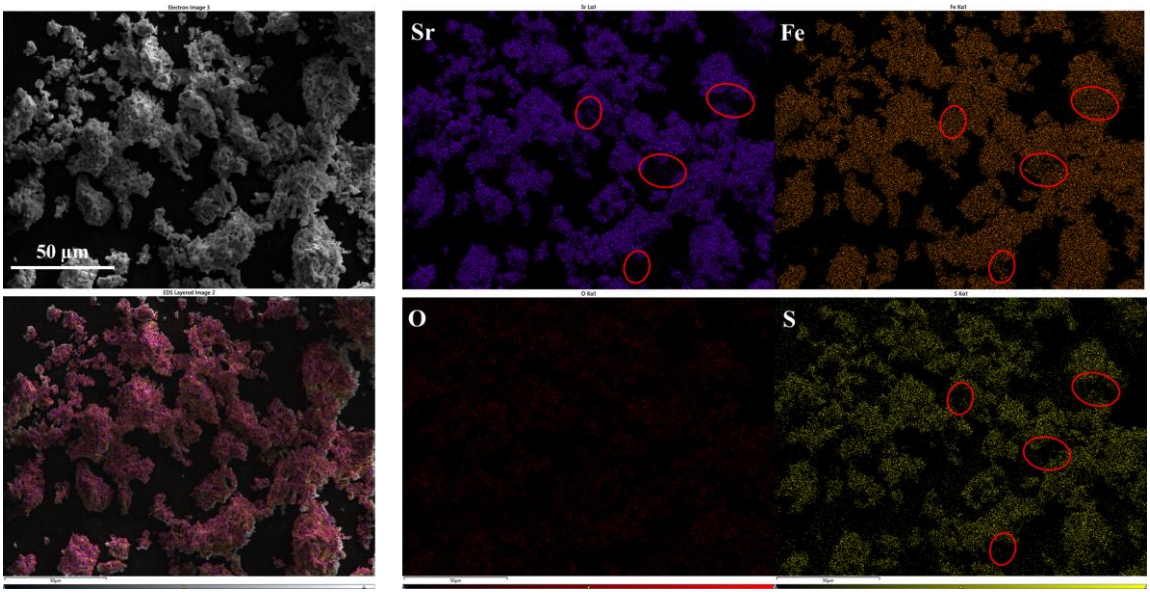


Figure 5.27. SEM imaging and EDX mapping of several particles of $Sr_3Fe_2O_4Fe_2OS_2$ (ANG066g2).

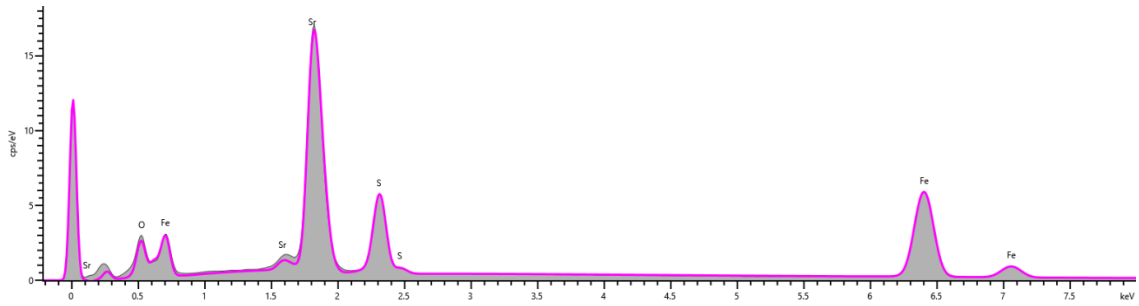


Figure 5.28. Sample SEM-EDX elemental analysis spectrum for $Sr_3Fe_2O_4Fe_2OS_2$ (ANG066g2).

Table 5.8. Average SEM-EDX elemental analysis for $Sr_3Fe_2O_4Fe_2OS_2$ (ANG066g2). Due to its low atomic mass, O content is estimated.

Sr (at %)	Fe (at %)	O (at %)	S (at %)
2.7(2)	3.6(5)	4.9(8)	2.0(1)

5.6. Conclusions

In conclusion, the topotactic reduction of $Sr_3Fe_2O_5Fe_2OS_2$ has been successfully carried out, producing a multiphase product. This multiphase product consists firstly of a fully reduced $Sr_3Fe_2O_4Fe_2OS_2$ phase wherein the axial bridging oxygen in the Fe1 layers of the parent material has been entirely removed and the Fe^{3+} reduced to Fe^{2+} as supported by the shifting of the Fe K-edge in the XANES spectra as well as the high-resolution neutron powder diffraction pattern refinements and the calculated bond valence sums. The other phase in the product is a partially reduced phase for which some, but not all, of the axial bridging oxygen has been removed, with a final occupancy of 0.62(4) on the O3 site as determined by high-resolution neutron powder diffraction. From the parent structure to the reduced phase, the *a* lattice parameter undergoes a slight expansion and the *c* lattice parameter is reduced by approximately 0.4 Å, with the largest reduction occurring in the distance between the FeO_2 planes within the Fe1 layer to resemble the phase $SrFeO_2$ [6]. Magnetically, the reduced phase also behaves very similarly to the parent material. The Fe1 layer is magnetically ordered at room temperature and adopts the same ordering pattern as the parent material and can be described with either a two-structure model or the twisting model, both of which are described in chapter 3.3.2. Each individual double-layer also magnetically resembles a fragment of $SrFeO_2$ in the antiferromagnetic order of moments

within the plane which agrees with predictions which consider HOMO-LUMO interaction and use spin-orbit coupling as perturbation [6,9]. One thing that is interesting is that the reduced halide $Sr_3Fe_2O_4Cl_2$ deviates from this trend, as has been noted in literature before [10], as it contained moments along *c* unlike even its respective parent $Sr_3Fe_2O_5Cl_2$ which also contained moments within the basal plane [3,4]. The moments in the reduced phase are saturated at room temperature though, unlike the parent material which saturates at 140 K. In addition to this, the Fe2 layer orders below 107 K in the same manner as the parent which ordered below 115 K.

Table 5.9. Comparison of the structure and magnetism of $Sr_3Fe_2O_5Fe_2OS_2$ and $Sr_3Fe_2O_4Fe_2OS_2$.

	$Sr_3Fe_2O_5Fe_2OS_2$	$Sr_3Fe_2O_4Fe_2OS_2$
a (Å)	3.96156(1)[1]	4.00218(7)[2]
c (Å)	13.51991(8)[1]	13.1075(4)[2]
V (Å^3)	212.181(2)[1]	209.94(1)[2]
RT Fe1 moment (μ_B)	3.58(4)	4.04(6)
5 K Fe1 moment (μ_B)	4.04(5)	4.23(4)
5 K Fe2 moment (μ_B)	3.31(7)	3.39(6)
Fe2 ordering Temp (K)	115 K	100-107 K

[1]From refinement of XRPD data collected on I11.
[2]From refinement of NPD data collected on HRPD.

The two-phase nature of the reduction product is a feature for which further experiments are required to resolve. While higher anneal temperatures (500°C and 900°C) resulted in decomposition, gentler annealing temperatures could result in a single-phase product. In addition to this, other reducing agents like CaH_2 may drive the reduction further into only a single, fully reduced phase and is worth exploring, given that each equivalent of CaH_2 can remove a whole equivalent of oxygen whereas two equivalences of LiH are required (generating CaO versus Li_2O). There is some precedence for this in the topochemical reduction of $LaSrCoRuO_6$ where the use of CaH_2 as a reducing agent resulted in a single-phase oxyhydride product with the largest number of vacancies while the use of LiH as a reducing agent yielded a multiphase oxyhydride product with fewer vacancies [11].

A single-phase, fully-reduced product would be interesting to investigate using Mössbauer spectroscopy, as it could be compared to the parent material and give further insight into the magnetic ordering of the iron sites at various temperatures by looking at the splitting patterns as

well as the oxidation states when comparing the chemical shifts. Alternatively, making a single, partially-reduced phase may be of interest to investigate if the magnetic order of the partially-reduced phase is fully or only partially suppressed. Further experiments may also give more insight, like investigating the reaction in-situ.

References

[1] Leib, W.; Muller-Buschbaum, H. *Z. anorg.allg. Chem.* **1984**, *518*, 115-119.
[2] Ackerman, J. F. *J. Solid State Chem.* **1991**, *92*, 496-513.
[3] Knee, C.S.; Field, M.A.L.; Weller, M.T. *Solid State Sci.* **2004**, *6*, 443-450.
[4] Dixon, E.; Hayward, M. *Inorg. Chem.* **2010**, *49*, 20, 9649-9654.
[5] Sheath, B.C.; Cassidy, S.J.; Clarke, S.J. *J. Solid State Chem.* **2021**, *293*, 121761.
[6] Tsujimoto, Y.; Tassel, C.; Hayashi, N.; Watanabe, T.; Kageyama, H.; Yoshimura, K.; Takano, M.; Ceretti, M.; Ritter, C.; Paulus, W. *Nature*. **2007**, *450*, 1062–1065.
[7] Cullity, B.D. "Introduction to Magnetic Materials." *Addison-Wesley Pub. Co*. **1972**, p 617.
[8] Shirane, G. *Acta Crystallogr*. **1959**, *12*, 282–285.
[9] Whangbo, M.-H.; Gordon, E. E.; Xiang, H.; Koo, H.-J.; Lee, C. *Acc. Chem. Res*. **2015**, *48*, 3080−3087
[10] Lu, D.; Yang, K.; Liu, L.; Wang, G.; Wu, H. *Inorg. Chem.* **2022**, *61*, 12692-12697.
[11] Liang, Z.; Batuk, M.; Orlandi, F.; Manuel, P.; Hadermann, J.; Hayward, M. A. *Inorg. Chem.* **2024.** *63*, 12910-12919.

Chapter 6: Further exploration into the structure and magnetism of $Ca_2Fe_{2.7-\delta}O_3S_{2-x}Se_x$

Contents

6.1. Nuclear structure of $Ca_2Fe_{2.7-\delta}O_3S_2$ 151
6.1.1. Introduction and previous work 151
6.1.2. Superstructure determination 153
6.1.3. Superstructure suppression 160
6.2. Magnetism of $Ca_2Fe_{2.7-\delta}O_3S_2$ in an applied-field 162
6.2.1. Introduction and motivation 162
6.2.2. Results and Discussion 163
6.3. Magnetism of $Ca_2Fe_{2.7-\delta}O_3S_{2-x}Se_x$ 165
6.3.1. Introduction and previous work 165
6.3.2. $Ca_2Fe_{2.7-\delta}O_3S_{1.5}Se_{0.5}$ (x = 0.5) 167
6.3.3. $Ca_2Fe_{2.7-\delta}O_3SSe$ (x = 1) 171
6.3.4. $Ca_2Fe_{2.7-\delta}O_3S_{0.5}Se_{1.5}$ (x = 1.5) 175
6.3.5. Summary of Trends 178
6.4. Conclusions 180
References 182

6.1. Nuclear structure of $Ca_2Fe_{2.7-\delta}O_3S_2$

6.1.1. Introduction and previous work

The phase $Ca_2Fe_{2.7-\delta}O_3S_2$ was first reported by Zhang *et al.* in 2016 [1]. It is synthesized using the same general ceramic method as described in chapter 3.1.1 and is formed as a side-phase when synthesizing targeted Ca-rich samples of the solid solution $Sr_{3-x}Ca_xFe_2O_5Fe_2OS_2$ as described in chapter 4. It adopts the layered structure shown in Figure 6.1, with the oxide-rich

Fe1 layer containing Fe in a distorted FeO_4S_2 octahedron and the sulfide-rich Fe2 layer containing Fe in distorted FeO_2S_4 octahedra (similar to those in the Fe_2OS_2 layers of $Sr_3Fe_2O_5Fe_2OS_2$). In that publication, it was reported that there were superstructure peaks that arose in the X-ray powder diffraction patterns which was likely due to vacancy ordering of the Fe in the Fe2 layer which refined to an occupancy of 0.800(6).

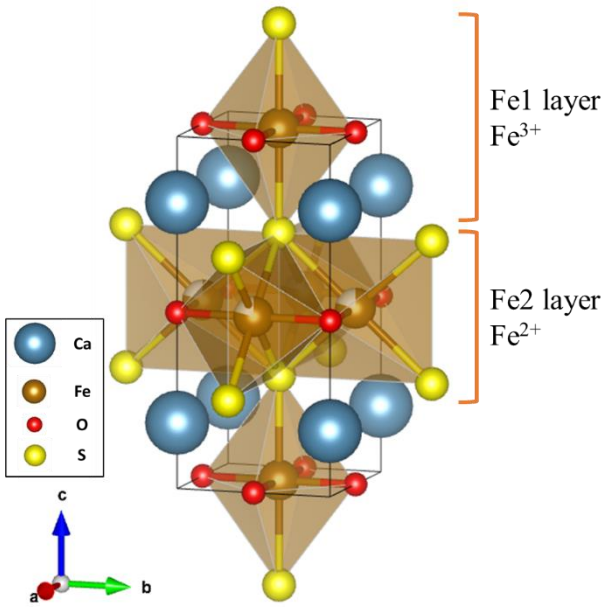


Figure 6.1. Reported unit cell of $Ca_2Fe_{2.7-\delta}O_3S_2$ by Zhang *et al.* [1]

Further work in determining the superstructure of $Ca_2Fe_{2.7-\delta}O_3S_2$ was carried out by Bradley Sheath and reported in his D.Phil thesis, and analysis of the SXRPD pattern revealed that the superstructure pattern could be modelled using the orthorhombic *Aea*2 or *Aeam* space groups (with the space group setting maintaining the *c*-axis as the stacking direction), though the two could not be resolved with powder diffraction data as they are nearly identical in that there is no difference in systematic absences (Figure 6.2) [2]. Single-crystal X-ray diffraction (SC-XRD) data was also discussed in Sheath's thesis, but only the proposed space groups *Pnn*2 and *Pnnm* were obtained from this data, neither of which fit the powder diffraction data very well [2]. With this ambiguity in mind, this section discusses SC-XRD data obtained for a new sample in an attempt to resolve the superstructure for $Ca_2Fe_{2.7-\delta}O_3S_2$ in addition to some cases wherein the superstructure is suppressed.

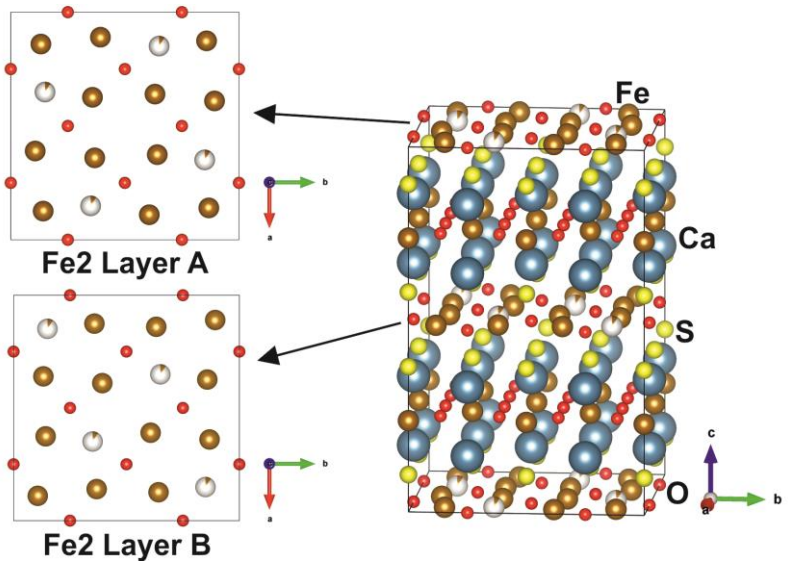


Figure 6.2. The structural models of $Ca_2Fe_{2.7-\delta}O_3S_2$ presented by Sheath in the *Aea2* space group alongside a 2*a* × 2*b* view of the Fe2 layers showing the vacancy order [2].

In conjunction to the structural analysis that he carried out, Sheath proposed that the Fe2 vacancies necessitate the oxidation of some of the Fe atoms to Fe^{3+}. XANES, XPS, and Mössbauer spectroscopy all support the existence of multiple Fe oxidation states (2+ and higher), and bond valence sums show that the oxidized Fe's are the Fe1 sites.

In addition to his work in solving the superstructure of $Ca_2Fe_{2.7-\delta}O_3S_2$ that arises from the long-range order of Fe vacancies, Sheath also characterized the magnetic structure of the compound which orders antiferromagnetically at 320 K in both the Fe1 and Fe2 layers and then undergoes some spin reorientation as a canting is introduced at low temperatures. The structure has a net ferromagnetic moment due to the Fe vacancy ordering as all of the vacant sites would order in the same direction and the vacancy means that that moment is undercompensated for in the overall antiferromagnetic order, making the layers ferrimagnetic (i.e. uncompensated antiferromagnet) [2].

6.1.2. Superstructure determination

Due to the remaining ambiguity pertaining to the space group of $Ca_2Fe_{2.7-\delta}O_3S_2$ when considering superstructure arising from the Fe^{2+} vacancy ordering, another sample was prepared with a long annealing time of one month at 900˚C. This synthesis resulted in small single crystals, and a crystal was chosen for SC-XRD with a size on the order of 0.1 mm (Figure 6.3).

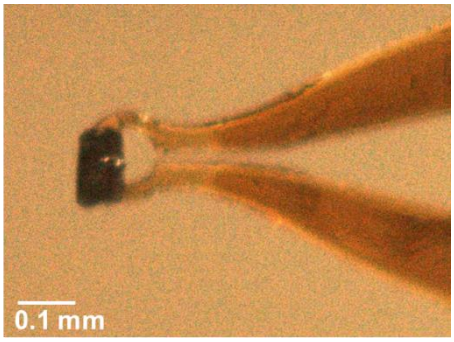


Figure 6.3. The crystal on which SC-XRD was performed.

Room-temperature SC-XRD was performed on an Oxford Diffraction Supernova A diffractometer using Mo-K_α (λ = 0.71073 Å) radiation. This data was collected and analysed by Lemuel Crentsil, the group member trained on these instruments. In an *ab initio* indexing of the cell, all of the reflections can be indexed using the cell parameters listed in Table 6.1, which confirms an orthorhombic space group and the supercell expansion of $2\sqrt{2}a_{nuc} \times 2c_{nuc} \times 2\sqrt{2}a_{nuc}$ as both Sheath and Zhang suggested [1,2]. Here the orthorhombic cell is defined with the *b* axis longest. From the reflection conditions and the assumption that all visible reflections belong to the same phase, the possible space groups would be *Pn*2*n* (No. 34) or *Pnmn* (No. 54). However, higher-order precession layers (see [1kl] pattern in Figure 6.4) are indicative of twinning in the sample, which appears to be intrinsic to the compound. Further analysis assuming this twinning suggests that the cell is not primitive, but is instead centred.

Table 6.1. Cell parameters of $Ca_2Fe_{2.58}O_3S_2$ (ANG019b) as determined by SC-XRD.

a (Å)	11.15648(13)
b (Å)	17.4988(2)
c (Å)	11.15738(3)
α = β = γ	90°

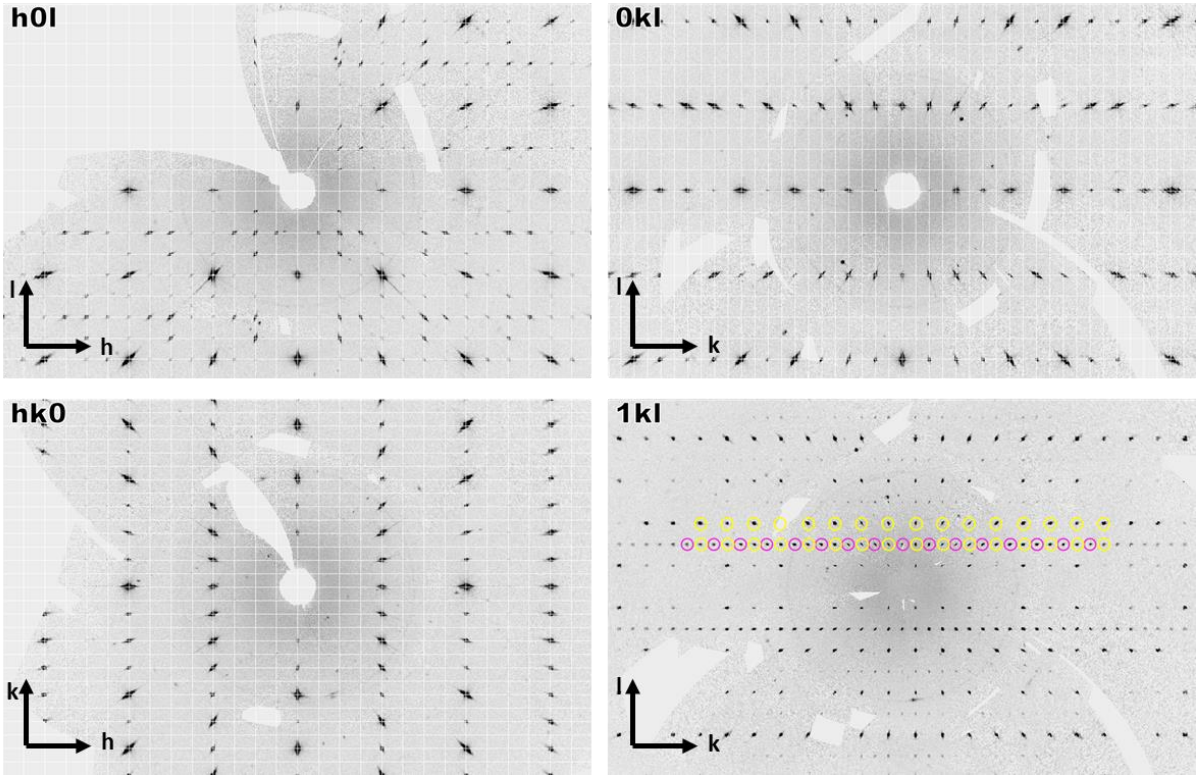


Figure 6.4. Single crystal X-ray diffraction patterns for $Ca_2Fe_{2.58}O_3S_2$ (ANG019b). These are precession photographs of particular layers in reciprocal space reconstructed from the full data collection. The peaks highlighted with the circles are described in the text.

The twin law describing the twinning present in this crystal is a 90° (four-fold) rotation about the *b*-axis (the stacking direction of the layers) (Figure 6.4, 6.5) which interconverts the basal *a* and *c* axes which is certainly possible given the closeness of their values. In the [1*kl*] image in Figure 6.4, the reflections encircled in yellow belong to one domain whilst those in pink arise from a 90° oriented domain [*hkl*] and also satisfy the general reflection condition *hkl*: h + k = 2n which is indicative of *C*-centering. The possible space groups that would describe this are *Cmce* (No. 64) or *C*2*ce* (No. 41). Converting these to *A*-centred space groups to make the stacking direction along the *c*-axis (for better comparison with the tetragonal sub-structure shown in Figure 6.1), these space groups become *Aeam* and *Aea*2 (which are the same two cells identified by Sheath via powder diffraction) with the lattice parameters listed in Table 6.2.

Table 6.2. Cell parameters of $Ca_2Fe_{2.58}O_3S_2$ (ANG019b) for the *A*-centred space groups.

a (Å)	11.15874(12)
b (Å)	11.15868(12)
c (Å)	17.50111(19)
α = β = γ	90°
V (Å^3)	2179.18(4)

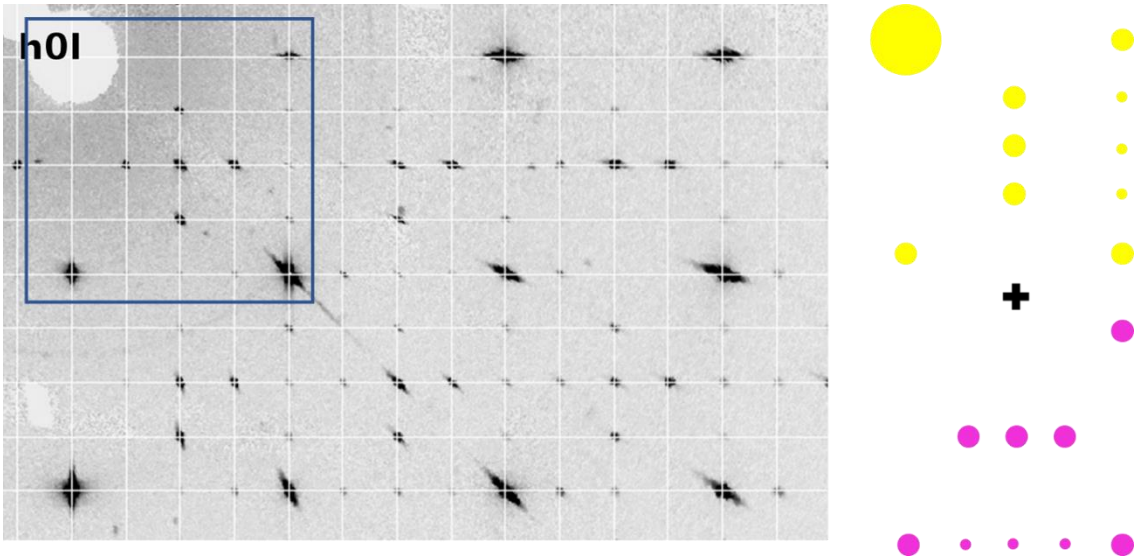


Figure 6.5. Evidence of the twinning from a *b*-axis rotation in the [h0l] plane.

Of the two *A*-centred cells, a refinement using the *Aea*2 space group gave a much better fit with an R value of 0.034 compared to the R value of 0.107 for the *Aeam* space group. In addition to this, the E-statistics most closely resembled those of a theoretical hypercentric symmetry which is consistent with a twinned non-centrosymmetric single crystal and the Flack coefficient refined to 0.5 which is indicative of a 50/50 ratio of the twins. The structure of $Ca_2Fe_{2.58}O_3S_2$ determined by SC-XRD is therefore in the *Aea*2 space group and the Fe vacancies are ordered as shown in Figure 6.6.

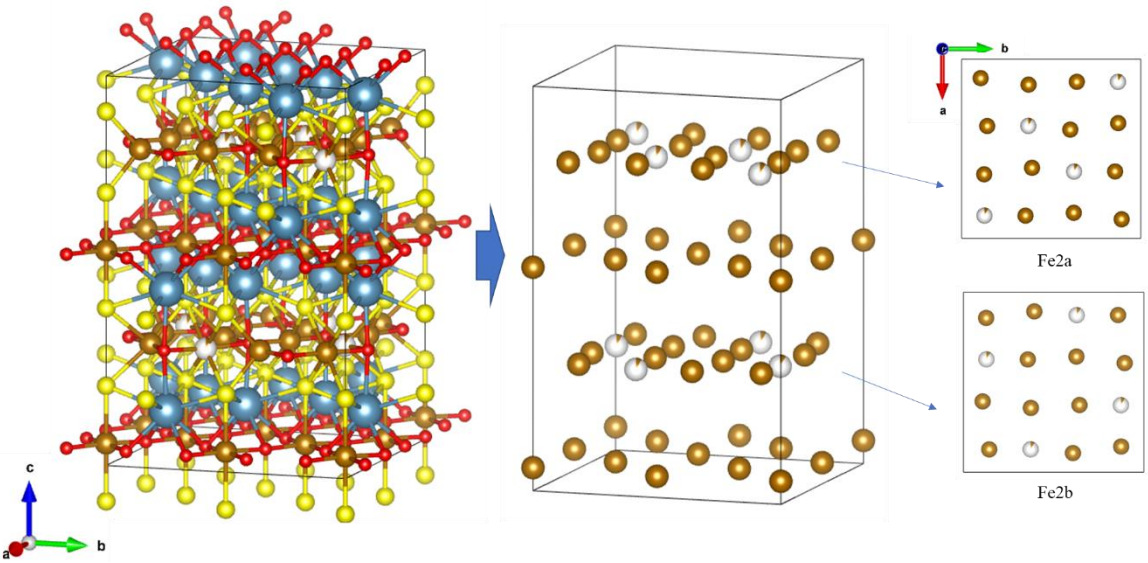


Figure 6.6. Refined unit cell of $Ca_2Fe_{2.58}O_3S_2$ with the *Aea*2 symmetry.

This result supports by the work done by Bradley Sheath, but it eliminates the ambiguity that had remained in the powder diffraction data. As Sheath asserted, the two Fe2 layers shown

individually in Figure 6.7 are related by a ½ unit cell translation along *b* (Figure 6.6), with one of the sites in the Fe2 layer (Fe2_1) having a very low occupancy (0.075(4) %). Bond valence sum calculations again support that the Fe1 sites are more oxidized rather than the Fe2 sites. All of the BVS calculations reported in Table 6.3 were completed assuming an Fe-valence of 2, but when an Fe-valence of 3 is used for the Fe1 sites, the BVS are closer to Sheath's reported BVS calculations for the Fe1 sites of 2.85(1).

Table 6.3. Refined atomic positions and occupancies from SC-XRD for $Ca_2Fe_{2.7-\delta}O_3S_2$ (ANG019b) in the *Aea*2 space group (No. 41) along with calculated Fe bond valence sums. The two Wyckoff sites that are occupied are the 4*a* and 8*b* sites.

atom	x	y	z	Occupancy	U_{iso} (Å^2)	Fe BVS
Ca1_1	0.49986(4)	0.24773(11)	0.46065(4)	1	0.0092(3)	-
Ca1_2	0.75222(11)	0.49931(5)	0.46066(4)	1	0.0091(3)	-
Ca1_3	0.50029(5)	0.25203(10)	0.64906(4)	1	0.0087(3)	-
Ca1_4	0.74793(11)	0.49882(6)	0.64895(4)	1	0.0092(3)	-
Fe1_1	0.5	0	0.55713(6)	1	0.0060(2)	2.661
Fe1_2	0.75057(5)	0.249427(9)	0.55493(6)	1	0.00611(13)	2.656
Fe1_3	0	0	0.55259(6)	1	0.0061(2)	2.640
Fe2_1	0.6275(3)	0.3727(3)	0.7998(2)	0.0754(8)	0.0030(5)	-
Fe2_2	0.64322(2)	0.37330(2)	0.30504(6)	1	0.01100(5)	2.095
Fe2_3	0.87384(2)	0.14274(2)	0.30482(5)	1	0.01084(5)	2.103
Fe2_4	0.606758(18)	0.106494(17)	0.30471(6)	1	0.00996(5)	2.109
O1_1	0.6237(4)	0.3731(5)	0.5490(2)	1	0.0111(8)	-
O1_2	0.8745(4)	0.1245(5)	0.5504(2)	1	0.0139(10)	-
O1_3	0.1247(4)	0.3756(5)	0.5528(2)	1	0.0103(8)	-
O1_4	0.3739(4)	0.1243(5)	0.5530(2)	1	0.0116(8)	-
O2_1	0.74549(18)	0.01241(7)	0.8059(3)	1	0.0116(3)	-
O2_2	0.48739(8)	0.24587(17)	0.8046(3)	1	0.0119(3)	-
S1_1	0.5	0.5	0.70035(7)	1	0.0059(4)	-
S1_2	0.5	0.5	0.40409(7)	1	0.0080(4)	-
S1_3	0.74910(5)	0.25034(7)	0.70247(6)	1	0.0061(3)	-
S1_4	0.75085(5)	0.24995(7)	0.40665(6)	1	0.0091(4)	-
S1_5	0.5	0	0.70470(7)	1	0.0069(4)	-
S1_6	0.5	0	0.40851(7)	1	0.0091(4)	-

Table 6.4. Anisotropic displacement parameters obtained from the SC-XRD refinement of $Ca_2Fe_{2.7-\delta}O_3S_2$ (ANG019b).

atom	U_{11}	U_{22}	U_{33}	U_{12}	U_{13}	U_{23}
Ca1_1	0.0067(6)	0.0075(6)	0.0135(6)	0.0004(3)	0.00008(17)	-0.0001(3)
Ca1_2	0.0073(6)	0.0062(6)	0.0137(6)	-0.0002(2)	0.0002(3)	-0.00068(18)
Ca1_3	0.0101(6)	0.0066(5)	0.0094(5)	-0.0002(3)	-0.00008(18)	0.0004(3)
Ca1_4	0.0100(6)	0.0086(5)	0.0090(5)	0.0002(2)	-0.0003(3)	-0.00085(18)
Fe1_1	0.0016(4)	0.0054(4)	0.0110(3)	-0.0001(3)	0	0
Fe1_2	0.0043(3)	0.0034(3)	0.01064(9)	0.0002(3)	-0.00012(4)	-0.0007(2)
Fe1_3	0.0067(4)	0.0019(4)	0.0098(3)	0.0000(3)	0	0
Fe2_2	0.01468(10)	0.00768(8)	0.01063(7)	-0.00486(6)	0.0007(3)	0.0000(2)
Fe2_3	0.00940(9)	0.01253(9)	0.01060(7)	-0.00479(7)	0.0010(2)	0.0011(3)
Fe2_4	0.01140(10)	0.00907(9)	0.00941(6)	0.00446(4)	-0.0002(3)	-0.0011(3)
O1_1	0.0150(16)	0.0118(16)	0.0064(7)	0.0082(7)	-0.0011(7)	-0.0011(7)
O1_2	0.0171(19)	0.015(2)	0.0091(8)	0.0109(8)	0.0004(8)	0.0003(8)
O1_3	0.0117(17)	0.0112(17)	0.0081(7)	0.0079(8)	0.0000(7)	0.0000(7)
O1_4	0.0133(17)	0.0135(17)	0.0079(8)	0.0094(7)	-0.0008(7)	-0.0018(7)
O2_1	0.0073(5)	0.0059(3)	0.0216(8)	-0.0008(4)	0.0013(15)	0.0081(13)
O2_2	0.0083(4)	0.0058(5)	0.0216(7)	0.0017(4)	-0.0042(13)	-0.0048(16)
S1_1	0.0074(8)	0.0051(7)	0.0054(5)	-0.0005(4)	0	0
S1_2	0.0079(9)	0.0088(7)	0.0073(5)	-0.0005(5)	0	0
S1_3	0.0063(7)	0.0060(6)	0.0059(4)	-0.0023(3)	-0.00005(19)	-0.00052(19)
S1_4	0.0102(7)	0.0083(6)	0.0089(4)	-0.0006(3)	0.0005(2)	-0.0001(2)
S1_5	0.0078(8)	0.0064(7)	0.0065(5)	0.0004(5)	0	0
S1_6	0.0081(9)	0.0093(8)	0.0099(6)	-0.0019(5)	0	0

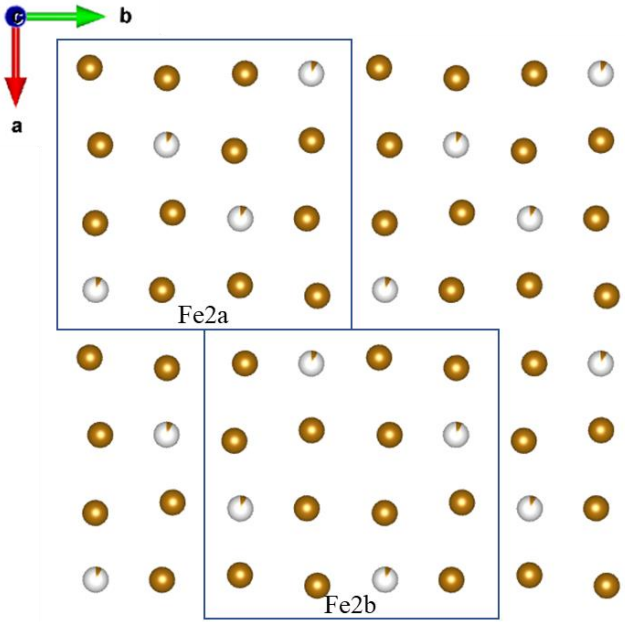


Figure 6.7. $2a_{supercell} \times 2a_{supercell}$ expansion of a single Fe2 layer showing that the two Fe2 layers are identical, just related by a ½ supercell translation along *b*.

In addition to this SC-XRD experiment, a different, larger, sample (ANG055) was prepared for NPD on D2B at the ILL and HRPD at the ISIS neutron and muon source (Figure 6.8). Refinements of the room temperature diffraction patterns of this sample were consistent with the structure determined by SC-XRD. In the refinements shown in Figure 6.8, only the lattice

parameters and Fe occupancy for the vacant site were allowed to refine from the refined structure derived from SC-XRD and described in Table 6.3. The refined lattice parameters from the D2B and HRPD neutron diffraction experiments agree with those from the SC-XRD refinement, and the structure obtained from the SC-XRD fits well to the powder diffraction patterns.

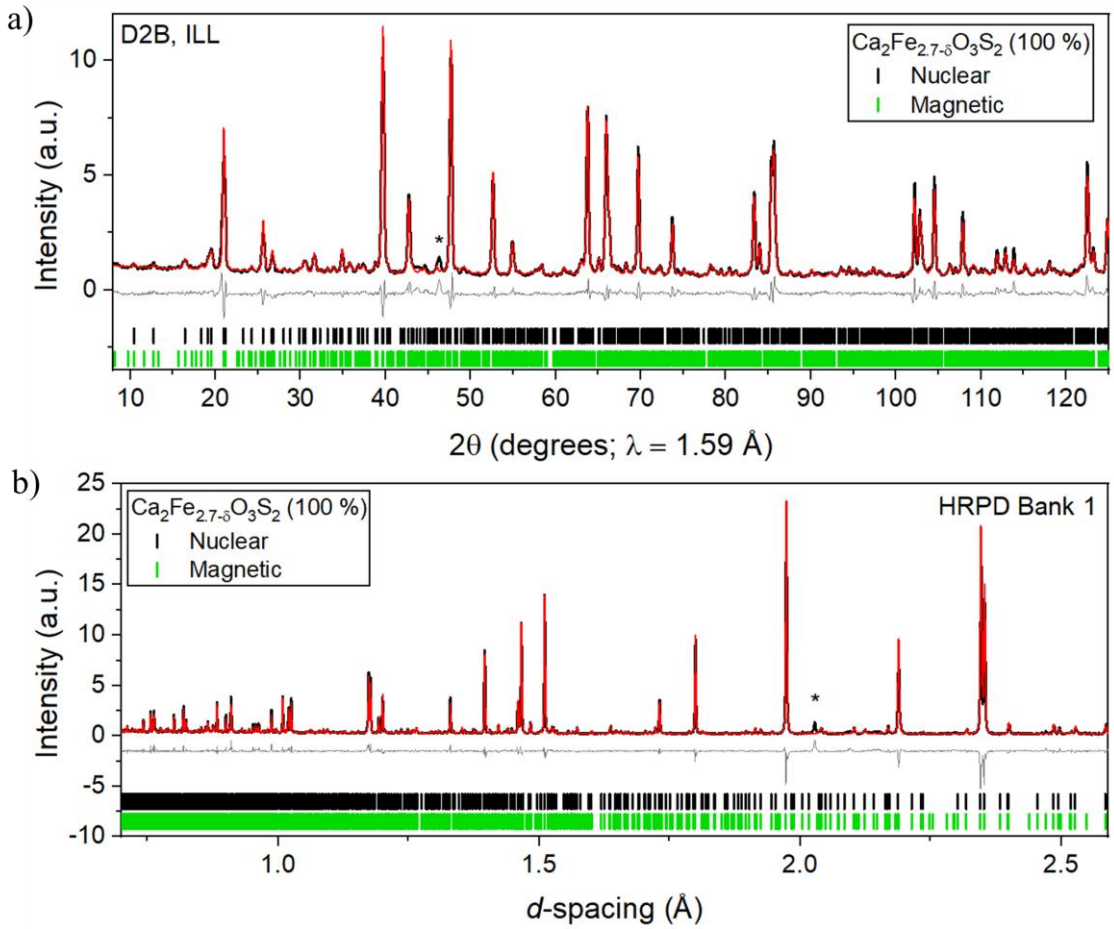


Figure 6.8. Rietveld refinements of neutron powder diffraction pattens collected on a) D2B and b) HRPD bank 1 for $Ca_2Fe_{2.6}O_3S_2$ showing the observed (black), calculated (red), and difference (grey) curves. Asterisks indicate an unindexed impurity peak.

Table 6.4. Comparison of refined lattice parameters and occupancies of XRD patterns from the single-crystal X-ray diffraction experiment (ANG019b) with those of the neutron powder diffraction experiments conducted on D2B and HRPD (ANG055) as well as XRPD (ANG055).

	SC-XRD	D2B	HRPD	I11 XRPD
a (Å)	11.15874(12)	11.157(1)	11.1696(3)	11.1603(2)
b (Å)	11.15868(13)	11.157(1)	11.1697(3)	11.1608(2)
c (Å)	17.50111(19)	17.5004(3)	17.5181(2)	17.50590(5)
V (Å^3)	2179.18(4)	2178.7(3)	2185.59(9)	2180.50(5)
*occ*Fe2_1	0.0754(8)	0.06(1)	0.138(7)	0.083(3)

6.1.3. Superstructure suppression

While the superstructure peaks are always evident in samples produced via ceramic solid-state synthesis in sealed silica tubes, there are a few circumstances in which the superstructure was observed to have been suppressed. The first of these is in the case of high-pressure synthesis that was carried out by Dr Birgit Fuchs at the University of Innsbruck, as reported in Bradley Sheath's D.Phil. Thesis. In this synthesis, the stoichiometry $Ca_2Fe_3O_3S_2$ was targeted by mixing the appropriate ratios of CaO (Alfa Aesar 99.95%), FeO, Fe (Alfa Aesar 99.998%) and S (Alfa Aesar 99.999%) until homogeneous. This mixture was then compressed to 7 GPa and then heated to 900°C in 10 minutes where it dwelled for 30 minutes after which the temperature was quenched to room temperature and the pressure then slowly released. Room temperature SXRPD collected on I11 at DLS revealed that the product displayed the peaks at comparable d-spacings as the phase synthesized at ambient pressure, with small FeS and Fe impurities, but there were no superstructure peaks present (Figure 6.9). In addition to this, the Fe2 site occupancy refines to 0.801(2). This indicates that high pressure synthesis will suppress the Fe-vacancy ordering, but still does not produce the stoichiometric target $Ca_2Fe_3O_3S_2$.

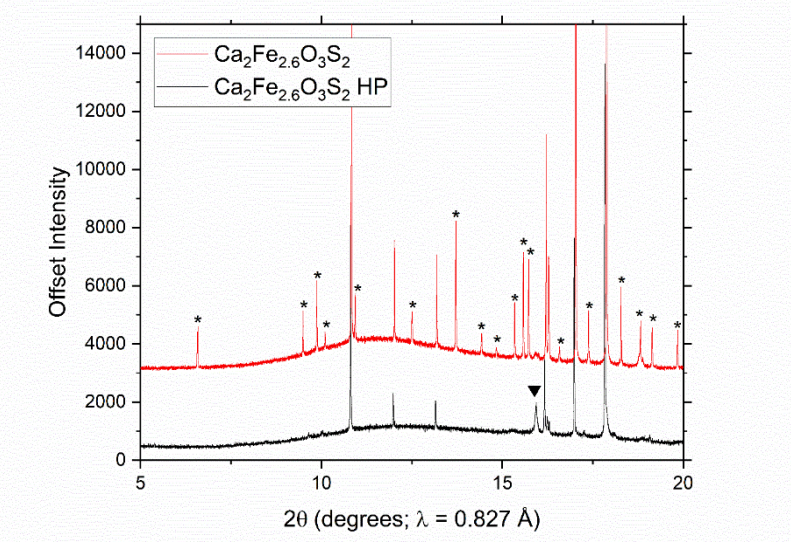


Figure 6.9. Comparison of XRPD patterns of $Ca_2Fe_{2.6}O_3S_2$ phases synthesized at ambient and high pressure measured on the MAC detector at I11. The peaks highlighted by a * denote superstructure peaks that arise due to Fe vacancy ordering and the black triangle denotes a peak from FeS.

The superstructure is also suppressed by introducing disorder on the chalcogen site by fractionally substituting S by Se [2].

A similar phenomenon was observed one other instance. In an attempt by Dr D. Prabhakaran (Department of Physics, University of Oxford) to grow a large single crystal via floating-zone crystal growth, the crystal growth was unsuccessful. A melt was leftover and sulfur deposition was observed on the quartz tube in which the crystal growth was attempted. XRPD of this melt revealed that the previous sample (that displayed the superstructure consistent with Fe-vacancy ordering) had changed. There were some binary impurities from decomposition, but in addition to this, the superstructure peaks had also been suppressed (Figure 6.10).

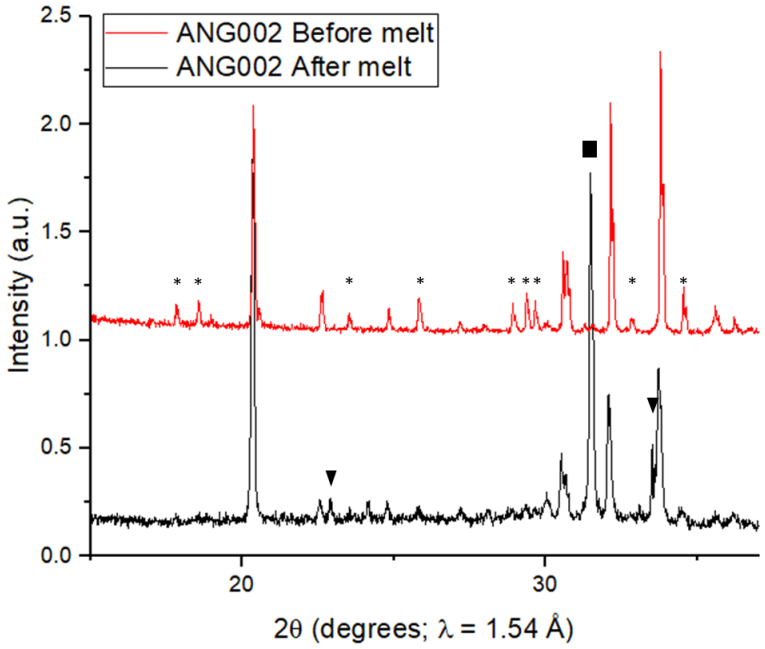


Figure 6.10. Comparison of the XRPD patterns of the samples ANG002 collected on the in-house Bruker D8 Advance Eco diffractometer before and after the melt, with * denoting superstructure peaks arising from the Fe-vacancy ordering and black triangles and squares indicating reflections from CaS and FeS respectively.

With this in mind, two other pelleted samples were melted on purpose in alumina crucibles with one being sealed in an evacuated silica tube and the other open to air. These samples were then heated to 1100°C for 5 hours before being cooled back to room temperature at an unspecific rate. The X-ray powder diffraction patterns of these samples revealed that melting in air resulted in complete decomposition into $Ca_2Fe_2O_5$, Fe_2O_3, $CaSO_4$ and other phases while the sample melted in an evacuated tube displayed suppression of the superstructure peaks and CaS and FeS impurities (Figure 6.11). So, while it is possible to suppress the superstructure of long-range Fe2

site vacancies by melting or use of high pressure, it does not seem possible both to suppress the superstructure and obtain a single-phase product.

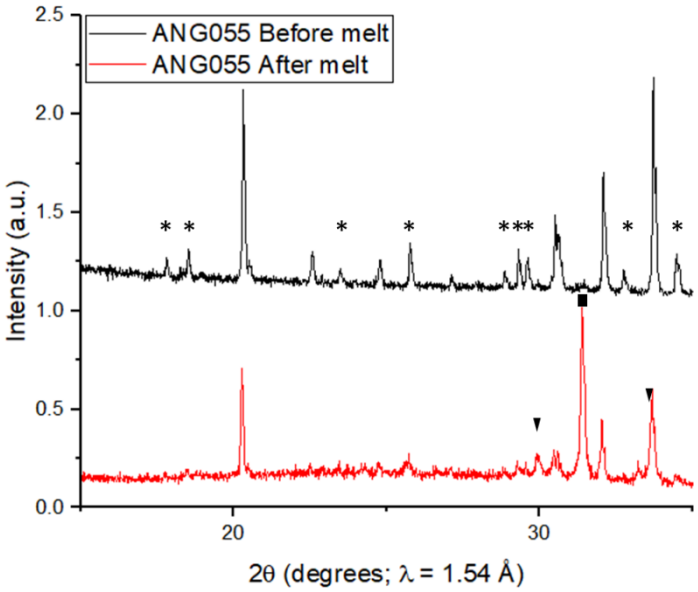


Figure 6.11. Comparison of the XRPD patterns of the sample ANG055 before being melted and after being melted in an evacuated quartz tube collected on the in-house Bruker D8 Advance Eco diffractometer. The * denotes superstructure peaks arising from the Fe-vacancy ordering in the Fe2 layer and black triangles and squares indicating reflections from CaS and FeS respectively.

6.2. Magnetism of $Ca_2Fe_{2.7-\delta}O_3S_2$ in an applied-field

6.2.1. Introduction and motivation

$Ca_2Fe_{2.7-\delta}O_3S_2$ displays magnetic ordering on two magnetic sublattices, as reported by Sheath, and undergoes complex change upon cooling which is associated with the fact that there is ordering of the Fe^{2+} cations and vacancies. This structural order is present up to the highest temperature measured (447 K) and above the magnetic ordering temperature. Magnetic order onsets around 350 K in the Fe1 and Fe2 layers (the crystallographic order is present at much higher temperatures) and below a 70 K phase transition, there is subtle structural distortion and an increase in the resistivity and saturation moment determined in the magnetization isotherms (Figure 6.12) [2]. At low temperatures, both the Fe1 and Fe2 layers order antiferromagnetically along the 180° Fe-O-Fe super exchanges with canting both within the basal plane and along *c*. The Fe2 vacancy ordering then causes a net ferromagnetic moment, as the moments that would occur on the irons in the vacant positions all contain the same component (i.e. the layers are

ferrimagnetic – uncompensated antiferromagnetic). The interesting features in the 5 K magnetization isotherm suggests that there may be an evolution in the magnetic ordering at low temperatures under an applied magnetic field, and this prompted the neutron powder diffraction experiment discussed in this section.

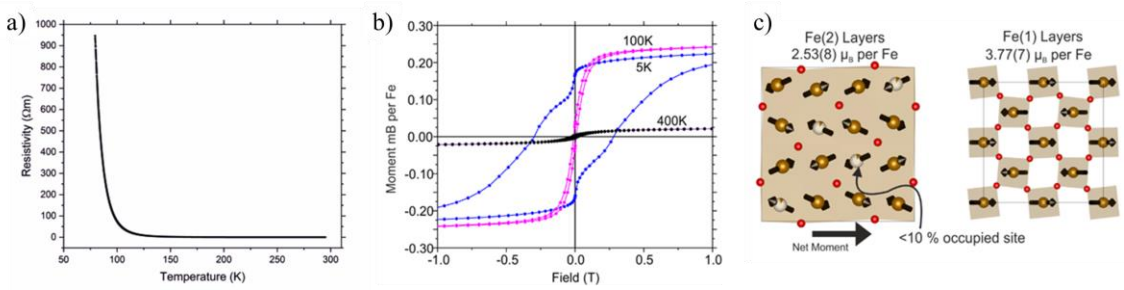


Figure 6.12. The a) magnetization isotherm, b) resistivity plot, and c) zero-field magnetic structure at 5 K of $Ca_2Fe_{2.6}O_3S_2$ [2].

6.2.2. Results and Discussion

Various in-field neutron powder diffraction measurements were carried out on $Ca_2Fe_{2.6}O_3S_2$ (ANG055) on the new XtremeD beamline at the ILL, which is designed for experiments under various extreme conditions [3]. In this, the sample was cooled to 5 K in zero field, at which point the field was applied up to 5 T. As the field is applied, there are some apparent changes to the diffraction patterns. The most evident of these are the growth of several peaks at high angles, of which the origin is ambiguous as the change in intensity can be fit either by small changes in the nuclear structure distortion modes or by changes in preferred orientation parameters. Either or both of these changes is perfectly plausible, as the Fe2 positions within the vacancy ordering pattern could be affected by the applied field, as could the grain orientation, given that there is a net ferromagnetic moment from the Fe2 vacancy order at low temperatures. There is also one peak at low angles (~20°) which cannot be fit by changes to these parameters and instead corresponds to slight changes in the magnetic structure (red triangle marker in Figure 6.13). However, all of the changes in the magnetic modes that are refined are still similar within error between the 0 T and 5 T refinements.

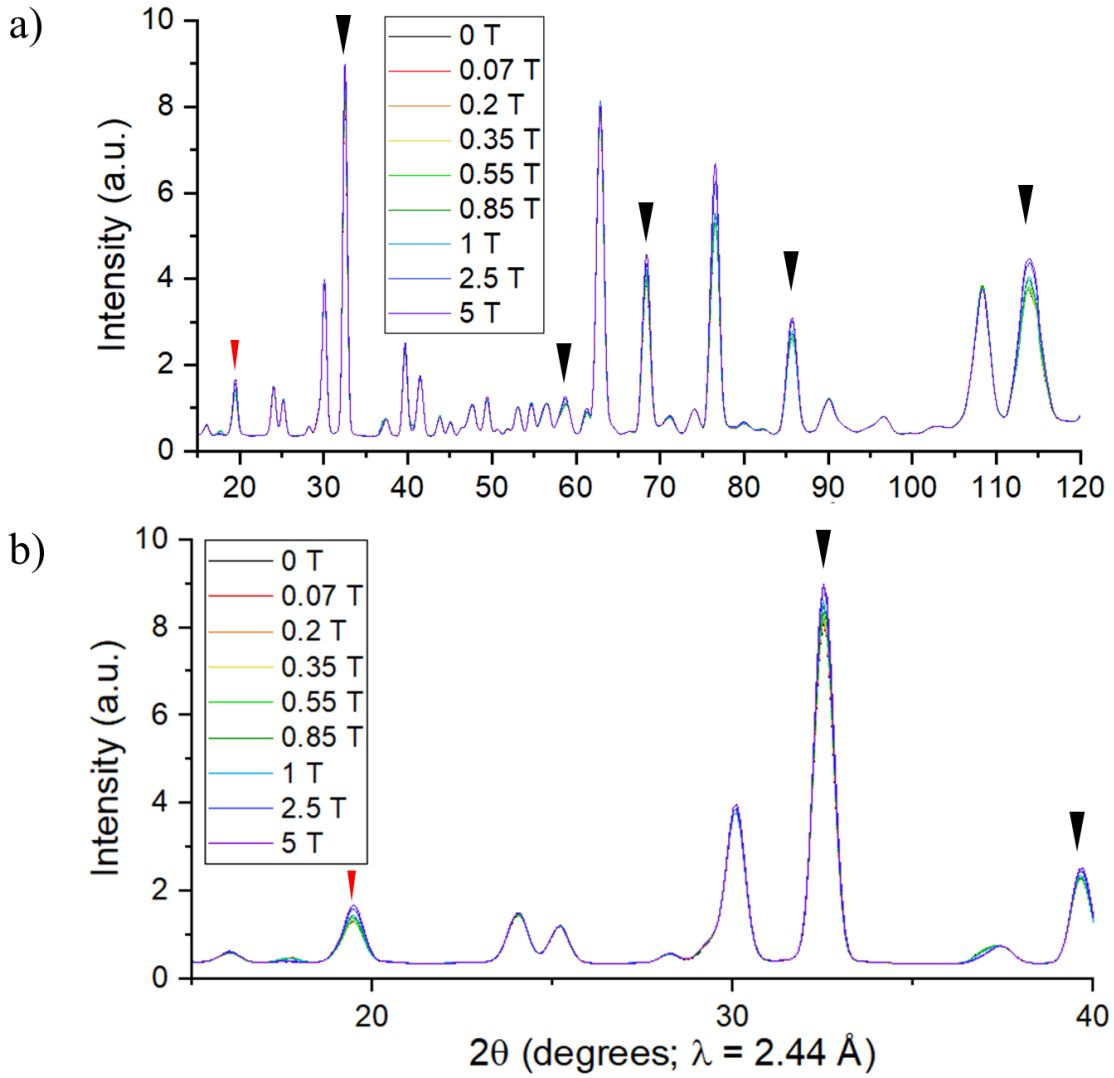


Figure 6.13. Variable field neutron powder diffraction patterns collected at T = 5 K with applied fields ranging from 0 to 5 T collected on XtremeD at the ILL shown a) at both high and low angles and b) zoomed in to only the low angle reflections. Black triangles indicate peaks that grow with increasing applied fields and can be fit with changes to the nuclear structure or preferred orientation, whereas the red triangle indicates the only peak that can only be fit with changes to the magnetic structure.

One thing that is of note, however, is that the zero-field magnetic model refined in this experiment ended up being slightly different from that reported by Sheath, with none of the moments having components along the *c*-axis and the moments refining to 3.91(6) μ_B per Fe1 and 4.2(1) μ_B per Fe2 (Figure 6.14a). The model used in this experiment was mostly the same model as was refined in Sheath's thesis, with the exception being that the modes corresponding to any canting along the *c*-axis were not active. The absence of the *c*-canting in ANG055 is supported by the absence of a low-angle peak at a *d*-spacing of around 6.84 Å (black triangles in Figure 6.14), corresponding to the (210)/(201) magnetic reflection. Activating the canting along *c* in the case

of BS018 as done in Sheath's thesis (Figure 6.14b) also places intensity in the refinement where there isn't an obvious reflection in the experimental data (red triangles in Figure 6.14), indicating that there is weak evidence for the canting that Sheath placed along *c*.

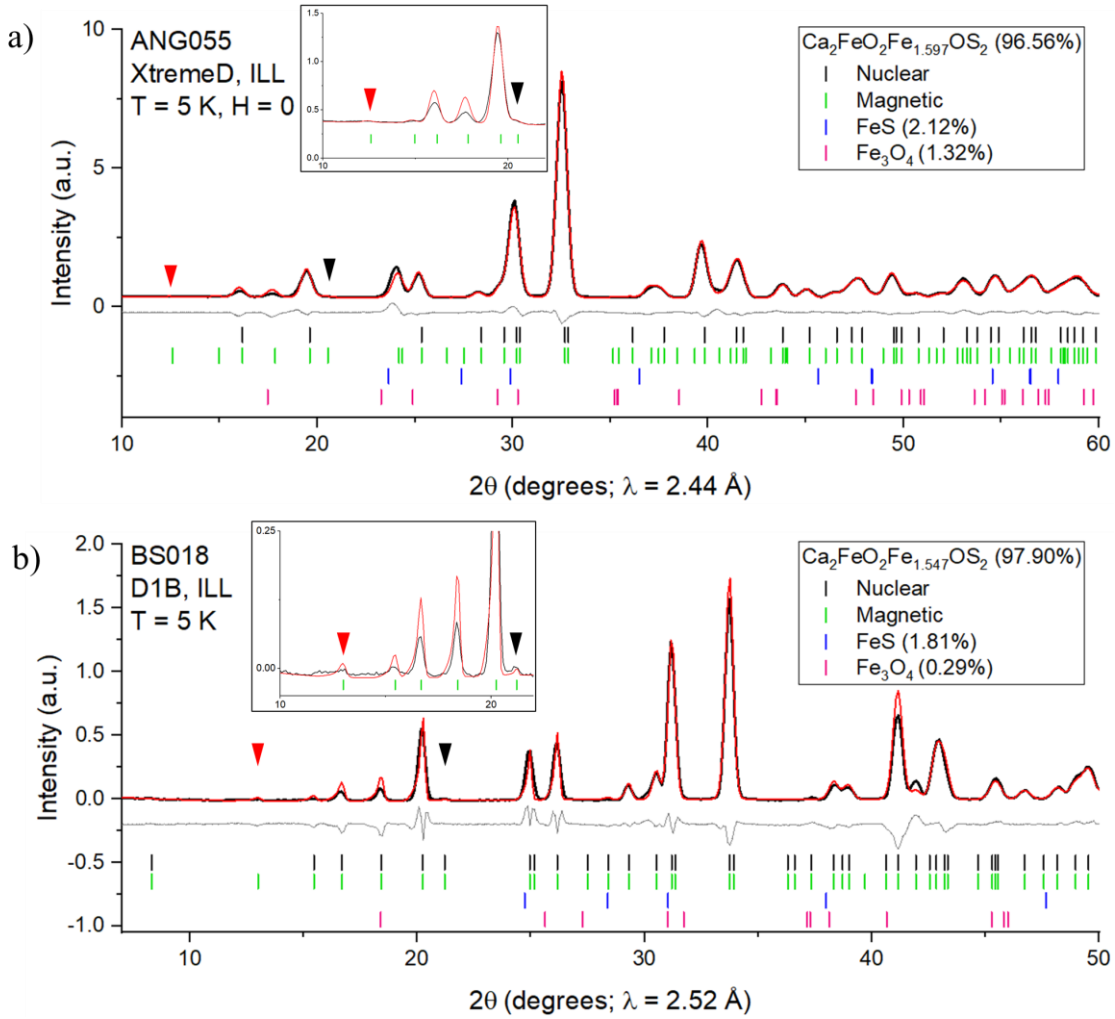


Figure 6.14. Rietveld refinements of zero-field 5 K neutron powder diffraction patterns for $Ca_2Fe_{2.6}O_3S_2$ samples a) ANG055 (R_{wp} = 5.42%) and b) BS018 (R_{wp} = 9.37%) [2] collected on beamlines XtremeD and D1B respectively at the ILL with black triangles indicating the (210)/(201) magnetic reflection which is present for BS018 and not ANG055. Note that the refinement for BS018 is from Bradley Sheath's thesis which uses a $P2_12_12$ space group due to a low-temperature structural transition that the XtremeD data is not well enough resolved to necessitate [2]. A red triangle indicates the (010)/(001) magnetic reflection that is assigned some intensity in the refinement of BS018 when canting of the moments is enabled, while there is not obvious peak in the experimental data for either sample.

6.3. Magnetism of $Ca_2Fe_{2.7-\delta}O_3S_{2-x}Se_x$

6.3.1. Introduction and previous work

Previous work characterizing the solid solution $Ca_2Fe_{2.7-\delta}O_3S_{2-x}Se_x$ was conducted by Bradley Sheath [2]. In his work, Sheath demonstrated that the solid solution was isostructural to the all-S

phase examined previously in this chapter with the exception that the superstructure that arises from Fe-vacancy ordering is disrupted by the disorder on the chalcogen site. Sheath also collected neutron powder diffraction patterns on D2B at the ILL for these phases at room temperature and 5 K which was then used to characterize the nuclear and magnetic structures. The magnetic modes that were refined for each member of the solid solution and the refined magnetic moments as determined by Sheath are summarized in Table 6.5. However, D2B is not ideal for magnetic characterization given that the best peak resolution is found at shorter *d*-spacings which is better suited for nuclear structure characterization than magnetic structure determination. With this in mind, variable-temperature neutron powder diffraction experiments were conducted for members across the solid-solution $Ca_2Fe_{2.7-\delta}O_3S_{2-x}Se_x$ on beamline D1B at the ILL which, given the high flux of neutrons, the larger wavelength of 2.52 Å, and the instrument geometry, is more optimized for both faster measurements at many temperatures and peak resolution at longer *d*-spacings where magnetic reflections are found.

Table 6.5. Magnetic modes and moments for $Ca_2Fe_{2.7-\delta}O_3S_{2-x}Se_x$ at T = 5 K as determined by Bradley Sheath [2].

x	0.5	1	1.5
Fe1 modes refined	mM5+	mM5+	mM5+, mA2+
Fe2 modes refined	mX1-, mX2-	mX1-, mX2-	mX1-, mX2-
Fe1 moment (μ_B)	3.58(4)	3.34(4)	3.27(6)
Fe2 moment (μ_B)	1.90(10)	2.02(10)	2.26(10)

One of the reasons that the wide temperature range is of interest comes from the transitions that are observed for each phase in the magnetometry data (Figure 6.15) [2]. Each phase as the Se content increases has different transition temperatures in the 5T-4T-3T susceptibility measurements conducted by Sheath (where the signals from magnetic impurities are subtracted between each pair of fields and averaged). For all of these phases, there is a broad hump in the signals at higher temperatures which is most evident for the $x = 1.5$ phase and which occurs at progressively lower temperatures as the Se-content increases. There are also peaks in all of the curves which also occur at consistently higher temperatures as the Se-content increases. Below this peak, there are additional features that arise with the $x = 1.5$ phase having the most. The zero-

field variable-temperature neutron diffraction discussed in this section provides insight that could help explain the origins of these features.

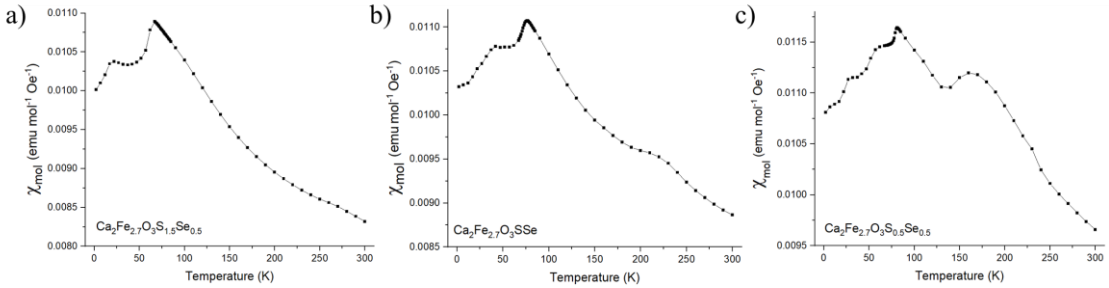


Figure 6.15. 5T-4T-3T susceptibility curves for a) $Ca_2Fe_{2.7-\delta}O_3S_{1.5}Se_{0.5}$, b) $Ca_2Fe_{2.7-\delta}O_3SSe$, and c) $Ca_2Fe_{2.7-\delta}O_3S_{0.5}Se_{1.5}$ [2]

6.3.2. $Ca_2Fe_{2.7-\delta}O_3S_{1.5}Se_{0.5}$ (x = 0.5)

At room temperature, $Ca_2Fe_{2.7-\delta}O_3S_{1.5}Se_{0.5}$ is not magnetically ordered. Magnetic reflections first appear around T = 260 K (Figure 6.16), and these can be fit in the Rietveld refinement by activating the mM5+ modes which has a **k** = (½, ½, 0) propagation vector. These peaks grow as the temperature decreases and saturate at around 100 K. This mode corresponds to moments on the Fe1 ions of 3.73(14) μ_B which order antiferromagnetically along the Fe-O-Fe super exchange (see Figure 6.18a). Then, at 60 K, another set of magnetic peaks emerges which can be fit by activating the mX1- and mX2- modes which correspond to ordering of the moments in the Fe2 layer, and the mX1- E_g(a) mode that corresponds to canting of the Fe1 moments in the basal plane (Figure 6.18b). At 5 K, the Fe1 and Fe2 moments refine to 3.66(20) μ_B and 0.80(9) μ_B respectively.

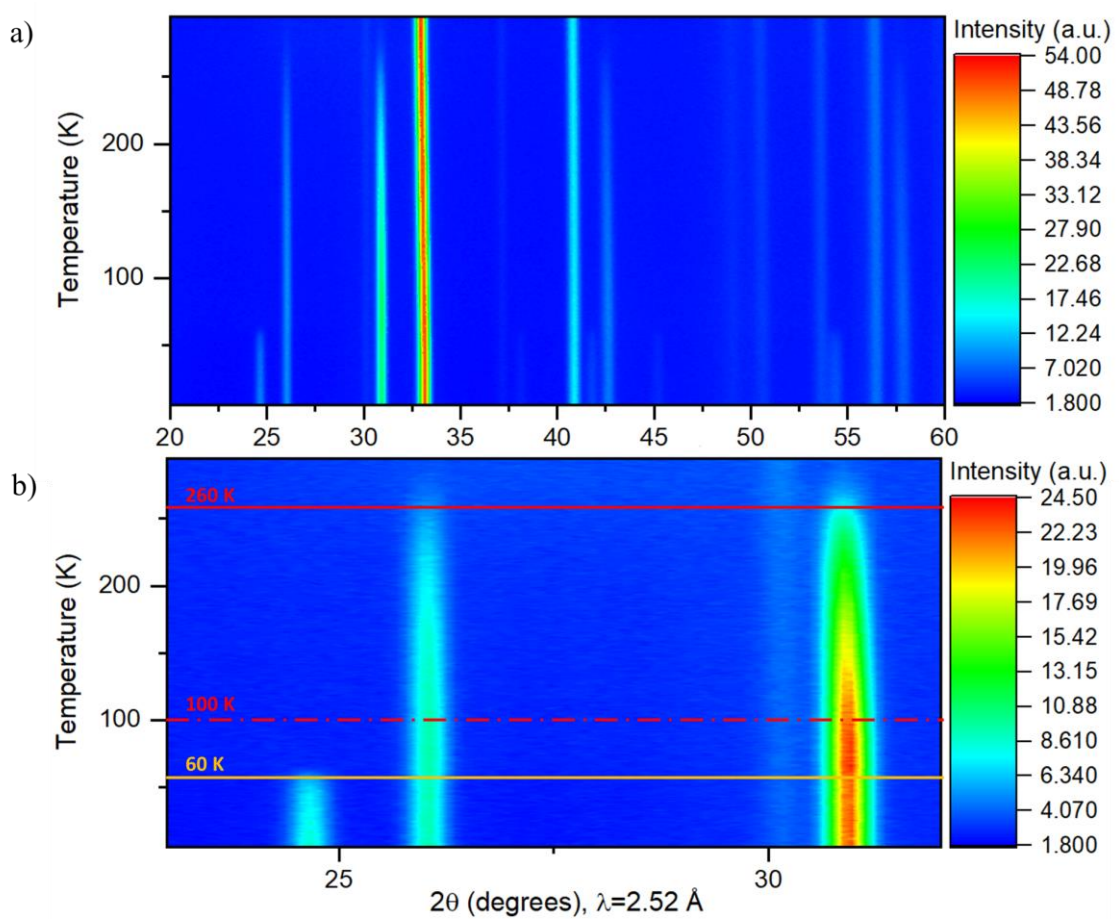


Figure 6.16. Contour plot showing a) the full and b) zoomed in neutron diffraction patterns of $Ca_2Fe_{2.7-\delta}O_3S_{1.5}Se_{0.5}$ with the onset of magnetic peaks indicated by solid lines and the saturation of those peaks indicated in dashed lines. The red lines indicate magnetic reflections corresponding to the Fe1 layer and orange lines indicate those of the Fe2 layer.

The temperatures at which the onset of magnetic reflections is observed in the variable-temperature neutron powder diffraction patterns do seem to correspond to some of the transitions observed in the magnetometry curves displayed in Figure 6.15. The onset of order in the Fe1 layer occurs around the same temperature as the broad feature in the magnetometry, and the onset of order in the Fe2 layer around 60 K occurs at about the same temperature as the peak that occurs in the magnetometry data around 67 K.

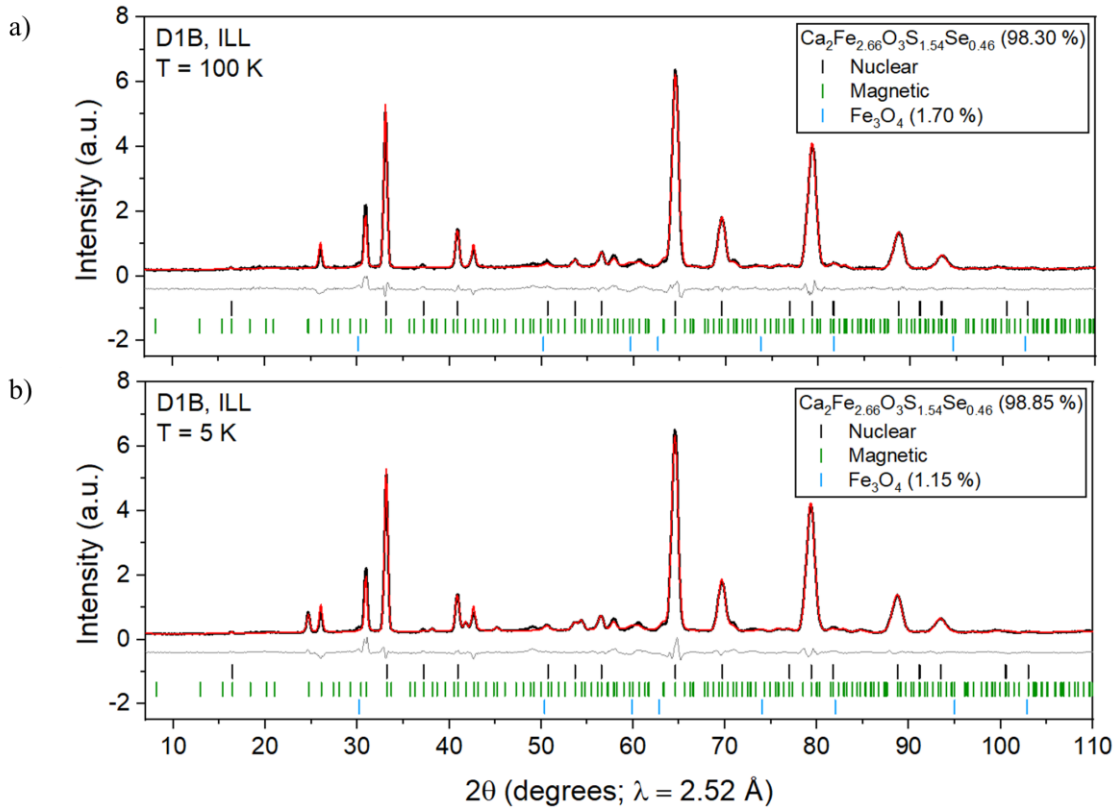


Figure 6.17. Rietveld refinements of NPD patterns of $Ca_2Fe_{2.7-\delta}O_3S_{1.5}Se_{0.5}$ collected on D1B at a) T = 100 K (R_{wp} = 8.68%) and b) T = 5 K (R_{wp} = 8.08%) showing the observed (black), calculated (red), and difference (grey) curves.

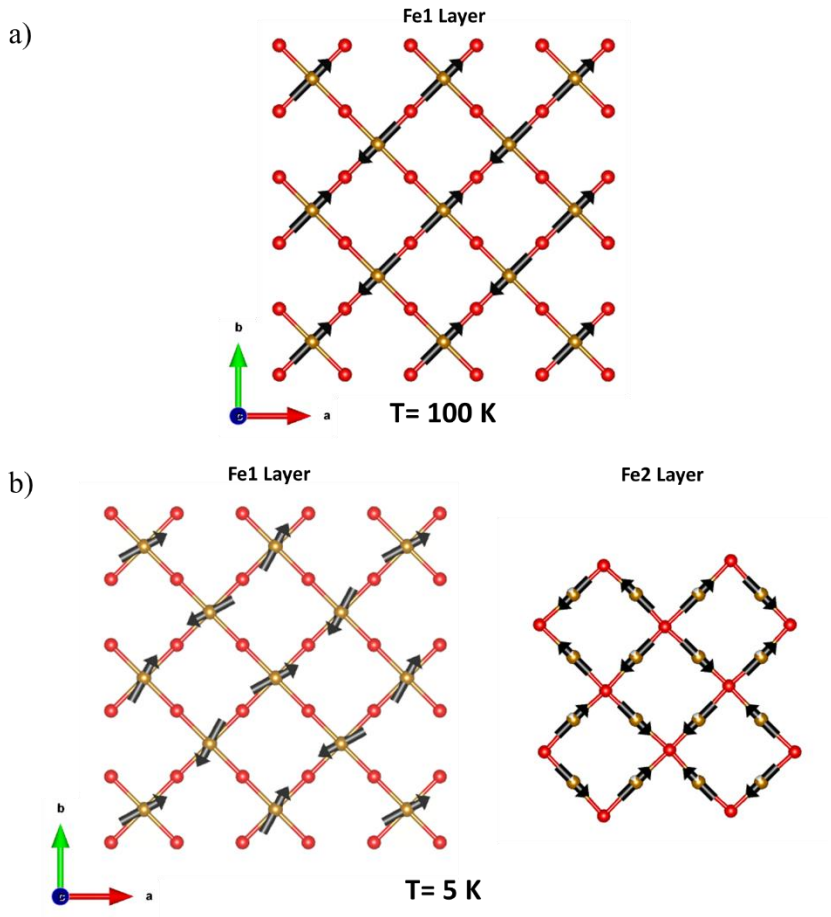


Figure 6.18. Refined magnetic models of $Ca_2Fe_{2.7-\delta}O_3S_{1.5}Se_{0.5}$ at a) T = 100 K and b) T = 5 K.

This magnetic model is similar to that proposed by Sheath in his thesis based on the D2B diffraction pattern refinements, but the differences come in when considering the refined moments themselves as well as which layer is canted. In Sheath's 5 K refinement, the magnetic model placed the canting in the Fe2 layer as opposed to the Fe1 layer, and consequently the moment in the Fe2 layer was larger (at 1.90(10) μ_B) and the Fe1 moment refined to a slightly smaller 3.58(4) μ_B. While the refinement placing the canting only in the Fe2 layer was similar, the refinement placing it in the Fe1 layer instead was a better fit as the Fe2 canting placed too much intensity on the (011) magnetic reflection around 18˚ where there is no peak in the diffraction pattern.

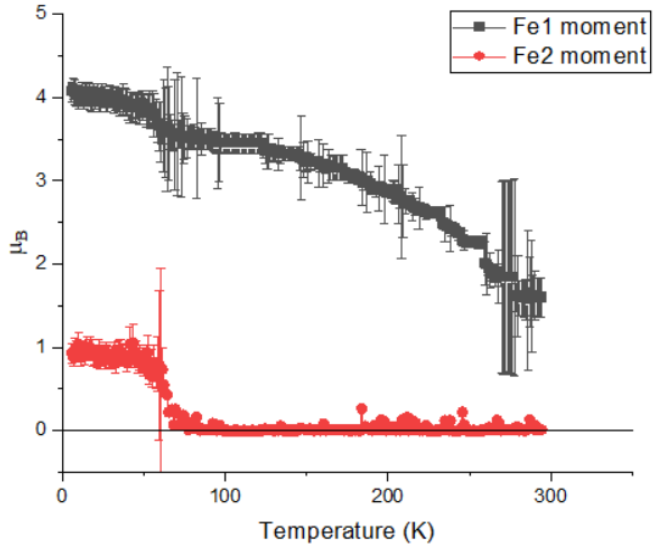


Figure 6.19. Evolution of the refined magnetic moments on the Fe1 and Fe2 sites as a function of temperature. Note that the error bars for the Fe2 moment were not included above 70 K for the sake of clarity.

A sequential refinement was also carried out in order to investigate how the magnitude of the Fe1 and Fe2 magnetic moments evolve over a wide range of 279 temperatures for which data was collected in the D1B experiment. In this, it is clear that on warming, the ordered Fe2 moment decreases starting around 60 K to freely refine to zero above approximately 67 K. The error bars were not shown in Figure 6.19 for the Fe2 moment above 63 K as the errors quickly become large and obscure data. In addition to this trend in the Fe2 moments, it is also evident that the Fe1 moment decreases slightly on warming around when the Fe2 layer loses long-range order which likely corresponds to the loss of the canting of the Fe1 layer on warming. The errors for the Fe1 moment also become quite large around 270 K which is where the magnetic reflections are first observed. Other variations in the errors and the Fe1 moments themselves come from the nature of the sequential refinement wherein a previous temperature's output file is copied to the next input file, so the refinement can become "stuck" on a less good fit before it corrects itself without manual intervention.

6.3.3. $Ca_2Fe_{2.7-\delta}O_3SSe$ (x = 1)

At room temperature, $Ca_2Fe_{2.7-\delta}O_3SSe$ is again not magnetically ordered. Magnetic reflections first appear at a lower temperature than in the x = 0.5 phase around T = 220 K (Figure 6.20). These magnetic reflections can be fit in the Rietveld refinement by activating the mM5+ mode

which has a **k** = (½, ½, 0) propagation vector and corresponds to the same antiferromagnetic ordering pattern along the Fe-O-Fe super exchange in the Fe1 layer as in the x = 0.5 phase, shown in Figure 6.17a. At T = 100 K, the Fe1 magnetic moment intensity refines to 3.53(7) μ_B. Then, at 60 K, another set of magnetic peaks emerge which can be fit by activating the mX1- and mX2- modes which correspond to the Fe2 layer, in addition to the mX1- E_g(a) mode that corresponds to the Fe1 layer and represents the canting of the Fe1 moments in the basal plane (Figure 6.22). The addition of the mX2- mode also means that the Fe2 moments are slightly canted within the basal plane. This is different from the x = 0.5 phase but is necessary in order to fit a small peak that arises at 18.2° for the x = 1 phase only. This peak is not shown in the film plots below (Figure 6.20) because it is very small compared to the other peaks and is not visible in comparison to the other peaks. At 5 K, the Fe1 and Fe2 moments refine to 3.77(6) μ_B and 1.61(3) μ_B respectively.

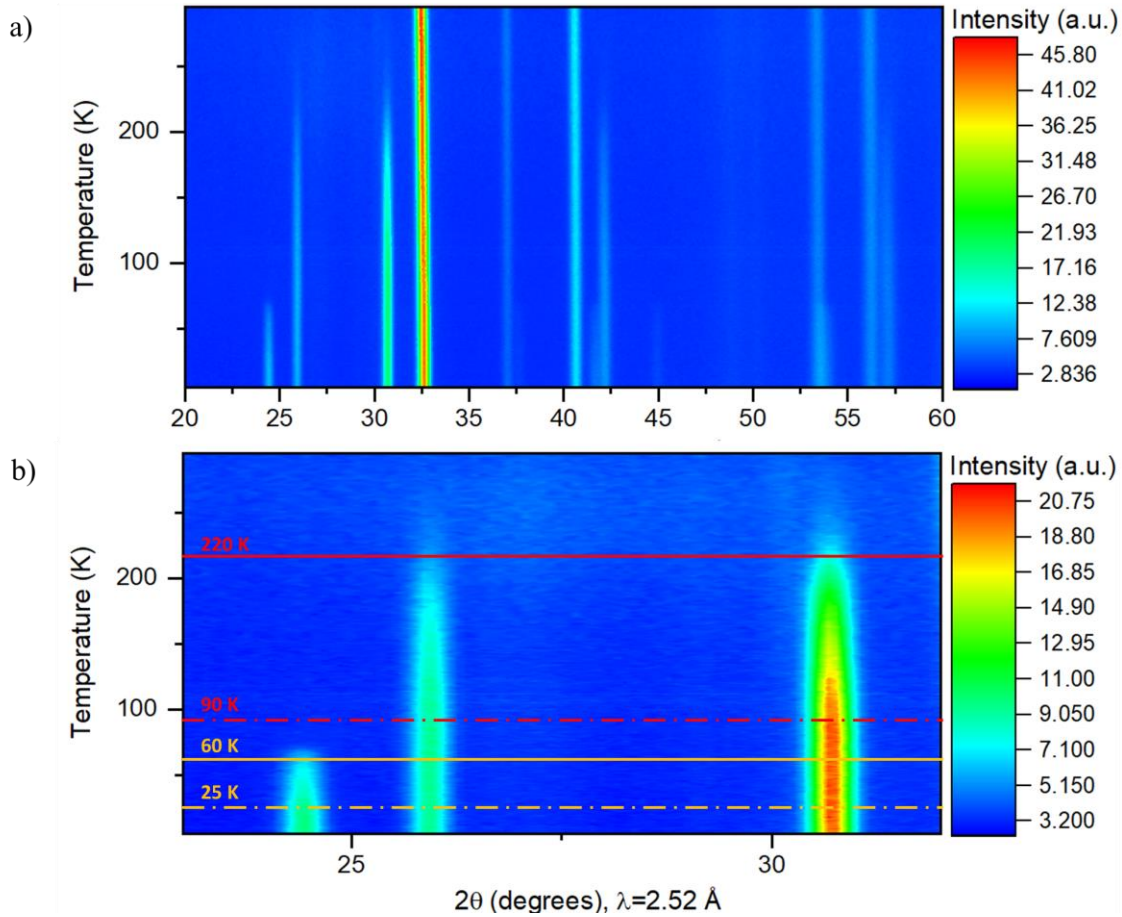


Figure 6.20. Contour plot showing a) the full and b) zoomed in neutron diffraction patterns of $Ca_2Fe_{2.7-\delta}O_3SSe$ with the onset of magnetic peaks indicated by solid lines and the saturation of those peaks indicated in dashed lines. The red lines indicate magnetic reflections corresponding to the Fe1 layer and orange lines indicate those of the Fe2 layer.

Like in the x = 0.5 case, the broad hump seen in the 5T-4T-3T susceptibility curve for the x = 1 phase roughly corresponds to the onset of the magnetic peaks that indicate the onset of magnetic order in the Fe1 layer at approximately 220 K. The peak in the susceptibility curve for the x = 1 phase occurs at approximately 75 K, and this again roughly corresponds to the appearance of the peaks corresponding to the ordering of the Fe2 layer and the canting of the Fe1 layer.

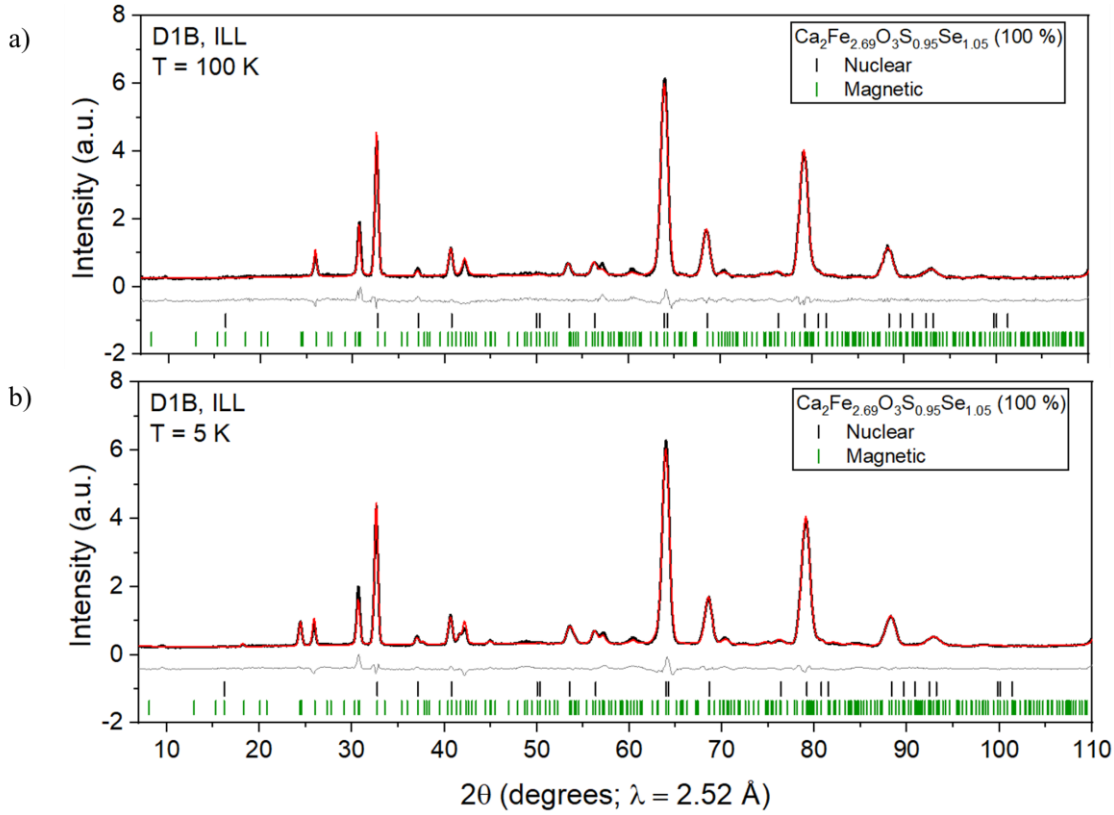


Figure 6.21. Rietveld refinements of NPD patterns of $Ca_2Fe_{2.7-\delta}O_3SSe$ collected on D1B at a) T = 100 K (R_{wp} = 7.64%) and b) T = 5 K (R_{wp} = 6.49%) showing the observed (black), calculated (red), and difference (grey) curves.

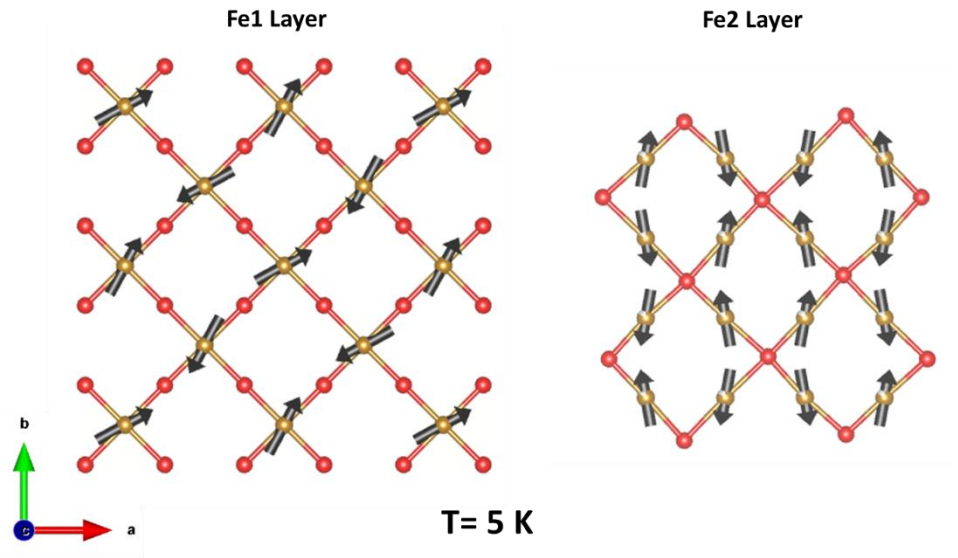


Figure 6.22. Refined magnetic models of the Fe1 and Fe2 layers of $Ca_2Fe_{2.7-\delta}O_3SSe$ at T = 5 K showing especially the canting of the moments in the Fe2 layer.

This low-temperature magnetic structure is similar to the one which Sheath obtained from his work with the D2B diffraction patterns, but the D1B patterns again reveal additional intricacies like the peaks that are not at all resolved in the D2B patterns (and are not even fully resolved in the D1B patterns like around 2θ = 37° and 37.5° for example). This reveals that the canting in the Fe1 layer at low temperatures, whereas Sheath's model only accounted for canting in the Fe2 layer, is necessary for the refinement.

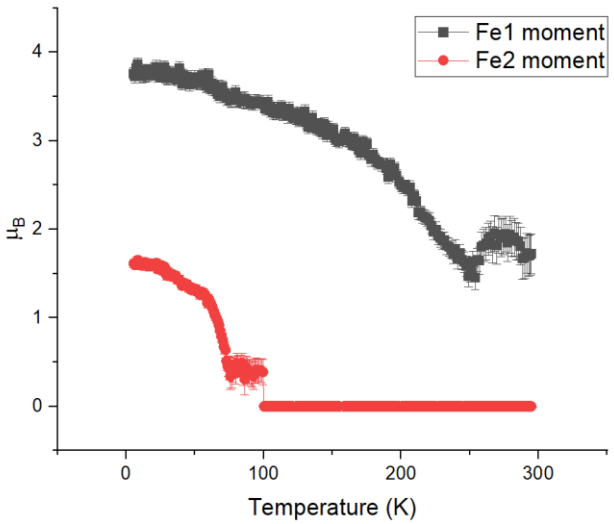


Figure 6.23. Evolution of the refined magnetic moments on the Fe1 and Fe2 sites as a function of temperature. The Fe2 moments above 100 K were fixed to 0 as described in the text.

Another multi-refinement was carried out for this data set, and like with the x = 0.5 phase, we can see clear points where the Fe1 and Fe2 layers lose magnetic order, this time indicated mainly

by when the errors become larger (Figure 6.23). These temperatures are around 250 K and 72 K for the Fe1 and Fe2 moments respectively, and the refined moments for the Fe1 layer above 250 K are artefact which is shown by individual refinements. Note also that above 100 K, the first multi-refinement for which all magnetic modes remained active frequently found local minima rather than a global minimum in the least-squares minimization which were not significant in that they gave unrealistic results and high errors. To rectify this and provide significant results, a second sequential refinement from 100-300 K was carried out with only the mM5+ Fe1 mode active and no canting. One other interesting feature is that there is no evident increase in the Fe1 moment with the onset of order in the Fe2 layer, though this could possibly be because the Fe1 and Fe2 moments in both layers are canted.

6.3.4. $Ca_2Fe_{2.7-\delta}O_3S_{0.5}Se_{1.5}$ (x = 1.5)

At room temperature, $Ca_2Fe_{2.7-\delta}O_3S_{0.5}Se_{1.5}$ is again not magnetically ordered. Magnetic reflections first appear around 220 K, but these include reflections that are different than the reflections that first arise for the x = 0.5 and 1 phases (Figure 6.24). These reflections represent the onset of magnetic order in the Fe1 layer and can be fit by activating the mM5+ and mA2+ modes, with the latter representing antiferromagnetic order along the *c*-lattice parameter and the mM5+ mode proving a slight canting towards the basal plane. Then, around 175 K, the canting towards the basal plane increases until at around 155 K the antiferromagnetic order has the moments all lying in the basal plane and the mA2+ Fe1 mode is no longer activated in the refinements (see Figure 6.25). At 75 K, there is then the onset of new magnetic reflections which correspond to the onset of magnetic order in the Fe2 layer and canting within the basal plane of the Fe1 moments. This means that at this temperature, the magnetic order in $Ca_2Fe_{2.7-\delta}O_3S_{0.5}Se_{1.5}$ is similar to that in the x = 1 phase at 5 K, with the same mX1- and mX2- modes being active for the Fe2 layer and the mX1- E_g(a) modes being active. Then, around 40-50 K, peaks emerge that are similar to those evident between 155-220 K which corresponded to the orientation of the Fe1 moments along the *c*-axis (see above). This intensity can be fit by activating the mA2+ modes for the Fe1 layer along with the mA5+ mode in the Fe2 layer meaning than both the Fe1 and Fe2

moments are canted along the *c*-axis at 5 K. At 5 K, the Fe1 and Fe2 moments refine to 4.11(8) μ_B and 2.04(6) μ_B respectively, and the model of the magnetic order is shown in Figure 6.26.

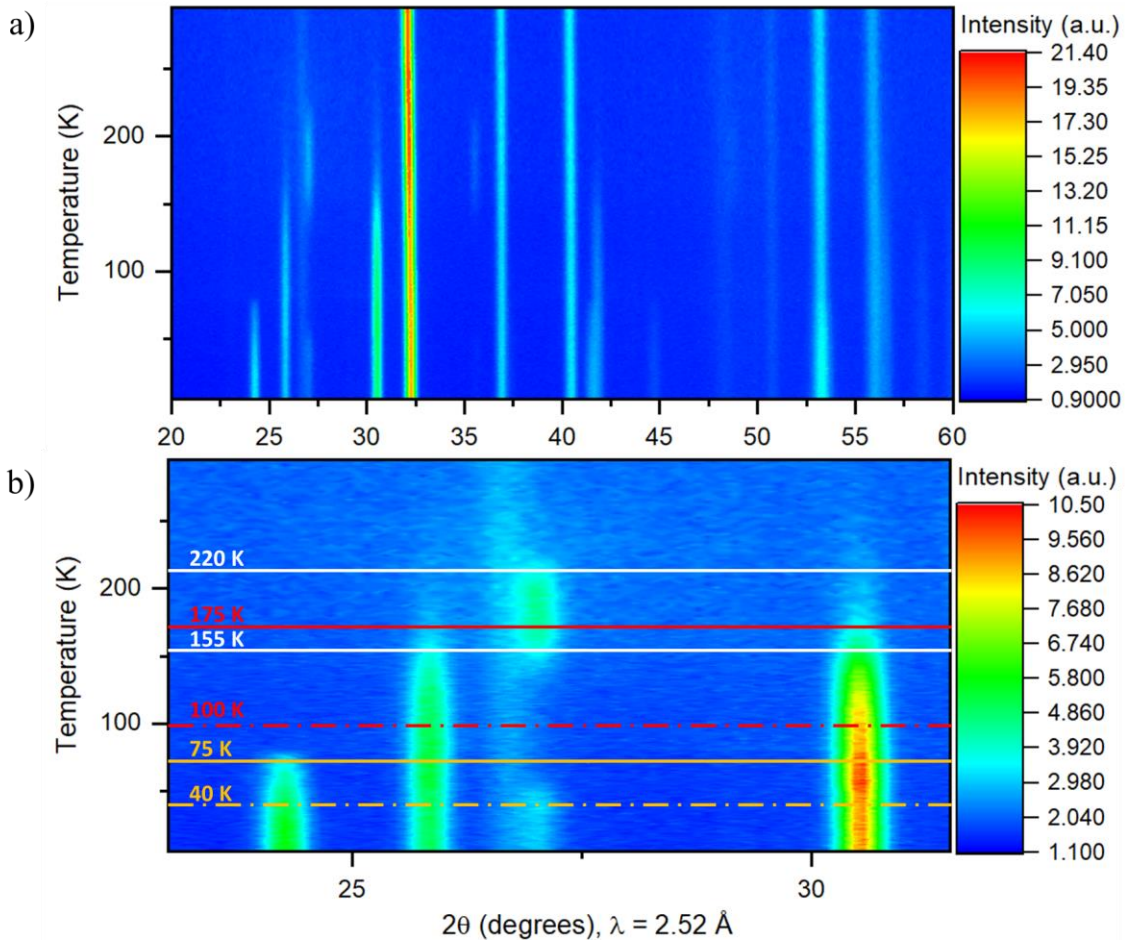


Figure 6.24. Contour plot showing a) the full and b) zoomed in neutron diffraction patterns of $Ca_2Fe_{2.7-\delta}O_3S_{0.5}Se_{1.5}$ with the onset of magnetic peaks indicated by solid lines and the saturation of those peaks indicated in dashed lines. The red lines indicate magnetic reflections corresponding to the Fe1 layer and orange lines indicate those of the Fe2 layer. White lines indicate the onset and then disappearance of magnetic peaks that indicate spin orientation along the *c*-axis.

In comparing the contour plot with the magnetometry data for these phases collected by Sheath, it is evident that the onset and change of order in the Fe1 layer corresponds to the broad 'hump' around 220-150 K and the peak around 70 K corresponds to the onset of order in the Fe2 layer like for the $x = 0.5$ and 1 phases.

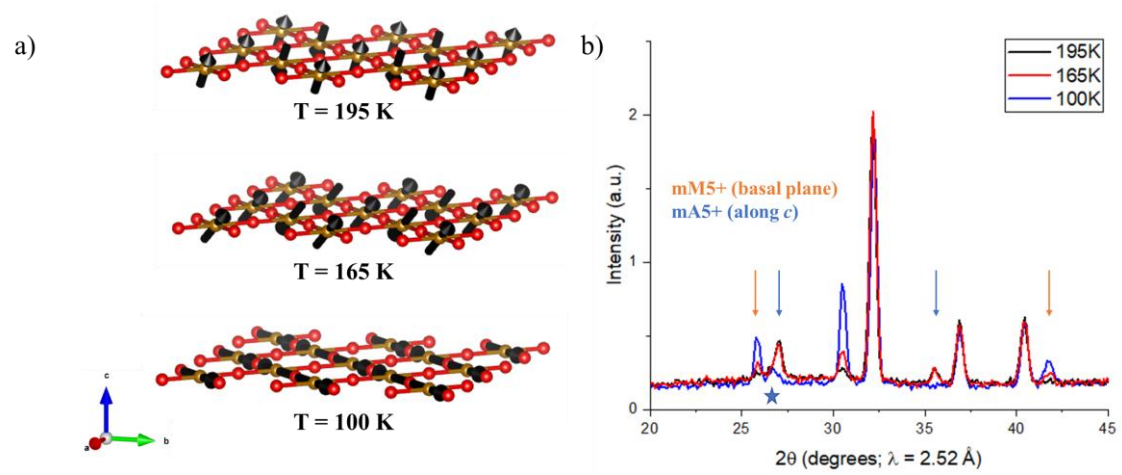


Figure 6.25. a) Refined magnetic models of the Fe1 layer in $Ca_2Fe_{2.7-\delta}O_3S_{0.5}Se_{1.5}$ at T = 195 K, 165 K, and 100 K alongside b) diffraction patterns at the same temperatures. Blue arrows indicate magnetic reflections that are accounted for by the mA5+ mode (corresponds to ordering of the moments along *c*) and orange arrows indicate magnetic reflections that are accounted for by the mM5+ (corresponds to ordering of the moments within the basal plane). The blue star in (b) indicates the location of a nuclear reflection that is unindexed but is present in the room-temperature pattern.

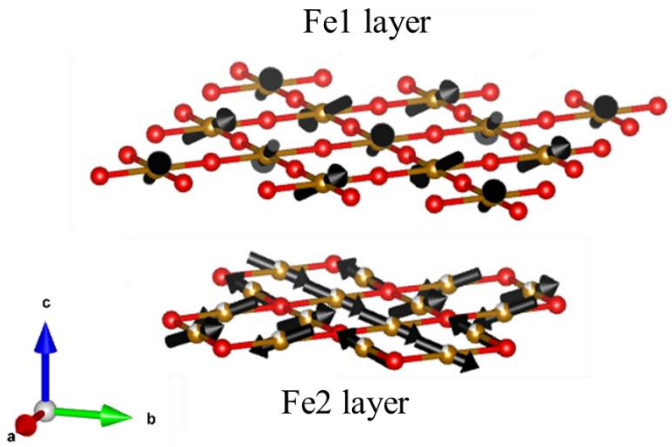


Figure 6.26. The magnetic model of the Fe1 and Fe2 layers in $Ca_2Fe_{2.7-\delta}O_3S_{0.5}Se_{1.5}$ at T = 5 K.

The magnetic models presented here are very similar to those presented by Sheath, with the exception that in Sheath's model, only the Fe1 layer was refined to be canted along *c* and only the Fe2 layer displayed canting in the basal plane whereas in the model displayed in Figure 6.26, both layers are canted both within the basal plane and along *c*. Both of these models were considered in the analysis of the D1B data, but allowing both layers to cant in both directions at 5 K resulted in the refinement with the lowest R_{wp} value and the lowest errors on the refined moments.

The evolution of the magnitude of the magnetic moments of the Fe1 and Fe2 irons is shown in Figure 6.27. Given the complexity in the changes of the magnetic structure of $Ca_2Fe_{2.7-\delta}O_3S_{0.5}Se_{1.5}$ upon cooling, a multi-refinement was not carried out since the errors on the magnetic moments often became quite unreasonable. However, individual refinements at selected temperatures still reveal a clear trend wherein the moments increase as the temperature decreases, with the Fe1 moment having an extra increase that seems to correspond to the onset of order in the Fe2 layer.

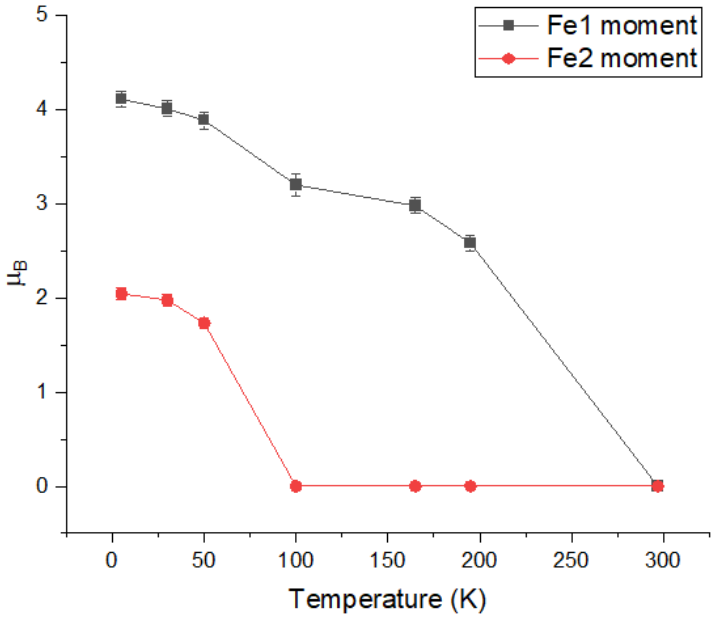


Figure 6.27. Refined magnetic moments of $Ca_2Fe_{2.7-\delta}O_3S_{0.5}Se_{1.5}$ as a function of temperature.

6.3.5. Summary of Trends

In general, the magnetic structures of the $x = 0.5$ and $x = 1$ phases go through very similar changes upon cooling. The ordering pattern is overall antiferromagnetic and governed by the Fe-O-Fe 180˚ superexchange. In addition to this, the Fe1 layer orders first, with the onset of magnetic order in the Fe2 layer occurring around 60 K. In both phases, the onset of order in the Fe2 layer is best modelled by the simultaneous appearance of a canting within the basal plane of the Fe1 moments. One difference between the two phases though is that in the $x = 1$ phase, the Fe2 layer also exhibits some canting within the basal plane whereas the $x = 0.5$ layer does not. In addition to this, the temperature at which the Fe1 layer orders is higher for the $x = 0.5$ phase than the $x = 1$ phase.

The member of this solid solution that is the most different, however, is the $x = 1.5$ phase. This is the only phase to exhibit any magnitude of the magnetic moments out of the basal plane and along the *c*-direction, with the Fe1 moments being mainly directed along *c* at the onset of long-range order in the Fe1 layer with a slight canting toward the basal plane. The Fe1 moments then re-orient to lie entirely in the basal plane by around 155 K on cooling. All of the moments then remain in the basal plane as the Fe2 layer orders magnetically at 75 K, when a canting in the basal plane of the Fe1 moments is induced as well as the Fe2 moments also being canted like in the $x = 1$ phase. Then around 40 K, the spins in both layers begin to undergo some reorientation and again are canted along c and out of the basal plane. The fact that the $x = 1.5$ phase is the only phase to display any spin orientation along *c* likely has to do with the size of the chalcogen. As Sheath proposed, one superexchange pathway is the pink Fe-*Ch*-*Ch*-Fe pathway in Figure 6.28. Since the Se^{2-} 4*p* orbitals are more radially distributed than the S^{2-} 3*p* orbitals, allowing for greater overlap with the Fe 3*d* orbitals involved in the pathway, which would lead to antiferromagnetic order along the Fe-*Ch*-*Ch*-Fe pathway. Since the moments of the Fe1 atoms in adjacent layers align ferromagnetically in the basal plane, this antiferromagnetic order is established as a component to the spins that is along *c*.

Table 6.6. Refined magnetic parameters of the solid solution $Ca_2Fe_{2.7-\delta}O_3S_{2-x}Se_x$ ($x = 0$, 0.5, 1, 1.5).

x	0[1]	0.5	1	1.5
Fe1 ordering temp (K)	>300	260	220	220
Fe2 ordering temp (K)	70	60	60	75
5 K Fe1 moment (μ_B)	3.77(7)	4.02(11)	3.77(6)	4.11(8)
5 K Fe2 moment (μ_B)	2.53(8)	0.97(10)	1.61(3)	2.04(6)

[1]As reported in Bradley Sheath's thesis [2].

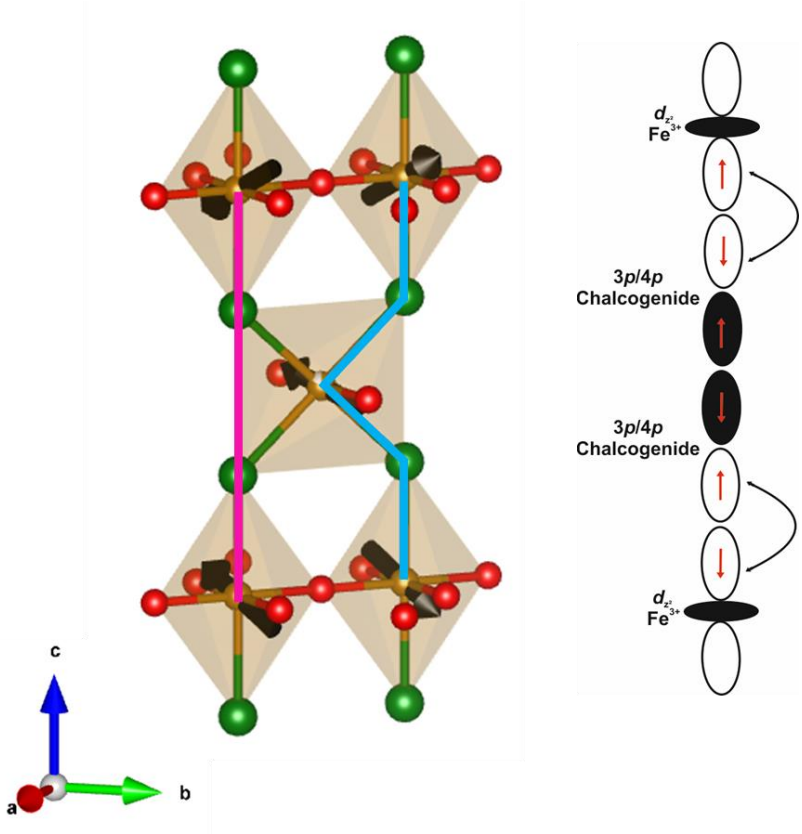


Figure 6.28. Possible superexchange pathways recommended by Sheath in his thesis over which the Fe1 atoms could interact. The orbital interactions along the pink Fe-*Ch*-*Ch*-Fe pathway are shown on the right. [2]

6.4. Conclusions

In this chapter, several experiments were conducted in an effort to expand upon previous work done on the solid solution $Ca_2Fe_{2.7-\delta}O_3S_{2-x}Se_x$ and give light to some of the intricacies that had not yet been resolved. In relation to the all-sulfide phase, the superstructure generated by the long-range order of Fe vacancies was determined via SC-XRD. The superstructure was determined to be in the space group *Aea*2 and not *Aeam*, as evidenced by the significant decrease in the *R*-factor which supports the non-centrosymmetric space group, thereby resolving a lingering question from work done by Bradley Sheath [2]. It was also determined that not only can this long-range order of Fe vacancies be suppressed by *Ch* disorder and high-pressure synthesis, but also by melting the sample, though neither high-pressure synthesis nor melting yields a phase-pure product. A neutron powder diffraction experiment in an applied magnetic field was also conducted on the all-sulfide phase in an effort to investigate the source of

anomalous features in the 5 K magnetization isotherm, but while there were changes to peak intensities with a change in applied field, the changes could be fit by changes in the nuclear structure, magnetic structure, preferred orientation, or any combination of the three thereby rendering the experiment inconclusive.

In addition to this, the magnetic structures of the solid solution phases x = 0.5, 1, and 1.5 were also investigated in more depth with an instrument (D1B) with better resolution at large *d*-spacings than that which was used in Bradley Sheath's investigations (D2B) as well as at more temperatures. This revealed that overall, the ordering of the solid solution phases was antiferromagnetic as suspected, but with different canting patterns than were determined from the refinements of patterns collected on D2B. In terms of the x = 0.5 and x = 1 phases, the Fe1 moments ordered in the same manner, being antiferromagnetically ordered along the Fe-O-Fe superexchanges beginning at 260 K and 220 K respectively and then canting within the basal plane with the onset of order in the Fe2 layer at 60 K for both phases. The difference between the two phases is that when the Fe2 layer orders, the moments are not canted for the x = 0.5 phase but they are for the x = 1 phase.

The x = 1.5 phase has an extra intricacy in that it is the only phase for which the moments order out of the basal plane. At 220 K, long-range magnetic order is onset for the Fe1 layer along *c* and canted towards the basal plane, but then undergoes a gradual reorientation and is fully oriented in the basal plane around 150 K. The Fe2 layer then orders around 75 K and induces a canting in the basal plane for the Fe1 layer, and like the x = 1 phase, the Fe2 layer is also canted in the basal plane. Then, at 40 K, the spins in both layers undergo a reorientation to cant along *c*. The reason this canting along *c* occurs in the phase with the largest amount of Se is likely because, as Sheath suggested, the Se^{2-} 4p orbitals are more radially distributed than the S^{2-} 3p orbitals allowing for greater overlap with the Fe 3d orbitals involved in the Fe-*Ch*-*Ch*-Fe pathway in Figure 6.28.

Chapter 7: Conclusions

This thesis has described the synthesis as well as the structural and magnetic characterization of several new layered mixed-valent iron oxychalcogenides that are variations of a targeted intergrowth of an $[Ae_{n+1}M_nO_{3n-1}]^{2+}$ (*Ae* = Sr, *M* = Fe, *n* = 2) layer and a $[M_2OCh_2]^{2-}$ (*M* = Fe, *Ch* = S) layer.

Chapter 3 first presents the new structure type formed in the successful intergrowth of these two layers. $Sr_3Fe_2O_5Fe_2OS_2$ crystallizes in the primitive, tetragonal *P*4/*mmm* space group, with BVS supporting the existence of Fe^{3+} in the square-pyramid coordination environment in the cationic Fe1 layer while Fe^{2+} exists in distorted FeO_2S_4 octahedra in the anionic Fe2 layer as expected from charge balancing the respective layers. However, there is some sample dependence concerning the symmetry of the product. Some structural intricacies in select products are evidenced by features of the powder X-ray diffraction patterns like diffuse features between two of the main reflections that may indicate modulation as well as peak splitting of the (200)/(020) reflections that indicate a small orthorhombic distortion. High-resolution neutron powder diffraction did not reveal any indication that this distortion may be due to oxygen position variation comparable to octahedral tilting in perovskites, but electron diffraction and microscopy revealed some interesting features that gave more insight into the possible origin of these distortions. In the case of electron diffraction on the orthorhombic samples ANG012 and ANG022b, there were modulation vectors identified that were incommensurate in *a* and consistent with a doubling in *c* in addition to some twinning in select crystallites. HAADF-STEM imaging on ANG022b suggests that this modulation could possibly originate from ordered Fe-vacancies in the Fe2 layer. In addition to this, TEM imaging on the flux-grown tetragonal samples ANG044a and ANG047b revealed additional structural features like anti-phase boundaries and extended perovskite-type layers that formed and resolved inconsistently. Analysis of all of the

microscopy and electron diffraction experiments is ongoing and being conducted by Sepideh Rahimi and Joke Hadermann at the EMAT University of Antwerp, Belgium, and will form a significant part of Rahimi's PhD thesis.

In addition to the investigation into the nuclear structure of $Sr_3Fe_2O_5Fe_2OS_2$, chapter 3 also describes the magnetic structure characterization of the phase mainly by variable temperature neutron powder diffraction. In this phase, the Fe1 and Fe2 layers order independently of one another and each orders similarly to their respective counterparts in literature. The Fe1 layer is ordered at room temperature (long-range order of this layer is lost between 200-300°C) and it orders antiferromagnetically within individual layers along the Fe-O-Fe ~180° superexchange pathways as seen in similar phases like $Sr_3Fe_2O_5Cu_2S_2$ and others (see chapter 1.3.1). However, most similar phases are body centred which means that subsequent 'Fe1'-like layers are offset and the relationship between adjacent layers isn't significant. Phases that do have similar layers and have primitive symmetry so that layers are stacked directly atop one another, like $Pb_4Fe_3O_8X$ [1] and $YBa_2Fe_3O_8$ [2] show strictly antiferromagnetic ordering between subsequent layers. However, this is not the case for $Sr_3Fe_2O_5Fe_2OS_2$. Instead, there are two ways of modelling the relationship between the Fe1 layers which cannot be resolved by powder diffraction: a two-phase model and a single-phase twisting model. In the two-phase model, two distinct magnetic phases exist in the bulk of the model: one which has subsequent Fe1 layers ordered antiferromagnetically (and the magnetic unit cell is therefore doubled along *c*) and one which has them ordered ferromagnetically. Alternatively, these two phases can be combined into a single-phase twisting model in which the two layers are related by a "twisting angle" (see chapter 3.3.2 for more). The moments of these layers saturate to a magnitude of 3.99(4) μ_B around 140 K, and the growth of the magnetic peak showing this saturation can be attributed to the change in ratios between the two phases in the two-phase model or the change in the twisting angle by the single-phase twisting model. In addition to this, the magnetic structure in how the Fe1 layers relate to one another is sample dependent, as different samples show different ratios of the magnetic structures or the twisting angle as some samples have all magnetic reflections that describe the two phases/

twisting, and others only have one set of magnetic reflections or another. The Fe2 layer then orders at 115 K in the 2-**k** model that is displayed in other structures that contain this same layer type [3] and is moderated mainly by the Fe-O-Fe 180° antiferromagnetic superexchange and the Fe-S-Fe ~90° superexchange. This layer orders at similar temperatures and to a similar magnitude of moment (3.31(7) μ_B) as similar layers as well (see chapter 1.3.2).

Chapter 4 involves the substitution of Ca for Sr on the *Ae* site of $Sr_3Fe_2O_5Fe_2OS_2$ to form the solid solution of $Sr_{3-x}Ca_xFe_2O_5Fe_2OS_2$. Members of this solid solution with $x < 1$ do not form readily with the exception of $x = 0.4$ which crystallizes in the orthorhombic *Pmmm* space group as a slight distortion from a tetragonal symmetry. For the members $1 < x < 1.7$, the products are multiphase with a tetragonal and an orthorhombic phase (with an occasional exception). There is cation ordering observed in both phases for all of the samples, with the larger Sr cation preferentially occupying the larger 12-coordinate *Ae* site and the smaller Ca cation preferentially occupying the smaller 8-coordinate *Ae* site. Additionally, the lattice parameters and unit cell volume decrease across the series as expected as the smaller Ca cation is substituted for Sr. However, there are no other apparent trends across the series as to a relationship between the two phases as more Ca is incorporated. Phases with $x > 1.7$ cannot be formed in phase purity as a competing side-phase $Ca_2Fe_{2.7-\delta}O_3S_2$ is formed. Magnetically, these phases also order in the same manner as the parent phase with the Fe1 layer being ordered at room temperature, saturating around 140 K, and the Fe2 layer ordering around 115 K. The twisting angles for all of the phases are different which is not surprising given the sample dependence of the magnetic structure that was observed for the $x = 0$ phase. Additionally, the $x = 1$ phase shows slightly lower magnitude of ordered moments than $x = 0$ or 1.5, but there is not currently enough data to deduce if this is a trend or an effect of a sample dependence.

Chapter 5 discusses the topochemical reduction of $Sr_3Fe_2O_5Fe_2OS_2$ wherein LiH is used as a reducing agent to remove the axial bridging oxygen in the connected FeO_5 pyramids in the Fe1 layer thereby reducing the Fe^{3+} to Fe^{2+}. This reduction is successful, but produces a multiphase product which contains a partially-reduced phase and a fully reduced phase. Both the shift in

peak positions in X-ray powder diffraction and the shift in Fe K-edge in XANES show the progression of this reaction as the lattice parameters change (*a* increases slightly and *c* decreases) and the Fe^{3+} is reduced. The fully reduced phase also orders magnetically in the same manner as the parent, with the Fe1 layer ordering at room temperature with a slightly greater magnitude of 4.04(6) μ_B at room temperature and 4.23(4) μ_B at 5 K in the same two-phase or twisting model as the parent. The Fe2 layer orders between 100-107 K saturating to a magnitude of 3.39(6) μ_B in the same 2-**k** model.

Chapter 6 expands upon work done by Bradley Sheath [4] on the similar structure $Ca_2Fe_{2.7-\delta}O_3S_{2-x}Se_x$. Firstly, single-crystal X-ray diffraction resolves the room-temperature superstructure arising from Fe-vacancy ordering of the all -sulfide phase to be in the non-centrosymmetric *Aea*2 space group. A neutron powder diffraction experiment in an applied magnetic field for this all-sulfide phase conducted in an effort to investigate the source of anomalous features in the 5 K magnetization isotherm revealed changes to peak intensities with a change in applied field, but the changes could be fit by alterations to the nuclear structure, magnetic structure, preferred orientation, or any combination of the three thereby rendering the experiment inconclusive. In addition to this, the magnetic structures for the x = 0.5, 1, and 1.5 were investigated in more depth over various temperatures to expand upon Sheath's work.

For the x = 0.5 and x = 1 phases, the Fe1 moments ordered antiferromagnetically along the Fe-O-Fe superexchanges beginning at 260 K and 220 K respectively and then canting within the basal plane with the onset of order in the Fe2 layer at 60 K for both phases. The difference between the two phases is that when the Fe2 layer orders, the moments in that layer are not canted for the x = 0.5 phase but they are for the x = 1 phase. In contrast to these two phases, the x = 1.5 phase is the only phase for which the moments order out of the basal plane. At 220 K, the Fe1 layer orders antiferromagnetically along *c* canted towards the basal plane, but then undergoes a gradual reorientation and is fully oriented in the basal plane around 150 K. The Fe2 layer then orders around 75 K which induces a canting within the basal plane for the Fe1 layer, and like the x = 1 phase, the Fe2 layer is also canted in the basal plane at the onset of order. Then, at 40 K,

the spins in both layers undergo a reorientation to cant along *c*. The reason this canting along *c* occurs in the phase with the largest amount of Se is likely because of greater overlap in orbitals with the larger Se^{2-} anions increasing the significance of exchange interactions between layers as Sheath suggested.

While this thesis presents a few ways in which the new structure type of $Sr_3Fe_2O_5Fe_2OS_2$ can be chemically altered to form further new phases, there are certainly more ways in which the structure could be altered. Firstly, work by Annabel Lyon [5] has shown that another equivalent of SrO may be included in the Fe1 layer which separates the joined FeO_5 pyramids and shifts them to introduce a body centring symmetry. Further work characterizing the magnetic structure of this phase at varying temperatures is included in Appendix F. In addition to this alteration, further substitutions on the metal site, perhaps making use of the difference in oxidation states, may be possible as well as substitution on the chalcogen site.

References

[1] Knee, C.S.; Weller, M.T. *J. Mater. Chem.* **2001**, *11*, 2350-2357.
[2] Azad, A.K.; Zakaria, A.K.M.; Ahmed, F.U.; Paranjpe, S.K.; Das, A. *J. Magn. Magn. Mater.* **2000**, *214*, 251-257.
[3] Fuwa, Y. Wakeshima, M. Hinatsu, Y. *J. Phys. Condens. Matter.* **2010**, *22*, 346003.
[4] Sheath, B.C. DPhil Thesis, *University of Oxford*, Exploring the Synthesis and Characterization of Oxychalcogenide, Oxypnictide and Chalcogenide Materials, **2023**.
[5] Lyon, A.L. MSc. Thesis, *University of Oxford*, "Structures and Magnetism of layered iron oxide chalcogenides," **2024**.

References

[1] Zhang, H.; Wu, X.; Li, D.; Jin, S.; Chen, X.; Zhang, T.; Lin, Z.; Shen, S.; Yuan, D.; Chen, X. *J. Phys.: Condens. Matter.* **2016**, *28*, 145701.

[2] Sheath, B.C. *DPhil Thesis, University of Oxford*, Exploring the Synthesis and Characterization of Oxychalcogenide, Oxypnictide and Chalcogenide Materials, **2023**.

[3] Rodríguez-Velamazán, J.A.; Noguera, P. *J. Phys: Conf. Ser.* **2011**, *325*, 012022.

Appendices

Contents

Appendix A: Example refinements of data collected in banks not included in the text 188

Appendix B: Reference table of $Sr_3Fe_2O_5Fe_2OS_2$ samples 190

Appendix C: Refinement of sample ANG020, targeted composition $Sr_3Fe_{3.9}O_6S_2$. 190

Appendix D: Comparison of orthorhombic vs monoclinic space groups for $Sr_3Fe_2O_5Fe_2OS_2$ (ANG022b) 191

Appendix E: High VT-NPD data collected on HRPD for tetragonal $Sr_3Fe_2O_5Fe_2OS_2$ (ANG074) 192

Appendix F: VT-NPD data collected on D1B for $Sr_4Fe_2O_6Fe_2OS_2$ 193

References 194

Appendix A: Example refinements of data collected in banks not included in the text

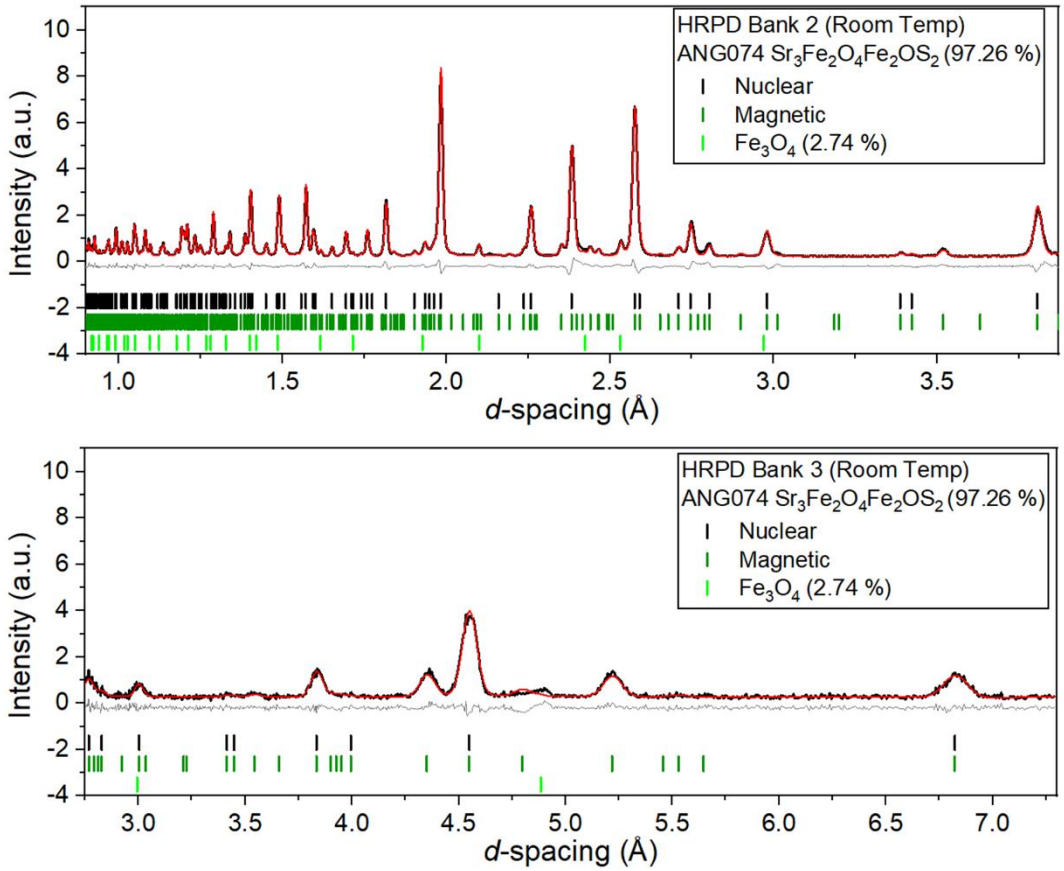


Figure A.1. Refined NPD patterns collected on HRPD banks 2 (top) and 3 (bottom) for $Sr_3Fe_2O_5Fe_2OS_2$ (ANG074) at room temperature showing the observed (black), calculated (red), and difference (grey) curves. Bank 1 is shown in the text as Figure 3.11.

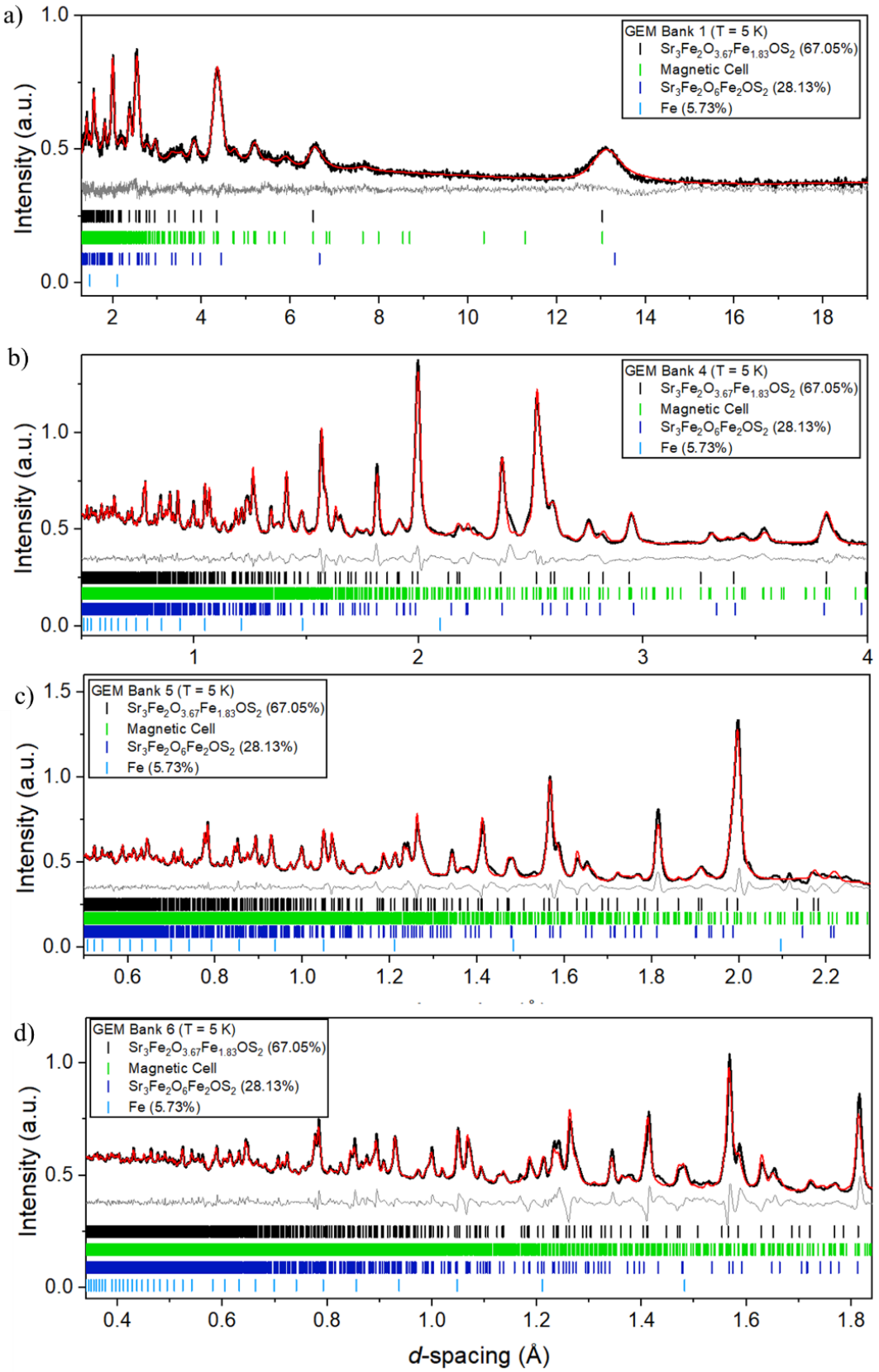


Figure A.2. Refined NPD patterns collected on GEM banks 1, 4, 5, and 6 for $Sr_3Fe_2O_4Fe_2OS_2$ (ANG086f) at T = 5 K showing the observed (black), calculated (red), and difference (grey) curves. Banks 2 and 3 are shown in the text as Figures 5.19 and 5.20a.

Appendix B: Reference table of $Sr_3Fe_2O_5Fe_2OS_2$ samples

Table B.1. Synthesis conditions and symmetries of various $Sr_3Fe_2O_5Fe_2OS_2$ samples discussed in Chapter 3.

Sample No.	Synthesis conditions	Crystal System
ANG012	Ceramic	Orthorhombic
ANG022	Ceramic	Tetragonal
ANG022b	Ceramic, long anneal	Orthorhombic
ANG044a	Flux	Tetragonal
ANG047b	Flux	Tetragonal
ANG072b	Ceramic, long anneal	Orthorhombic
ANG074	Ceramic	Tetragonal
ANG075b	Ceramic, long anneal	Tetragonal

Appendix C: Refinement of sample ANG020, targeted composition $Sr_3Fe_{3.9}O_6S_2$.

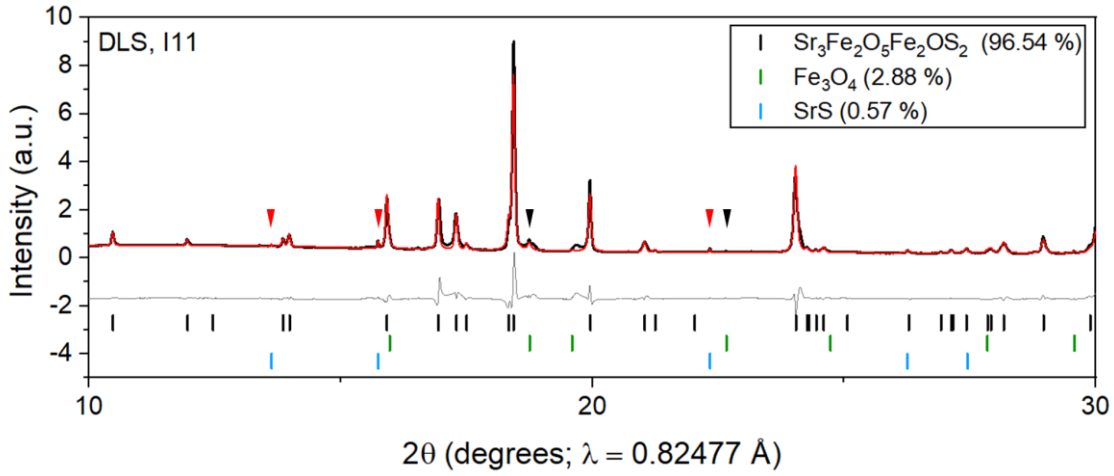


Figure C.1. Rietveld refinement of room temperature SXRPD pattern collected on I11 for sample ANG020 which targeted the iron-deficient composition $Sr_3Fe_{3.9}O_6S_2$ showing the observed (black), calculated (red), and difference (grey) curves (R_{wp} = 7.373 %). Black triangles indicate impurity peaks from Fe_3O_4 and red triangles indicate those for the impurity SrS.

Appendix D: Comparison of orthorhombic vs monoclinic space groups for $Sr_3Fe_2O_5Fe_2OS_2$ (ANG022b)

Table D.1. Comparison of refined parameters for $Sr_3Fe_2O_5Fe_2OS_2$ (ANG022b) with an orthorhombic and monoclinic space group from SXRPD data collected on I11.

Space Group	*Pmmm*	*P*2/*m*
R_{wp} (%)	4.682	4.432
a (Å)	3.95571(2)	3.95565(2)
b (Å)	3.93948(3)	3.93892(3)
c (Å)	13.5644(1)	13.5645(1)
β (°)	90	90.0545(8)
V (Å^3)	211.381(3)	211.348(3)
*z*Sr2	0.22734(7)	0.22728(7)
*z*Fe1	0.3622(1)	0.3623(1)
*z*O1	0.3407(2)	0.3407(2)
*z*S	0.1280(2)	0.1381(2)

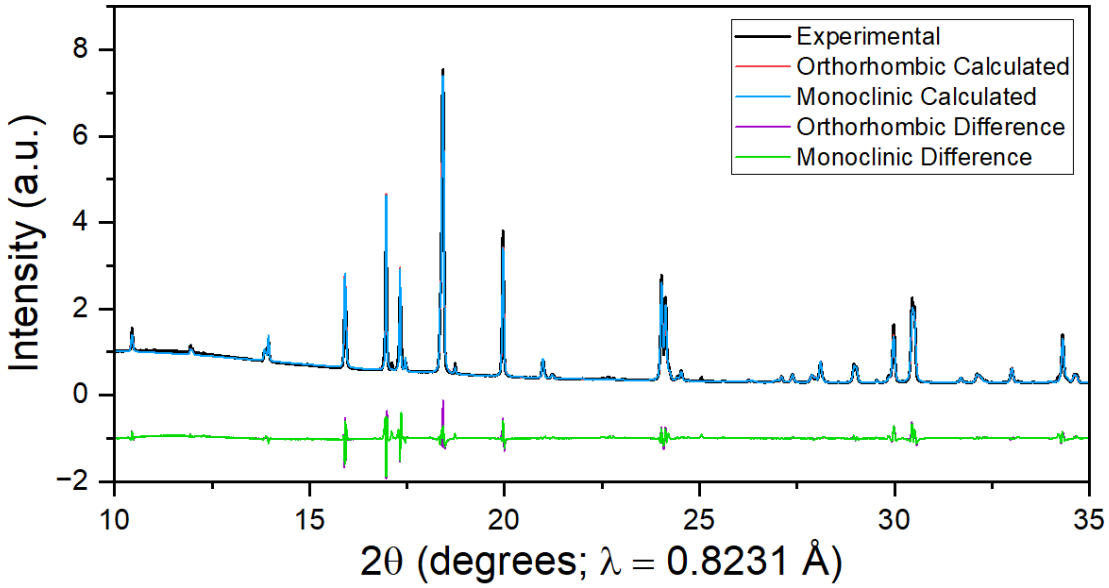


Figure D.1. Comparison of refinements for $Sr_3Fe_2O_5Fe_2OS_2$ (ANG022b) with an orthorhombic and monoclinic space group from SXRPD data collected on I11.

As Figure D.1. shows, there is not an observable difference in the refinements themselves when using an orthorhombic vs tetragonal space group, with the difference curves showing that the most observable difference is on the main (104) reflection which can be accounted for a bit better in the orthorhombic refinement by adding more preferred orientation parameters. Table D.1. also shows that there are only minute differences in the cell from an orthorhombic to monoclinic distortion, with the β angle refining to only slightly more than 90°. With this in mind, it was determined that there was not enough support for a monoclinic distortion and the rest of the

analysis on phases distorted from tetragonal symmetry were carried out using the orthorhombic *Pmmm* space group.

Appendix E: High VT-NPD data collected on HRPD for tetragonal $Sr_3Fe_2O_5Fe_2OS_2$ (ANG074)

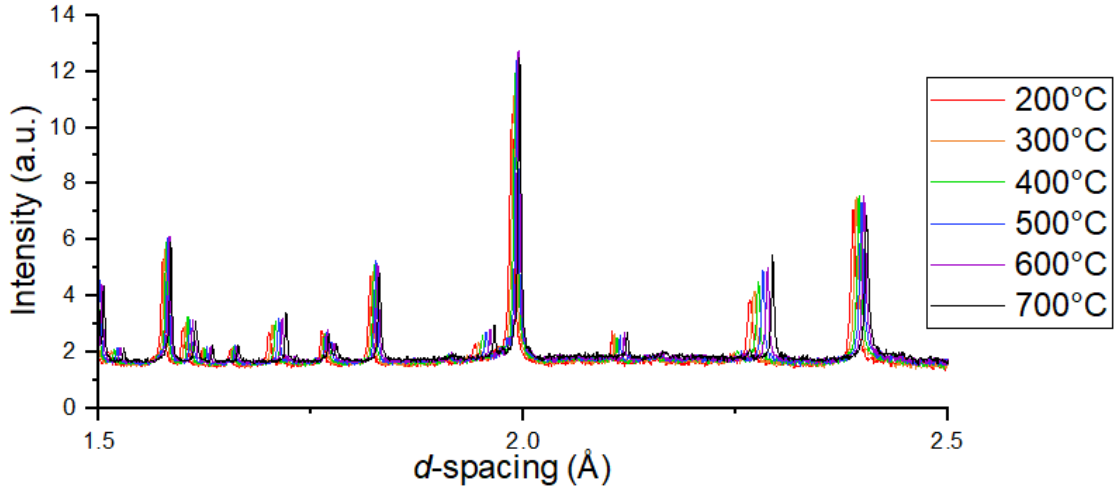


Figure E.1. Neutron powder diffraction patterns collected on HRPD bank 1 for $Sr_3Fe_2O_5Fe_2OS_2$ (ANG074) at various temperatures.

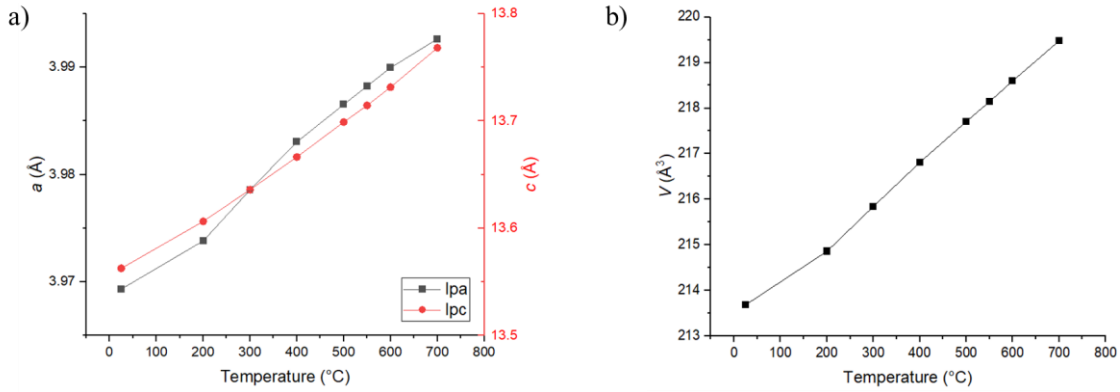


Figure E.2. Change in a) the refined lattice parameters and b) the unit cell volume as a function of temperature for $Sr_3Fe_2O_5Fe_2OS_2$ (ANG074) from NPD patterns collected on HRPD. Note that the error bars are smaller than the points. Note also that all of the refinements above 300°C were carried out without the magnetic structure, as the structure is no longer magnetically ordered at these temperatures.

As Figure C.2 shows, there is a slight change in the expansion of the *a* lattice parameter between 200°C and 300°C which coincides with the loss of long-range magnetic order. This is also above the temperature at which the sample measured for SXRPD at I11 (Figure 3.10) becan decomposing. There are no other changes that indicate a phase change on heating, though, and this shows that the compound $Sr_3Fe_2O_5Fe_2OS_2$ is stable in an inert atmosphere up to 700°C

meaning that the change in peak shape shown in Figure 3.10b is an artefact supposedly from decomposition in air due to a leaking capillary.

Appendix F: VT-NPD data collected on D1B for $Sr_4Fe_2O_6Fe_2OS_2$

The magnetic structure of $Sr_4Fe_2O_6Fe_2OS_2$ was previously characterized and reported by Annabel Lyon, a former master's student and current DPhil student in the Clarke group [1]. Lyon reported the magnetic structure of this phase at low temperatures (T = 5 K) and room temperature from diffraction pattens collected on XtremeD at the ILL and GEM at ISIS neutron and muon source. Another neutron powder diffraction experiment was planned on beamline D1B at the ILL to collect neutron powder diffraction patterns at a continuous heating rate to observe more minute changes in the magnetic structure over a temperature range. The refinements performed to generate Figure F.2 used the magnetic model identified by Lyon [1].

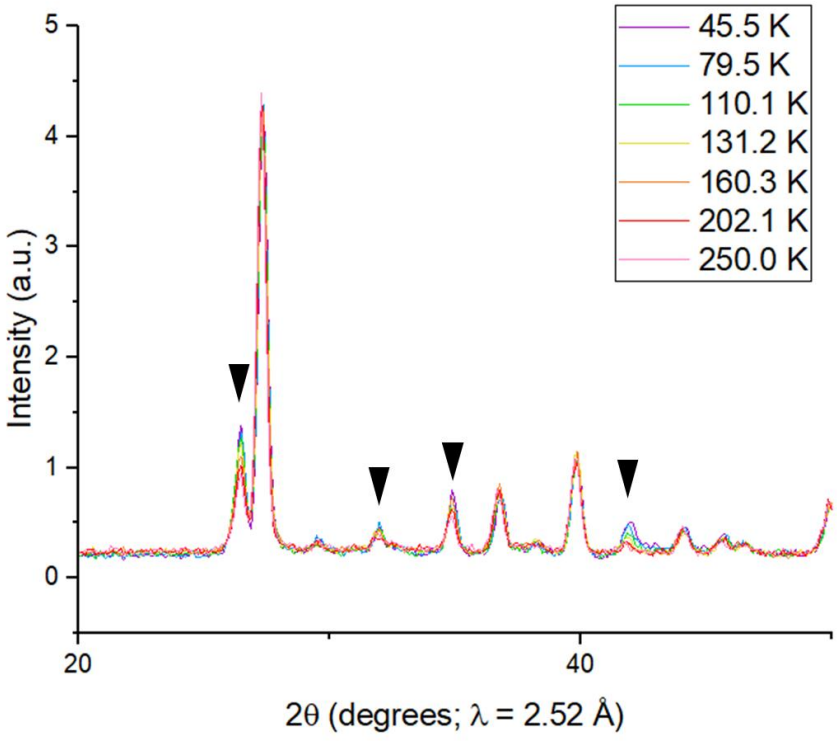


Figure F.1. Comparison of NPD patterns of $Sr_4Fe_2O_6Fe_2OS_2$ collected on D1B at the ILL at various temperatures.

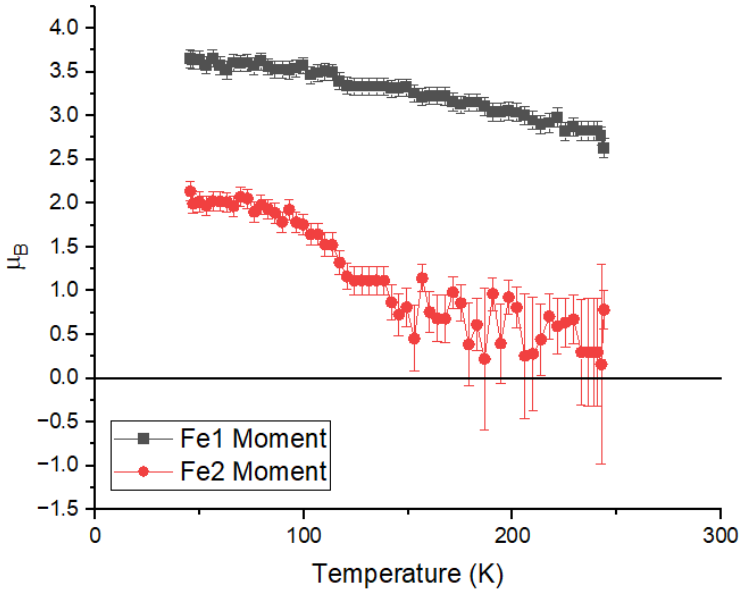


Figure F.2. Refined moments of the Fe1 and Fe2 ions in $Sr_4Fe_2O_6Fe_2OS_2$ from T = 45 K to 250 K refined from NPD data collected on D1B at the ILL.

As Figure F.1 shows, there is a decrease in the intensity of several magnetic peaks over the temperature range. In a sequential refinement, it is shown that the magnitude of the Fe1 moment decreases somewhat linearly over the temperature range whereas the Fe2 moment has a more dramatic drop-off after around 100 K where there is also an increase in the calculated errors. It seems as if by around 150 K, the Fe2 moment has likely reduced to zero which is around the temperature which Lyon [1] had identified as the likely temperature where the Fe2 layer loses long-range magnetic order in this structure. Note that this is a higher temperature than usual for $[M_2OCh_2]^{2-}$ layers normally in literature (see chapter 1.3.2), which may indicate that the *c*-canting of the moments in the Fe1 layer may have a stabilizing effect on the Fe2 magnetic lattice.

References

[1] Lyon, A.L. MSc. Thesis, *University of Oxford*, "Structures and Magnetism of layered iron oxide chalcogenides," **2024**.